A Probabilistic and Multi-Objective Conceptual Design Methodology for the Evaluation of Thermal Management Systems on Air-Breathing Hypersonic Vehicles

A Thesis
Presented to
The Academic Faculty

by

Irian Ordaz

In Partial Fulfillment
of the Requirements for the Degree
Doctor of Philosophy

School of Aerospace Engineering
Georgia Institute of Technology
December 2008

A Probabilistic and Multi-Objective Conceptual Design Methodology for the Evaluation of Thermal Management Systems on Air-Breathing Hypersonic Vehicles

Approved by:

Prof. Dimitri N. Mavris, Advisor
Committee Chair
School of Aerospace Engineering
Georgia Institute of Technology

Prof. Daniel P. Schrage
School of Aerospace Engineering
Georgia Institute of Technology

Prof. Brian J. German
School of Aerospace Engineering
Georgia Institute of Technology

Prof. Stephen M. Ruffin
School of Aerospace Engineering
Georgia Institute of Technology

Dr. Jan Osburg
Associate Engineer
The RAND Corporation

Date Approved: November 2008

To my parents, brother, and wife Tracy, for your patience, love, and support.

ACKNOWLEDGEMENTS

First and foremost I need to thank Dr. Mavris for believing in me and giving me this wonderful opportunity. I can honestly say I would not have pursued my PhD if it wasn't for him. The energy, drive, and motivation which he brings to ASDL have been great inspiration to me throughout my years here. I would like to thank all other members of my committee: Dr. Schrage, Dr, German, Dr. Ruffin, and Dr. Osburg. I am honored to have had their extensive experience and expertise during this process. I also need to specifically thank Dr. German, for his great input and feedback, and for devoting his valuable time to our very helpful monthly review meetings.

To Dr. Kirby I am grateful for her belief in me and for her help to transition me into ASDL. I received my first taste of actual aerospace research and gained a lot of experience while working with her during my undergraduate years. I would like to thank Dr. Villeneuve for his guidance, and expertise regarding trajectory and sizing of high speed vehicles. I would like to express my appreciation to ASDL in general and especially Kristin Kelly, Ousmane Diallo, Kyunghoon Lee, Dr. Tetsushi, Dr. Dufresne and many others that are just too many to mention. I also cannot forget my great friend Mandy Goltsch, for putting up with my numerous questions and helping me along the process.

I have to thank my family for always being there, especially my brother Ivan Ordaz, and parents Rolando A. Ordaz and Miriam Ordaz. Their devotion and self-sacrifice to my brother and I cannot be expressed in a few sentences. I owe everything to you and you are the reason I am. Last, but not least, to the love of my life, my wife Tracy. I cannot imagine what my life would have been if you were not by my side. You have been there for me through the tough times, and your love and support is what continues to drive me daily.

Thank you all,

Irian

November 2008

Contents

List of Tables

List of Figures

LIST OF ABBREVIATIONS AND SYMBOLS

Abbreviations

Ac	Scramjet capture area
ACC	Advanced carbon composite
AETB	Alumina enhanced thermal barrier
AFRSI	Advanced flexible reusable surface insulation
AMHC	Advanced metallic honeycomb
AoA	Angle of attack
ARES	Affordable responsive spacelift
ARSM	Adaptive response surface methodology
CCD	Central composite design
CDF	Cumulative distribution function
CEF	Cost escalation factor
CFD	Computational fluid dynamics
DoE	Design of experiments
DSM	Design structure matrix
EDF	Empirical distribution function
ESA	Energy state approximation
F	Fahrenheit
FOM	Figure of merit
FPI	Fast probability integration
FPR	Fan pressure ratio
FRCI	Fibrous refractory composite insulation
FRSI	Felt reusable surface insulation

GP	Goal programming
GRG	Generalized reduced gradient
HS	High-speed shock-on-lip Mach number
SA/HC	Super alloy honeycomb
IMI	Internal multiscreen insulation
IPPD	Integrated product and process development
JPDM	Joint probability decision making
K	Kelvin
L/D	Lift-to-drag ratio
LATCH	Langley approximate three-dimensional convective heating
LCC	Life cycle cost
LI	Silica fibrous insulation
LP	Linear programming
LS	Low-speed shock-on-lip Mach number
MADM	Multiple attribute decision making
MCO	Multiple criteria optimization
MCS	Monte Carlo simulation
MER	Mass estimating relationship
MFE	Model fit error
MODM	Multi-objective decision making
MoFD	Method of feasible directions
MPP	Most probable point
MRE	Model representation error
NAI	National aerospace initiative

NBI	Normal boundary intersection
NPF	Net propulsive force
OPR	Overall pressure ratio
PBI	Polybenzimidazole blanket insulation
PDF	Probability density function
PF	Pareto fitness
PJPDM	Pareto-based joint probability decision making
POS	Probability of success
QFD	Quality function deployment
RASAC	Rapid Access to Space Analysis Code
RASAC	Rapid access to space analysis code
RCC	Reinforced carbon-carbon
RFP	Request for proposal
RLV	Reusable launch vehicles
RSE	Response surface equation
RSM	Response surface methodology
SHABP	Supersonic hypersonic arbitrary body program
SM	Safety margin
SQP	Sequential quadratic programming
TABI	Tailorable advanced blanket insulation
TBCC	Turbine-based combined cycle
TI/HC	Titanium honeycomb
TMC	Titanium matrix composite
TMS	Thermal management systems

TMSS	Thermal management system sizer
TOGW	Takeoff gross weight
TOPSIS	Technique for order preference by similarity to ideal solution
TPS	Thermal protection system
TR	Throttle ratio
TSFC	Thrust specific fuel consumption
TUFI	Toughened unipiece fibrous insulation
VSP	Vehicle sketch pad
WS	Weighted sum

Mathematical Symbols

AC_{sj}	Scramjet capture area
AC_{tj}	Turbojet capture area
AC_{total}	Total engine capture area
b_{ii}	Second order regression term for response surface equation
b_{ij}	Cross-product regression term for response surface equation
b_i	First order regression term for response surface equation
b_o	Intercept term for response surface equation
$\bar{C}_{D,i}$	Average induced drag coefficient at each time interval for Jackson Energy Method
$\bar{C}_{L,o}$	Average lift coefficient at zero degree angle of attack during each interval of Jackson Energy Method
$\bar{C}_L$	Average coefficient of lift at each time interval for Jackson Energy Method
c	Numerical optimizer constraints Wing chord length

C_p	Coefficient of pressure Specific heat
$C_{(e+a)_m}$	Cost of engine and avionics for the airplanes and airframes required for the manufacturing phase, USD
$C_{(e+a)_r}$	Cost of engine and avionics for the airplanes and airframes required for the RDTE phase, USD
C_{acq}	Total cost of acquisition, USD
C_{aed_m}	Airframe engineering and design cost during manufacturing phase, USD
C_{aed_r}	Airframe engineering and design cost during RDTE phase, USD
C_{apc_m}	Airplane production cost, USD
$C_{avionics_m}$	Cost of avionics equipment per airplane during manufacturing phase, USD
$C_{avionics_r}$	Cost of avionics equipment per airplane during RDTE phase, USD
C_{conmat}	Program cost of consumable materials used in conjunction with maintenance, USD
C_{crewpr}	Crew cost for airplane program, USD
C_{depot}	Program cost associated with depots, USD
C_{disp}	Total cost of the disposal phase, USD
C_{dst_r}	Development support and test cost during RDTE phase, USD
C_D	Total coefficient of drag
C_{e_m}	Cost per engine during manufacturing phase, USD
C_{e_r}	Cost per engine during RDTE phase, USD
C_{fin_m}	Financing cost during manufacturing phase, USD
C_{fin_r}	Financing cost during RDTE phase, USD
C_{fta_r}	Cost for flight test airplanes during RDTE phase, USD
C_{fto_m}	Flight test operations cost during manufacturing phase, USD

C_{fto_r}	Flight test operations cost during RDTE phase, USD
C_{int_m}	Cost of interior, USD
C_L	Total coefficient of lift
C_{man_m}	Manufacturing cost of the flight test airplanes during manufacturing phase, USD
C_{man_r}	Manufacturing cost of the flight test airplanes during RDTE phase, USD
C_{man}	Total cost of manufacturing phase, USD
C_{mat_m}	Cost of materials to manufacture the flight test airplanes during manufacturing phase, USD
$C_{mat_{program}}$	Total materials cost associated with building $N_{program}$ airplanes, USD
C_{mat_r}	Cost of materials to manufacture the flight test airplanes during RDTE phase, USD
C_{misc}	Program miscellaneous cost, USD
$C_{mpersdir}$	Program cost for direct maintenance personnel, USD
$C_{ops/hr}$	Airplane operating cost per hour, USD/hr
C_{ops}	Total cost of the operations phase, USD
C_{p_m}	Cost per propeller during manufacturing phase, USD
C_{p_r}	Cost per propeller during RDTE phase, USD
$C_{persdir}$	Program cost of direct personnel (aircrew and maintenance), USD
$C_{persind}$	Prorgam cost of inderect personnel, USD
C_{pol}	Program cost of fuel, oil and lubricants, USD
C_{pro_m}	Manufacturer's profit, USD
C_{pro_r}	RDTE profit, USD
C_{qc_m}	Quality control cost associated with manufacturing phase, USD

C_{qc_r}	Quality control cost associated with manufacturing of the flight test airplanes during RDTE phase, USD
C_{rdte}	Total cost of the RDTE phases, USD
C_{spares}	Program cost of spares, USD
C_{tool_m}	Tooling cost associated with the manufacturing phase, USD
C_{tool_r}	Tooling cost associated with the manufacturing of flight test airplanes during RDTE phase, USD
C_{tsf_r}	Test and simulation facilities cost during RDTE phase, USD
$C_{D,i}$	Induced drag coefficient
D	Vehicle drag force
D_{body}	Body drag
D_{plume}	Plume drag
$D_{ram_{sj}}$	Scramjet ram drag
$D_{ram_{tj}}$	Turbojet ram drag
$D_{spill_{sj}}$	Scramjet spill drag
$D_{spill_{tj}}$	Turbojet spill drag
E	Total energy
F	Objective function for numerical optimizer
F_{cad}	Judgement factor which accounts for the effect of computer aided design capability on airframe engineering and design cost. For manufactures which are in a CAD learning mode use 1.2, for manufacturers which are using "manual" drafting techniques use 1.0, and for manufacturers which are experienced in the use of CAD use 0.8.
f_{depot}	Depot cost fraction of C_{ops}
F_{diff}	Judgement factor which accounts for the difficulty of a new airplane program. For conventional airplanes use 1.0, for moderately aggressive use of

advanced technologies use 1.5, and for programs involving very aggressive use of advanced technologies use 2.0.

F_{fin_m} Finance cost fraction during manufacturing phase (0.10-0.20 depending on interest rates available)

F_{fin_r} Finance cost fraction during RDTE phase (0.10-0.20 depending on interest rates available)

F_{ftoh} Overhead factor associated with the production flight test activities. Lacking overhead data it is suggested to use 4.0.

F_{int} Interior cost factor which depends on number of passengers, USD/pax. For military airplanes use 0, for light general aviation use 500, for regional transports use 1000, for jet transports use 2000, and for business jets use 3000.

F_{mat} Judgement factor which depends on the type of materials used in the construction of the airplane. For airframes made primarily of conventional aluminum alloys use 1.0, for stainless steel airframes use 1.5, for airplanes where the primary structure is made with "conventional" composite materials, Li/Al alloys and/or ARAL use 2.0-2.5, and for carbon composite airframes use 3.0.

f_{misc} Miscellaneous cost fraction of C_{ops}

F_{obs} Judgement factor to account for observables characteristics. For commercial and military airplanes without a "stealth" requirement use 1.0, for "stealthy" airplanes use 3.0.

F_{ol} Factor which accounts for the cost of oil and lubricants. In the absence of better data it is acceptable to use 1.005.

$f_{persind}$ Indirect personnel cost as a fraction of C_{ops}

F_{pro_m} Profit fraction of privately held enterprise during manufacturing phase (typically 0.10)

F_{pro_r}	Profit fraction of privately held enterprise during RDTE phase (typically 0.10)
f_{spares}	Indirect cost of spares as a fraction of C_{ops}
F_{tsf_r}	Cost adjustment factor extra test and simulation facilities during RDTE phase. For no extra facilities required use 0, for extensive test and simulation facilities use 0.20.
FD	Density of fuel, lbs/gal
FG_{sj}	Gross thrust of scramjet engine
FG_{tj}	Gross thrust of turbojet engine
$FOMvalue$	Value for figure of merit
$FOMweight$	Weighting factor for figure of merit
FP	Price of fuel per gallon, USD/gal
W_{TO}	Judgement factor which accounts for the effect of computer aided design capability on airframe engineering and design cost. For manufactures which are in a CAD learning mode use 1.2, for manufacturers which are using "manual" drafting techniques use 1.0, and for manufacturers which are experienced in the use of CAD use 0.8.
g	Gravitational constant
G_R	Generalized reduced gradient
$\dot{h}$	Same as $\dot{y}$
$\triangle H_{vap}$	Heat of vaporization
h	Altitude
h_f	Flare height
h_{OB}	Takeoff obstacle height
I_sp	Specific impulse
L	Vehicle lift force

L_{inlet}	Inlet lift
L_{nozzle}	Nozzle lift
$\dot{m}_{coolant}$	Coolant mass flowrate
$\dot{m}_{fuel}$	Fuel flow rate
m	Point mass of vehicle
M_∞	Freestream Mach number
$MHR_{aed_{program}}$	Total number of engineering manhours required for the entire airplane program (for all $N_{program}$ airplanes), hr
MHR_{aed_r}	Total number of engineering manhours required for RDTE phase, hr
MHR_{flthr}	Number of maintenance manhours required per flight hour, hr
$MHR_{man_{program}}$	Total number of manhours required for the production of $N_{program}$ airplanes, hr
MHR_{man_r}	Number of manufacturing manhours required during RDTE phase, hr
$MHR_{tool_{program}}$	Total number of tooling manhours required to build $N_{program}$ airplanes, hr
MHR_{tool_r}	Tooling manhours required during RDTE phase, hr
$\widetilde{\mathbf{n}}$	Normal vector for normal boundary intersection
n	Load factor
N_t	Number of discretized time points for heat equation
N_x	Number of discretized thickness points for heat equation
N_{crew}	Number of crew members
N_e	Number of engines per airplane
N_{flight}	Number of flights
$N_{mission}$	Number of missions flown per year
N_m	Total number of airplanes manufactured to production standards
N_{pax}	Number of passengers

$N_{program}$	Total number of airplanes produced
N_p	Number of propellers per airplane during RDTE, USD
N_{r_r}	RDTE production rate in units per month (typically 0.33)
N_{rdte}	Number of airplanes produced for the RDTE phase. This number includes flight test airplanes as well as airframes used for static testing. For military programs use 6-20, for commercial programs use 2-8.
N_{serv}	Number of airplanes in actual service
N_{st}	Number of static test airplanes (not equipped with engines or avionic systems)
N_{yr}	Number of years an airplane is operated
$NConcepts$	Number of concepts in Maximin and Maximax techniques
$NumofFOMs$	Number of figures of merit in Maximin and Maximax techniques
NAttributes	Number of TOPSIS attributes
OHR_{crew}	Overhead rate factor associated with the actual crew pay. Lacking actual data it is suggested to use 3.0.
P_{cost}	TPS material purchase cost
Pay_{crew}	Annual crew pay, USD/yr
$\bar{q}$	Average dynamic pressure at each time interval for Jackson Energy Method
$\dot{q}_{coolant}$	Heatrate being removed by coolant
q	Dynamic pressure
$q_{backplate}$	Heatrate at the backplate of TPS
q_{conv}	Convective heatrate
R	Response value of response surface equation Turn radius
R_{conmat}	Average cost for consumable materials, USD/hr. It is suggested to use $R_{conmat} = 6.50\,(CEF_{then\,year})\,/\,(CEF_{1989})$.

R_{cr}	Crew ratio per airplane
R_{e_m}	Engineering manhour rate during manufacturing phase, USD/hr
R_{e_r}	Engineering manhour rate during RDTE phase, USD/hr
$R_{m_{ml}}$	Military maintenance labor rate, USD/hr
R_{m_m}	Manufacturing manhour rate during for the entire program, USD/hr
R_{m_r}	Manufacturing manhour rate during RDTE phase, USD/hr
R_r	Rolling resistance
R_{t_m}	Tooling labor manhour rate during manufacturing phase, USD/hr
R_{t_r}	Tooling labor manhour rate during RDTE phase, USD/hr
$Reuse_{flight}$	Number of flights a TPS material can be reused
s	Ranking criteria for Simple Additive Weighting technique
Re	Reynolds number
S	Vehicle reference area
	Numerical optimizer search direction
s_a	Airborne distance
s_{fr}	Free roll distance
s_f	Flare distance
s_g	Ground roll distance
S_i^+	Euclidian distance to positive ideal solution
S_i^-	Euclidian distance to negative ideal solution
S_{wet}	Vehicle wetted are
C	TOPSIS relative closeness
T	Vehicle thrust
	Temperature
t	Time

T_{boil}	Coolant boiling temperature
$T_{initial}$	Coolant initial temperature
t_{mis}	Average mission time, hr
T_{nozzle}	Nozzle thrust
t_{pft}	Number of flight test hours flown by the manufacturer before airplane delivery to customer, hr
T_{rev}	Reverse thrust
T_s	Surface temperature of TMS/TPS
$U_{ann_{flt}}$	Annual utilization in flight hours
$\dot{V}$	Vehicle acceleration
V	Vehicle velocity
V_a	Landing approach speed
V_{fr}	Free roll velocity
V_f	Landing flare velocity
V_{LO}	Liftoff velocity
V_{max}	Maximum design speed, kts
V_{stall}	Stall speed
V_{TD}	Touchdown velocity
$\bar{W}_{fuel}$	Average fuel burn at each time interval of Jackson Energy Method
W	Vehicle weight
W_{ampr}	Aeronautical Manufacturers Planning Report Weight, lbs
$W_{f_{used}}$	Mission fuel used, lbs
W_{fuel}	Total fuel weight
$\dot{x}$	Same as V
$\mathbf{X}$	Design variable vector for numerical optimizer

$\dot{y}$	Vehicle climb speed

Greek Symbols

α	Angle of attack
β	Vehicle sideslip
	Fast point iteration safety index
ϵ	Thrust vector angle relative to body centerline
ε	Emissivity
	Error associated with 2nd order approximation of response surface equation
$\dot{\gamma}$	Rate of change of flight path angle
γ	Flight path angle
γ	Flight path angle
$\mathcal{H}$	Convex hull for normal boundary intersection
θ	Surface inclination angle
κ	Thermal conductivity coefficient
μ_r	Rolling coefficient of friction
ϕ	Equivalence ratio
ρ	Density
σ	Stefan-Boltzman constant
θ_a	Landing approach flight path angle
θ_f	Flare flight path angle
θ_{OB}	Takeoff included angle

SUMMARY

This thesis addresses the challenges associated with thermal management systems (TMS) evaluation and selection in the conceptual design of hypersonic, air-breathing vehicles with sustained cruise. The proposed methodology identifies analysis tools and techniques which allow the proper investigation of the design space for various thermal management technologies.

The design space exploration environment and alternative multi-objective decision making technique defined as Pareto-based Joint Probability Decision Making (PJPDM) is based on the approximation of 3-D Pareto frontiers and probabilistic technology effectiveness maps. These are generated through the evaluation of a Pareto Fitness function and Monte Carlo analysis. In contrast to Joint Probability Decision Making (JPDM), the proposed PJPDM technique does not require preemptive knowledge of weighting factors for competing objectives or goal constraints which can introduce bias into the final solution. Preemptive bias in a complex problem can degrade the overall capabilities of the final design. The implementation of PJPDM in this thesis eliminates the need for the numerical optimizer which is required with JPDM in order to improve upon a solution.

In addition, a physics-based formulation is presented for the quantification of TMS safety effectiveness corresponding to debris impact/damage and how it can be applied towards risk mitigation. Lastly, a formulation loosely based on non-preemptive Goal Programming with equal weighted deviations is provided for the resolution of the inverse design space. This key step helps link vehicle capabilities to TMS technology subsystems in a top-down design approach. The methodology provides the designer more knowledge up front to help make proper engineering decisions and assumptions in the conceptual design phase regarding which technologies show greatest promise, and how to guide future technology research.

Chapter I

INTRODUCTION

1.1 Design Process

Design is an iterative process for the conception, invention, visualization, calculation, refinement, and detailing which will define the form of an engineering product [40]. This iterative process often times involves a lot of trial and error and demands great creativity and engineering expertise on the part of the designer by being well versed in many other fields of aerospace. The design process is driven by a need or set of requirements typically defined by the customer. The goal of the designer is to identify existing or new concepts and technologies that will meet the customer needs and hopefully improve on earlier designs.

Aircraft design has traditionally been made up of three major phases as depicted in Figure 1 [75]. Each of these phases consist of different levels of decision making, analysis fidelity, and analysis tools. The fidelity and complexity of analysis tools increases as one progresses further into the later phases of design.

Figure 1: Phases of the Design Process [75]

Conceptual design is characterized as the design phase where the major and most important decisions for a program are made [40]. This phase places the greatest challenges and demands on the designer because assumptions and decisions made in these early stages will have the greatest impact on the program as it matures. In the conceptual phase, the designer is asked to answer customer requirements in the form of broad solutions by bringing together engineering science, practical knowledge, production methods, and commercial aspects [40]. It also involves a large number of trade studies, and leads to a fluent and evolutionary change to the solutions being considered as shown in Figure 2 depicting Raymer's

design wheel [75]. The designer is ultimately trying to answer a series of key questions as shown below [75]:

- What requirements drive the design?
- What should it look like? Weight? Cost?
- What tradeoffs should be considered?
- What technologies should be used?
- Do these requirements produce a viable and scalable plane?

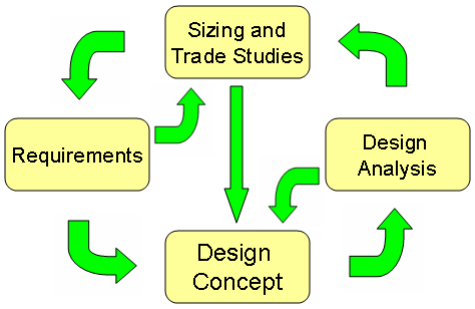

Figure 2: Design Wheel Conceptual Design Approach [75]

The preliminary design phase can begin once the major decisions that will guide the program have been made. This means that the general concept configuration has been defined and only minor revisions are expected from here on. At this point the concept is handed down to disciplinary experts who will take each element (structures, aerodynamics, propulsion, control systems), study it and gain knowledge of the concept to contribute to the maturity of the program. This increases the level of confidence that the decisions made early on will indeed work. The ultimate goal is to produce a "frozen" concept that the company feels confident enough to carry on to the detail design phase [75].

Once the concept has been frozen, the detail design phase can commence. Detail design is characterized as the most expensive of the three phases and involves the preparation and drawing of all subsystems, and the smaller parts which make up the concept down to the lowest level of detail. At this stage the different components such as structures are tested

and production specialists decide how the concept will be produced and assembled. Often times there are compromises which need to be made in order to simplify production and assembly [75].

It is important to note that most of the engineering effort and cost are expended during the preliminary and detail design stages [75]. This emphasizes the importance and ramifications of the assumptions and decisions made by designers in the conceptual phase. Because of this, many approaches and techniques have been brought forward throughout the years in order to improve the way that conceptual design is performed.

1.2 Hypersonic Flight

The field of hypersonics can be thought of as the ultimate aerospace systems integration problem because it brings together the expertise from nearly all fields of aerospace [38]. *Hypersonic* flight is generally accepted to encompass speeds equal or greater than five times the speed of sound ($Mach$ 5). Although there is no clear cut boundary, hypersonics is a flight regime where effects such as thin shock layers, vorticity interaction, viscous interactions and high temperature flows begin to become more noticeable. These high-speed flow phenomena will be explained in more detail in a later . Nonetheless, one item important to recognize early on is that most of these phenomena are degrative to the vehicle's performance by increasing drag, generating nonlinear moments affecting stability, and creating an adverse thermal environment for the vehicle and the pilot. In addition, they render many traditional aerodynamic computational techniques and tools useless. Even more advanced aerodynamic fields such as computational fluid dynamics (CFD) become inadequate in the hypersonic flight regime because many of the assumptions in the Navier-Stokes equations such as no-slip boundary condition, and shock-boundary layer interactions are violated. As a result more specialized hypersonic tools are required when studying hypersonic vehicles [75].

Hypersonic vehicles emphasize even more the importance of compromise between the aerodynamic, aerothermodynamic and propulsion disciplines. Aerodynamics and aerothermodynamics will drive up the design altitude where the vehicle spends most of its time cruising. A higher altitude leads to decreased drag, lower thermal requirements imposed

on the vehicle, and theoretically lower thrust requirements to drive the vehicle. However, at the same time the propulsion discipline drives the design cruise altitude lower because air-breathing engines perform better and are more efficient in the denser and more oxygen-rich atmosphere. There is also the additional problem in that there is no single engine that can operate in the entire flight regime ranging from subsonic to hypersonic speeds. A single engine capable of operating from takeoff to hypersonic speeds would require a high level of compromise which would render it ineffective. Turbojets have a maximum temperature constraint which begins to become significant at speeds around *Mach* 3. The solution to this limit is the ramjet which eliminates the requirement of the compressor altogether, while maintaining the flow velocity inside the combustor subsonic. Scramjet engines can operate at higher Mach numbers than ramjets by taking the ramjet concept a step forward and allowing combustion to take place under supersonic flow conditions. A scramjet was successfully flight tested at speeds reaching *Mach* 9.6 in 2004 aboard NASA's Hyper-X research vehicle (X-43) [75].

Designers have proposed the idea of utilizing multiple specialized engines for the different stages of a flight which has to some degree solved the aforementioned inadequacy of current engines, but at the same time adversely affected the complexity and reliability of the design. One of these multi-stage engine concepts is commonly known as turbine based combined cycle (TBCC). A turbojet can be employed in the lower subsonic and supersonic flight regimes while a ramjet or scramjet is used once hypersonic speeds are reached.

A major aspect associated with high supersonic and hypersonic vehicles is the high thermal requirements placed on the vehicle which have been non-existent in more conventional aircraft. An entire new aerospace discipline dealing with thermal management has emerged to allow the survival of the vehicle under such adverse environments.

1.3 Thermal Management Systems

Systems engineering is an orderly process for bringing a system into reality [10]. A *system* is defined by Dieter as "The entire combination of hardware, information, and people necessary to accomplish some specified mission" [24]. Systems can be categorized as natural,

human-made, physical, conceptual, closed-loop, open-loop, static, and dynamic [10]. Complex aerospace systems usually fall into more than one of these categories and can be very subjective depending on the point of reference. A high level of interaction can exist between the different elements or disciplines that constitute the design such as aerodynamics, propulsion, aerothermodynamics, and thermal management.

Thermal management systems can therefore be identified as a combination of hardware and technology enablers which allow hypersonic vehicles to survive the extremely high temperature environment to which they are subjected. Although the ultimate function of different thermal management systems is usually the same, these systems can vary greatly depending on the application. Applications such as missiles and planetary probes can afford to utilize thermal management systems which are disposable or non reusable since they usually have single flight requirements. Other applications such as reusable launch vehicles (RLV) and high-speed aircraft will favor thermal management systems with better life cycle characteristics. The differences in mission trajectory between a RLV and a high-speed aircraft will also play a role in the selection of the thermal management system since the thermal profiles will vary.

1.4 Motivation

In 1949 the United States Army successfully launched the first man made vehicle to reach hypersonic flight speeds. The program, called Bumper, used a multistage V-2 rocket to achieve a record 5,150 mph at a maximum altitude of 244 miles. Just twelve years later in 1961, hypersonic flight would be revolutionized by numerous successes in manned flight, beginning with the USSR's launch of Vostok, the first spacecraft carrying astronaut Yuri Gagarin which reached speeds in excess of $Mach$ 25. Later that year, Major Robert White of the U.S. Air Force became the first man to pilot an X-15 experimental aircraft to hypersonic speeds reaching $Mach$ 5.3 and $Mach$ 6 just a few months later. In a mere 58 years mankind had achieved what the Wright Brothers never could have imagined as they worked on the first man-piloted airplane. Despite these great achievements, sustained hypersonic powered flight has had a checkered track record and encountered significant problems and technological

hurdles. There have been several attempts to develop high-speed aircraft and technology demonstrators in the past (including the XB-70 Valkyrie, X-30 NASP, X-33 Venture Star, X-34, and X-43), with varying degree of success, but most have never been fully realized.

As a result of these hurdles and failures, there has been criticism and claims that there is no need for such hypersonic aircraft, no defined requirement, nor customer demand. However, as Richard P. Dillon, a senior adviser for air and space issues, eloquently expressed it; "There was no defined requirement, no customer demand at the time the Wrights invented the airplane for the global air transport system, and even if there had been, it is extremely doubtful that anyone could have possibly predicted how globally-encompassing, how utterly ubiquitous, that system would be a century after Kitty Hawk". The *6-60-600* trend in speed of mobility shown in Figure 3 is bound to continue its growth in the years to come as mankind continues to envision the far-reaching benefits and possibilities that hypersonic flight may offer [38]. In this sense the definition of design given earlier is contradictory as in many cases it is the vision of the designer which precedes actual customer needs.

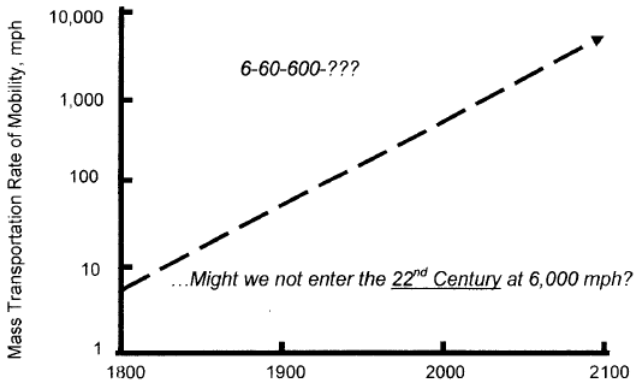

Figure 3: Mass Transportation Rate of Mobility [38]

In the Fall of 2001, the Secretary of Defense called for an initiative seeking the integration of air and space technologies for the purpose of advancing long strike, space launch and persistent intelligence, surveillance, and reconnaissance capabilities [76]. The effort known as the National Aerospace Initiative (NAI) places emphasis on technology development in three major area: High-Speed / Hypersonics, Space Access, and Space Technology. These

areas all contribute to technologies which will facilitate long-range time-critical strikes, on-demand space launch air-breathing propulsion, and responsive space payload capability [76]. The NAI technology development approach places emphasis on three key system attributes or measures of effectiveness (MoE) including *speed*, *survivability* (1 / vulnerable time), and *payload capacity*. More precisely weapons systems capable of achieving $Mach\ 4-12$, and reusable vehicle systems capable of achieving up to $Mach\ 7$ [76].

1.5 Problem Definition

Early hypersonic vehicle concepts were based on extrapolations from earlier experience with supersonic vehicles. In the past thermal protection systems (TPS) or more general thermal management systems design has played a secondary role in high-speed vehicle design. This is a byproduct of earlier aircraft design processes which did not require the implementation of thermal management systems. As a result, current aircraft design processes continue to focus first on aerodynamic optimization leaving thermal management systems design to the end. Despite great innovations in thermal management systems, this traditional design process has made it challenging for the incorporation of new technologies into the vehicle. As a program matures the initial weight estimates typically grow which as a result affect the original trajectory estimates. This increase in weight results in a much greater increase in thermal management system weight. Ehrlich et al found a 35% increase in thermal management system weight for every 20% increase in dry weight for reusable launch vehicles [27]. This means that as a program matures, the capabilities of the vehicle such as payload and overall system effectiveness tend to degrade. Lower system capabilities such as payload lead to increase in operational cost and ultimately life cycle cost (LCC) since the vehicle needs to be operated more frequently to meet a certain demand. This issue contradicts the paradigm shift that the aerospace industry has experienced in the last several years shifting from design for performance to design for overall effectiveness while taking into account life cycle cost as a key measure of system effectiveness.

Furthermore, there are still many technological hurdles that need to be addressed before

hypersonic flight can transition from feasible to also viable and practical. The main technical challenges identified by the Technical Fellowship Advisory Board study are centered on propulsion, thermal environment prediction, protection and management, integrated airframe structures vehicle design, optimization, and simulation [13].

The field of hypersonics can be thought of as the true aerospace system integrator as shown in Figure 4 bringing in expertise from many different areas of engineering [38]. One of the major problems encountered in hypersonics is the high level of complexity when integrating all the different disciplines. An additional problem is the lack of historical-based performance and economic databases in existence due to the small number of hypersonic vehicles actually flown.

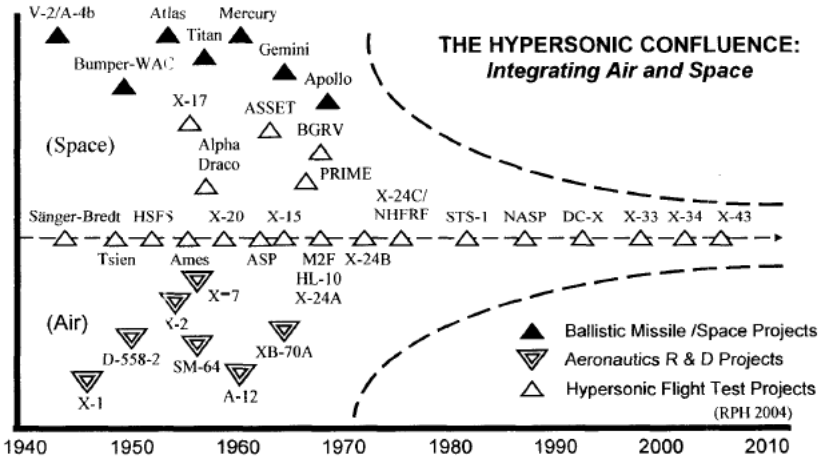

Figure 4: Hypersonic Integration of Air and Space [38]

Hypersonic air-breathing vehicles have thermal management system requirements which include rapid turn around time, long life, increased operability, durability, capabilities and safety, all of which point to a need for consideration of life cycle cost. Although great strides have been made in the performance aspect of thermal protection systems, such as that of the Space Shuttle, there still exists a large gap in viability and practicality for more general use. Most of the thermal protection systems employed in the Space Shuttle today have maintenance requirements that are excessive even for military operations and simply unacceptable for commercial use.

The literature review in the following will show that there is a plethora of new innovative thermal management concepts in existence today with various degrees of maturity. As previously mentioned, the implementation of new TMS concepts into the vehicle design becomes difficult due to traditional design processes emphasis on aerodynamics. The large number of available technologies lead to an even more complex problem within the hypersonics integration problem and another issue arises as to how to go about comparing thermal management systems that are so different in nature. One must be able to look across the wide spectrum of thermal management technologies instead of focusing on the optimization of one specific technology to meet the system requirements.

The high complexity of the problem may result in several parameter combinations that yield multiple near optimum designs. In these cases the initial condition used to start an optimization algorithm would play a great role in the final optimized solution [48]. Further complicating the problem is the possible existence of discontinuities, and large number of design space constraints. Attempting to optimize such a complex system on a global scale is an unrealistic undertaking, and so an alternative and probabilistic approach must be found to allow the designer to make smarter decisions.

The problems associated with the design and selection of thermal management systems are summarized in Figure 5 and three key technical challenges are identified. These technical challenges lead to several observations shown in Figure 6 which will become the foundation for the research questions which will be presented at a later time.

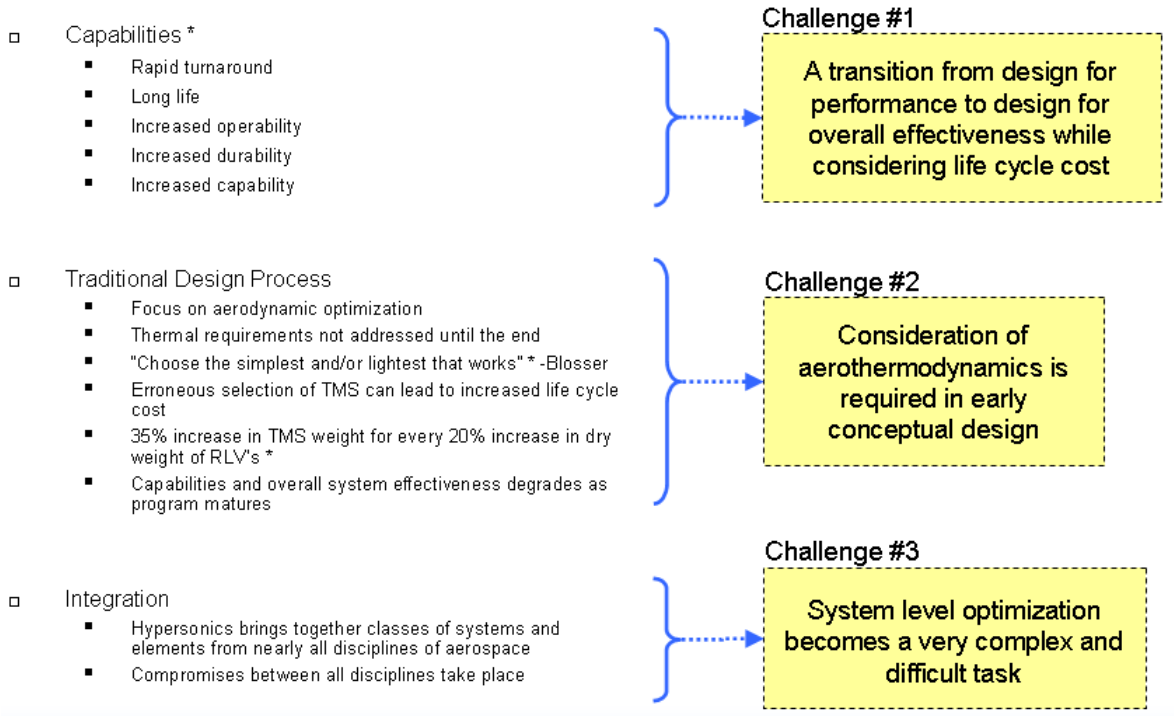

Figure 5: Technical Challenges Associated with TMS Design *[11]

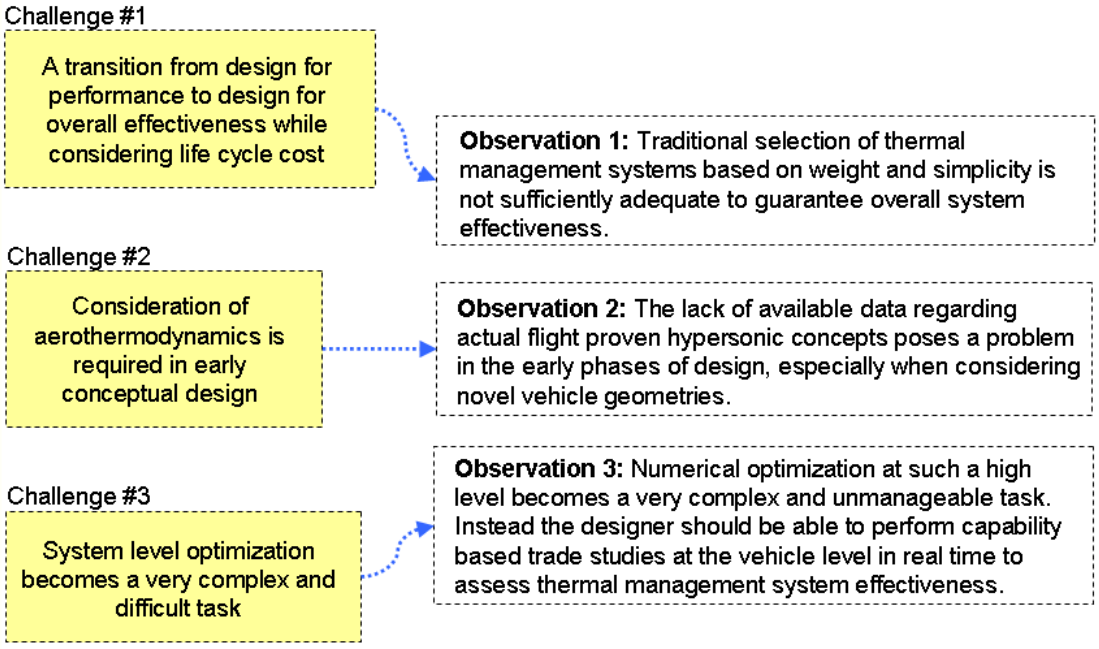

Figure 6: Observations from Technical Challenges

Finally, the problem that this thesis is trying to address can be stated as:

> *How can thermal management technology selection be performed in a way that is structured, robust, accounts for the variability of factors beyond the designer's control, and can provide the most information to the designer early in the phases of conceptual design?*

1.6 Dissertation Outline

The dissertation follows a research process based on the scientific method which is shown in Figure 7 [60]. In addition, a simplified case study will also be utilized to demonstrate the prospective results and capabilities of the proposed work.

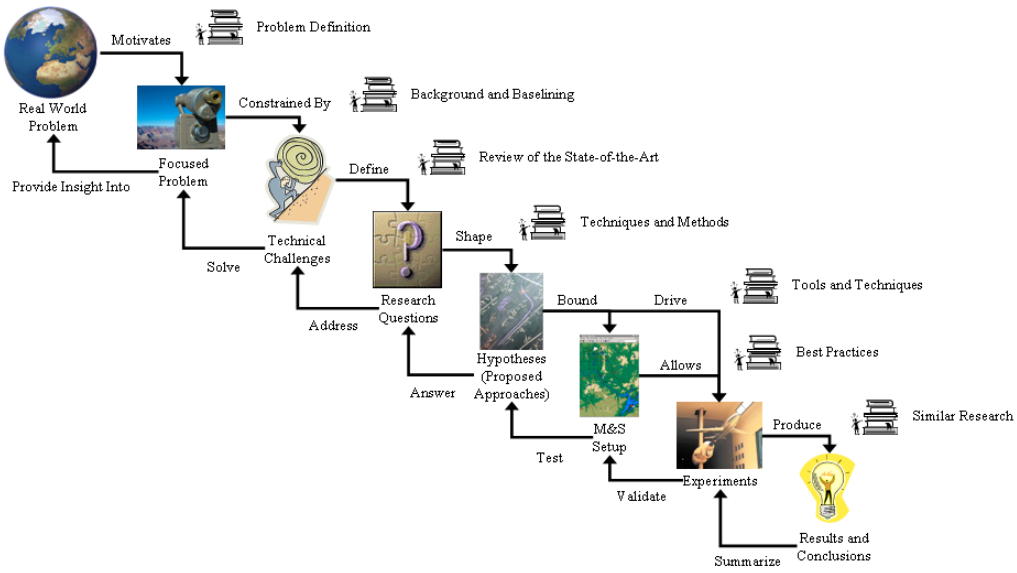

Figure 7: Research Process Based on Scientific Method [60]

The real world problem and motivation on the subject of thermal management technology selection has already been discussed in earlier sections of I. The next step in the scientific method requires research and gathering of information pertaining to the problem in order to identify the existing technical challenges. This is presented in II which reviews background information and the state of the art methods and technologies pertaining to

this subject. III will identify any gaps that have been found in the literature search which prevent the resolution of the defined problem. Research questions will be formed based on the observation of the technical challenges and gaps. A series of hypotheses will then be formulated attempting to answer each one of the research questions. The proposed work and case study will be presented in IV which will attempt to close the technical gaps and answer each of the hypotheses. IV will also define the modeling and simulation environment, including analysis tools, and techniques which will be key in the testing of the proposed methodology and hypotheses.

Validation for the physics-based analysis tools (aerodynamics, aerothermodynamics, sizing and synthesis, TMS sizing) used in the modeling and simulation environment will be presented in V. In VI, a demonstration of the proposed methodology will be presented based on the case study. In VII the research questions and hypotheses will be revisited to summarize how they have been tested and whether or not they have been validated. From here the research questions can finally be answered while providing more information or knowledge regarding the original problem statement given in the previous section. Finally, a summary of the contributions, lessons learned and recommendations for future iterations will be presented. It is important to realize that the scientific based research process may consist of many continuous iterations if the original problem is not resolved or as new derivative questions arise along the way.

Chapter II

LITERATURE REVIEW

2.1 Research Objectives

The literature review presented in this is driven by the motivation and problem definition presented earlier. This will cover the methodologies, processes and techniques that are pertinent to the study of hypersonic vehicles as well as the main elements that make up the proposed work which will be presented in a later .

Before one delves into the bulk of the literature review, it is important to explain how these elements fit together. The proposed work will highlight several elements which are listed below. These elements are intelligently selected by determination of an existing gap, finding enablers to close that gap, benchmarking the different techniques and processes, and selecting the most adequate solution. This more detailed process of determination is provided in IV covering the proposed methodology. However, for now it is important to recognize that these are the main topics that will be covered in the literature review.

- Identification of Need
- Design Space Definition
- Concept Down-Selection
- Surrogate Modeling
- Probabilistic Analysis
- Modeling and Simulation
- Design Space Exploration

The first step needed is an understanding of what the customer is looking for regarding a thermal management system. This step will also aid in the definition of the design space that

is relevant to the engineer by means of engineering characteristics. The wide variety and modeling complexity of thermal management systems will be demonstrated in the modeling and simulation section. This leads to a need for down-selection of the technologies that make most sense and reduction of the amount of time and effort placed on technologies that may not be as applicable. In order to achieve these several qualitative multi-attribute decision making techniques will be presented.

A probabilistic analysis is needed in order to properly assess the effect of variability on the thermal management technology selection and allow for more robust decision making. The transition from design for performance to design for overall effectiveness requires the inclusion of a new cost discipline. Cost brings uncertainty into the design which can only be assessed through probabilistic techniques. The probabilistic analysis demands the quick evaluation of responses of interest which leads to the need for surrogate modeling. The design of experiments (DoE) and surrogate modeling are enablers which will provide the link between the modeling and simulation and the design space exploration environment. In this several approaches to surrogate modeling and probabilistic analysis will be provided and their strengths and weaknesses will be indentified depending on the application.

The modeling and simulation defines the behavior and interrelationships between the different engineering characteristics for a hypersonic vehicle. This will require an in-depth look into various disciplinary topics including trajectory simulation, aerodynamics, aerothermodynamics, propulsion, thermal management sizing, and economic prediction. In addition, a catalog of the characteristics and behavior of the main categories of thermal management technologies will be presented.

Finally, the design space exploration techniques will provide a way to identify the behavior of the thermal management technologies and how they perform compared to each other in the design space. The design space exploration environment will allow trade studies to be performed, hopefully highlighting new information and knowledge that would not be available otherwise.

2.2 Identification of Need and Engineering Solutions

The techniques presented in the following sections provide a means to translate in a qualitative fashion the needs of the customer from the problem definition into possible engineering solutions. The customer needs will feed into the Quality Function Deployment (QFD) which will yield a ranking for the engineering characteristics of most importance. A morphological matrix of alternatives will define possible technologies or alternatives which can be used to meet the customer needs. The engineering characteristics rankings and alternative solutions can then be fed into a multi-attribute decision making technique which will provide a ranking of the proposed alternatives which can possibly satisfy the customer needs [84]. These techniques make the down-selection process of engineering solutions more systematic and transparent.

2.2.1 Quality Function Deployment

The Quality Function Deployment developed by Dr. Yoji Akao and Dr. Shigeru Mizuno is a systematic, interactive and mathematical process by which to translate the voice of the customer into the voice of the engineer [24]. This means translating the vision of the customer into characteristics that the engineer can quantify and analyze. The result is a process which provides a communication bridge for the customer and the engineer and can yield a design of greater quality. An example of a QFD or House of Quality is given on the left hand side of Figure 8 [9]. The diagram of the different rooms that make up such House are shown on the right hand side of Figure 8. These QFD rooms 1-6 are known respectively as customer requirements, importance rating, engineering characteristics, correlation matrix, relationship matrix, and overall importance. A more detailed description of these rooms and how they are completed are given next.

Room 1: Customer requirements or customer desires are what drive the problem definition and development of the final product or process. Good communication with the customer is therefore imperative to the success of the project. There are various ways to obtain the needed information including customer interviews, focus groups, and customer surveys.

Room 2: Importance ratings define the level of importance of each requirement to the customer and they are typically rated on a scale from 1-9.

Room 3: Engineering characteristics are enablers which allow the engineer to meet the customer needs. Examples of engineering characteristics can be engine thrust, fuselage weight, stability, fuel consumption, etc. Each engineering characteristic is assigned an up or down arrow which denotes the preferred direction of its magnitude value. For example, an engineering characteristic based on weight would be classified with a down arrow indicating that lighter is preferred, while stability would be classified with an up arrow.

Room 4: Correlation matrix defines the relationship between the engineering characteristics. These are typically described as no relationship, low relationship, medium relationship, and strong relationship.

Room 5: Relationship matrix shows how much impact the engineering characteristics will have on the customer requirements. This is represented on a scale of 0-no correlation, 1-slight correlation, 3-medium correlation, and 9-strong correlation.

Room 6: Overall importance can be computed for each engineering characteristic (column) using Equation 1 where i is the index for each customer requirement (row), j is the index for the engineering characteristics (columns), and N_i is the total number of customer requirements. It can also be useful to incorporate a relative importance for each engineering characteristics which can be found by dividing each absolute importance by the sum all the absolute importance values and multiplying by 100.

$$\begin{matrix} Absolute \\ importance \end{matrix} = \sum_{i}^{N_i} \left(\begin{matrix} importance \\ rating \end{matrix} (i) \right) * \left(\begin{matrix} relationship \\ matrix \end{matrix} (i,j) \right) \quad (1)$$

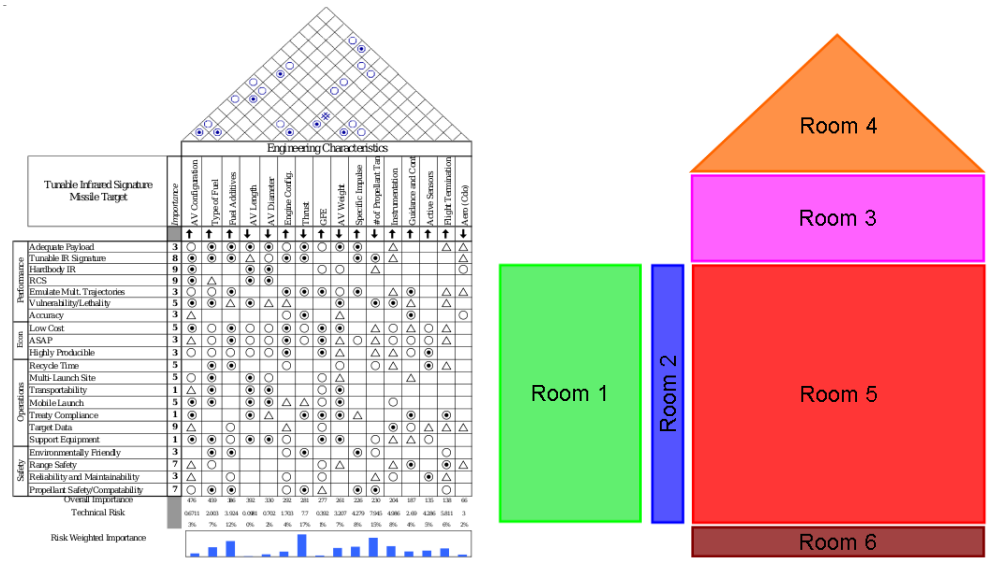

Figure 8: Quality Function Deployment Example and Diagram

2.2.2 Morphological Matrix

First proposed by Zwicky in the 1960s, the morphological matrix is a simple but powerful method for uncovering combinations of ideas and elements which can shape a design concept [24]. The method also gives insight into new design concepts that would otherwise never be considered. An example morphological matrix is shown in Figure 9 for a basic aircraft design problem. It is important to note that not all combinations will be feasible or practical to implement. However, even this rather simple example shows the large number of combinations that can be formed making the study and evaluation of all the possible concepts impractical. This creates a need for a process to help down select from a sample of these design combinations.

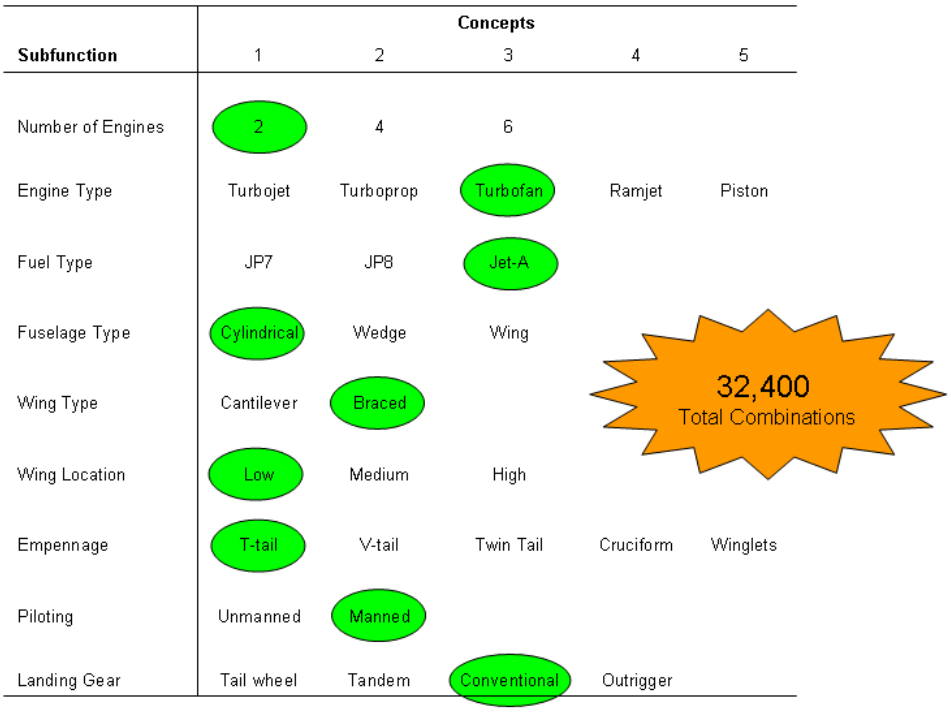

Figure 9: Sample Morphological Matrix

2.2.3 Design Concept Down-Selection

Multiple Attribute Decision Making (MADM) techniques refer to the making of decisions regarding product selection in the presence of many and often conflicting evaluation criteria [9]. There are numerous techniques with various levels of sophistication which can be utilized to down select from a large sample of design concepts including Dominance, Maximin, Simple Additive Weighting, and TOPSIS. These decision making techniques are categorized in Figure 10 and some will be explained in more detail in the following sections [60].

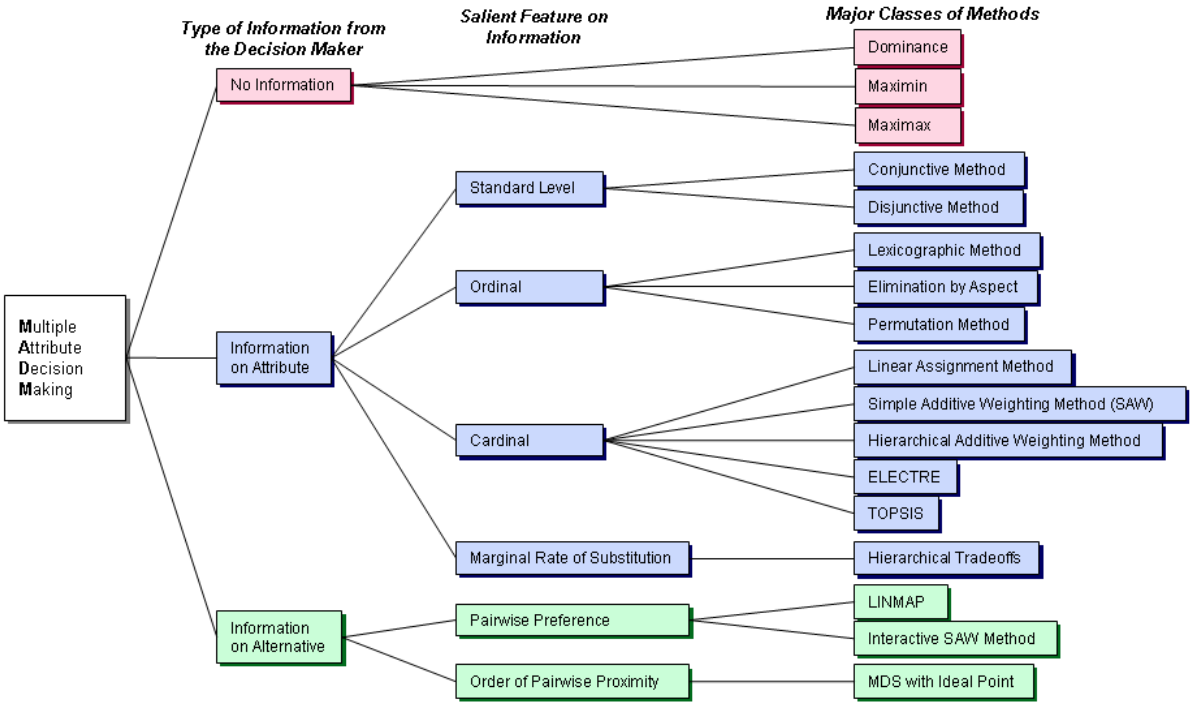

Figure 10: Multi-Attribute Decision Making Techniques [60]

2.2.3.1 Dominance

The Dominance method achieves a ranking by comparing the relative figure of merit (FOM) between two concepts. The Dominance matrix is composed of concepts shown as rows, and engineering characteristics shown as columns. Although this method does not require normalization of the Figures of Merit, it is often useful to assign an ordinal rank to the different concepts based on how well they perform with respect to a specific figure of merit as shown in Figure 11. These ordinal rankings can then be plotted in the form of a radar plot as shown in Figure 12. The radar plot is a better and more straightforward way to rank the different concepts. The ranking is produced by comparing the area that each of the concepts encompass. The greater the area encompassed by a concept on the radar plot the more it excels in the various Figures of Merit and thus the better the ranking. The Dominance matrix should only be used during the early screening process before other down-selection methods are utilized [97].

	Turn Around Time	Per Flight Cost	Call Up Time	LCC	First Unit Cost	Payload to LEO
Nose Mounted Rocket-back	**4**	**2**	3	2	2	2
Metallic Rocket-back Heavy	**6**	**1**	6	6	6	**1**
Metallic Rocket-back Medium	3	5	4	3	5	3
Composite Jet-back	5	**3**	**2**	4	4	3
Composite Rocket-back	2	**6**	**1**	5	3	3
Metallic Jet-back	**1**	4	5	**1**	**1**	6

Figure 11: Sample Dominance Matrix [97]

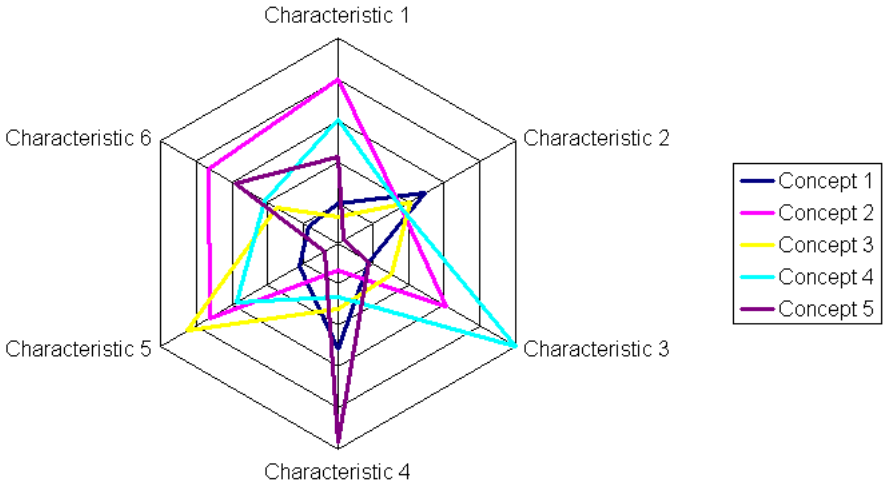

Figure 12: Sample Dominance Radar Plot

2.2.3.2 Maximin and Maximax

The Maximin method is similar to the Dominance method but it relies on normalization of the different Figures of Merit. The FOMs can be normalized on a scale from [0-1] using Equations 2-3 [97], where i and j are the indices for each concept and figure of merit, respectively. The worst possible outcome of each decision is considered and the concept with the highest minimum value is selected as the winner. The Maximin method lends itself well to scenarios where a failed decision can be most harmful. On the other hand, Maximax bases its selection of the winning solution by identifying the best outcome of each decision and choosing the highest maximum value of these. The Maximax method lends itself well when risk taking is acceptable.

The disadvantage of these two methods is that they do not look at the big picture and

may rule out a concept simply because it performs badly for one FOM, yet it may perform well overall across the rest of the FOMs. In other words, it may eliminate a good compromise solution simply because it does not perform well with respect to one FOM. A way to avoid this problem is to rely once again on the radar plot shown earlier in Figure 12 which can show a better overall picture.

$$\overline{FOM}_{i,j} = \frac{min_j \{FOM_{i,j}\}}{FOM_{i,j}},\ i = 1, ..., NConcepts, j = 1, ..., NumofFOMs \tag{2}$$

$$\overline{FOM}_{i,j} = \frac{FOM_{i,j}}{max_j \{FOM_{i,j}\}},\ i = 1, ..., NConcepts, j = 1, ..., NumofFOMs \tag{3}$$

2.2.3.3 Simple Additive Weighting

The Simple Additive Weighting method requires, as the name implies, a weighting factor which is typically decided by a decision maker. The ranking criteria is computed using Equation 4 for each concept. The concepts with the highest ranking criteria 's' are chosen as the most desirable.

$$s = \sum_{j=1}^{NumberofFOMs} FOMweight_j * FOMvalue_j \tag{4}$$

2.2.3.4 Technique for Order Preference by Similarity to Ideal Solution (TOPSIS)

The TOPSIS method takes the engineering characteristics (attributes) identified in the QFD which now become the FOMs and the engineering concepts found from the Morphological matrix to form what is called a decision matrix as shown in Figure 13. The next step is to work together with the experts in the field to complete the decision matrix by assigning a scale of [1-low, 3-moderate, 9-high] based on how well each concept answers each engineering attribute. Once the decision matrix is completed, it needs to be non-dimensionalized by dividing all the values in the matrix by the Euclidean norm (Equation 5) of their respective column. A weighting factor can be applied at this point to each engineering attribute (columns) to reflect a level of importance ranking if needed. The next step is to determine

the ideal positive and negative solutions which can be found by identifying the highest and lowest value for each attribute (column) respectively. Now the Euclidean distances to the ideal positive and negative solutions for each of the concepts can be computed using Equations 6-7 [65], respectively. The final step is to determine the relative closeness of each concept to the positive ideal solution using Equation 8 [65]. The greater the value of C_i the more desirable the concept is and the better the ranking. TOPSIS has the advantages of being somewhat simple, repeatable and transparent but the results can be highly influenced by cardinal information such as weights and expert bias introduced into the decision matrix.

$$N_j = \sqrt{A_{1,j}^2 + ... + A_{N,j}^2},\ i = 1, .., NConcepts,\ j = 1, ..., NAttributes \tag{5}$$

$$S_i^+ = \sqrt{\sum_{j=1}^{NumofFOM} (Value_{i,j} - PositiveIdealValue_j)^2},\ i = 1, ..., NConcepts \tag{6}$$

$$S_i^- = \sqrt{\sum_{j=1}^{NumofFOM} (Value_{i,j} - NegativeIdealValue_j)^2},\ i = 1, ..., NConcepts \tag{7}$$

$$C_i = \frac{S_i^-}{S_i^+ + S_i^-},\ i = 1, .., NConcepts \tag{8}$$

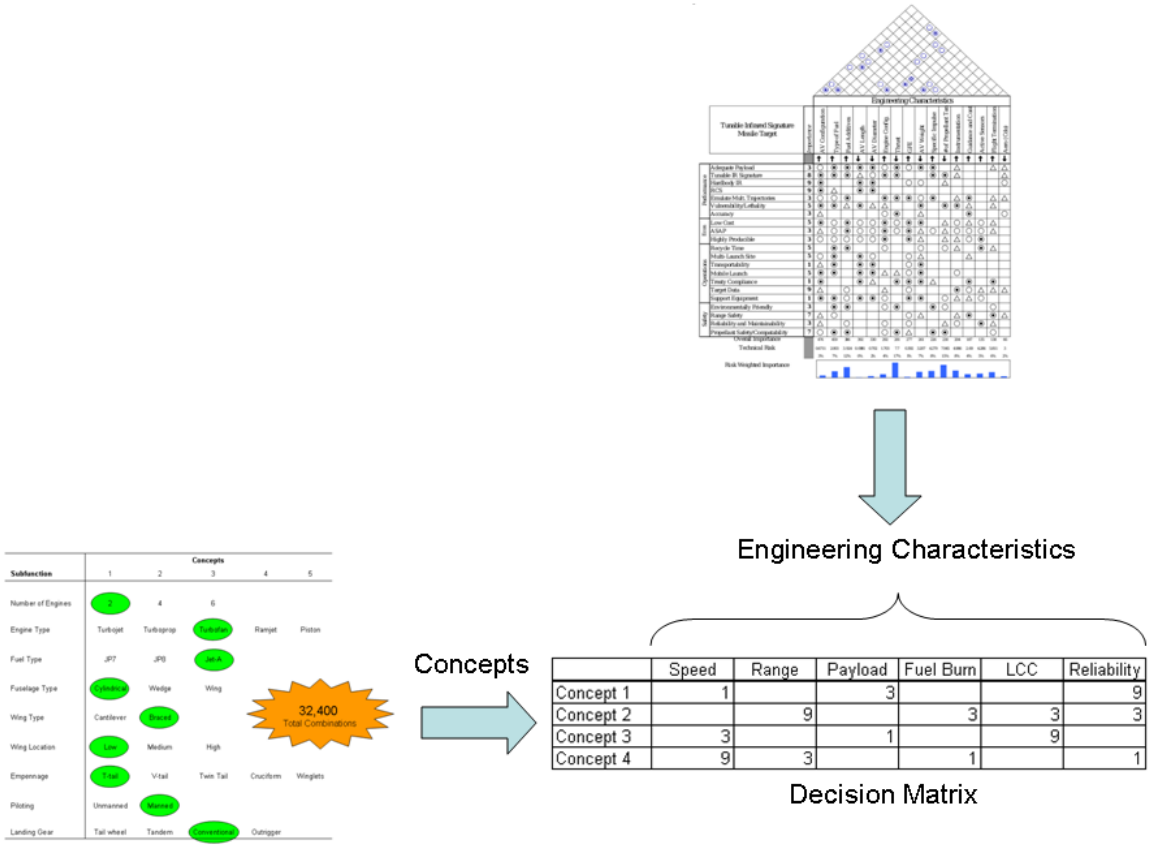

Figure 13: Sample TOPSIS Decision Matrix

2.3 Hypersonic Flow Phenomena

Hypersonic flight is generally accepted to encompass speeds equal to or greater than five times the speed of sound (*Mach* 5). However, it is important to note that there is no clear cut boundary for hypersonic flight, it is simply flight regime where certain effects begin to become more noticeable. These effects include thin shock layers, vorticity interaction, viscous interactions and high temperature flows.

Thin shock layers are a result of the increasing density of the flow behind the shock as Mach number increases allowing for the same flow to squeeze through a smaller region in space. High-speed flows where Reynolds number (Re) is small can experience what is called a viscous shock layer which means that most or the entire shock layer lies inside the boundary layer. Newtonian flow theory becomes applicable in cases of high Reynolds number hypersonic flows where the viscous shock layer is very small. Newtonian theory

argues that when air molecules strike a surface, they will lose all their momentum normal to the surface but continue to move without any loss of momentum in the tangential direction. This theory is elegant and finds that pressure and force on the surface varies as the squared sine of the surface inclination angle θ as shown in Equation 9 [6].

$$C_p = 2sin^2\theta \tag{9}$$

Vorticity interactions are the interactions between the entropy layer and the boundary layer both of which are growing downstream along the surface. The entropy layer introduces high vorticity to the boundary layer. This leads to poor performance by the analytic models used to predict the growth of the boundary layer because the value of the entropy at the edge is non-unique [81].

Viscous dissipation in the boundary layer is the conversion of high kinetic energy in the flow into internal energy. Thus viscous dissipation leads to an increase in temperature in the boundary layer. These temperatures can be so high that they can produce dissociation and ionization of the air molecules. The increase in temperature and constant pressure normal to the surface leads to lower density flow within the boundary layer. Therefore the boundary layer needs to grow in order to accommodate the required mass flow. As a result the growing boundary layer affects the outer inviscid flow and this in turn reflects back in the boundary layer. In addition, the boundary layer can grow so much that it overlaps and interacts with the thin shock layers transforming the shock layer from inviscid to viscous. These interactions between the boundary layer and the shock layer are known as viscous interactions. The increase in boundary layer thickness makes the body appear bigger or thicker to the incoming flow which can affect lift, drag, and stability of the vehicle [81].

The high temperature flows lead to three important phenomena: vibrational excitation, chemical reactions, and non equilibrium flows. Vibrational excitation gives way to molecular dissociation as chemical bonds are torn apart, ionization as electrons are torn from chemical species, and also leads to electronic excitation whereby species move to higher orbital energy configurations [81].

When analyzing hypersonic vehicles one must also consider the effects of high altitudes

where such vehicles operate. As altitude increases, and density decreases, the mean free path of air molecules also increases. Once the mean free path becomes too large the traditional aerodynamic concepts begin to fail and one must rely on the concept of kinetic theory to predict the aerodynamics in this regime of low density flow. As a result of the low density, the boundary condition at the surface transitions from no-slip to a velocity slip and temperature slip condition. As altitude continues to increase and density continues to decrease, the molecules reflecting from the surface cease to interact with other molecules coming in. This effect is called *free molecular flow* and is governed by the Knudsen number which relates mean free path and characteristic dimension of a body.

The heatloads experienced by a vehicle during hypersonic flight are highly dependent on the trajectory, geometry, aerodynamics, aerothermodynamics, and transient heat transfer. Therefore there are several ways to optimize a vehicle so that it can deal with the extreme flight conditions. These include trajectory optimization, shape optimization, and thermal protection technologies such as thermal protection systems consisting of different insulating material stack ups and cryogenic and vaporization cooling systems. Each of these previously described methods will be presented in this .

2.4 Aerothermodynamic Optimization

Aerothermodynamic optimization can be divided into three main categories of trajectory, shape, and technology infusion and optimization. In an ideal scenario a designer would attempt to optimize all three of these approaches simultaneously to obtain a globally optimum design solution. However, this poses an extremely complex optimization problem which may end up having many non-unique solutions. It may not be practical to perform a trajectory optimization for applications such as aircraft which, unlike reentry vehicles, require the missions to be flexible. Nonetheless all of these approaches have been researched in the literature and will be presented below in more detail.

2.4.1 Trajectory Based Methods

Traditionally, a trajectory is optimized according to a specified maximum skin temperature which is not to be exceeded. This maximum temperature limit is given by a prescribed TPS

layout, whose thickness is then manipulated to be able to handle the heatloads and account for the temperature limit of the internal structure.

The problem with this approach is that the trajectory is not optimized based on heatload and the result is a non optimal TPS that is most likely very thick. In order to address this issue, Garcia and Fowler proposed the use of an integrated function of stagnation point heatrate and angle of attack (AoA) as the objective function for the optimization of trajectory and showed that this function is directly related to TPS weight [33]. The authors successfully demonstrated a reduction in TPS weight of the Space Shuttle by optimizing this newly proposed objective function.

In 1993, NASA Langley lead the effort of the design of the HL-20 which was a prospective backup for the Space Shuttle. During this time, Powell showed that one could restrict the heatrate as a way to meet the maximum temperature constraints of the TPS by maintaining a constant angle of attack while adjusting the bank angle [72]. However, he did not account for the effect of heatload on the TPS weight. Wurster and Stone took the trajectory proposed by Powell and created an aerothermodynamic database through the use of computational fluid dynamics in order to determine the TPS design and materials needed in the HL-20 [94]. Prabhu et al took this idea a step further with the X-33 and successfully decoupled the aerothermodynamics from the trajectory [73]. This major contribution allows the aerothermodynamics and the resulting effect on TPS to be estimated for any trajectory. This means that trades can be conducted between the trajectory and the TPS design in order to find the best combination for a given vehicle.

None of the methodologies presented up to this point contain a constraint on the heatload, which has a direct effect on the TPS. However, several studies have been conducted on constraining the heatload itself and not just the external maximum temperatures. A study by Sachs and Dinkelmann developed a mathematical model for the 1-D unsteady heat transfer equation with the purpose of trajectory optimization [82]. They applied this model to the wall containing the thermal protection system of a vehicle while coupling it to the aerodynamics, propulsion and equations of motion. The objective function was to minimize the amount of fuel consumed by varying the trajectory of a cruiser subject to the constraints

of the equations of motion, heat flux, load factor, dynamic pressure, angle of attack, throttle setting, and equivalence ratio. They demonstrated a 22% heat input decrease to the internal structure by imposing the heat flux limit into the optimization with a minimal penalty on fuel. Two years later, Windhorst et al followed a similar methodology to obtain the optimum trajectories for 1) minimum thermal energy absorbed at the vehicles surface, 2) minimum total heatload applied to the vehicle, and 3) minimum thermal energy absorbed by the internal structure [93]. However, in his study the objective function was integrated with respect to total energy. This is ideal since for every trajectory with same initial and final boundary conditions, the total change in energy will be identical. The same year, Chow et al performed a similar study optimizing for minimum time, minimum surface temperatures, and minimum heatload [19]. However, in this study the transient heat equation was not utilized for the minimum heatload trajectory, and instead the authors optimized the total heat input through the surface of the TPS alone.

2.4.1.1 Equations of Motion

The equations of motion shown in Equations 10-13 form the basis for nearly all trajectory models used today [14]. In these equations the aircraft is modeled as a point mass, where the lift, weight, drag and thrust are all forces applied to the vehicle in an inertial reference frame. Figure 14 shows the free-body diagram of the aircraft modeled as a point mass with all acting forces. In Equations 10-13, x is the down range, y is the altitude, α is the angle of attack, ϵ is the thrust vector angle relative the body centerline, γ is the flight path angle relative to the horizon and T is the thrust. These equations also assume a flat Earth or an Earth radius which approaches ∞. The equations of motion can be simplified by using the small angle approximations shown in Equations 14-15 [14].

$$m\dot{V} = T\cos(\alpha + \epsilon) - D - mg(\sin\gamma) \tag{10}$$

$$mV\dot{\gamma} = T\sin(\alpha + \epsilon) + L - mg(\cos\gamma) \tag{11}$$

$$\dot{y} = V sin\gamma \tag{12}$$

$$\dot{x} = V cos\gamma \tag{13}$$

$$where: \; T = T(V,h), \; L = L(V,h\alpha), \; D = D(V,h\alpha)$$

$$sin(\alpha + \epsilon) \cong \alpha + \epsilon \tag{14}$$

$$cos(\alpha + \epsilon) \cong 1 \tag{15}$$

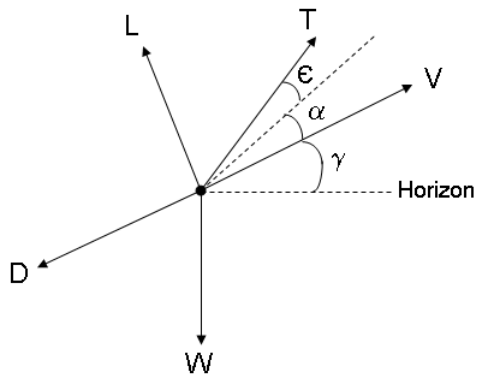

Figure 14: Free Body Diagram of Forces on a Vehicle Modeled as a Point Mass

In some segments of flight it is possible to further simplify the system of equations by assuming a quasi-steady approximation. For this approximation the rate of change of all the state variables ($\dot{V}$,$\dot{\gamma}$,$\dot{y}$,$\dot{x}$) are neglected or assumed equal to zero resulting in a new set of equations shown in Equations 16-17 [14].

$$0 \cong T - D - mg(\sin\gamma) \tag{16}$$

$$0 \cong T(\alpha + \epsilon) + L - mg(\cos\gamma) \tag{17}$$

2.4.1.2 Energy-State Approximation

Solving the equations of motions can be a computationally intensive task and for some problems the Energy-State Approximation (ESA) becomes the method of choice. Initially developed by Bryson et al, this method assumes that the potential and kinetic energies can be traded instantaneously, the acceleration normal to the flight path $V\dot{\gamma}$ can be neglected and the flight path angle is small enough so that $cos\gamma \cong 1$ and $sin\gamma \cong \gamma$ [14]. From these assumptions it is now possible to use the total energy (E) as the only state variable for performance optimization.

The total energy per unit mass equation on a point mass shown in Equation 18 becomes the basis for the Energy-State Approximation. This equation can be differentiated with respect to time, then using the equations of motion in Equations 10-13, $\dot{V}$and $\dot{y}$ can be eliminated to obtain the Energy-State Approximation in Equation 19.

$$E = \frac{1}{2}V^2 + gh \tag{18}$$

$$\dot{E} = V\frac{(T-D)}{m} \tag{19}$$

Furthermore by assuming that the thrust component normal to the flight path is small, one can neglect the term $T\sin(\alpha+\epsilon)$ and thus the equation for the forces in the direction normal to the flight path can be simplified to $L(\alpha, V, h) = mg$. This equation states that lift is equal to the weight and can be used to compute the angle of attack (α) in terms of velocity (V) and altitude (h). Finally, the altitude can found by solving the original equation for total energy (Equation 18) for altitude (h) as function of total energy (E), and velocity (V). The velocity becomes a control variable since both equations for α and h are functions of velocity and the total energy (E). The optimization objective is typically to maximized the ratio of excess power to fuel mass flowrate given in Equation 20.

$$Objective = \frac{(T-D)}{\dot{m}_{fuel}} \tag{20}$$

2.4.1.3 Jackson Energy Method

The Jackson Energy Method is an approximate method for estimating the performance of an air-breathing vehicle during climb or acceleration [41]. The method begins with the basic equations of motion (Equations 10-13) and linearizes them to obtain a closed form expression of the performance parameters. The approximation is applicable to successive finite velocity intervals where the aerodynamics, propulsion, and flight path parameters are assumed to be constant [41].

In order to carry out the linearization of the equations of motion, the rate of change of flight path angle $\dot{\gamma}$ must be assumed equal to zero and neglected and the flight path angle is assumed to be small enough so that $cos\gamma \cong 1$ and $sin\gamma \cong \gamma$. In addition, the angle of attack α and the thrust offset angle ϵ are assumed to be equal to zero. Given these assumptions the equations of motion (Equations 10-13) can be linearized as shown in Equations 21-24.

$$m\dot{V} = T - D - mg\gamma \tag{21}$$

$$0 = L - W \tag{22}$$

$$\dot{y} = V\gamma \tag{23}$$

$$\dot{x} = V \tag{24}$$

It is now possible to combine Equation 21 and Equation 23 to obtain the differential form of the Energy-State Approximation as shown in Equation 25. The left hand side of Equation 25 represents the total energy of the vehicle represented by a point mass. This equation is essentially the Energy-State Approximation in terms of velocity and altitude.

$$\frac{V\dot{V}}{g} + \dot{h} = \frac{(T-D)}{mg}V \tag{25}$$

The method also requires the assumption of a parabolic drag polar, and thrust being a function of fuel flowrate ($T = -\frac{dW_{fuel}}{dt}I_{sp}$) or ($T = -\frac{dW}{dt}I_{sp}$) if fuel is the only mass being

burned or expelled out of the vehicle where W is the mass of the vehicle itself. In addition, the parameter $\frac{dh}{dV}$ is introduced to define the flight path. Knowing these assumptions and after some algebraic manipulation the Jackson Energy expression for climb with acceleration can be obtained as shown in Equation 26 [41]. This expressions allows the computation of the weight variation at the end of the finite velocity interval. Once the weight variation is known Equations 27-28 can be used to compute the time and range change during this interval where $\bar{W}_{fuel}$ is the average fuel burned during the interval [41].

$$\ln\left(\frac{W_1}{W_2}\right) = \frac{(V_2 - V_1) + g\left(\frac{\triangle h}{\triangle V}\right)\ln\left(\frac{V_2}{V_1}\right)}{g\frac{\bar{I}_{sp}}{(W1/S)}\left\{\frac{W1}{S} - \left[\frac{\bar{q}S\bar{C}_{D,min} + \frac{\left[\bar{C}_{D,i}/\left(\bar{C}_L - \bar{C}_{L,o}\right)^2\right]}{\bar{q}}\left(\frac{W_1}{S} - \bar{C}_{L,o}\bar{q}\right)^2}{\frac{\bar{T}}{W_1}}\right]\right\}} \tag{26}$$

$$t_2 - t_1 = \frac{W_2 - W_1}{\bar{W}_{fuel}} \tag{27}$$

$$R_2 - R_1 = \frac{V_2 + V_1}{2}(t_2 - t_1) \tag{28}$$

Similarly by integrating the linearized equation of motion and setting $dV = 0$, one can obtain an expression for climb at constant velocity as shown in Equation 29. An expression for descent (Equation 30) can be derived by solving the Equation 25 for the flight time variation over the velocity interval and assuming no variation in weight or no fuel being burned [41].

$$\ln\left(\frac{W_1}{W_2}\right) = \frac{h_2 - h_1}{\frac{V_1\bar{I}_{sp}}{(W1/S)}\left\{\frac{W1}{S} - \left[\frac{\bar{q}S\bar{C}_{D,min} + \frac{\left[\bar{C}_{D,i}/\left(\bar{C}_L - \bar{C}_{L,o}\right)^2\right]}{\bar{q}}\left(\frac{W_1}{S} - \bar{C}_{L,o}\bar{q}\right)^2}{\frac{\bar{T}}{W_1}}\right]\right\}} \tag{29}$$

$$t_2 - t_1 = \frac{(V_2 - V_1) + g\left(\frac{\triangle h}{\triangle V}\right)\ln\left(\frac{V_2}{V_1}\right)}{g\left\{\frac{\bar{T}}{W_1} - \left[\frac{\bar{q}\bar{C}_{D,min} + \frac{\left[\bar{C}_{D,i}/\left(\bar{C}_L - \bar{C}_{L,o}\right)^2\right]}{\bar{q}}\left(\frac{W_1}{S} - \bar{C}_{L,o}\bar{q}\right)^2}{\frac{W_1}{S}}\right]\right\}} \tag{30}$$

2.4.2 Shape Based Methods

Another approach to minimizing the heatrate experienced during high-speed flight is through shape optimization. Ogasawara and Nishioka produced a formulation of an approximate heating design index that can quantitatively estimate the total integrated heatloads of a candidate shape without conducting extensive numerical analysis [68]. The design index gives an estimation of the configuration with lowest total aerodynamic heating. The authors argue this will yield lower TPS weight however they do not look into the TPS configuration itself. The design index approach presented is only appropriate at the initial reentry phase called the constant aeroheating phase where one can say. The heating rate is constant because the optimal trajectory follows the aeroheating limit of the vehicle. At this phase the flight conditions, such as angle of attack, and Reynolds number are constant. The heating index assumes small elevation and side slip angles and it still requires full numerical integration of the heating rates over the whole vehicle surface.

Sudmeijer and Mooij focus only on a general reentry module shape that can be described by only four geometric design variables: nose radius, cone and flare angles, and maximum length of module [88]. The aerodynamics of the problem is modeled using response surface methodology (RSM). An L16 central composite design (CCD) DoE developed by Bob & Wilson (1951) is implemented which results in 25 different concepts. This results in a second-order response surface equation (RSE) which includes linear, interaction, and quadratic terms. A separate L9 DoE is used for mission simulation of three initial reentry conditions, entry velocity, entry path angle, and mass which describe nine ballistic reentry trajectories. Interactions between the three initial reentry conditions are ignored and only main effects are looked at. A panel code (NRLAERO) is used to compute aerodynamics of each configuration for each of the nine trajectories which result in a total of 225 DoE runs. Signal-to-Noise ratio is used to check trajectory sensitivity for each of the 25 concepts. However, the vehicle is optimized using the 2nd order RSEs. The RSEs are not entirely accurate due to the lack of higher order interactions. A more sophisticated DoE would be needed for a more appropriate simulation of the design space but this would also result in a higher number of simulation runs. The capabilities of response surface methodology are

exploited more by Chen et al by coupling it to more sophisticated analysis tools [18]. The authors have developed an environment which can provide aerodynamic and aerothermodynamic responses as functions of geometrical design variables, flight conditions, and flight regime. The aerodynamic RSEs are generated using a combination of a 3-D panel code and CFD code while aerothermodynamic RSEs are generated using an aerothermal code call LATCH. However, increasing fidelity comes at great computational cost. Setup of an RSM for aerodynamics and aerothermodynamics requires a significant amount of computational time and effort, although this can be done offline of the actual optimization process.

Some have taken optimization a step further and opted to simultaneously optimize the trajectory along with the vehicle shape. An example of this is Tava and Suzuki, who investigate the simultaneous optimization of shape and trajectory for a simple reentry module consisting of two cones, and a spherical cap which can be described with only three design variables [89]. Their study tackles the aerodynamics, aerothermodynamics, flight dynamics, and weight sizing analysis of the problem. They do not deal with TPS directly, but simply assume that decreasing heatload leads to decreased TPS weight. The problem is optimized using an all-at-once method, where the sub disciplines are computed independently and the optimizer takes care of any feed-back or feed-forward loops. This puts more work on the optimizer but simplifies the setup of the problem. The use of shape functions to describe aeromechanic parameters such as angle of attack and bank angle has facilitated the job of the optimizer in multidisciplinary design as seen in Mor and Livne [62]. This results in a decrease in the number of design variables which describe the profile of such parameters throughout the entire flight.

2.4.3 Technology Infusion

Another approach to dealing with the adverse aerothermal environments of high-speed vehicles is through technology infusion. New technologies can allow a capability gap to be filled and thus allowing the vehicle to perform its intended task. The type of technologies that are used to deal with aerothermal heating are known as thermal management systems. Within this field there are a wide variety of approaches and concepts including heatsink

structures, hot structures, insulating structures, heat pipes, and convective cooling. All of these concepts will be categorized and described in more detail in the following section.

2.5 Thermal Management Systems

This section will shed more light on what exactly a thermal management system actually is. The different systems will be categorized based on their functionality and an explanation on how they work, how they can be sized and optimized, and what are some of their advantages and disadvantages will be provided.

2.5.1 Description of Concepts

There are numerous types of thermal management system in existence today with varying levels of maturity. These technologies can be divided into the categories of passive and active cooling. In this thesis, an active cooling technology refers to a technology which requires some form of external energy source to operate. Passive cooling technologies include the traditional and most well known TPS, hot structures, and heat pipes. Active cooling technologies include thermoelectric systems, sensible heat systems, and latent heat systems. Some of these systems have been successfully employed to protect against the elevated heatloads associated with high-speed flight while others have their roots in other applications such as electronics. All of these candidate technologies will be explained in further detail in the following sections.

2.5.1.1 Passive Cooling

Heatsink Structure Heatsink structures do not have a practical application in aircraft or reusable launch vehicles nonetheless they are included here for the sake of completeness. The mechanism by which heatsink structures work is shown in Figure 15 [11]. This schematic shows that the bulk of the heatload generated by the aerothermal environment is distributed into the structure itself but some of it is also radiated back into the freestream. These types of structures are more suitable to applications with very short heating pulse. This means they cannot be used in sustained hypersonic flight where the integral heatload on the vehicle can continue to grow to unacceptable levels unless there is another secondary heat

loss mechanism in place to actively remove the buildup of heatloads. The plot in Figure 16 [11] shows the heat storage characteristics of different materials. The ability to sustain heatload will be highly dependent to the heat capacity of the selected material.

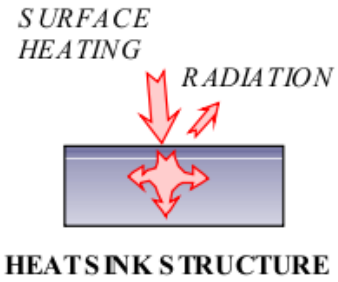

Figure 15: Principle of a Heat Sink Structure [11]

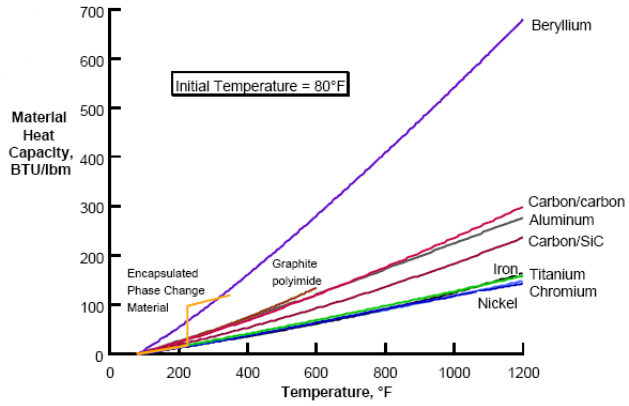

Figure 16: Materials Heat Storage Characteristics [11]

Hot Structure Structures which have high specific properties and can heat up to significantly high temperatures without damage or need of TPS are called hot structures. A schematic of the principle behind hot structures is shown in Figure 17 [11]. Not requiring as much TPS or any TPS at all is a significant advantage since TPS is generally considered dead weight whose only value is to protect the vehicle from the thermal loads. This means that a hot structure is technically the most light weight solution for a high-speed vehicle. They are ideal for use in wing and vertical tail leading edges, as well as control

surfaces which are volume limited since hot structures have no need for bulky TPS. In addition, these structures tend to be less brittle than ceramic TPS and have lower maintenance requirements which lead to increased robustness and reliability [64]. The principal issue associated with hot structures is that they cannot be used near electronics or other thermally sensitive equipment.

One of the most common types of hot structure is carbon-carbon (CC). A step up from CC is reinforced carbon-carbon (RCC) which is carbon-carbon encased in a graphite matrix to improve its strength. RCC is still used along the wing leading edges of the Space Shuttle. Titanium matrix composite (TMC) is another hot structure which is generally used for lower temperature applications. TMC offers a significant reduction in weight for applications operating within $1,500\ ^{\circ}F$ temperatures. This type of hot structure was successfully used on the X-30 and demonstrated a 50% weight reduction when compared to other metallic TPS and other super alloys [64].

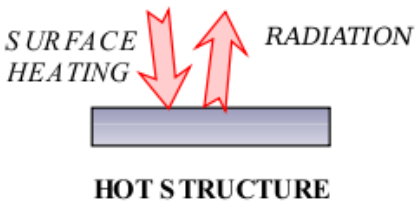

Figure 17: Principle of a Hot Structure [11]

Insulated Structure Insulated structures play a large role in what is commonly known as a thermal protection system consisting of tiles and blankets. They can be considered a passive system and are usually the first line of defense to aerothermal heatloads for a high-speed vehicle. The working principle behind the insulated structures is shown in Figure 18 [11]. The types of materials used in the TPS are dictated by the maximum temperatures the vehicle is experiencing on its surface, while the heatload determines the thickness of the TPS in order to limit the temperature in the internal structure. There are various kinds of systems including blankets, tiles, and standoff TPS.

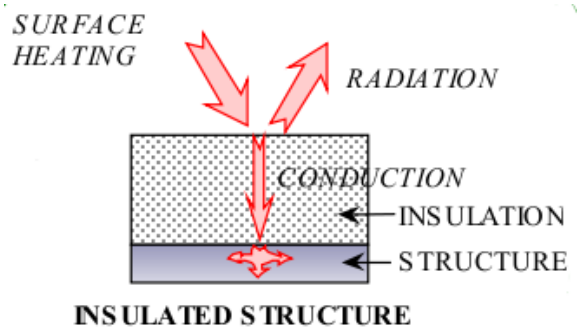

Figure 18: Principle of an Insulating Structure [11]

Ceramic blankets generally have a lower initial cost and are easy to install given their flexibility. Two of the most popular blanket TPS are AFRSI and TABI. AFRSI can withstand temperatures of up to $1,200\ ^{\circ}F$ and is relatively easier to maintain than the previous FRSI blankets which it intended to replace. It has a rough surface which increases aerodynamic drag and heating. TABI is a next generation blanket designed by NASA Ames Research Center to improve on the AFRSI design. It has a higher maximum temperature than AFRSI at $2,200\ ^{\circ}F$, higher strength thanks to corrugations in the Q-fiber felt insulation, and a smoother surface improving drag and aerodynamic heating. Q-fiber is a pure silica fiber which is extremely stable, with no thermal expansion, contraction, or distortion, and with very high thermal capabilities [43]. However, both of these concepts still require a lot of maintenance to waterproof and can become brittle after exposed to high temperatures [64]. There is ongoing research in order to move from bonded TPS towards mechanically attached TPS. This has the promise of reduced maintenance costs by making the replacement much easier than before [64].

Ceramic tiles such as LI-900 and AETB can generally operate at higher maximum temperatures than ceramic blankets and any other type of TPS. LI-900 are all silica rigid fibrous insulation that can operate are up to $2,300\ ^{\circ}F$. The AETB concept is an improvement to the LI-900 tiles which improves the strength of the tiles by adding a toughened uni-piece fibrous insulation (TUFI) coating to the surface of the tile. The AETB concept also increases the maximum temperature at which it can operate to $2,500\ ^{\circ}F$. Despite their great performance, both of these ceramic tile designs are still very brittle and require extensive

maintenance which can be costly and time consuming. Due to their brittleness, ceramic tiles need to be isolated from the vibrations of the internal structure. In addition, they also need to be waterproofed just like ceramic blankets [64].

Standoff TPS is a new concept or view on what TPS should be able to achieve. This concept has been around since the early 1980s and consists of either metallic or ceramic matrix composite designs with greater durability, lower maintenance, and lower costs. These designs are inherently waterproof since even the ceramic material in the ceramic matrix composite is encapsulated by a metallic material. This eliminates one of the largest maintenance issues associated with ceramic blankets and tiles. The thermal growth of metals is one of the greatest issues inherent with metallic TPS. This requires the size of the metallic panels to be kept relatively small at around 18-20 in [64]. This results in a very large number of panels which in turn means greater number of fasteners, indirect complexity, and unforeseen maintenance costs. Ceramic matrix composites on the other hand tend to be much heavier than blankets, tiles, and metallic TPS but at the same time panels of this kind can be made much bigger resulting in a less complex system [64]. Some of these metallic TPS are the super alloy honeycomb (SA/HC) which contains the typical Q-felt fiber and cerrachrome between an Inconel 617 and a titanium honeycomb panel and can withstand maximum temperatures between 1,800 and $2,000\ ^{\circ}F$. Inconel alloys have the advantage of being resistance to oxidation and non-corrosive. The SA/HC2 is a second generation of the same type of metallic TPS but the Q-felt insulation is replaced by an advanced saffil insulation which is lighter while still withstanding the same maximum temperatures as the first generation SA/HC. The titanium honeycomb (TI/HC) metallic TPS is very similar in design to SA/HC with its Q-felt insulation but it is meant to be a lower weight concept with lower maximum temperature. The main difference to the SA/HC concept is that the exterior metallic panel composed of Inconel 617 in SA/HC is replaced by another titanium honeycomb panel. Another significant metallic TPS to mention is advanced metallic honeycomb (AMHC) which is being researched by NASA LaRC. It consists of a low conductivity and low density material called internal multiscreen insulation (IMI) encased by an outer PM2000 honeycomb panel which can withstand higher maximum temperatures between 2,000 and $2,200\ ^{\circ}F$, while the

lower panel is made of titanium [64].

Parametric studies show that metallic TPS particularly AMHC tend to be lighter and most efficient for applications with greater integrated heatloads which can be attributed to their low density and low conductivity cores of fibrous materials. The AFRSI and TABI concepts are found to be more efficient at lower heatloads, and ceramic tiles are the most promising option for the highest temperature applications [64].

2.5.1.2 Semi-Passive Cooling

Heat Pipes Generally, heat pipes can be categorized as a form a latent heat system. The principle behind a heat pipe is the passive transportation of heat from one region to another as shown in Figure 19 [11]. A small amount of coolant is placed within the heat pipe while leaving some volume so that such coolant can vaporize within the pipe. The pipe is pressurized accordingly so that the coolant condenses at one extreme of the heat pipe and evaporates at the other extreme of the heat pipe. The coolant in liquid form flows towards an evaporator through gravity or wick. Once it vaporizes, the gas flows back towards the lower temperature condenser and the cycle continues. A heat pipe is based on the ideal thermodynamic cycle show in Figure 20 [30].

Heat pipes are attractive because of the large amount of heat that can be transported by exploiting the latent heat of a coolant. They also contain no moving parts which makes them more robust, less complex, and require less maintenance. However, they can only operate most efficiently within the temperature range for which it has been optimized through the pipe pressurization. This makes them less efficient for high-speed vehicles with highly varying flight conditions and missions which lead to varying surface temperatures on the vehicle. A variety of working fluids and their typical temperature operating ranges are given in Table 1 [30]. Heat pipes have some similarities to the process of active convective cooling and can be though of as a semi-passive form of this process which will be explained in later sections.

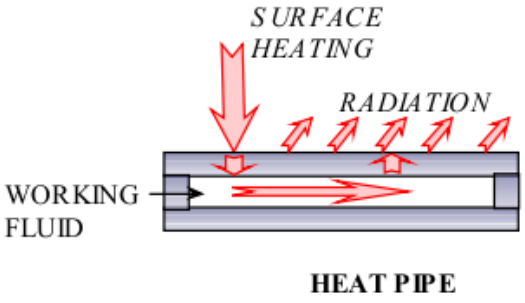

Figure 19: Principle of a Heat Pipe Structure [11]

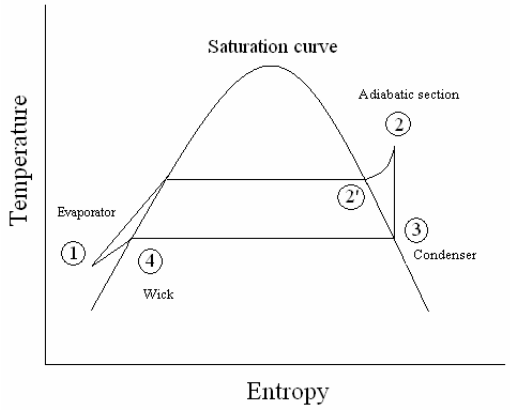

Figure 20: T-s Diagram for the Ideal Thermodynamic Cycle [30]

Table 1: Heat Pipe Working Fluids and Temperature Ranges [30]

MEDIUM	*MELTING PT. (°C)*	*BOILING PT. AT ATM. PRESSURE (°C)*	*USEFUL RANGE (°C)*
Helium	- 271	- 261	-271 to -269
Nitrogen	- 210	- 196	-203 to -160
Ammonia	- 78	- 33	-60 to 100
Acetone	- 95	57	0 to 120
Methanol	- 98	64	10 to 130
Flutec PP2	- 50	76	10 to 160
Ethanol	- 112	78	0 to 130
Water	0	100	30 to 200
Toluene	- 95	110	50 to 200
Mercury	- 39	361	250 to 650
Sodium	98	892	600 to 1200
Lithium	179	1340	1000 to 1800
Silver	960	2212	1800 to 2300

Ablative Structure Ablation is a complex process in which the thermal protective layer undergoes changes in physical state and in some cases chemical reactions as shown in Figure 21 [11]. Those ablation processes which only experience changes in the physical state of the material are referred to as non-charring. However, most aerospace applications include charring ablators in which chemical reactions occur in addition to changes in physical state. A more detailed description of an example char ablative structure is shown in Figure 22. After the temperature of the ablative material reaches a certain point it changes physical state through melting and vaporization, sublimation, chemical reactions, or a combination of these depending on the material itself. The result of these processes is a combination of gases and char. Char is a porous solid material which forms a layer at the surface of the ablative structure. A gaseous layer is also formed between the ablative material and the char layer. As the pressure builds in the gaseous layer it is forced out through the porous char layer where further chemical reactions can occur. Heat is absorbed by the newly formed gases and insulated from the structure by the ablative material itself. In addition, as the gases are released they form a thin gaseous layer over the surface of the vehicle which helps further insulate from the aerothermodynamic induced heatrates.

Despite its high degree of effectiveness in applications experiencing very high heatrates, ablation is impractical for use in RLV due to the nature of the process. This type of thermal protection lends itself better for single use, and extreme heatrate applications such as disposable planetary probes and the high-speed missile nose caps. Although not considered an active cooling thermal management solution, ablation displays properties similar to transpiration cooling. The transpiration process and others will be described further in the next section.

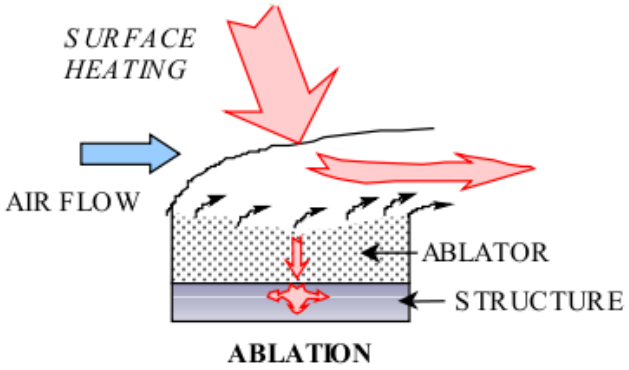

Figure 21: Principle of an Ablative Structure [11]

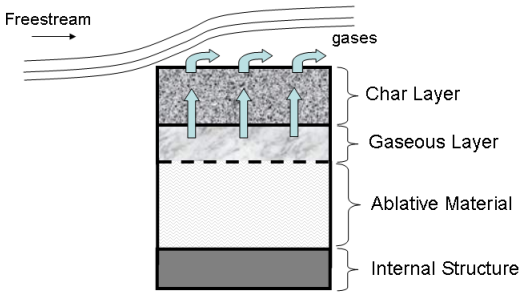

Figure 22: Char Ablative Structure

2.5.1.3 Active Cooling

Transpiration and Film Cooling Transpiration cooling is the process of injecting a coolant into the boundary layer through a porous surface as shown in Figure 23 [11]. As the coolant reaches the surface it vaporizes and produces a thin layer of coolant which flows near the surface. This gaseous layer mixes with the boundary layer near the surface and has the ability to remove and insulate heat intended to reach the surface of the vehicle as shown in Figure 24 [11].

Transpiration cooling is desired in small areas experiencing extreme aerothermodynamic heatrates such as nose tips, leading edges, and air-breathing engine structures. However, it typically becomes less practical and inefficient for larger surfaces and requires the carrying and storage of coolant on board.

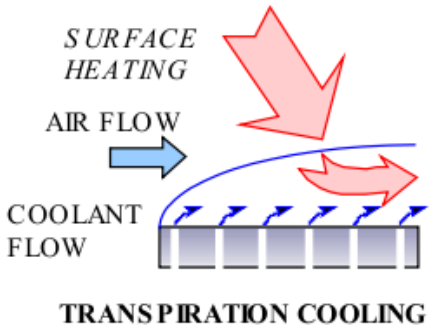

Figure 23: Principle of a Transpiration Cooling [11]

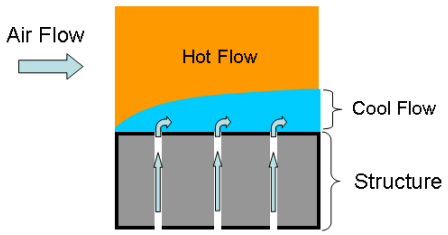

Figure 24: Transpiration Cooling Boundary Layer

Film cooling is very similar in nature to transpiration cooling but the coolant is infused into the boundary layer by means of discrete slots on the surface as shown in Figure 25 [11]. Similar to transpiration cooling it is more efficient in localized areas experiencing very high heatrates.

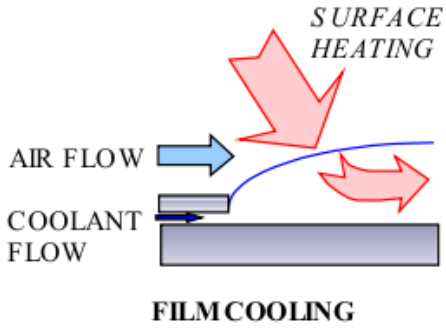

Figure 25: Principle of a Film Cooling [11]

Convective Cooling The process of convective cooling is one by which heatrates are passed on to an underlying channel or heat exchanger as shown in Figure 26 [11]. Heat is transferred to the coolant flow by convection and removed before it reaches the internal structure. Once the coolant is heated, it can then be managed in different ways. One option is to simply expel the heated coolant overboard into the atmosphere and effectively reducing the weight of the vehicle while improving performance. The heated coolant can also be managed by transferring it to even hotter components before its eventual expulsion overboard into the atmosphere. Last but not least, the coolant could be cycled from hotter to cooler regions on the vehicle and vice versa to essentially provide an endless supply of coolant flow. This could potentially reduce the total amount of coolant need to be carried on take off and can significantly impact the performance of the vehicle. However, such a system will also require an extensive infrastructure with pumps, and heat exchangers which need to be accounted for. Convective cooling systems can be further divided into the categories of sensible heat and latent heat systems. The differences between these two approaches are describes in the sections following.

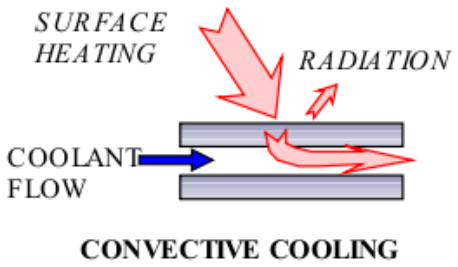

Figure 26: Principle of a Convective Cooling [11]

Sensible Heat Systems Sensible heat cooling systems rely on the convection of heat produced at the surface of the vehicle into another medium such as a hydrocarbon or hydrogen fuel. The hydrocarbon or hydrogen fuel can then be sent to the propulsion system and burned. This serves the purpose of eliminating excess aerothermodynamic heat from the surface and makes for a more efficient combustion of the fuel. An example of this system can be found on Lockheed's SR-71 which utilized the hydrocarbon fuel JP-7 for propulsion

and as a coolant. The fuel JP-7 has the advantage of being the only hydrocarbon fuel which displays endothermic properties during chemical decomposition. This means that for a specific temperature range and pressure JP-7 will be able to absorb and remove more heat than what is expected through convection into a liquid fluid [17].

The main disadvantage of this concept is that it does not take advantage of the large heat extraction capabilities of a fluid's phase change. Known as the latent heat, it is the heat required to produce the phase change from liquid to gas. In addition, there are problems associated with the use of hydrocarbon and hydrogen fuels as a coolant. Hydrocarbon fuels are prone to coking which is the formation of carbon deposit and is related to the heat flux, surface temperature of heat exchanger, and the temperature, pressure and composition of the fuel [50]. There are various types of coke including filamentous coke which is produced by the diffusion of carbon into the metal. Filamentous coke can lead to deterioration of metal properties such as strength and ductility. The carbon deposit can also act as an insulator in the surface of the heat exchanger resulting in reduced heat transfer and clogging small passages [50]. Similar to hydrocarbon fuels, hydrogen can lead to loss of strength and ductility in metals [64]. It is therefore necessary to carefully choose materials that are hydrogen compatible.

Latent Heat Systems Up to this point, active latent heat cooling system have focused mostly on the vaporization of a coolant typically being water which is then expelled from the vehicle after absorbing excess heat. This can be specifically labeled as a non-cyclic active latent heat cooling system. The coolant reservoir is considered a hindrance and dead weight which deteriorates the vehicle's overall performance because it is not reused.

On the other hand, it is possible to have a cyclic active latent heat system which is essentially the same concept as that of a refrigeration system. Latent heat systems exploit the relatively large energy or heat transfer associated with the breaking and formation of chemical bonds during a thermodynamic phase change. Although this technology is significantly mature, there has not been much work done to explore the potential benefits and issues associated with its application to future hypersonic aircraft. There are three main

thermodynamic cycles used for refrigeration including the reversed Carnot cycle, vapor-compression cycle, and the reversed Brayton cycle [15].

2.5.2 Sizing

Thermal management systems are traditionally sized based on mass estimating relationships (MERs) which can be a result of historical data, or engineering approximations. In the case of thermal protection systems advancements have been made with the use of physics based methodologies which make use of the 1-D transient heat equation, and shape functions to properly size the TPS thickness. Thermal protection systems can be sized once the heatrates are determined over the surface of a vehicle. Traditionally the surface temperatures yield the type of material required for the TPS, while the heatrates decide the thickness required to achieve a temperature limit at the internal structure [61]. The objective is ultimately to decrease the TPS thickness which in general leads to less weight and minimization of the maximum surface temperatures which can help make the material selection easier and less costly.

The sizing of more complex technologies such as heat pipes and convective cooling thermal management systems can be more difficult. These technologies require not only the weight estimation of the coolant but also the weight estimation of the underlying support structure of pipes, veins, pumps and storage tanks that can only be estimated using engineering approximations and historical regressions based on other similar systems.

2.5.2.1 Mass Estimating Relationships

Mass estimating relationships are historical-based parametric relations which estimate the component weights based on some related sizing and performance characteristics [47]. In the case of thermal management systems they can provide the TPS weight or acreage required for a vehicle given certain geometrical and flight parameters. They can also be used along side other physics-based formulations and engineering approximations to estimate the weight of more complex thermal management systems such as heat pipe, and water boiling systems. For example in the case of water boiling, the total water required to be boiled at various points during the mission can be estimated using the conservation of energy equation.

MERs are a useful tool for TMS weight estimation in the early phases of the design process when not much is yet known about the vehicle. However, MERs are typically constrained to a historical database, therefore, any design that steps outside the boundaries of concepts within the database will require extrapolation and will not be properly modeled.

2.5.2.2 One-Dimensional Transient Heat Equation

The transient heat equation provides a more accurate methodology for estimating and sizing thermal protection systems. The 1-D transient heat equation is given in Equation 31.

$$\frac{\partial T}{\partial t} = \alpha \left(\frac{\partial^2 T}{\partial x^2} + \frac{\partial^2 T}{\partial y^2} + \frac{\partial^2 T}{\partial z^2} \right) \tag{31}$$

$$\alpha = \frac{\kappa}{\rho C_p}$$

It will be shown, the heat profile solution for the surface of a vehicle can be approximated by the 1-D transient heat equation. This approximation helps simplify and speed up the numerical computations for the solution of the heat equation. The diagram in Figure 27 shows a notional view of the thermal protection system layer where direction x is normal to the surface of the vehicle. One can imagine that this layer is the entire thermal protection layer over the vehicle that has been unwrapped for easier visualization. Therefore, the integration of distances over dimensions y and z would yield the total wetted area of the vehicle.

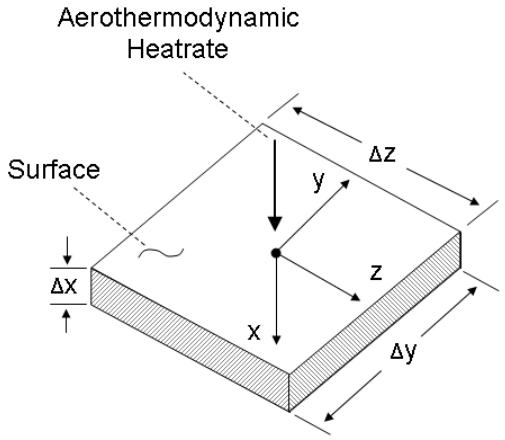

Figure 27: Notional Thermal Protection Layer

In order to simplify the problem, one can assume that the thermal protection layer is symmetric in the yz plane which leads to the relationship shown in Equation 32. Knowing this one can rewrite the 3-D transient heat equation given in Equation 31 as shown in Equation 33. After some simple algebraic manipulation shown in Equations 33-35, one arrives at the expression shown in Equation 36. The assumption in Equation 37 is appropriate if one acknowledges that the surface area made up by the dimensions y and z of the thermal protection layer is much greater than its depth. Hence, the temperature gradient in the x direction is more significant than that in the y and z directions.

$$\frac{\partial^2 T}{\partial y^2} = \frac{\partial^2 T}{\partial z^2} \tag{32}$$

$$\frac{\partial T}{\partial t} = \alpha \left(\frac{\partial^2 T}{\partial x^2} + 2\frac{\partial^2 T}{\partial y^2} \right) \tag{33}$$

$$\frac{\partial T}{\partial t} = \frac{\alpha}{\partial y^2} \left(\frac{\partial^2 T}{\partial x^2} \partial y^2 + 2\frac{\partial^2 T}{\partial y^2} \partial y^2 \right) \tag{34}$$

$$\frac{\partial T}{\partial t} = \frac{\alpha}{\partial y^2} \left(\partial^2 T \left(\frac{\partial y^2}{\partial x^2} \right) + 2\partial^2 T \right) \tag{35}$$

$$\frac{\partial T}{\partial t} = \frac{\alpha}{\partial y^2} \left[\partial^2 T \left(\frac{\partial y^2}{\partial x^2} + 2 \right) \right] \tag{36}$$

$$\frac{\partial y^2}{\partial x^2} \ggg 2 \tag{37}$$

After applying the assumption in Equation 37, the 1-D transient heat equation shown in Equation 38 is obtained [22]. The 1-D transient heat equation can now be used to solve the temperature profile normal to the surface at discretized points on the vehicle surface.

$$\frac{\partial T}{\partial t} = \alpha \frac{\partial^2 T}{\partial x^2} \tag{38}$$

A simplified thermal model for a TPS is shown in Figure 28. One must apply boundary conditions to the top and bottom surfaces of the TPS before solving for the required TPS thickness. The external surface boundary condition at ($x = 0$) and the internal boundary condition at the internal structure ($x = L$) are given in Equation 39 [22].

$$q_{conv} - \varepsilon \sigma T_s^4 + \kappa \frac{\partial T}{\partial x} = 0 \;\; (x = 0) \tag{39}$$

$$\frac{\partial T}{\partial x} = 0 \;\; (x = L)$$

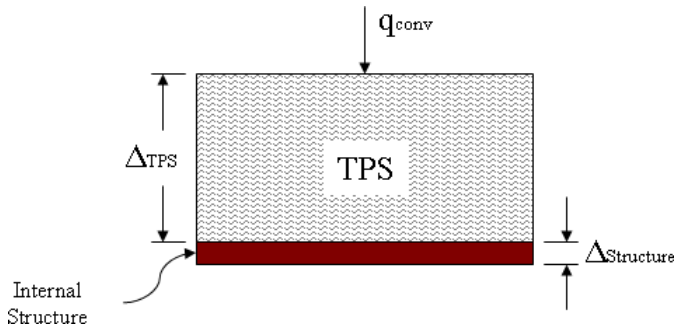

Figure 28: Simplified Thermal Model of TPS

The unsteady 1-D heat equation can be discretized using the fully implicit method shown in Equation 40 [22]. The discretized fully implicit formulation in Equation 41 can be obtained by replacing $r = \alpha \frac{\Delta t}{\Delta x^2}$ into Equation 40. The boundary conditions shown in Equation 39 can be similarly discretized as shown in Equation 42, respectively.

$$\frac{T_i^{n+1} - T_i^n}{\Delta t} = \alpha \left(\frac{T_{i+1}^{n+1} - 2T_i^{n+1} + T_{i-1}^{n+1}}{\Delta x^2} \right) \tag{40}$$

$$f_i = -rT_{i-1}^{n+1} + (1+2r)T_i^{n+1} - rT_{i+1}^{n+1} - T_i^n = 0 \tag{41}$$

$$f_1 = \left(-\kappa - \varepsilon\sigma\Delta x \left(T_1^{n+1} \right)^3 \right) T_1^{n+1} + \kappa T_2^{n+1} + q_{conv}\Delta x = 0 \;\; (x = 0) \tag{42}$$

$$f_{Nx} = T_{Nx-1}^{n+1} - T_{Nx}^{n+1} = 0 \;\; (x = L)$$

As seen above the radiative term in the boundary condition at the external surface introduces a nonlinear term which means the system of nonlinear equations must be solved by an iterative method. The Newton-Raphson method is ideal for this type of problems because of its high convergence rate. The formulation for this method is shown in Equations 43-44 along with the chosen convergence criterion in Equations 45-46 where dT is a vector with length N_x (number or points) [22].

$$J_{i,j} = \frac{\partial f_i}{\partial T_j^{n+1}} \;\; (for\, i, j = 1, ...N_x) \tag{43}$$

$$Tnew = Told - J * f \tag{44}$$

$$dT = T_{new} - T_{old} \tag{45}$$

$$\|g\|_2 = \sqrt{dT * dT'} < 1e-6 \tag{46}$$

2.5.2.3 Coolant Sizing

There are certain thermal management systems that fall into the category of an open system. This means that the mass within the system is changing or decreasing for this application through out the trajectory. An example of such a system is a convective cooling system by which a coolant typically water is pumped to a heat exchanger at a leading edge or nose and

the water is allowed to vaporize while the vapor is later expelled into the atmosphere. The coolant mass flowrate required to remove a certain amount of heatrate from a component is defined in Equation 48. This relation is derived from the energy equation given in Equation 47. The coolant mass flowrate decreases as a function of heatrate which is also dependent on the trajectory itself. The total coolant mass that must be carried onboard can be obtained by integrating the mass flowrate at each discrete point on the vehicle over the entire vehicle surface and as a function of time. This type of system typically leads to a relatively heavy aircraft on takeoff but the performance improves as the trajectory progresses and a lot of the residual coolant weight is expelled out of the system. Phase changing systems are very effective means of removing heat because the heat of vaporization ($\triangle H_{vap}$) is usually much greater than the sensible heat by which traditional radiators operate. A more detailed explanation of how the coolant heatrate is obtained is given later in section 4.2.6.6.

$$\dot{q}_{coolant} = \dot{m}_{coolant} \triangle H_{vap} + \dot{m}_{coolant} C_{p_{coolant}} (T_{boil} - T_{initial}) \tag{47}$$

$$\dot{m}_{coolant} = \frac{\dot{q}_{coolant}}{\triangle H_{vap} + C_{p_{coolant}} (T_{boil} - T_{initial})} \tag{48}$$

2.5.3 Optimization

The partial differential heat equation solver can be integrated with a constrained optimizer as shown in the design structure matrix (DSM) given in Figure 29. The optimizer will be used to solve for the required thickness of the TPS while meeting an internal wall temperature boundary constraint. This constraint prevents damage to the underlying structure and to heat sensitive equipment onboard. The internal temperature constraint is typically assumed to be 300 K, and some times it is relaxed in areas of the wing where there is less temperature sensitive equipment.

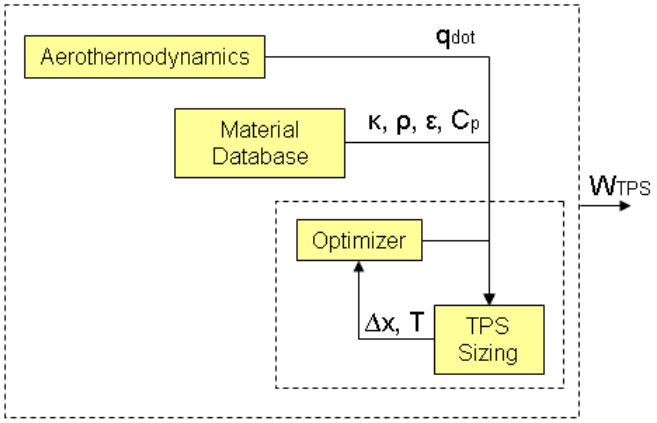

Figure 29: Design Structure Matrix for TPS Sizing

The nature of the problem requires the use of an optimization technique for a constrained, continuous and nonlinear design space. There are various optimization techniques which can handle such a problem including the Method of Feasible Directions (MoFD), Generalized Reduced Gradient method (GRG), and Generalized Reduced Gradient (SQP).

2.5.3.1 Method of Feasible Directions

The Method of Feasible Directions differentiates the design space into two distinct regions known as feasible and usable sectors as shown in the schematic in Figure 30. The feasible sector refers to the direction in the design space which will yield a solution that does not violate the imposed constraints. The usable sector refers to the direction in the design space which will yield an improvement in the objective function of the optimizer. The job of the optimizer is to find a search direction S which is both feasible and usable and continue to move along this path to a more optimized solution. Once the search direction S is determined, a scalar step size α^* is found by means of a Polynomial Approximation or Golden Section methods.

The polynomial approximation method can be used when the objective function is unimodal and continuous. It attempts to find the minimum of an approximation polynomial which is fitted to three computed point solutions along the search direction. This minimum point in the polynomial yields the step size α^* where the new optimized solution is

to move. The Golden Section can be applied in cases when the solution is still unimodal but non-continuous. In this method the search direction is discretized into three regions by four different points. Each of these points represent point solutions on the design space which have been evaluated. The algorithm compares the objective functions of each of these points and iteratively eliminates one of the exterior sectors which cannot contain the minimum point. This process of elimination is repeated until some convergence criteria is met and the minimum point is found within some accepted tolerance. The Golden Section method is more robust than Polynomial Approximation but it comes at the expense of higher number of objective function calls which can be computationally expensive in some case.

Once the new step size is found, Equation 49 can be used to update the new improved solution. This process is shown in Figure 31 and these steps are repeated until no feasible or usable sectors are found in which case the optimum solution has been found.

$$\mathbf{X}^{q+1} = \mathbf{X}^q + \alpha^* \mathbf{S}^q \tag{49}$$

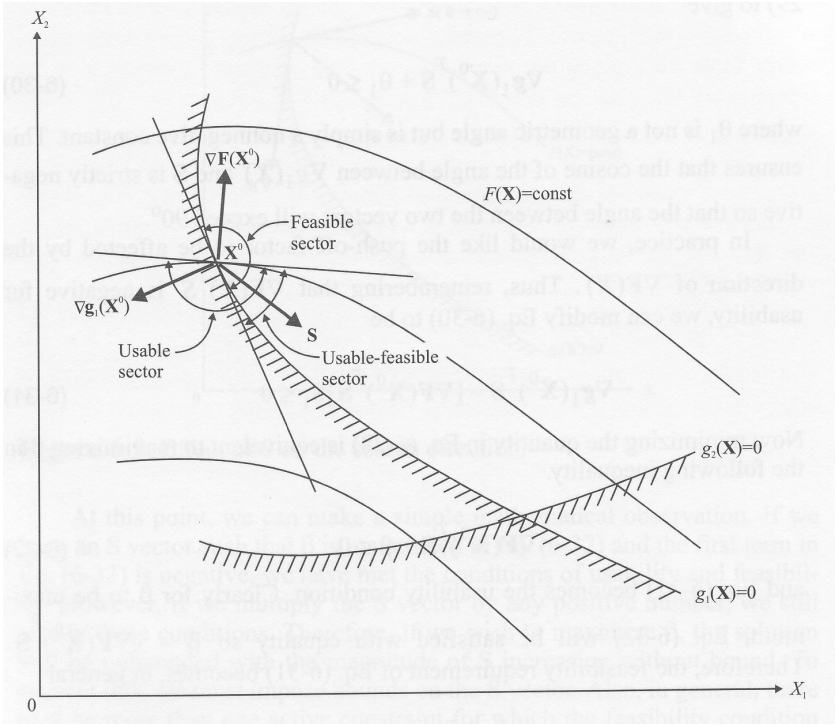

Figure 30: Method of Feasible Directions Sketch [90]

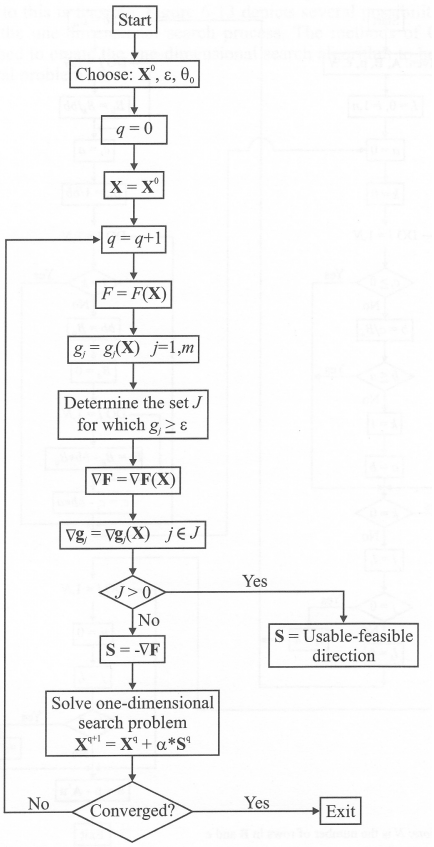

Figure 31: Method of Feasible Directions Algorithm [90]

2.5.3.2 Generalized Reduced Gradient Method

The Generalized Reduced Gradient method is an extension of the Reduced Gradient Method (RG) which now allows the optimization of nonlinear problems including nonequality constraints by the addition of slack variables. A slack variable is required for each nonequality constraint thus the method becomes impractical for problems containing numerous nonequality constraints due to large computational storage requirements. This method however lends itself well to problems containing a small number of nonequality and numerous equality constraints [90].

The method attempts to solve a constrained problem in the form shown in Equation 50. The inequality constraints then need to be converted into equality constraints by adding non-negative slack variables as shown in Equation 51 and the problem definition can now be re-written in the standard form as given in Equation 52. This now makes it possible to

define the basic variables or original variables denoted by subscript b, and non-basic variables which refer to the slack variables denoted by subscript nb.

$$min: \ F(\mathbf{X}) \tag{50}$$

$$s.t. \ g_j(\mathbf{X}) \leq 0, \ j = 1, m$$

$$h_k(\mathbf{X}) = 0, \ k = 1, l$$

$$X_i^l \leq X_i \leq X_i^u, \ i = 1, n$$

$$g_j(\mathbf{X}) + \mathbf{X}_{n+j} = 0, \ j = 1, m \tag{51}$$

$$X_{n+j} \geq 0, \ j = 1, m$$

$$min: \ F(\mathbf{X}) = F(\mathbf{X}_{nb}, \mathbf{X}_b) \tag{52}$$

$$s.t. \ h_j(\mathbf{X}) = 0, \ j = 1, m + l$$

$$X_i^l \leq X_i \leq X_i^u, \ i = 1, n + m$$

The derivation of this Generalized Reduced Gradient method is obtained by acknowledging that both the objective function ($F(\mathbf{X})$) and the equality constraints ($h_j(\mathbf{X})$) are functions of both basic and non-basic variables. One can decompose the problem by performing a partial differentiation of both the objective and constraint equations with respect to the basic and non-basic variables. A more detailed description of all the steps and equations involved in the derivation of the reduced gradient equation is given by Vanderplaats

[90]. The next step is to solve the Generalized Reduced Gradient equation shown in Equation 53 and evaluate it knowing the current point location [90].

The Generalized Reduced Gradient (G_R) computed can be used to determine the search direction $\overline{S}$ in Equation 49 and this provides a relationship for the non-basic variables in terms of a step size (α) as $\mathbf{X}_{nb} = function(\alpha)$. It is now possible to solve the equality constraints (h) for the basic variables ($\mathbf{X}_b$) as functions of the non-basic variables ($\mathbf{X}_{nb}$) by substituting Equation 49 into the set of equations defining the basic variables ($\mathbf{X}_b$). Since the non-basic variables have now been completely replaced, the result is a system of equations for the basic variables ($\mathbf{X}_b$) in terms of only step size (α). These equations for the basic variables can be plugged into the original objective function essentially making it the objective function (F) only a function of step size (α).

$$G_R = \frac{dF}{d\mathbf{X}_{nb}} = \nabla_{nb} F(\mathbf{X})^T - \left[B_b^{-1} B_{nb}\right]^T \nabla_b F(\mathbf{X}) \tag{53}$$

$$B_b = \nabla_b^T h(\mathbf{X})$$

$$B_{nb} = \nabla_{nb}^T h(\mathbf{X})$$

The last step requires the differentiation of the objective function (F) with respect to (α) to find the minimum point and the appropriate step size to move to. This differentiation cannot always be performed analytically and thus the line search problem may require the use of a numerical technique such as the Newton-Raphson method shown in Equation 43-46 or one of the other line search methods described previously. Most of the computational time and effort is typically spent at this step trying to solve the root-solving numerical scheme.

Once the appropriate step size is found one can update the solution to this new point using the equations already obtained for the basic variables in terms of step size. This entire process can be repeated until some predetermined convergence criteria is met, at which time the optimization is stopped. The algorithm for the Generalized Reduced Gradient method is given in Figure 32 [90].

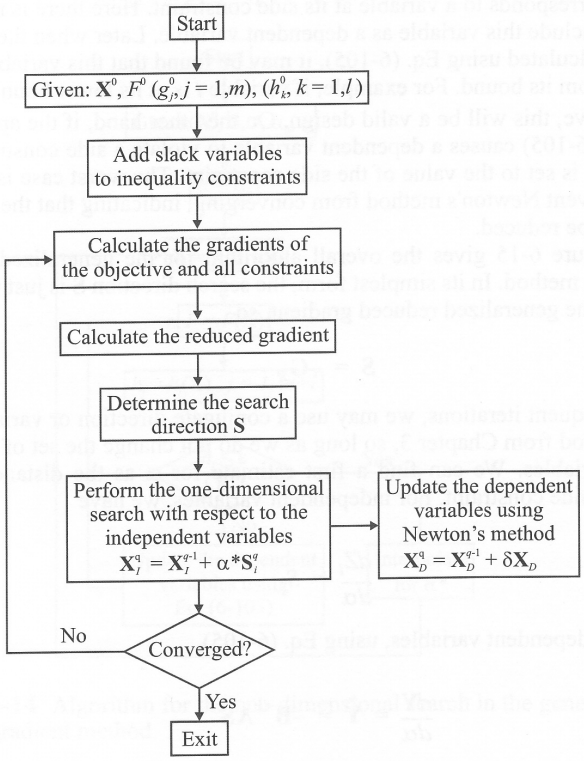

Figure 32: Generalized Reduced Gradient Algorithm [90]

2.5.3.3 Sequential Quadratic Programming

The objective of the optimizer is typically to minimize the thickness of the TPS which translates to a reduction of TPS weight. Generalized Reduced Gradient, one of the most popular optimization methods is a generalization of Newton's method for unconstrained problems [16]. The main optimization problem is shown in Equation 54, where $F(\mathbf{X})$ is the objective function.

$$min: \ F(\mathbf{X}) \tag{54}$$

$$s.t. \ g_i(\mathbf{X}) = 0, \ for \ i \ \epsilon \ E$$

The SQP sub-problem given in Equation 55 is a second order approximation of the Lagrangian given in Equation 56 [36]. This sub-problem is used to approximate the search direction $\mathbf{S}$ which can later be used to solve the main problem. In Equation 57, the objective

function is replaced with an exterior penalty function ϕ which is minimized while varying step size α [90]. The step size is used to update the solution as shown in Equation 58. Once the optimum step size α^* is found, the new values of $\mathbf{X}$ are computed using once again Equation 58. The process is then repeated iteratively as shown in the diagram in Figure 33, where $\mathbf{B} = \nabla^2 L(\mathbf{X}; \lambda)$ [90]. The matrix $\mathbf{B}$ can be difficult to obtain if the evaluation of the objective function is computationally intensive. Time and computational effort can be saved by approximating the matrix $\mathbf{B}$ using the Broydon-Fletcher-Shannon-Goldfarb update formula instead of solving for it at every iteration. The Broydon-Fletcher-Shannon-Goldfarb update formula can be found in Vaanderplaats [90].

$$min: \ \frac{1}{2}\mathbf{S}^T \nabla^2 L(\mathbf{X}; \lambda)\mathbf{S} + \nabla L(\mathbf{X}; \lambda) + L(\mathbf{X}; \lambda) \tag{55}$$

$$s.t. \ \nabla g(\mathbf{X})^T \mathbf{S} + g(\mathbf{X}) = 0$$

$$Where: \ L(\mathbf{X}; \lambda) = F(\mathbf{X}) - \sum_{i \epsilon E} \lambda_i g_i(\mathbf{X}) \tag{56}$$

$$min: \ \phi = F(\mathbf{X}) + \sum_{i \epsilon E} u_i |g_i(\mathbf{X})| \tag{57}$$

Where:

$$u_i = |\lambda_i| \qquad first\ iteration$$
$$u_i = max\left[|\lambda_i|, \tfrac{1}{2}\left(u_i' + |\lambda_i|\right)\right] \qquad subsequent\ iterations$$

$$\mathbf{X}^{q+1} = \mathbf{X}^q + \alpha \mathbf{S} \tag{58}$$

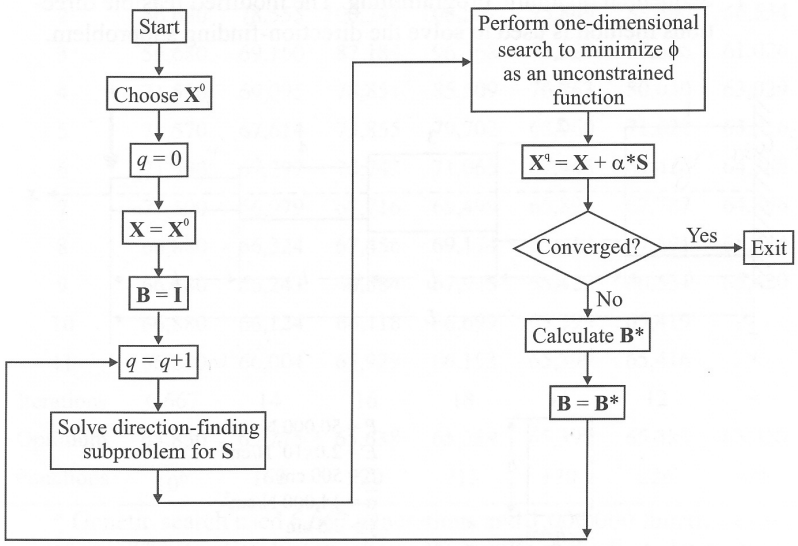

Figure 33: Sequential Quadratic Programming Algorithm [90]

2.6 Economics

The process of aircraft design has undergone a paradigm shift in the last several years. Traditionally aircraft design has been based solely on the optimization of performance attributes such as maximum speed, maximum altitude, and payload capacity. The focus for designers has now been shifted towards the overall effectiveness of a system when it comes to achieving a mission or intended purpose. This requirement demands the inclusion of life cycle cost as another key aspect aside from performance effectiveness [85].

2.6.1 Definition of Life Cycle Cost

Life cycle cost is the cumulative cost of a vehicle from the point of inception until the end of its operational life with disposal. The estimation of life cycle cost in the early phases of conceptual design is important because these early engineering decisions and assumptions account for up to 70%-80% of the total cost of the program [45]. Traditionally engineers have dealt with life cycle cost by relating it directly to various vehicle weights such us takeoff gross weight (TOGW), empty weight, of fuel burned [45]. The assumption that minimization of weight leads to a minimization of life cycle cost is generally valid, but not always true for systems of increasing complexity. In the case of TPS for example, it is possible to have

a material which is lighter but much more costly to produce and maintain than another heavier but cheaper material.

2.6.2 Estimation of Life Cycle Cost

2.6.2.1 Vehicle Cost Model

The life cycle cost of a vehicle is typically estimated through the use of mass estimating relationships. These equations are usually historical-based regressions on past or existing systems, which relate vehicle characteristics such as vehicle geometry, number of engines, maximum velocity, and takeoff gross weight to program costs such as RDTE, acquisition, operational, and disposal costs. An economic cost model for a military vehicle is provided in Appendix B.

2.6.2.2 Thermal Management Systems Cost Model

The life cycle cost of thermal management systems associated with high-speed vehicles contributes greatly to the overall cost of the vehicle. The estimation of life cycle cost for these thermal management systems is highly dependent on the materials and components in use. There is sufficient data found in NASA's TPSx material database in Appendix A to formulate Equations 59-63 which define the life cycle cost model for TMS composed solely on insulating materials (TPS) for a 100 flight life cycle.

$$Total\ Purchase\ Cost = P_{cost} * S_{wet} * \frac{N_{flight}}{Reuse_{flight}} \tag{59}$$

$$Installation\ Cost = (Installation\ time) * Labor * S_{wet} * \frac{N_{flight}}{Reuse_{flight}} \tag{60}$$

$$Inspection/Repair\ Cost = N_{flight} * (Maintenance\ Cost) * Labor * S_{wet} \tag{61}$$

$$Replacement\ Cost = \left(S_{wet} * \frac{N_{flight}}{Reuse_{flight}} * \left(\begin{array}{c} Replace \\ fraction \end{array} \right) \right) * ...$$

$$\left[P_{cost} + \left(\begin{array}{c} Installation \\ time \end{array} \right) * Labor \right] \tag{62}$$

$$LCC = Purchase + Installation + (Inspection/Repair) + Replacement \tag{63}$$

Where:

P_{cost} - initial purchase cost of the material

S_{wet} - wetted area of the vehicle

N_{flight} - number of flights (100) in the life cycle

$Reuse_{flight}$ - number of flight the TPS material can be reused

$Labor$ - labor wage

$Replace\ fraction$ - percent of area that needs to be replaced after each flight

2.7 Surrogate Models

Surrogate models are a way of representing a complex analysis model using a single or a set of simplified equations that can be evaluated quickly and without the need for high computational requirements. This is a very useful concept in conceptual design where focus is placed on rapid evaluation and computations. In addition, surrogate models allow for the infusion of physics-based analysis models into the conceptual phase of design which eliminates erroneous assumptions that can be costly as the program develops. A surrogate model can also be used to share information regarding the behavior of a model without actually having to give away the analysis tool used to create the model. The general process by which surrogate models are typically created is very similar to response surface methodology as shown in Figure 34 but the specific methods used in each of the steps can vary as will be shown in the next sections.

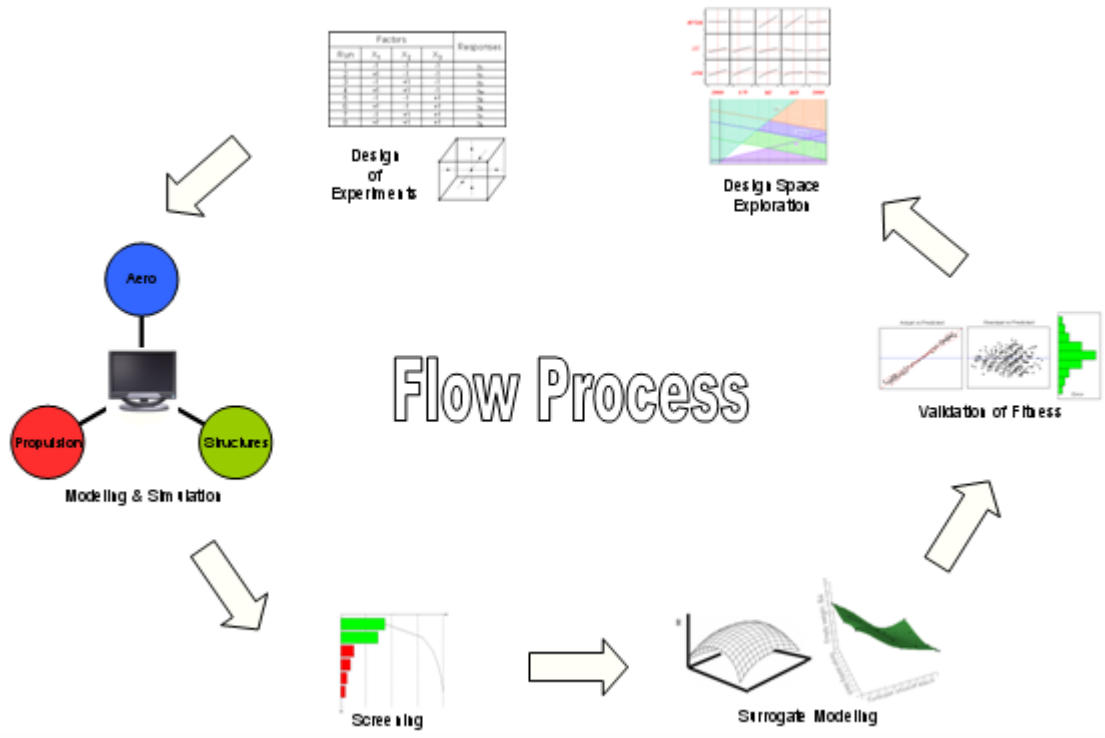

Figure 34: Response Surface Methodology

2.7.1 Design of Experiments

A design of experiment is an intelligent way to select the appropriate experimental settings in order to obtain the most knowledge about a system with the least amount of effort. It can be applied to the problem areas including comparative, screening, modulation, and optimization. In the case of computer modeling and simulation this corresponds to a lower number of runs, lower computational time and effort. The concept is conducive to investigate the relations between the design variables and response metrics in conceptual design.

Design of experiments have been classified into classical and modern design by Giunta et al [34]. Classical DoE design are those experiments designed for laboratory and field experiments which incorporate random error sources by placing sample points at the corners of the design space. Classical design of experiments include the Full Factorial, Fractional Factorial, Box-Behnken, and Central Composite. Modern design of experiments are aimed towards deterministic computer simulations. These modern designs tend to place sample points in the interior of the design space in an effort to minimize bias error. Bias error

is the difference between the functional form of the true trend and the functional form of the estimated trend. Examples of these modern "space-filling" designs include quasi-Monte Carlo, Latin hyper cube, orthogonal arrays, and Hammersley sequence.

Once the different designs are categorized they can be dissected in more detailed as given below. Figure 35 provides a better visual aid for the design space to each of these types of design of experiments [65].

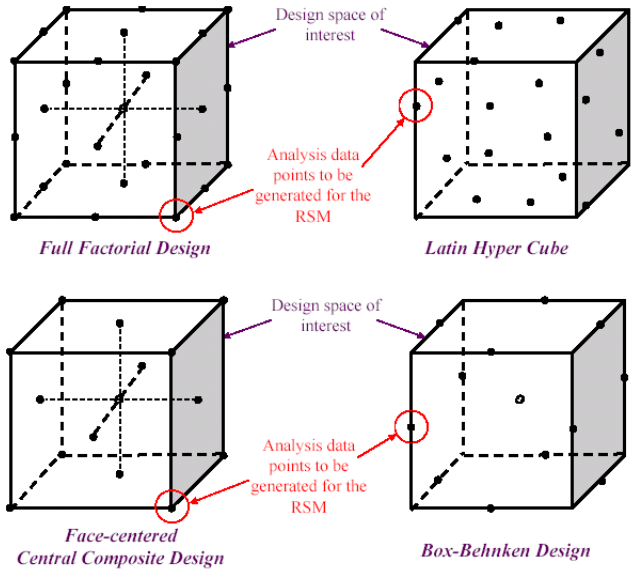

Figure 35: Design Space for Various Experiment Designs [65]

Full Factorial: In this experiment, responses are measured at all combinations of the experimental factor levels. The placement of design point at the corner of the design space reduces bias error. This design's high level of fidelity however carries the penalty of an excessive number of cases to run. This can make it impractical for implementation with experiments or simulations which are time consuming and computationally demanding. The full factorial design is also known as a 3-level design because each variable has three different levels or settings. This makes it possible to model responses with quadratic behaviors. The factorial design is capable of handling discrete variables and is the basis for various other types of design of experiments [65, 67].

Fractional Factorial: A simplified form of the full factorial design with the main

difference being that it does not include the mid-points of the design space. This makes it a 2-level factorial design and is typically used in the screening process of the main effects and their interactions. The 2-level design helps reduce the number of runs required to sample the design space at the expense of fidelity.

Central Composite: This design is based on a resolution IV fractional factorial which captures all main effects and the second order interactions without confounding. The fractional factorial is then merged with a center point in the hyper-cube and a set of face-centered axial points to create the final design shown in the figure above. The central composite design has an important advantage in that it includes the extreme points (corners) of the design space. This means that extrapolation outside of the design space is minimized. A problem that rises when evaluating points at the extremes of the design space boundary is that an analysis code may fail to converge because it may be going beyond the limits it was designed for. This in turn can mean a large number of unconverged solutions in larger design spaces [65, 67].

Box-Behnken: This design places the points at the center of each of the edges or design space boundaries, and one point at the center. This forms in essence a spherical design which requires fewer executions and offers better convergence by the analysis model. The improved convergence is a direct result of the design points not being placed at the extremes of the boundaries where some analysis codes may fail. The biggest disadvantage of the spherical design is that extrapolation to the extremes introduces errors to more nonlinear design spaces [65, 67].

Random Sampling: The simplest of the experimental designs, it is as the name suggests simply a random generation of points within the design space. This type of design makes a compromise between the number of experimental runs required and the correlation of effect estimates. In order to decrease the correlation between the terms one must increase the number of runs. This makes it easy to implement but highly impractical when computing the large number of cases required to obtain any meaningful results [67].

Space Filling: This type of design attempts to distribute equally spaced design points all throughout the design space. The optimization of the distances between points requires

a degree of computational time and effort [67].

Latin Hyper Cube: This design features a combination of traits from random sampling and space filling designs. Latin hypercube fills the design space with a set of random design points and matches the number of points scattered in a dimension with the number of settings for each dimension. This rich sampling of the interior points yields a highly accurate interior but at the same time may introduce a high level of correlation in nonlinear design spaces as is the case in random sampling [65, 67].

2.7.2 Data Fitting

The surrogate model or data fitting step in RSM can be substituted with various techniques depending on the complexity of the model and the nature of the design space. Some of these techniques include response surface equations, neural networks, and Gaussian process, all of which will be explained next.

2.7.2.1 Response Surface Equation

Response surface methodology is a multivariate regression technique which can be used to model the behavior of a complex system using simplified equations known as response surface equations. RSE utilizes a set of data obtained after computing cases from a predefined DoE and can produce a quadratic equation under the assumption that the higher order terms can be ignored. The generalized equation for a 2nd order response equation is shown in Equation 64.

$$R = b_o + \sum_{i=1}^{k} b_{ii} x_i + \sum_{i=1}^{k} b_{ii} x_i^2 + \sum_{i=1}^{k-1} \sum_{j+1}^{k} b_{ij} x_i x_j + \varepsilon \tag{64}$$

Where:

R - response of interest

b_o - intercept term

b_i - regressed coefficient for 1st order terms

b_{ii} - regressed coefficient for 2nd order terms

b_{ij} - regressed coefficient for cross-product terms

x_i - main effect of independent design variables

x_i^2 - quadratic effect of independent design variables

ε - error associated with 2nd order approximation

Response surface equations are easy to understand and simple to use but they are not able to handle large nonlinear design spaces well. A way to get around this limitation is to reduce the size of the variable ranges and effectively linearize the problem to more closely match the form of the response surface equation. The process of systematically reducing the design space is known as adaptive response surface methodology (ARSM) and it can be cumbersome and impractical for certain problems.

2.7.2.2 Neural Networks

Neural networks are an alternative to RSE when the design space is highly nonlinear and polynomial fitting just does not perform well. They are also ideal when fitting responses which display erratic type behaviors. The idea of neural nets evolved from attempts to create a model of the human brain but it has since evolved into the statistical field. Neural nets work by mapping a set of input variables to a set of responses through a set of filters, called the hidden layer. The hidden layer consists of hidden nodes, analogous to neurons in the biological model. The data being regressed is called the training set for a neural network. The training algorithm is the optimization method used to determine the coefficients for the network that minimize the training error [44]. The accuracy of the regression can be improved by increasing the number of "neurons" at the cost of computational time and effort. A diagram of the concept behind neural networks is giving in Figure 36 [44].

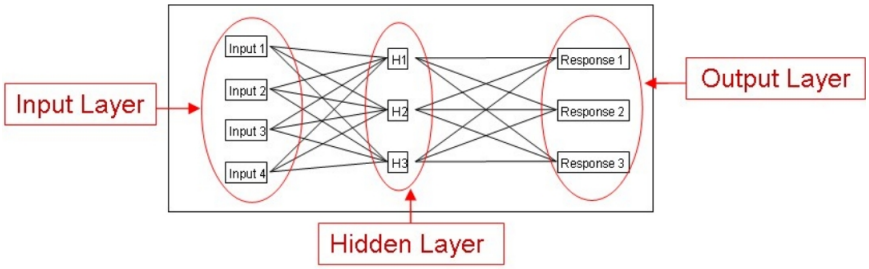

Figure 36: Neural Network Conceptual Diagram [44]

Two major disadvantages of this technique is the lack of a well-defined methodology for neural network regression and the selection of the number of hidden nodes [44]. The proper number of hidden nodes needs to be found experimentally through trial and error. Fortunately, this process has been automated by Johnson with a tool called BRAINN [44].

2.7.2.3 Gaussian Process

Gaussian processes are based on nonlinear, Bayesian theory and work under similar idea of data training. In a Bayesian regression, there is no longer an explicit model to be fitted to an available set of data points. The information contained in the data set is used to create a prediction through training, and therefore the prediction is in essence a statistical estimate [23]. Training in a Gaussian process involves maximizing the logarithmic likelihood that the predicted process matches the training data [39].

2.8 Surrogate Model Validation

Surrogate models need to be validated in order to assure they properly represent the behavior predicted by the modeling and simulation analysis tools. There are five key aspect to the surrogate model validation process which are listed below.

- Coefficient of Determination (R^2)
- Actual versus Predicted
- Residual versus Predicted
- Model Fit Error (MFE)
- Model Representation Error (MRE)

The coefficient of determination (R^2) values for all responses should show greater than 95% agreement to the original data. Actual versus predicted plots should show most points well clumped along a tight confidence interval denoting a good fit. Residual versus predicted plots should demonstrate random scatter patterns, which shows there are no higher order (nonlinear) effects. It is in some cases allowable to have nonlinear effects as long as the residual is acceptably small.

The response error distributions based on the DoE data can then be plotted for each response to analyze the model fit error. The model fit error is expected to ideally show normal error distributions with means that are close to zero and standard deviations that are less or equal to 1%. The last validation step is the model representation error which requires an additional set of random cases to be run through the modeling and simulation. Now the RSEs can be used to predict the responses for these new random cases and the new error distribution can be plotted. This error is ideally expected to be once again normally distributed with means near zero, and standard deviations of 1% or less.

The fitness values provided in this section are ideal scenarios for what a good fitness response should look like. The designer must be able to decide what he/she considers to be an acceptable fit.

2.9 Probabilistic Analysis

In order to transition from a design for performance to a design for overall system effectiveness, one needs to introduce the economics aspects into the analysis. The inclusion of cost brings in additional uncertainty which needs to be assessed using probabilistic techniques. Most probabilistic methodologies treat the cost parameters as random variables with assigned probability distributions [4]. In cases where the shape of the probability distribution is unknown then one needs to look at stochastic approaches based on Fuzzy Logic [4].

There are three main approaches to probabilistic analysis as shown in the diagram in Figure 37 [59, 4]. The first approach involves the integration of sophisticated analysis codes with a Monte Carlo simulation (MCS). This approach is the most accurate of the three but is at the same time very time consuming and computationally intense because each probabilistic case needs to be run through the sophisticated analysis code. The second approach involves the use of surrogate models which replace the sophisticated analysis code along with a Monte Carlo simulation. This method typically provides a good balance between computational speed and accuracy. The last approach requires the use of sophisticated analysis codes along with Fast Probability Integration (FPI), a computer method developed by researchers at Southwest Research Institute [96]. Fast Probability Integration is based

on the determination of the most probable point (MPP). The concept of the most probable point has its roots in structural reliability analysis [96]. A more detail look of Monte Carlo analysis and Fast Probability Integration is presented in the following two sections.

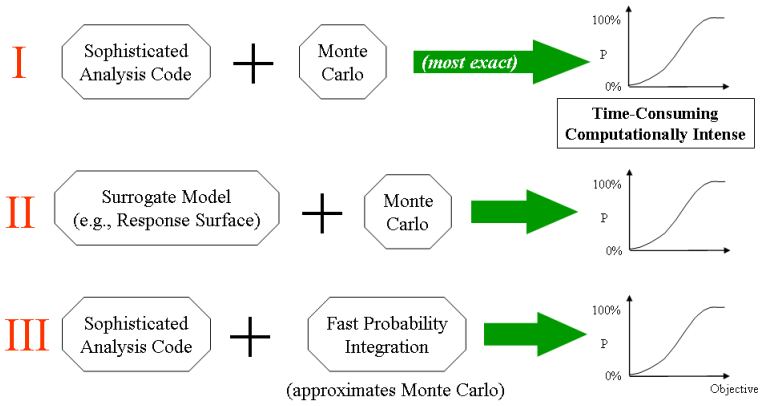

Figure 37: Approaches to Probabilistic Analysis [59]

2.9.1 Monte Carlo Simulation

A Monte Carlo simulation is a technique that can be utilized to simulate a random process by assigning probability functions to the random variables [74, 4]. This technique helps analyze how perturbations or variations from the mean values of the design variables affect the overall process. These perturbations can arise from the manufacturing process or from other elements that the designer has no control over. Once probability functions have been assigned to the random variables each case can be run through the simulation to obtain the random process. Some of the probability distributions that can be employed on the random variables are show in Figure 38.

The process by which a Monte Carlo sampling takes place is shown in Figure 39 for a uniform probability distribution. The random number (rand1) is found using the computer's uniform random number generator which produces a random number between 0 and 1. The relationship between a probability density function (PDF) and cumulative distribution function (CDF) is shown in Equation 65 [42]. It is possible to see that the cumulative distribution function is the integral of the probability density function. Using these relationships and assuming a uniform probability density function for the random variable one

can derive the equation for the value (x1) of the random sample for a given random number generated by the computer (Equation 66).

A set of random samples (x) is run through the sophisticated analysis code or surrogate models depending on the probabilistic process being used and the corresponding responses are obtained in the form of probability density functions. These probability density functions can then be integrated using Equation 65 to obtain the cumulative distribution functions (CDF) for each response. The cumulative distribution function defines the probability of hitting a certain target for an objective. This concept of CDF is illustrated in Figure 40 for lower is better and higher is better objectives.

$$F(rand1) = \int_{0}^{rand1} p(rand)d(rand) = F(x1) = \int_{a}^{x1} p(x)dx = rand1 \tag{65}$$

$$x1 = \left[rand1 + \left(\frac{a}{b-a}\right)\right](b-a) \tag{66}$$

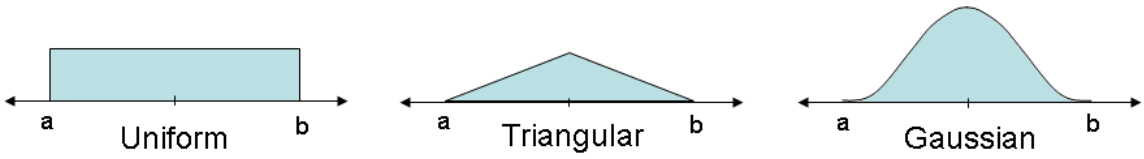

Figure 38: Probability Distribution for Random Variables

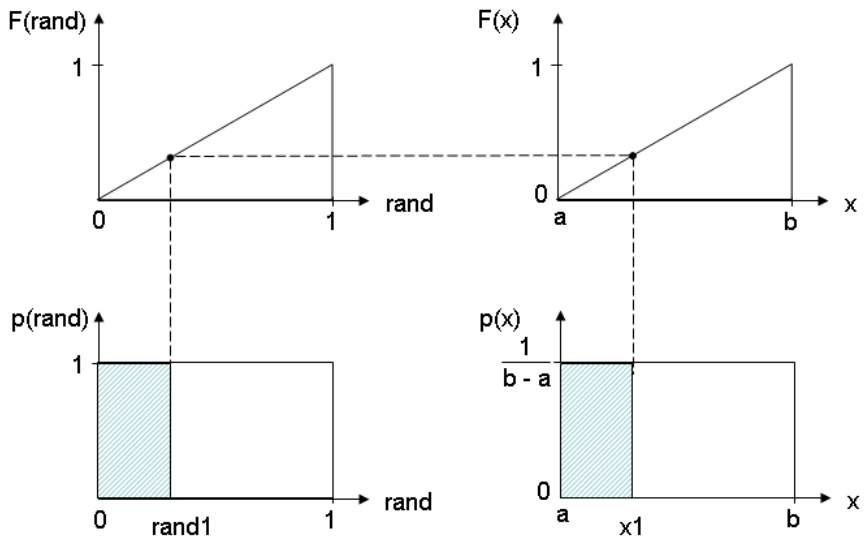

Figure 39: Monte Carlo Random Sampling Process

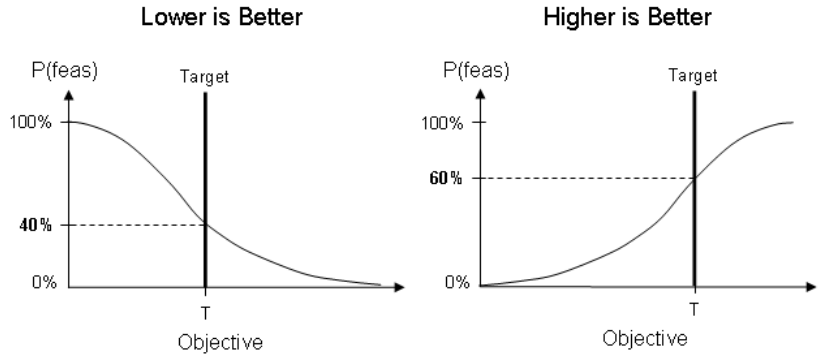

Figure 40: Cumulative Distribution Functions

2.9.2 Fast Probability Integration

As stated earlier, Fast Probability Integration is an approach developed at the Southwest Research Institute which works based on the estimation of the most probable point. In essence FPI attempts to approximate the cumulative function distribution (CDF) generated by Monte Carlo simulations. It should be able to approximate the CDF of the objectives while reducing the computational time and effort.

The process of estimating the value of the most probable point is detailed by Du [25, 4]. Figure 41 shows a sample x-space and the limit-state which defines the safe and unsafe

regions. Safe and unsafe is used to denote feasible and non-feasible because as one may recall this type of analysis has its roots in reliability analysis. The x-space needs to be normalized into the u-space as shown in Figure 42. This is typically performed using Equation 67 which is the inverse of the normal distribution function.

$$u_i = \Phi^{-1}\left[F_i\left(x_i\right)\right] \tag{67}$$

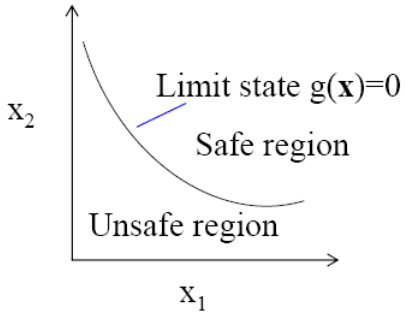

Figure 41: Fast Probability Integration x-Space [25]

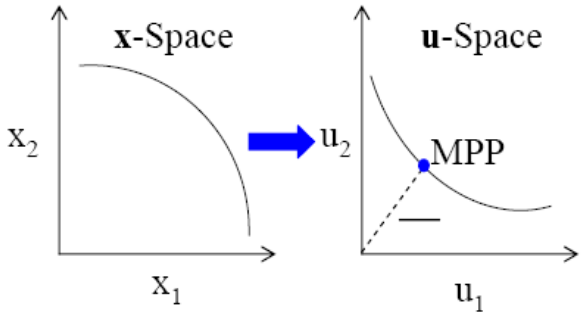

Figure 42: Fast Probability Integration Space Normalization [25]

The optimization algorithm shown in Equation 68 is used to compute the parameter β which is the distance from the origin to a point on the limit-space in the u-space with greatest probability density function. This point is the most probable point as depicted in the plot on the right of Figure 42 [25]. It is also important to note that the parameter c denotes a constant. This critical value c is discretized and the corresponding values of β are computed. The algorithm is essentially searching the design space contour with constant

critical value c for the point with greatest probability density function. The cumulative distribution function can then be put together knowing the constant values of c and the safety index β as seen in Figure 43 [25].

$$\beta = \min_{u} \|\mathbf{u}\| \tag{68}$$

$$s.t.\ g(\mathbf{u}) - c = 0$$

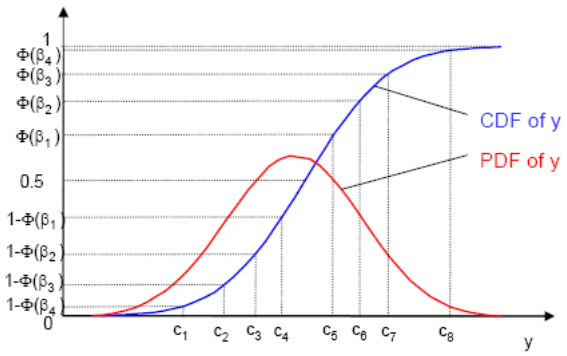

Figure 43: Fast Probability Integration Approximation of CDF [25]

The probability approximation of $f(\mathbf{u})$ can be obtained using the first order approximation by Taylor series expansion as given in Equation 69 where n is the total number of dimensions, and ε is a truncation error of higher order terms. This approximation is only accurate if the curvature of the limit-state function is not too large. In the case of high curvature design spaces a more accurate second-order approximation is required. In more extreme cases with highly nonlinear design spaces, a nonlinear constraint optimizer needs to be employed. However, this more sophisticated optimizer can be computationally and time intensive when coupled with more complex and sophisticated analysis tools.

$$f(\mathbf{u}) = f(\bar{\mathbf{u}}) + \sum_{i=1}^{n} \frac{\partial f}{\partial u_i} \triangle u_i + \varepsilon \tag{69}$$

2.10 Multi-Objective Decision Making and Design Space Exploration

The concept of Multi-Objective Decision Making (MODM) has been defined in Section 2.2.3 and various qualitative techniques have been provided. These MODM qualitative techniques are useful for early concept down-selection. This section will be used to describe several MODM techniques which can be used in the later part of the conceptual phase once numerical results have been obtained.

Design space exploration is a general term for techniques which allow an engineer to better visualize and analyze the relations and trends of resulting data. The design space exploration environment should provide a better understanding of the trade offs that are taking place between the different design metrics.

2.10.1 Goal Programming

Goal Programming (GP) is a generalization of Linear Programming (LP) capable of handling multiple conflicting objectives. The technique is non-probabilistic, therefore, optimization is carried out to obtain a single point solution with no uncertainty information. Global Programming requires knowledge of a desired goal or target value. The LP algorithm attempts to minimize the detrimental deviations from the desired goal constraints while satisfying other functional constraints (ie. design space variable limits).

There are two major categories of the GP problem including preemptive and non-preemptive problems. Preemptive problems are those where there are a series of goals that need to be achieved in a specific order to succeed. Non-preemptive problems do not consist of goals that need to be achieved in a specific order but instead have relative importance weighting factors for the different goals. The objective function in both of these cases still aims to minimize the detrimental deviation from the desired goal or target value [20, 54, 87].

Goal Programming has several disadvantages that appear as a result of the LP implementation. Linear Programming cannot account for of risk, can produce fractional solutions that often have no meaning, and reducing a problem to a set of linear equations can often be a very difficult task. In addition, it is restricted to problems with linear objective functions

with no correlation among variables, and no positive or negative synergies [78]. The GP requirement of predetermined goals and relative importance of competing objectives can also become a problem when the customer is unsure what the most capable solution really means.

2.10.2 Joint Probability Decision Making

Joint Probability Decision Making is a very simple MODM making technique which as the name implies makes use of a joint probability distribution function based on multiple attributes of interest.

The joint probability mass function ($f(x_1, x_2, ..., x_n) = P(X_1 = x_1, X_2 = x_2, ..., X_n = x_n)$) describes the probability that events $X_1 = x_1$, $X_2 = x_2$, ... , $X_n = x_n$ occur concurrently, where X_1, X_2, ..., X_n is a set of *discrete* random variables. The joint probability mass function has the following properties [5]:

$$0 \leq f(x_1, x_2, ..., x_n) \leq 1$$

$$\int_{\Omega} .. \int f(x_1, x_2, ..., x_n) dx_1 dx_2 ... dx_n = 1$$

$$P\left[(X_1, X_2, ..., X_n) \epsilon A\right] = \int_{A} .. \int f(x_1, x_2, ..., x_n) dx_1 dx_2 ... dx_n, \; A \subseteq \Omega$$

Where: Ω is a discrete probability space

Similarly, the joint probability density function ($f(x_1, x_2, ..., x_n) = P(X_1 = x_1, X_2 = x_2, ..., X_n = x_n)$) describes the probability that events $X_1 = x_1$, $X_2 = x_2$, ... , $X_n = x_n$ occur concurrently, where X_1, X_2, ..., X_n is a set of *continuous* random variables. The joint probability density function has the following properties [5]:

$$0 \leq f(x_1, x_2, ..., x_n)$$

$$\sum_{(x1, x2, ..., xn) \epsilon \Omega} \sum f(x_1, x_2, ..., x_n) = 1$$

$$P\left[(X_1, X_2, ..., X_n)\epsilon A\right] = \sum_{(x1,x2,...,xn)\epsilon A}\sum f(x_1, x_2, ..., x_n),\ A \subseteq \Omega$$

Where: Ω is a continuous probability space

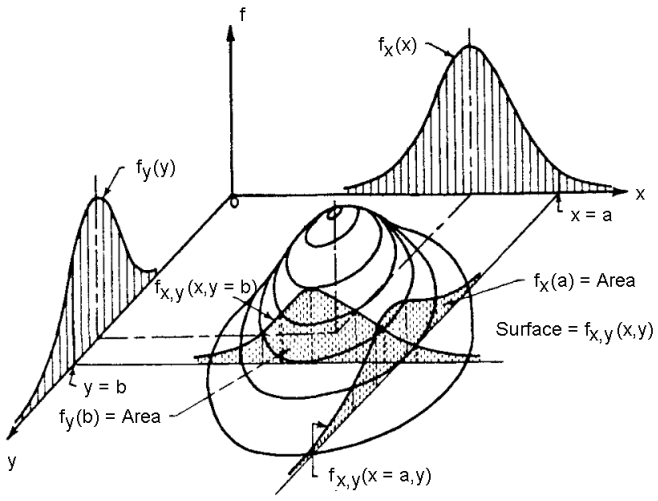

Figure 44: Joint Probability Distribution [5]

The generation of univariate and joint probability distributions can be achieved by using the Empirical Distribution Function (EDF), which relies on the collection of empirical data samples. The univariate probability mass function for a random variable X can be defined for n samples as shown in Equation 70 [5].

$$f_x(x) = \frac{1}{n}\sum_{i=1}^{n} I(a_i = x) \tag{70}$$

$$I(a_i = x) = \begin{cases} 1\ for\ a_i = x \\ 0\ otherwise \end{cases}$$

Here a_i are criterion sample values obtained through a probabilistic method such as Monte Carlo simulation, and x is the criterion of interest. Knowing this the cumulative probability function can be defined as given in Equation 71 [5]. This formulation can be extended to derive the joint probability mass function given by Equation 72 [5]. Similarly the joint cumulative probability distribution function is given by Equation 73 [5].

$$F_x(x) = \frac{1}{n}\sum_{i=1}^{n} I(a_i \leq x) \tag{71}$$

$$I(a_i = x) = \begin{cases} 1\ for\ a_i \leq x \\ \\ 0\ otherwise \end{cases}$$

$$f(x_1, x_2, ..., x_n) = \frac{1}{n}\sum_{i=1}^{n} I\left((a_{i1}, a_{i2}, ..., a_{in}) = (x_1, x_2, ..., x_n)\right) \tag{72}$$

$$I\left((a_{i1}, a_{i2}, ..., a_{in}) = (x_1, x_2, ..., x_n)\right) = \begin{cases} 1\ for\ \ (a_{i1}, a_{i2}, ..., a_{in}) = (x_1, x_2, ..., x_n) \\ \\ 0\ otherwise \end{cases}$$

$$F(x_1, x_2, ..., x_n) = \frac{1}{n}\sum_{i=1}^{n} I\left(a_{i1} \leq x_1, a_{i2} \leq x_2, ..., a_{in} \leq x_n\right) \tag{73}$$

$$I\left(a_{i1} \leq x_1, a_{i2} \leq x_2, ..., a_{in} \leq x_n\right) = \begin{cases} 1\ for\ \ (a_{i1} \leq x_1, a_{i2} \leq x_2, ..., a_{in} \leq x_n) \\ \\ 0\ otherwise \end{cases}$$

In more complex systems with a high number of attributes, the problem can be simplified by combining attributes of interest under a weighted overall evaluation criterion (OEC). The use of an OEC however introduces two major problems *i*) a lot of information is lost by convoluting all the attributes together, and *ii*) the selection of weighting factors plays a major role in the process and is up to the personal choice of the designer. An alternative to the use of OEC is the implementation of a probability of success (POS). The POS refers to the probability that a chosen design will meet various criteria and is defined in Equation 74. This criteria is specified as limits for each attribute which defines an "area" of interest within the design space. In Equation 74 [5], M is the total number of samples, and z_{jmin} and z_{jmax} are the minimum and maximum limits of the attributes interest.

$$POS = \frac{1}{M}\sum_{j=1}^{n} I\left(z_{jmin} \leq z_j \leq z_{jmax}\right) \tag{74}$$

It is important to note that JPDM itself does not provide an optimized design point. In order to obtain an improved design point solution an optimizer needs to be wrapped around the JPDM formulation. The optimizer in this case attempts to maximize an OEC, or a POS based on an attribute "area" of interest by manipulating the design variables and accounting for uncertainty from the random variables. An example of such optimization is shown in Figure [5].

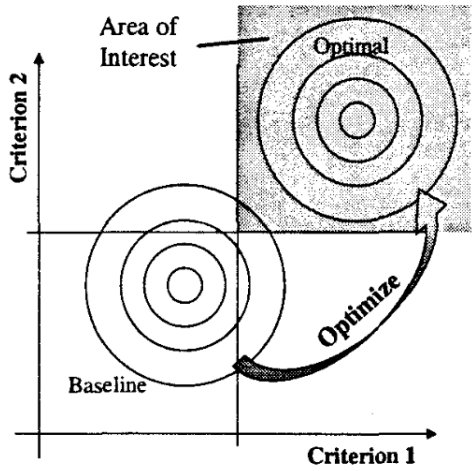

Figure 45: JPDM Optimization [5]

2.10.3 Pareto Frontiers

A Pareto frontier is an attractive approach for performing multi-objective decision making by selecting only solutions which are Pareto optimal [12]. A notional Pareto frontier for "lower is better" is shown in Figure 46. Pareto optimal solutions or non-dominated solutions are those points which cannot be improved in one attribute without degrading another. The locus of these Pareto optimal solutions make up what is known as the Pareto frontier depicted by a red line in Figure 46. The positive ideal solution is a theoretical best solution which does not compromise in any of the decision making attributes. Points located on the Pareto frontier have the smallest Euclidean distance to the positive ideal solution. It is also important to note the difference between the true Pareto frontier and a weak Pareto frontier depicted in Figure 46 by a green line. The weak Pareto frontier contains points which are simply located at the edge of the solution cloud in the design space. These weak

Pareto solutions identify the best solutions out of the cloud of existing alternatives but are not necessarily true Pareto optimal solutions. Special numerical techniques have been developed to properly compute the true Pareto frontier of a design space.

There is a plethora of MODM algorithms which attempt to define the Pareto frontier. A comprehensive survey of various MODM techniques has been compiled by Ehrgott et al [26]. These algorithms usually fall among the two major categories of prediction and identification. It is important to differentiate between these two distinct approaches. Pareto frontier prediction techniques attempt to compute the location of the actual Pareto frontier (red curve) through some form of optimization algorithm. There is also the case of Pareto frontier identification where an algorithm will attempt to identify the discrete solution points on the vehicle which define the weak Pareto frontier (green curve).

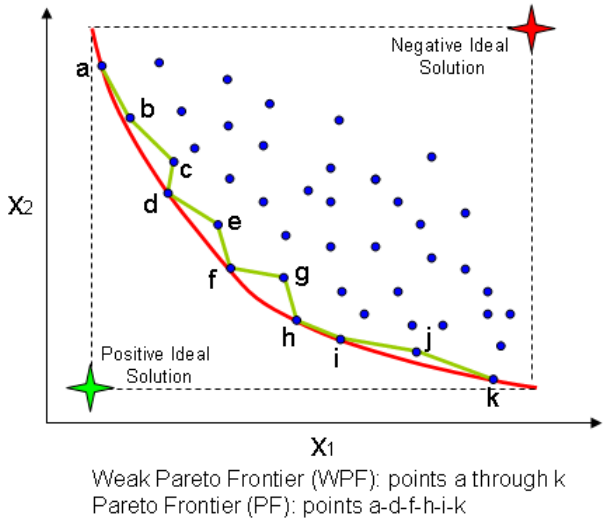

Figure 46: Sample Pareto Frontier

2.10.4 Pareto Frontier Prediction

The approximation of the Pareto frontier is the first and fundamental problem in multiple criteria optimization (MCO) [55]. In this section several methods capable of Pareto frontier prediction will be reviewed. Recall that Pareto prediction refers to the estimation of the actual Pareto points denoted as the red curve in Figure 46.

2.10.4.1 Weighted Sum

The Weighted Sum (WS) method is one the most fundamental and well known approaches for Pareto frontier prediction. The technique employs an optimizer to minimize or maximize a single objective function. As the name implies, this objective function is a weighted sum of all the multiple-objectives within the problem. The formulation for WS is shown in Equation 75, where $\mathbf{x}$ is the design variable vector, $\mathbf{p}$ is a fixed parameter vector, $\mathbf{g}$ and $\mathbf{h}$ are the inequality and equality constrains, respectively; and $x_{i,min}$, $x_{i,max}$ are the lower and upper bounds of the i*th* design variable, respectively [46]. As one can expect, for problems with two or more objectives there are many non-unique design variable sets which can yield the same weighted sum. The Pareto points computed with this method are highly depended on the selection of weighting factors for the competing objectives.

$$min: \ \mathbf{J}(\mathbf{x},\mathbf{p}) = [J_1, J_2, ..., J_m]^T \tag{75}$$

$$\mathbf{g}(\mathbf{x},\mathbf{p}) \leq 0$$

$$\mathbf{h}(\mathbf{x},\mathbf{p}) = 0$$

$$x_{i,min} \leq x_i \leq x_{i,max} \ \ (i = 1, ..., n)$$

2.10.4.2 Epsilon-Constraint

Epsilon-Constraint is another well known Pareto prediction method. The method works by optimizing only one objective function while the remaining objective functions become constraints [49]. The objective constraints are systematically varied and the respective value for the single objective is determined with the numerical optimizer. The formulation for this optimization algorithm is shown in Equation 76 [49], where $f : X \rightarrow \mathbb{R}^m$ and $\Phi : \mathbb{R}^m \rightarrow \mathbb{R}$, or reports that the feasible region is empty and no Pareto point exists. The Epsilon-Constraint method requires a total of k^{m-1} calls to the numerical optimizer, where k is the total number

of Pareto points desired on the Pareto front and assuming that all optimizations k find their way to the feasible region.

$$max: \ \Phi\left(\mathbf{f}\left(\mathbf{x}\right)\right) \equiv \Phi\left(f_1(x), ..., f_m(x)\right) \tag{76}$$

$$s.t. \ f_i(x) > \epsilon_i \ \ \forall \in \{1, ..., m\}$$

$$x \in X$$

2.10.4.3 Normal Boundary Intersection

Das and Dennis [92] have examined the drawbacks of using weighted sums to approximate Pareto frontiers. They have shown that the use of evenly distributed weights leads to non-evenly distributed points on the actual Pareto frontier. This can be a problem if the analysis fails to produce enough accuracy in certain places of the Pareto front. These issues were later addressed by Das and Dennis through the implementation of the Normal Boundary Intersection (NBI) technique which parameterizes the frontier and results in evenly distributed points.

The process through which NBI works is demonstrated by the diagram shown in Figure 47 [86, 37]. The formulation for the NBI algorithm is found in Gupta and the steps are given below [86, 37]:

1. Determine individual minima (f^*)
2. Define convex hull of individual minima ($\mathcal{H}$)
3. Define the normal vectors to the convex hull
4. Solve the NBI optimization problem

The first step involves the computation of individual minima in each of the competing objectives or dimensions. This will guarantee that no search is initiated in a region where no feasible points can be found or that the search is always conducted in the direction where

a Pareto frontier exists [86]. This is performed by an optimization routine on one objective at a time as given by the formulation in Equation 77, where $\mathbf{p}$ is vector of parameter values that define the objectives $f = f(\mathbf{p})$ [86]. The optimization finds a total of n sets of $\mathbf{p}$ vectors that minimize each individual objective, where n is the total number of objectives. These $\mathbf{p}$ vectors can be used to solve for the points f^{*a} and f^{*b} in Figure 47 [86].

$$\mathbf{p}^{*i} = \underset{\mathbf{p}}{argmin}\ f_i(\mathbf{p}) \tag{77}$$

$$s.t.\ \mathbf{c}(\mathbf{p}) \geq 0$$

The individual minima need to be normalized using Equation 78 [86]. Since this formulation is for a minimization the upper boundary is not as important and the individual maxima are approximated using Equation 79, which simply takes the maximum of the individual minima found earlier [86]. These normalized individual minima will form the edge points of the convex hull ($\mathcal{H}$) with dimensionality $n-1$ as shown in Figure 47 [86]. Thus, the convex hull is a line connecting the two individual minima if the design space is 2-D or a plane if the design space is 3-D. The main idea is that the Pareto frontier will lie somewhere underneath this convex hull.

$$\hat{f}_i = \frac{f_i - f_{i,min}}{f_{i,\widetilde{max}} - f_{i,min}},\ \ i \in \{1,2,3,...,n\} \tag{78}$$

$$f_{i,\widetilde{max}} = max\left(f_i^{*1}, f_i^{*2}, ..., f_i^{*n}\right),\ \ i \in \{1,2,3,...,n\} \tag{79}$$

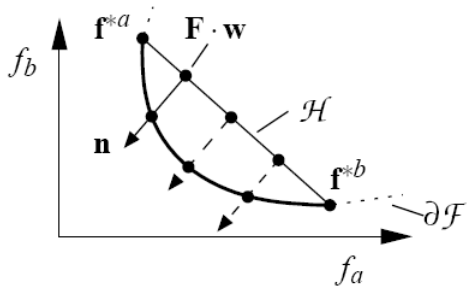

Figure 47: Normal Boundary Intersection Process [86]

The second step describes how a set of points are distributed on the convex hull $\mathcal{H}$ using Equation 80, where $\mathbf{F}$ is given by Equation 81, and $\mathbf{w}$ is given by Equations 82-83. In the case of two objectives, then the total number of points on the convex hull defines the total number of points on the Pareto front. This is no longer true for cases with higher dimensions; the total number of sample points on a 3-D Pareto frontier is given by Equation 84, where k is the number of points along the edge of the convex hull $\mathcal{H}$. According to this equation, NBI is more efficient than Epsilon-Constraint for 3-D design spaces because it searches in the direction where the Pareto point is always expected to be located. In 3-D design spaces, it is possible for the Epsilon-Constraint to call on the optimizer to search in a direction where a Pareto point does not exist.

$$\mathcal{H} = \mathbf{F} \cdot \mathbf{w} \tag{80}$$

$$\mathbf{F} = \left[\hat{\mathbf{f}}^{*1}, \hat{\mathbf{f}}^{*2}, ..., \hat{\mathbf{f}}^{*n} \right] \tag{81}$$

$$\mathbf{w} = [w_1, w_2, ..., w_n]^T \tag{82}$$

$$w_i \geq 0, \ \sum_{i=1}^{n} w_i = 1, \ \ i \, \epsilon \, \{1, 2, ..., n\} \tag{83}$$

$$NumberOfSamples = \frac{k\,(k+1)}{2} \tag{84}$$

The third step involves the definition of a vector $\mathbf{n}$ normal to the convex hull. A line search in the direction normal to the convex hull will yield through an optimization routine the solution which lies on the Pareto frontier. The use of a normal vector to the convex hull yields equally distributed point solutions on the Pareto frontier. However, a quasi-normal approximation of the normal vector which is very easy to calculate still produces adequate point distribution over the Pareto front. The approximation for computing the normal vector at each point on the convex hull is given in Equation 85.

$$\widetilde{\mathbf{n}} = -\mathbf{F} \cdot \mathbf{l},\ \mathbf{l} = [11...1]^T \tag{85}$$

The final step involves an optimization routine which can be seen as a line search in the performance space at each of the vector normal to the convex hull [86]. The formulation for this line search algorithm is provided in Equation 86 [86].

$$\begin{bmatrix} \mathbf{p}^* \\ t^* \end{bmatrix} = \underset{\mathbf{p},\, t}{argmax}\ t \tag{86}$$

$$s.t.\ \mathbf{F}\cdot\mathbf{w} + t \cdot \widetilde{\mathbf{n}} = \hat{\mathbf{f}}\,(\mathbf{p})$$

$$\mathbf{c}\,(\mathbf{p}) \geq 0$$

Normal Boundary Intersection is a very elegant and promising technique that can theoretically approximate the absolute (strong) Pareto frontier points. This technique does however, have a major disadvantage in that it requires the implementation of a numerical optimizer to solve for the Pareto points. In addition, the optimizer has to work with a very restrictive feasible domain consisting of a single line in 3-D space. This guarantees that the optimizer is almost always working in the unfeasible domain or approaching the optimum solution from the unfeasible region. This is not only bad practice but it also guarantees that the starting point will almost certainly be unfeasible. In highly complex problems, this can cause the optimizer to never find its way back to the feasible domain, and thus no true Pareto point is ever found.

2.10.5 Pareto Frontier Identification

The Pareto Fitness (PF) function given in Equation 87 was proposed by Schaumann et al [83]. The objective function values going into the Pareto Fitness functions ($f1_i, f2_i, ..., fn_i$) need to be normalized as shown in Equation 88 for a "lower is better" problem. Wilson et al [92] took the idea of Pareto Fitness function further and approached design space exploration through the use of surrogate modeling techniques. Pareto Fitness is a robust non-weighted

technique capable of handling concave or convex frontiers, linear and nonlinear constraints, as well as discrete variables. In addition, it is simple to program, adaptable to accuracy and computational demands, and lends well for future probabilistic studies. The accuracy and computational requirements can be met by modifying the fineness of the design space grid.

$$F_i = [1 - max_{i \neq j} (min (f1_i - f1_j, f2_i - f2_j))]^p \tag{87}$$

$$f1_i = \frac{raw f1_i - f1_{min}}{raw f1_{max} - raw f1_{min}} \tag{88}$$

Where:

F_i - Pareto fitness value of ith design ($F_i \geq 1$, ith design is Pareto optimal)

$f1_i$ - first objective function value of the ith design

$f2_i$ - second objective function value of the ith design

p - Pareto exponent (typically p = 1)

The main disadvantage of this technique is the exponential increase in computational requirements as the number of variables (design and random) increases. Benchmarking of these requirements will be performed to demonstrate these limitations in later a chapter. When not coupled with a numerical optimizer, the PF technique does not directly predict the Pareto point, instead it identifies the Pareto point from a design space sampling. This nearly guarantees that the identified Pareto point will be a weak Pareto point. The application of a numerical optimizer would transform the PF method into a Pareto prediction method.

2.11 Conclusions

The existing state of the art technology concepts have been presented along with the various methods that are currently available for dealing with thermal requirements. Despite the large amount of disciplinary work which has been done in this field, a gap still exists which must be accounted for before aircraft thermal management system selection can be brought forward to the conceptual design stages. This will require the identification and integration of some of the aforementioned disciplinary methods with modern conceptual design techniques.

Chapter III

RESEARCH QUESTIONS AND HYPOTHESES

3.1 Research Focus

The problem definition has identified existing challenges and several observations were drawn which will produce a series of research questions. The literature review in the previous was intended to shed light on how the engineering community currently deals with such challenges. The research produced in the literature review shows that there are numerous approaches one can take when considering the thermal management system for a hypersonic vehicle. The bulk of the work and contributions within this thesis are contained to steps 5 and 6 in the Georgia Tech IPPD framework given in Figure 48.

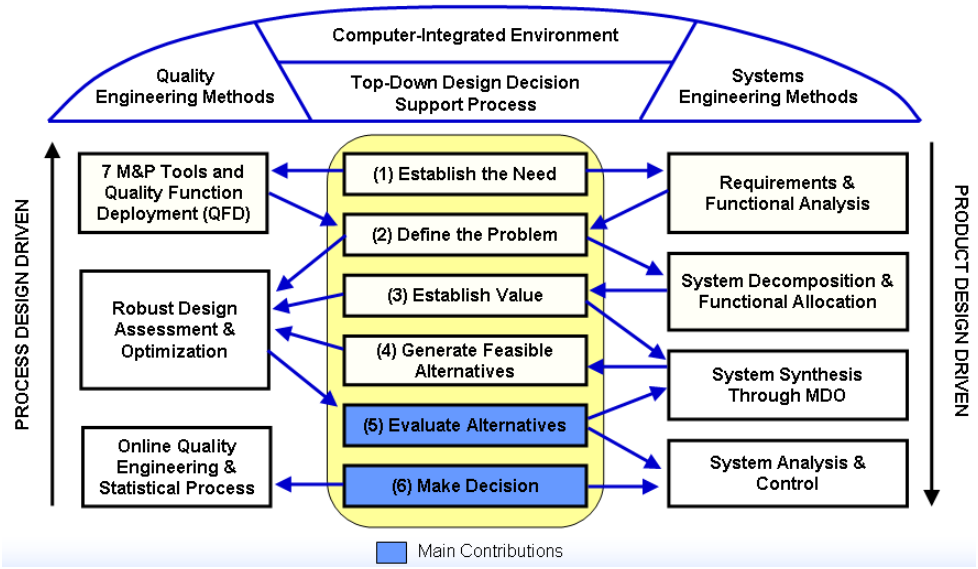

Figure 48: Georgia Tech IPPD Framework

This thesis will focus mainly on the intelligent selection of thermal management systems for hypersonic vehicles under certain assumptions which will help narrow down the problem to a manageable degree. The first assumption will be that the mission profile of an aircraft

needs to be flexible and should not be constrained to an optimal but very specific trajectory as is the case for reusable launch vehicles. Therefore the trajectory optimization of the vehicle will not be considered, and instead of fixating on a single optimal trajectory, this thesis will study the requirements on thermal management systems for a wider range of mission trajectories. The author also acknowledges that the shape optimization is an integral part of the hypersonic problem with regards to the aerothermal environment, which has a direct effect on thermal management systems. For the context and time frame of this thesis the aerothermodynamic shape optimization will not be considered due to the large level of complexity which this would bring into the modeling and simulation. The thesis will instead focus on improving the methods for technology selection. The results will not only provide a transparent analysis and comparison of the technologies but will also provide more detailed sizing information regarding the placement and characteristics of individual thermal managements systems.

3.2 Research Questions

The technical challenges reviewed in the previous gave rise to a series of observations which in turn give rise to a series of research questions and hypotheses, as outlined below. These hypotheses form the basis for the work which will be described in the next . In some cases, new questions may arise from a hypothesis which can lead to an entire new group of sub-research questions and sub-hypotheses. The reason for the specific numbering of the research questions and hypotheses will become clear once the methodology is presented in the next .

Observation 1. Traditional selection of thermal management systems based on weight minimization and simplicity is not sufficient to guarantee overall system effectiveness.

Research Question 1. How can a design methodology be formulated to allow for a comparative and systematic evaluation and selection of various classes of thermal management systems in the early phases of conceptual design?

Observation 2. The lack of available data regarding actual flight proven hypersonic concepts poses a problem in the early phases of design, especially when considering novel vehicle geometries.

Research Question 2.1 What level of aerothermodynamic analysis fidelity is most suitable for the conceptual design phase?

Research Question 2.2. What would be the most suitable probabilistic analysis approach, which is not only the most computationally effective but also ties well into the design exploration environment?

Research Question 2.3. What surrogate modeling technique would be most adequate for the implementation of the probabilistic analysis?

Observation 3. Numerical optimization at such a high level becomes a very complex and unmanageable task. Instead, the designer should be able to perform capability-based trade studies at the vehicle level in real time to assess thermal management system effectiveness.

Research Question 3. How can the design space exploration be formulated to allow the designer to make intelligent decisions regarding options and utilization of the various thermal management technologies?

Research Question 3.1. What would be the most appropriate approach for the determination of technology Pareto frontiers: identification or prediction?

Research Question 3.2. How can a capability inverse design space be generated at the vehicle level?

3.3 Hypotheses

The hypotheses presented here are constructed based on the newly gained knowledge of techniques and approaches pertaining to the problem and which were identified in the literature review. They will try to address each of the research questions with an educated answer, but most importantly will help guide the investigation process within the thesis.

> Hypothesis 1. A design methodology can be formulated to evaluate thermal management technologies through the implementation of a capability-based inverse design approach at the vehicle level.

The design methodology needs to include thermal management considerations in the conceptual design phase. This means that the measures of effectiveness for the concepts need to include not only performance but also other aspects of design which may be of importance to the customer. A key measure of effectiveness for thermal management which has traditionally been overlooked is life cycle cost. In order to claim greater overall system effectiveness for a concept, life cycle cost will need to be included along with performance and safety effectiveness measurements. A top-down design methodology will allow the engineer to expand the concept design space and ultimately find a solution which achieves greater overall system effectiveness. Surrogate modeling will serve as an enabling tool for the implementation of a vehicle's capability-based inverse design approach. They will also make it possible to conduct probabilistic studies for a better understanding of how early assumptions will guide the thermal management system selection process.

> Hypothesis 2.1 Simplified physics-based tools consisting of 2-D flow analysis and engineering approximations will provide a good compromise between computational speed, fidelity, and flexibility for the aerothermodynamic analysis.

The analysis tools need to be flexible enough to be able to handle non-historical based designs. In the case of hypersonic aircraft this type of data is very costly and hard to come by, thus leading to the interest in physics-based analysis tools. To make this design methodology possible given the high level of integration complexity of hypersonic vehicles,

the level of fidelity must be brought down to allow for full exploration of the design space in a timely manner while still maintaining adequate accuracy using physics-based methods. The simplified physics-based tools consisting of 2-D flow analysis will need to be validated against more sophisticated analysis tools or experimental data to determine if the tradeoff between accuracy and speed is justifiable.

> Hypothesis 2.2. The implementation of surrogate models along with a Monte Carlo simulation will be the most adequate probabilistic approach because it will be able to provide joint probability density functions, and at the same time be the most computationally effective.

There are three main approaches that can be used in probabilistic analyses. These include *i*) a sophisticated analysis code couple with Monte Carlo simulation, *ii*) surrogate models coupled with Monte Carlo simulation, and *iii*) sophisticated analysis code coupled with Fast Probability Integration. Qualitative and quantitative benchmarks will need to be conducted to verify that surrogate models combined with Monte Carlo simulation is the most appropriate technique for this methodology.

> Hypothesis 2.3. Response surface equations will provide the appropriate level of accuracy for data fitting of the physics-based analysis.

As mentioned earlier, surrogate models are the key enabler for probabilistic analysis because in many cases the run time of sophisticated analysis codes is simply too much. There are, however, many ways to generate surrogate models of the underlying physical problem. Typically, it is good practice to begin with the implementation of simpler surrogate models such as response surface equations. If the model is not capable of properly capturing the physics of the problem then one can move incrementally to more complex models such as neural networks. A decision flow diagram will be used to better demonstrate the surrogate model benchmarking process.

> Hypothesis 3. A probabilistic design space exploration environment can be

achieved by implementing surrogate modeling along with numerical techniques for prediction of multi-objective Pareto frontiers.

The physics-based models used in the design methodology will form the basis for the surrogate models. These surrogate models can be integrated with numerical techniques for computing 3-D Pareto frontiers along the three performance metric dimensions: performance, economics, and safety, which make up the vehicle's capability-based design space. Once the basis for obtaining these Pareto frontiers is created, one can assign a variability to the design capabilities and observe the corresponding effects on the thermal management technologies. The surrogate modeling will again serve as an enabler to allow the quick evaluation and resolution of the probabilistic design space and in addition will provide full transparency of the physics-based model which the designer can analyze for discrepancies, errors, or incorrect assumptions. The probabilistic technology frontiers will allow the designer to make more robust decisions early on in the conceptual design phase. The design space exploration environment should contribute not only a measure of goodness but also a probability of success for a volume of interest in the 3-D design space. Finally, the DSE should be able to map an optimum or desired solution in terms of the original design variables in order to achieve a true inverse design environment as was proposed by the first hypothesis.

Hypothesis 3.1. Pareto frontier identification through the implementation of Pareto Fitness will provide the most robust approach for complex 3-D design spaces.

Two different approaches to Pareto frontier identification were presented in the literature review including Normal Boundary Intersection and Pareto Fitness. The Pareto identification technique will need to be benchmarked together with the probabilistic analysis since the design exploration environment is probabilistic in nature as stated in hypothesis 3. The type of application will also play a large role in this technique selection since the two approaches seem to be most practical for entirely different type of problems.

Hypothesis 3.2. The inverse design space describing vehicle capabilities can be produced by implementing a numerical optimizer which manipulates design

variables in order to decrease the deviation between the current and desired effectiveness solutions.

Once the desired effectiveness levels are agreed upon by the customer and designer, the design space can be transformed and defined in terms of the vehicle's capability characteristics which the customer is ultimately most interested in. The vehicle's capability characteristics which the inverse design space is based on is in line with those key measures of effectiveness defined by the National Aerospace Initiative (speed, survivability, and payload capacity).

Chapter IV

A METHODOLOGY FOR THE EVALUATION AND SELECTION OF THERMAL MANAGEMENT SYSTEMS

Traditional design typically follows a bottom-up approach as shown in Figure 49. This essentially means there is one concept solution which is developed to meet the vehicle's capability requirements. A morphological matrix of design method alternatives is given in Table 2 showing how thermal requirements have been previously assessed. The table shows a summary from various sources of three additional concepts (Aztec, Space Shuttle, ARES) and the general method path (top to bottom) taken for thermal protection system design and optimization. The problem definition for the proposed methodology is assumed to be explicitly stated in the request for proposal. Benchmarking of the different alternative techniques or approaches needs to be performed when necessary to determine which should be used within the design methodology.

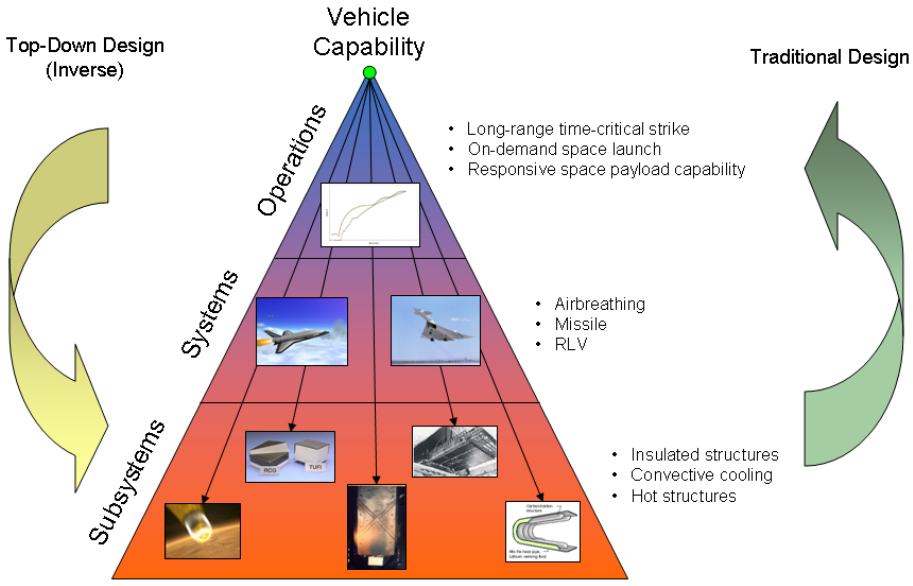

Figure 49: Top-Down Design Approach

Table 2: Morphological Matrix for Method Alternatives [47, 7, 63]

	Alternatives							
Problem Definition	Affinity Diagram	Interrelationship Diagraph	Tree Diagram	Prioritization Matrix	Matrix Diagram	Request for Proposal	N/A	Unknown
Need Identification	QFD	Customer Surveys	Customer Interviews	Focus Groups	Customer Complaints	N/A	Unknown	
Concept Down-Selection	TOPSIS	Dominance	Maximin	Maximax	Simple Additive Weighting	Expert Knowledge	N/A	Unknown
Design of Experiments	Factorial	Central Composite	Box-Behnken	Random Sampling	Space Filling	Latin-Hypercube	N/A	Unknown
Aerothermal Analysis	Analytical	Potential	CFD	Experimental	N/A	Unknown		
Thermal Management Sizing	MER	1-D Transient Heat Equation	Complex Tile Acceptance Logic	N/A	Unknown			
Surrogate Modeling	RSE	Neural Network	Gaussian	N/A	Unknown			
Pareto Estimation	NBI	PF	Epsilon Constraint	Weighted Sums	N/A	Unknown		
Probabilistic Analysis	Sophisticated + MCS	Surrogate + MCS	Sophisticated + FPI	Sensitivity Studies	N/A	Unknown		
Solution Process	Iterative Optimization	Multivariate Design Space Exploration	Unknown					
Multi-Objective Decision Making	GP	JPDM	PJPDM	Single Point Solution	N/A	Unknown		
Inverse Design Resolution	GP	Modified GP	N/A	Unknown				

Proposed Methodology
Aztec: Two-stage to orbit RLV
Space Shuttle
ARES

The TPS design process implemented for the Aztec vehicle is a traditional bottom-up design approach as shown in Figure 49. Aztec is a two-stage-to-orbit, horizontal takeoff, horizontal landing RLV designed to deliver a $20,000$ lbs payload to space. The design of the Aztec vehicle is based on a multidisciplinary design process which includes trajectory, propulsion, aerodynamics, aerothermodynamics, weight sizing, aeroheating, safety, and economics. The multidisciplinary design process inherently involves feed-forward and feedback loops for the flow of disciplinary information such as lift, drag, fuel flow, thrust, and vehicle weight.

A baseline trajectory profile is defined and the design solution is solved through iteration of the multidisciplinary process until convergence is achieved. In addition, the process can be coupled with an optimizer to help drive certain goals such as minimization of fuel

consumption or cost. If there is more than one goal, a weighting system needs to be defined relating the relative importance between the different objectives. The end result is a single point design solution that is capable of meeting the desired goal.

The thermal protection system for Aztec is sized through the use of MINIVER and MERs. MINIVER is used to determined the aerothermal requirements for the TPS including heatrate, heatload, and skin temperatures. As is typically the case, determination of mass properties is performed through the use of mass estimating relationships which are parametric relationships based on historical data, or engineering approximations. The TPS mass for Aztec is determined through a scale factor based on existing data from a previous scramjet rocket-based combined cycle flying a similar trajectory and using similar technologies [69, 70]. The selection of the TPS technologies is based on expert knowledge to assure that the TPS temperature limit is not violated and an attempt is made to reduce complexity. Another approach implemented with ARES [7] uses the physics-based 1-D transient heat equation to size the TPS once the heatrate requirements are defined. Both MERs and the 1-D transient heat equations have distinct advantages and disadvantages. MERs can be very accurate if the relationships are based on experimental data and the design being studied is very similar in terms of trajectory, shape, and technologies. The 1-D transient heat equation is more useful for cases consisting of novel designs for which there is no existing experimental data.

Some of the key characteristics of this design process includes a single point design solution with no uncertainty information regarding the variability of uncontrollable variables. The solution is highly driven by the relative weighting factors between competing objectives such as performance, economics, and safety. The selection of TPS technologies, and objective weighting factors based on expert knowledge is bound to bring in bias into the design process which can lead to degradation of the overall effectiveness of the system.

The proposed methodology is based on an inverse design approach also shown in Figure 49. Inverse design is a top-down approach which starts with a high-level capability and branches down into various non-unique solution that can answer that capability. As a result the top-down approach considers various families of solutions instead of focusing on a single

technology. A top-down approach is more likely to result in a solution with greater overall system effectiveness by allowing the designer to explore a larger design space. In traditional numerical optimization this can be thought of as a more globally optimized solution in a complex multi-modal design space. As will be shown, surrogate modeling will be the key enabler for successful implementation of inverse design approach and the determination of uncertainty by allowing the modeling and quick evaluation of such a complex design space.

4.1 Design Methodology Overview

The overall design methodology proposed through hypothesis #1 for the selection of thermal management systems in conceptual design is shown in Figure 50. The core of the IPPD framework given earlier in Figure 48 is repeated on the left side of Figure 50. From here the methodology can be expanded into three major phases: *i*) Identification, *ii*) Evaluation, and *iii*) Decision making. The main contributions of this thesis come in to play during the evaluation and decision making phases. The methodology is composed of 10 major steps which are listed below and will be explained in more detail later in this chapter. The diagram in Figure 50 also shows where each research question comes into play within the methodology.

1. Problem Definition
2. Identification of Need and Concept Down-Selection
3. Definition of Vehicle Capability-Based Design Space
4. Definition of Design Space Ranges
5. Definition of Design of Experiments
6. Modeling and Simulation
7. Surrogate Modeling
8. Probabilistic Analysis
9. Pareto-based Joint Probability Decision Making (PJPDM)

10. Inverse Design Space Resolution

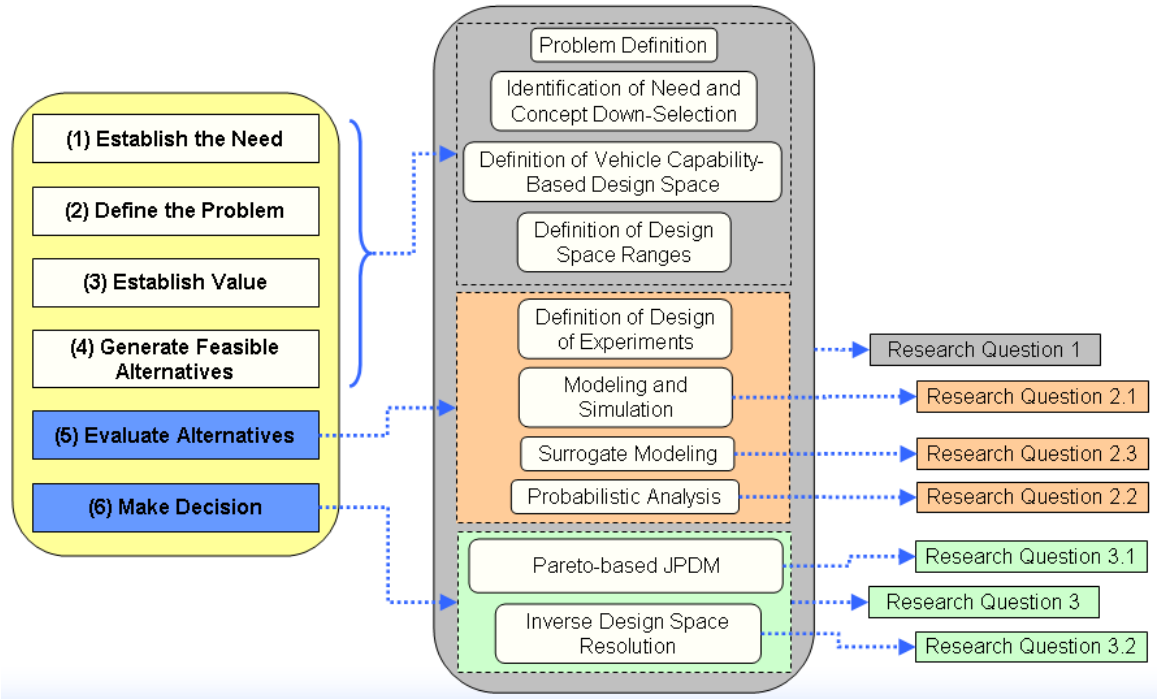

Figure 50: Methodology Overview

The problem definition is required in order to make sure one is attempting to solve the correct problem and so that money, time, and resources are not wasted. Once the problem has been defined, the identification of need will shed light on the aspects that the customer is most interested in and what these mean to the engineer. This will help indentify the characteristics that allow the engineer to quantify and analyze the problem. In addition, a concept down-selection will be performed to narrow the number of technology alternatives which are found through the morphological matrix. The down-selection will still allow for the implementation of a top-down design approach but will also help concentrate the resources of the program on those technologies that are most promising. The next logical step is the definition of the design space where studies can be performed to derive the best design solution. This design space is composed of the engineering characteristics identified through the need identification process. The design space can then be bound while taking into consideration the interest of the customer and the limitations of the analysis tools being

employed.

The modeling and simulation is a key step which will help identify the physical relations between all the disciplines and elements of the design. As it will be shown, the implementation of a probabilistic methodology will require the introduction of surrogate modeling. The design of experiments step will help obtain the most information regarding the design space while spending the least amount of computational effort. The design space sampling from the design of experiments can then be used for the generation of the surrogate models. With the surrogate models in place, a probabilistic analysis will help introduce uncertainty into the methodology and allow assessment of the risk involved when selecting a design.

The last phase involves creation of an environment which will utilize the probabilistic information produced and help make decisions regarding the options and utilization of the alternatives. The last step involving the design space resolution will help map the technologies to the vehicle capabilities of ultimate interest to the customer in a top-down design approach.

4.2 Definition of Design Methodology

In the following section, the steps presented in the design methodology overview will be described in greater detail. In addition, any existing gaps will be identified and alternatives will be postulated and benchmarked in order to fill these gaps.

4.2.1 Problem Definition

The problem definition and application typically comes from a request for proposal (RFP) provided by the customer. This step provides a definition for the activity, task, or action that needs to be accomplished. Improper understanding of the problem can have disastrous effects on a program. It is important to properly understand the problem early on so that money, time, and resources are not spent attempting to solve the wrong problem. In some cases, however, the problem can be vague and not properly well defined. In these case, the seven management and planning tools described below can be employed to help shed light on what needs to be accomplished [24]. A case study which will be presented in a later section will provide an example problem and application and will be used to demonstrate

the proposed design methodology.

1. Affinity Diagram - organize data and information through natural relationships grouping
2. Interrelationship Diagraph - helps explore and visualize case-and-effect relationships of a complex problem
3. Tree Diagram - breaks down broad categories into more detailed sublevels required to solve a problem
4. Prioritization Matrix - prioritizes items based on a pair-wise comparison of items
5. Matrix Diagram - establishes the strength and relationships between items
6. Process Decision Program Chart - extension of tree diagram sublevels to identify risks and countermeasures
7. Activity Network Diagram - can help plan the appropriate sequence of tasks and subtasks that need to be accomplished

4.2.2 Identification of Need and Concept Down-Selection

The needs of the customer is what typically drive the development of a product or process [24]. Understanding who the customer is and what they want is key for a program to be successful. There are several approaches which can be used to properly understand the customer's need including: focus groups, customer interviews, surveys, and complaints.

Quality Function Deployment was selected for the identification of need because it is a more robust, repeatable, and transparent approach. The QFD which is shown in Figure 51 maps the voice of the customer to the voice of the engineer. This will identify the relevant engineering characteristics that the engineer should be considering, and will help define the way the design space is going to look. The House of Quality provided in Figure 51 is only shown as an example at this point but will be further discussed in Chapter VI. The morphological matrix shown in Table 3 will be utilized to open up the design space and uncover as many possible thermal management configurations as possible. The broader the

technology design space the more likely the designer is to find a more capable and suitable concept. This also poses the problem of increasing complexity and can make the task of studying all identified concepts daunting. A MADM technique can be employed in this case to narrow down the extensive number of concepts to a manageable number depending on the resources and time available for the program. Ideally, one should include as many thermal management technologies as resources allow.

TOPSIS will be applied and a down-selection will be performed based on the concepts that best answer the engineering characteristics which ties back to the need of the customer. At this early stage this is all done qualitatively since no modeling and simulations has been done so far. A team of disciplinary experts in the field needs to be assembled to define the relationships between concept and engineering characteristic. The down selected concepts can be carried through to the modeling and simulation phase, and they will be the alternatives which ultimately will be pitted against each other.

The overall process for need identification and concept down-selection is shown in Figure 52. This provides a ranking for the different families of thermal management concepts. The thermal management system families that were selected are highlighted in green in Figure 52 under the TOPSIS section. The column on the right of the TOPSIS table labeled "change" shows the change in the technology's ranking from a baseline value. The selected TMS families are convective cooling (active) and insulated structure (passive). The top-ranked technology from each family (passive, semi-passive, active) were taken into consideration. However, heat pipes which are representative of a semi-passive technology had to be neglected due to difficulties encountered while trying to model them.

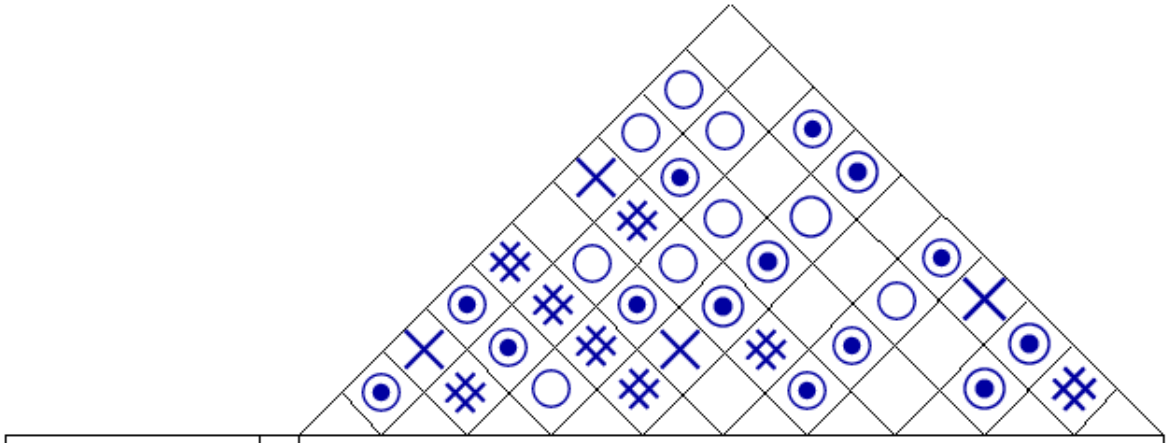

Thermal Management Technology Selection		Customer Importance	HOWs (Voice of the Engineer)									
			Performance								Economic	Safety
			Total Gross Weight	TMS Weight	Range	Maximum Mach	Payload	Block Time	Maximum Altitude	TMS Configuration	Life Cycle Cost	Safety Margin
Direction of Improvement			↓	↓	↑	↑	↑	↓	↑		↓	↑
WHATs (Voice of the Customer)	Rapid Turn Around	5.0	△	◌						✹		
	Vehicle Capability	8.0	◌	◌	✹	✹	✹	✹	✹	✹	✹	◌
	Safety	7.0			△	✹		◌	△	✹	◌	✹
	Durability	4.0			◌	◌		◌		✹	✹	
	Cost	6.0	◌	◌	◌	◌	◌			✹	✹	△
	Integration	1.0		◌			◌			✹	◌	
	Operational Complexity	2.0	△	◌						✹	◌	
	Maintenance	3.0			◌	△		△	◌	✹	✹	◌
Weighted Importance			49	66	118	168	93	108	88	324	219	102
Relative Importance												
Units			lbs	lbs	nmi		lbs	min	ft		US$	K
Target Value			100000	20000	3000	6	5000	80	80000		100	200
Risk Levels			3	3	9	3	9	9	1	3	9	9
Relative Risk												

Correlation:

- ◉ Strong positive
- ○ Positive
- # Negative
- \+ Strong negative

Relationship:

- ◉ Strong
- ○ Neutral
- △ Weak

Figure 51: House of Quality

Table 3: Morphological Matrix for Thermal Management Systems

		Categories			
		1	2	3	4
Characteristics	TMS Type	Passive	Semi-passive	Active	
	Passive Type	Heatsink Structure	Hot Structure	Insulated	
	Semi-passive Type	Heatpipe	Ablation		
	Active Cooling Type	Convective	Transpiration	Film	
	Coolant Type	Air	Water	Ethylene Glycol	Lithium
	Thermodynamic System	Closed	Open		
	Convective Process	Sensible	Latent		
	Thermodynamic Cycle	Ideal	Vapor Compression	Reversed Brayton	
	Degenerative Materials	Yes	No		
	Number of Materials	3	4	5	15

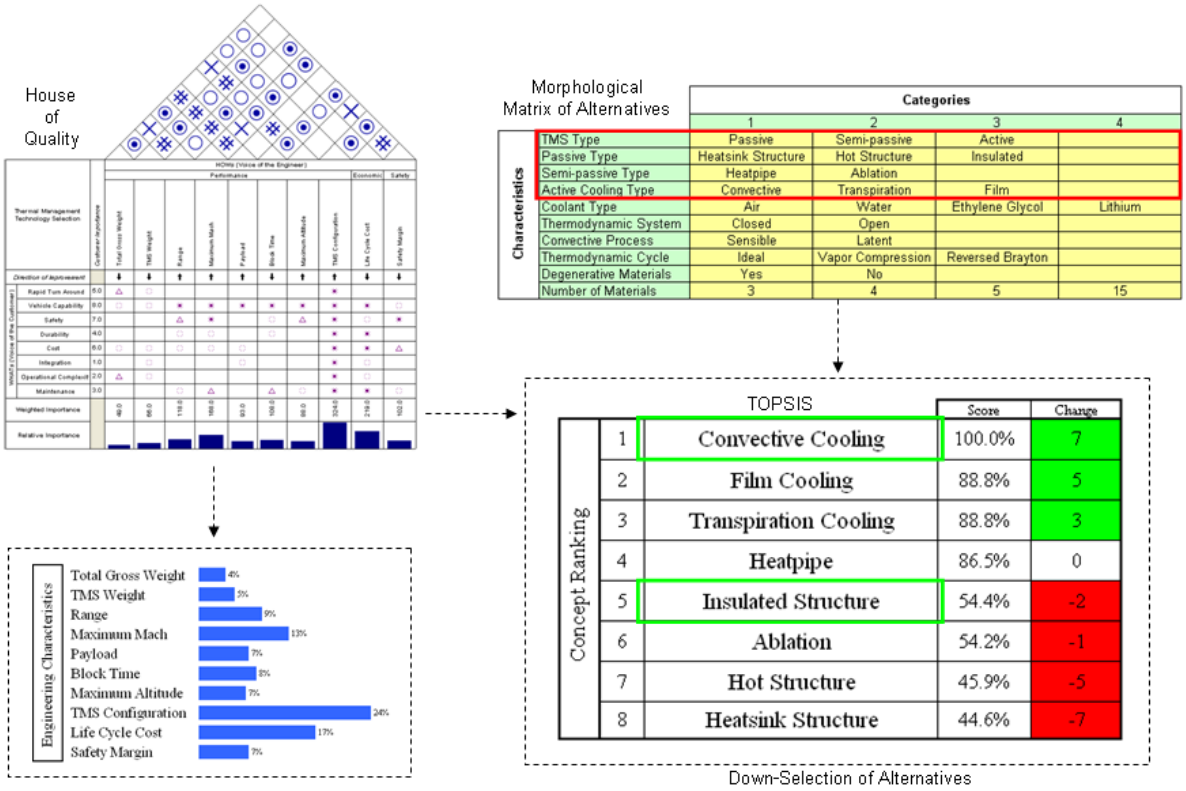

Figure 52: Overall Process for Need Identification and Concept Down-Selection

4.2.3 Definition of Vehicle Capability-Based Design Space

The motivation and literature review have established the need for a vehicle's capability-based design space comprised of not only performance effectiveness metrics but also life cycle cost and safety. The ultimate goal is to find a thermal management system that produces better overall system effectiveness instead of focusing only on high performance as it has traditionally been done. A 3-D design space will be created with axes consisting of

performance, economic, safety measures of effectiveness as shown in Figure 53.

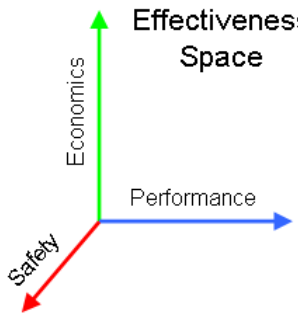

Figure 53: Effectiveness Design Space

These measures of effectiveness were carefully selected while taking into consideration the key system attributes desired according to the National Aerospace Initiative technology development approach. Recall these desired system attributes included: speed, survivability, and payload capability [76]. Knowing this, the performance dimension will include parameters such as range, maximum Mach number, and payload. The economic dimension will focus on life cycle cost for a 100 flight life and includes the parameters: range, maximum Mach number, payload, and fuel cost per barrel. The safety dimension will consist of range, maximum Mach number, payload, and a metric defined as the safety margin (SM). The safety margin which will be defined in greater detail later in this , represents the minimum thickness that a surface material can reach before it violates the maximum surface temperature constraint. A violation of this constraint could lead to a catastrophic failure due to melting through the skin of the vehicle. Each of these three dimensions will be represented by an overall evaluation criterion composed of engineering characteristics pertaining to that dimension. The evaluation criteria or measures of effectiveness for the dimensions are shown below in Equations 89-91. The three dimensions are normalized on a $(0, 1)$ basis using Equation 92.

$$OEC_{Performance} = Productivity = f(range,\ maximum\ Mach,\ payload) \tag{89}$$

$$OEC_{Economics} = LCC = f(range,\ maximum\ Mach,\ payload,\ fuel\ cost) \tag{90}$$

$$OEC_{Safety} = SM = f(range,\ maximum\ Mach,\ payload,\ TPS\ thickness\ failure) \quad (91)$$

$$OEC_i = \frac{f_i - f_{i,min}}{f_{i,max} - f_{i,min}},\ f_i\ is\ to\ be\ maximized \quad (92)$$

$$OEC_i = 1 - \frac{f_i - f_{i,min}}{f_{i,max} - f_{i,min}},\ f_i\ is\ to\ be\ minimized$$

It is important to note that not all of the engineering characteristics will become design variables as not all of them can be used as inputs to the analysis tools in the modeling and simulation. Those characteristics which are not design variables will be obtained as responses or outputs of the modeling and simulation.

4.2.4 Definition of Design Space Ranges

After having defined the design space, the ranges need to be specified for which the modeling and simulation will be run. Although this step seems straightforward, it is important to specify a design space that is large enough to capture enough of the behavior but at the same time one must make sure that the ranges are within the allowable limits of the modeling and simulation tools. Failure to remain within the limits of the modeling and simulation environment will lead to failed cases or worse inaccurate estimates which will bias the results. This step will generally require the contribution of disciplinary experts as the selection of ranges is not a trivial task.

4.2.5 Definition of Design of Experiments

The implementation of a DoE will help yield the proper sampling of the design space while at the same time reducing the computational effort by reducing the number of cases that need to run. The selection of the DoE is highly dependent on the type of problem or application, analysis tools assumptions and restrictions, as well as the selected data fitting technique.

4.2.6 Modeling and Simulation

The modeling and simulation DSM is shown in Figure 54 including some of the most important variables being passed between disciplines. The DSM contains only the feed-forward and feedback loops which are included within the modeling and simulation environment. However, it is important to note the possible existence of additional feed-forward and feedback loops for more complex hypersonic applications. MATLAB [57] was selected for the integration of the analysis environment because it will help eliminate the overhead associated with more sophisticated high level integration software.

The disciplinary analysis tools for the modeling and simulation environment are shown in Table 4. The selection of the aerodynamics and aerothermodynamics analysis tools was based on benchmarking performed comparing tools and techniques with various levels of fidelity. These benchmarking exercises will be presented in the respective following sections describing aerodynamics and aerothermodynamics analysis. The modeling for the safety and economic disciplines was developed by the author and the specifics of this modeling will be presented in more detail in following sections. Modeling validation for the selected physics-based analysis tools including NASCART, RASAC, MINIVER, and TMSS will be presented in a later .

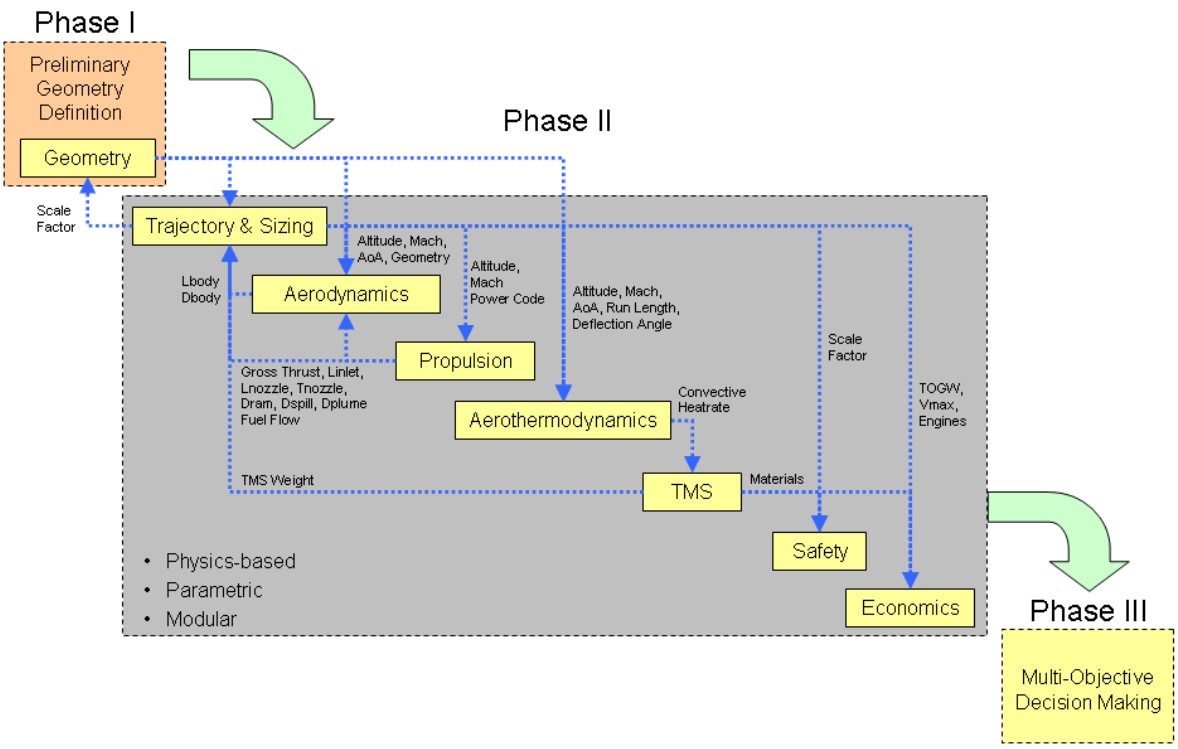

Figure 54: Modeling and Simulation Design Structure Matrix

Table 4: Proposed Disciplinary Tools

Discipline	Tool
Geometry	VSP
Aerodynamics	NASCART
Propulsion	P&W Engine Decks
Trajectory	RASAC
Aerothermodynamics	MINIVER
Thermal Management Systems	TMSS

4.2.6.1 Geometry

Vehicle Sketch Pad (VSP) is an extension of Rapid Aircraft Modeler [35], a program developed by NASA for quick and easy 3-D geometry generation during conceptual design. It takes as inputs general geometry parameters such as taper ratio, aspect ratio, and fuselage length and makes use of built-in general shape components of an aircraft like wing, fuselage, and engine to create a model on the fly. The ability of the geometry creator is confined to only building external shapes, but is capable of exporting geometry formats for either simple panel codes or even CFD codes. VSP was selected for geometry generation because

it is a well established, versatile, and generally accepted NASA tool.

4.2.6.2 Aerodynamics

In this section, the alternative approaches and tools for aerodynamic prediction will be described and compared. The most appropriate of these tools will be selected for the prediction of the aerodynamic deck which will be later used in the sizing and synthesis case study. A wide range of aerodynamic tools and their features are described in Table 5. There are four major categories of aerodynamic tools based on their solver methods including *i*) analytical, *ii*) linearized potential, *iii*) non-linearized potential, and *iv*) CFD solvers [81]. These four categories are listed in order of increasing accuracy and complexity.

Table 5: Aerodynamics Tools Database [53]

Code	Method	Computational Efficiency	Grid Generation	Flight Regime	Multibody Interference	Ground Effect	Aeroheating	Design Space Exploration
CFL3D	Euler / NS	30 hrs	Needed	All	Yes	Yes	Yes	No
NASCART	Euler / Euler+BL / NS	30 hrs	Automatic Cartesian	All	Yes	-	No	No
ZONAIR	Potential + Perturbed Euler	20 min	No	All	Yes	Yes	Yes	Yes
APAS	Potential + Empirical	< 10 min	No	Empirical Hypersonics	Subsonic + Supersonic	Subsonic + Supersonic	Yes	No
MUSTANG	Potential + Empirical	< 10 min	No	Empirical Hypersonics	Subsonic + Supersonic	Subsonic + Supersonic	Yes	Yes
PANAIR	Potential	20 min	No	Subsonic + Supersonic	Yes	Yes	No	No
Component Build-up Method	Analytical + Empirical	<< 10 min	No	All	No	No	Yes	No

The simplest of these methods is the component build-up method which combines analytical and empirical aerodynamic solutions. In this case aerodynamic contributions can be determined through very simple formulations and experimental data and added together to form the drag polar or the vehicle. This approach is fast and simple, but highly dependent on the given design and generally the least accurate of the three major approaches.

Another category of solvers are based on linear or nonlinear potential flow theory. The full potential equation is derived by Anderson, pp. 589-591 [2]. The simplified linear flow theory can be obtained by assuming small perturbations due to a slender body with low angle of attack. Small velocity perturbations can be assumed to be much smaller than free stream velocity, and thus relatively small terms or products of perturbation velocities can

be neglected in the full potential equation. The linearization process makes it inadequate to use the simplified linear flow solver in transonic flow, and assumes a steady, inviscid, irrotational, and isentropic flowfield in addition to slender body and low angle of attack.

An alternative approach for modeling hypersonic aerodynamics includes the use of simplified impact and shadow methods. An example of a code employing these methods is Supersonic Hypersonic Arbitrary Body Program (SHABP). SHABP is a code widely used in government and industry which lends itself very well to design [52]. As already mentioned, SHABP employs a simplified suite of impact and shadow methods such as modified Newtonian, tangent-wedge, shock expansion to solve for the pressure field around hypersonic vehicles in a very short period of time [52]. SHABP can also be used in the supersonic ($Mach \geq 2$) and hypersonic flight region.

At the other end of the spectrum are CFD solvers such as CFL3D and NASCART. These codes are far more accurate, as well as independent of vehicle design since they use more sophisticated physics-based formulation such as Euler and Navier-Stokes to predict the flowfield. The full Navier-Stokes formulation is provided by Anderson [2], pp. 850. The Euler equations can be derived from the full Navier-Stokes equations by neglecting any terms consisting of viscous and thermal conduction effects [81].

The aerodynamic deck for the TBCC vehicle geometry was computed with NASCART based on Euler CFD analysis solutions. NASCART is a solution adaptive, Cartesian grid based flow solver developed by Dr. Ruffin at Georgia Tech, and capable of handling complex 2-D and 3-D geometries [80, 75]. NASCART holds several important advantages and features over other aerodynamic codes. One of these advantages is its automatic Cartesian grid generation feature which is capable of reading a geometry from VSP. In addition, being an in-house built tool at Georgia Tech, there is readily available support for it. Although NASCART is listed in Table 5 as having a 30 hour running time, in reality this is only an approximation for maximum computational time. The actual computational time is, as can be expected, highly dependent on grid size, flow conditions, and flow solver utilized. For the proposed case study which will be presented in a later section the computational time to convergence for each Euler CFD analysis solution was approximately 5-6 hours. The Euler

solutions used in the aerodynamic deck are shown in Tables 6-7 and plotted in Figure 55.

Table 6: Coefficient of Lift from NACSART (Euler) Aerodynamic Deck

		AoA					
	Mach	-2	0	2	4	6	8
CL	0.3	-0.3404	-0.25863	-0.17249	-0.07972	0.039883	0.189975
	0.8	-0.31089	-0.23568	-0.15212	-0.04547	0.090973	0.252968
	1.2	-0.34627	-0.26867	-0.17398	-0.05152	0.096716	0.281783
	2	-0.2017	-0.10959	0.000862	0.135923	0.293706	0.46669
	3	-0.09335	0.000758	0.106116	0.226539	0.358885	0.496697
	4	-0.05056	0.038333	0.133241	0.237568	0.349049	0.463312
	6	-0.01884	0.052452	0.13026	0.199712	0.278106	0.355408
	8	-0.00901	0.044433	0.096527	0.149536	0.206766	0.270058

Table 7: Coefficient of Drag from NACSART (Euler) Aerodynamic Deck

		AoA					
	Mach	-2	0	2	4	6	8
CD	0.3	0.029877	0.017457	0.012509	0.014407	0.026112	0.050753
	0.8	0.033573	0.022107	0.018719	0.023459	0.039416	0.068647
	1.2	0.093646	0.083134	0.080878	0.08842	0.104128	0.142481
	2	0.057569	0.054429	0.059039	0.073397	0.099757	0.1396
	3	0.034209	0.035104	0.043301	0.06043	0.087704	0.12559
	4	0.022882	0.024661	0.033424	0.049729	0.074559	0.108699
	6	0.012887	0.014735	0.022674	0.033872	0.050922	0.073307
	8	0.007669	0.00987	0.014963	0.023101	0.035074	0.052144

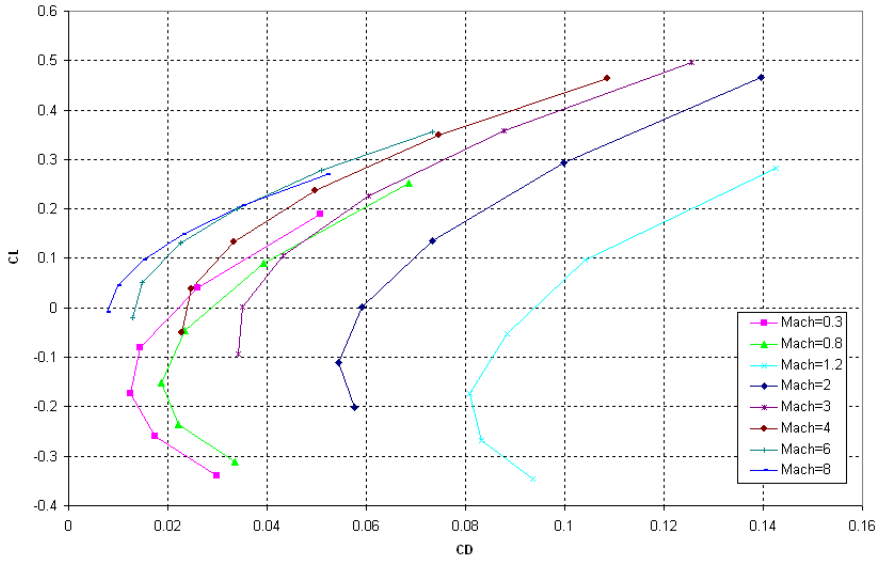

Figure 55: NASCART (Euler) Vehicle Drag Polar

4.2.6.3 Propulsion

The propulsion discipline will be handled by low speed and high-speed rubberized engine decks provided by Pratt & Whitney. The low speed engine will be a low bypass ratio turbofan, and the high-speed engine will be an axisymmetric scramjet upgraded to operate up to *Mach* 7.24. A more specific description of the engine configurations and transition from turbojet to scramjet will be provided in Section 4.3 detailing the proposed case study.

4.2.6.4 Trajectory and Vehicle Sizing

The trajectory analysis and vehicle sizing will be performed by Rapid Access to Space Analysis Code (RASAC) which has been developed by Dr. Villeneuve and specifically refined during work with Pratt & Whitney on the TBCC effort to help guide future technology investment decisions [71].

RASAC is a MATLAB code which supports multiple trajectory models that emphasize fast computational time, minimization of the number of trajectory points and avoids the need for complex control schemes [71]. These trajectory models include: takeoff / landing, climb, cruise, turn, and descent.

In all trajectory models, the aircraft is modeled as a point mass. The lift, weight, drag, and thrust forces are all applied at this singular point mass as was shown in Figure 14 on page 28. The equations of motion for this system were also given in Equations 10-13 on page 27.

Takeoff and Landing The formulation utilized by RASAC to predict the takeoff and landing performance is found in Mattingly [58] and Anderson [1]. The equations of motion in Equations 10-13 can be simplified as shown in Equations 93-96 by assuming small angle of attack, flight path angle, no engine thrust offset, and neglecting rate of change of flight path angle.

$$m\dot{V} = T - D \tag{93}$$

$$L = W \tag{94}$$

$$\dot{y} = 0 \tag{95}$$

$$\dot{x} = V \tag{96}$$

It is important to note that the drag term (D) in Equation 93 is not the same as the in-flight drag polar. The drag term (D) must also account for drag resulting from the open under carriage and extended flaps. This additional drag can be estimated using analytical approximations found in Anderson [1]. The new Equation 98 shows the updated performance equation for takeoff including an additional term for rolling resistance (R_r) as given by Equation 97 [1].

$$R_r = \mu_r \left(L - W\right) \tag{97}$$

$$m\dot{V} = T - D - R_r \tag{98}$$

As shown in Figure 56 the takeoff segment is divided into two parts: ground roll (s_g) and airborne distance (s_a) [1]. The liftoff velocity (V_{LO}) marks the limit between the two segments as shown in Figure 57 [1].

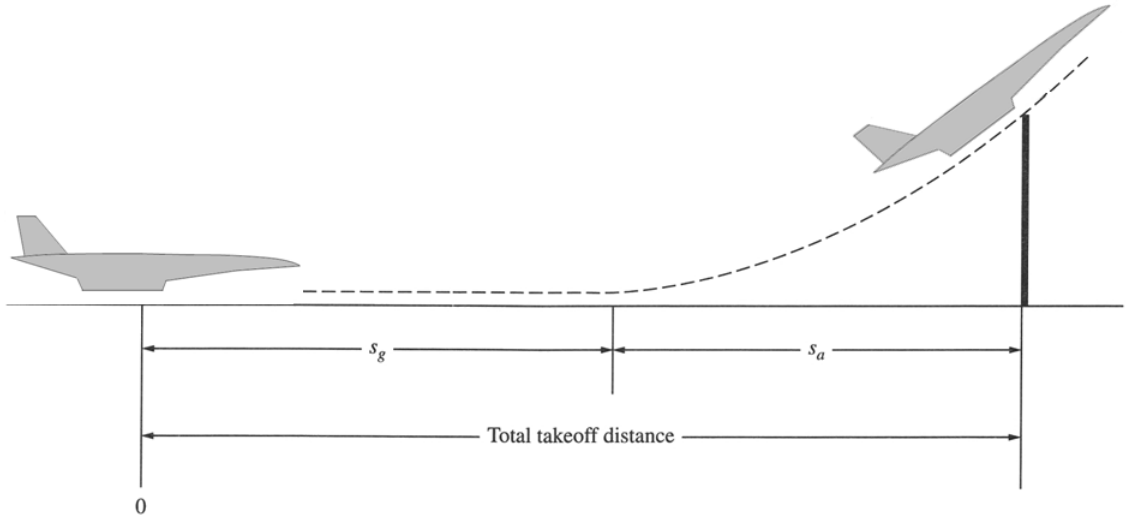

Figure 56: Takeoff Distance Denotation

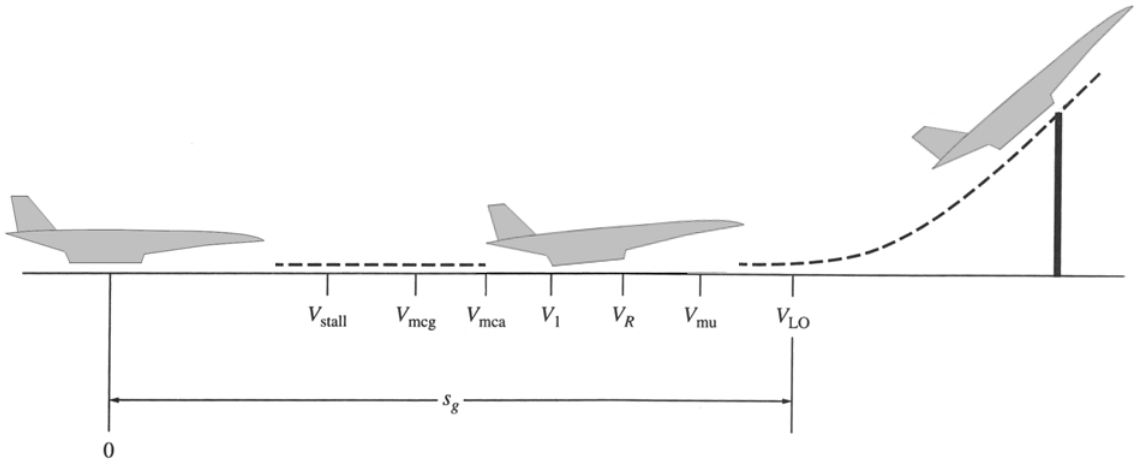

Figure 57: Takeoff Velocity Denotation

The liftoff velocity (V_{LO}) can be computed from Equation 94 by solving for the velocity parameter as shown in Equations 99-101 [58]. The total liftoff time can be computed by numerical integration of Equation 93 over finite time intervals until the takeoff velocity in Equation 101 is reached. Once the total takeoff time has been computed, it can be used to integrate Equation 103 and obtain the total ground roll distance (s_g) and total fuel burned during takeoff [58]. The weight variation of the vehicle can then be updated knowing how much fuel was burned during the takeoff segment.

$$L = \frac{1}{2}\rho V^2 S C_L = W \tag{99}$$

$$V_{stall} = \sqrt{\left(\frac{2}{\rho C_{L,max}}\right)\left(\frac{W}{S}\right)} \tag{100}$$

$$V_{LO} = 1.2 V_{stall} \tag{101}$$

$$\frac{dW}{dt} = -\frac{dW_{fuel}}{dt} = -T\,(TSFC) \tag{102}$$

$$\frac{dW}{W} = -\frac{T}{W}\,(TSFC)\,dt \tag{103}$$

The second segment of takeoff which is the obstacle clearance can be accomplished by a pull-up maneuver as shown in Figure 58. The turn radius of the pull-up maneuver can be computed with Equation 104. The included angle (θ_{OB}) can be solved using a geometrical given in Equation 105. The distance (s_a) can be computed using Equation 106 once the radius (R) and the included angle (θ_{OB}) has been determined [1].

$$R = \frac{V_\infty^2}{g\,(n-1)} \tag{104}$$

$$\theta_{OB} = \cos^{-1}\left(1 - \frac{h_{OB}}{R}\right) \tag{105}$$

$$s_a = R \sin\left(\theta_{OB}\right) \tag{106}$$

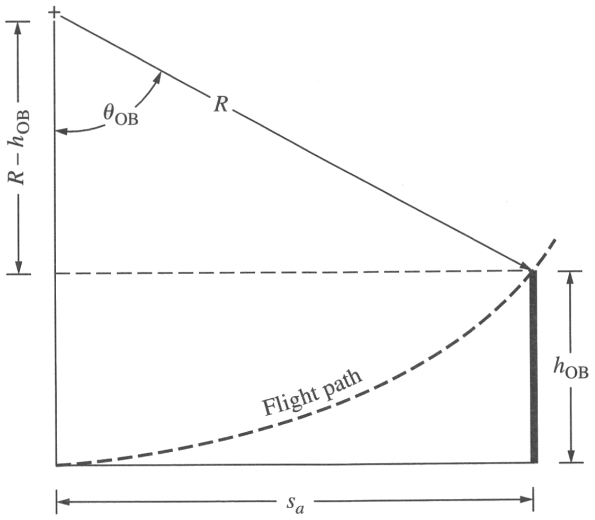

Figure 58: Geometry of Takeoff Obstacle Clearance [1]

The total landing distance is divided into four segments: approach distance (s_a), flare distance s_f, free roll distance s_{fr}, and ground roll distance s_g as shown in Figure 59 where θ_a and θ_f denote the approach flight path angle and included flare flight path angle respectively [1]. The approach, flare, free roll, and touchdown velocities denoted as V_a, V_f, V_{fr}, V_{TD} can be computed using Equations 107-110 for a military vehicle [1].

$$V_a = 1.2V_{stall} \tag{107}$$

$$V_f = 1.15V_{stall} \tag{108}$$

$$V_{TD} = 1.15V_{stall} \tag{109}$$

$$V_{fr} = V_{TD} \tag{110}$$

The approach distance (s_a) can be obtained by simplifying the equations of motions while assuming no rate of change in velocity or flight path angle into the relations given in Equations 111-112. In these performance equations the flight path angle γ is substituted

with the relationship $\gamma = -\theta_a$ since the flight path angle in descent is negative. These two resulting equations can be solved to obtain a relation for θ_a as given in Equation 113. Once this angle is known one can solve for the approach distance (s_a) geometrically as shown in Equation 114 [1].

$$L = W \cos\theta_a \tag{111}$$

$$D = T + W \sin\theta_a \tag{112}$$

$$\theta_a = \sin^{-1}\left(\frac{1}{L/D} - \frac{T}{W}\right) \tag{113}$$

$$s_a = \frac{h_{OB} - h_f}{\tan\theta_a} \tag{114}$$

By assuming a circular flare maneuver as shown in Figure 60, it is possible to see that the approach flight path angle and included flare flight path angles are equal ($\theta_a = \theta_f$). The flare height (h_f) can be computed with the geometrical relation given by Equation 116 and the radius (R) is given by Equation 104 while assuming a loading factor (n) of 1.2. Having relations describing the flare radius and angle, the flare distance can be approximated with Equation 117. The free roll distance (s_{fr}) is dependent on pilot technique and is given by Equation 115 where N denotes a time interval of 1-3 seconds.

$$s_{fr} = NV_{TD} \tag{115}$$

Finally, the landing ground roll distance can be computed by employing the same equation used for the takeoff ground roll in Equation 98. However, now the thrust (T) is replaced by a reverse thrust (T_{rev}) as shown in Equation 118 and rolling resistance (R_r) remains equal to the relation in Equation 97. This simple differential equation can be numerically integrated to solve the total time needed for the ground roll deceleration from the touchdown velocity (V_{TD}) to a complete stop. The computed velocities at each time step during the ground roll can then be integrated to solve for the total landing ground roll distance (s_g).

$$h_f = R - R\cos\theta_f = R\left(1 - \cos\theta_a\right) \tag{116}$$

$$s_f = R\sin\theta_f = R\sin\theta_a \tag{117}$$

$$m\dot{V} = -T_{rev} - D - R_r \tag{118}$$

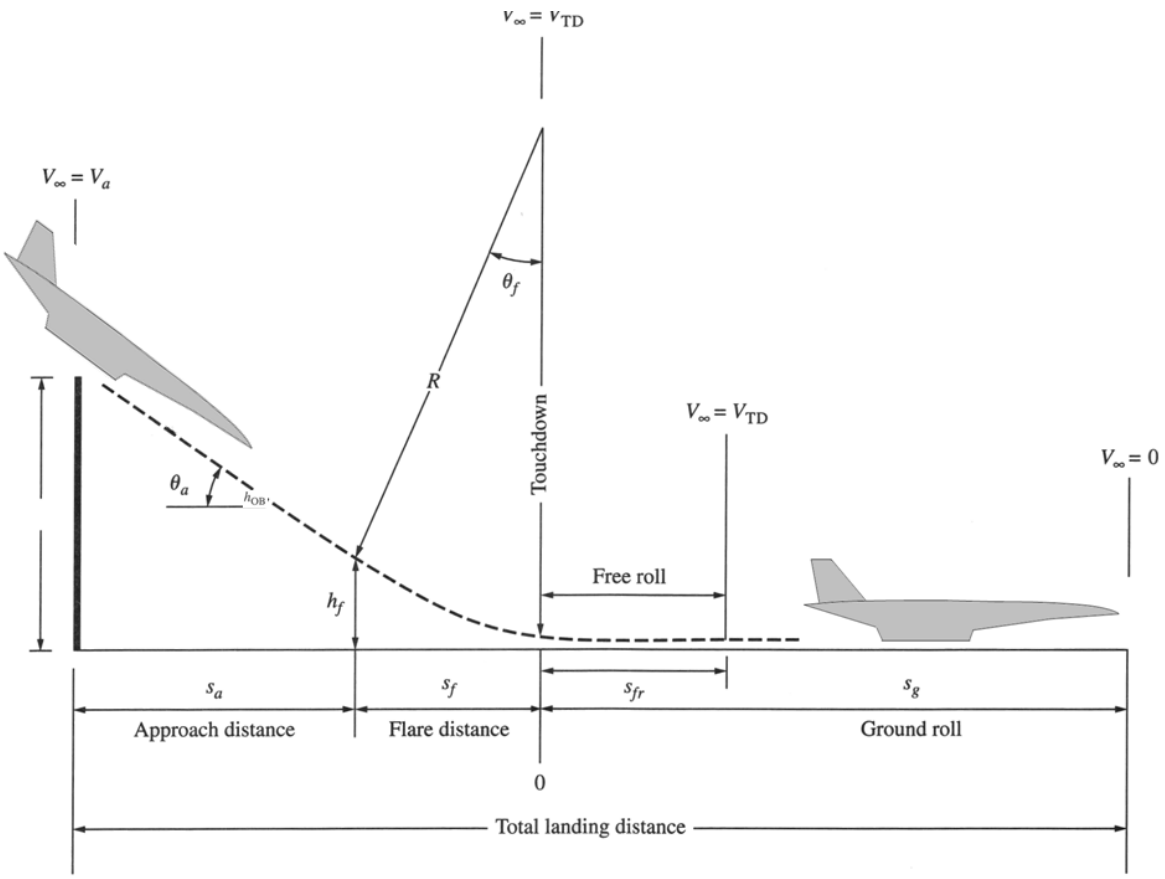

Figure 59: Landing Segments [1]

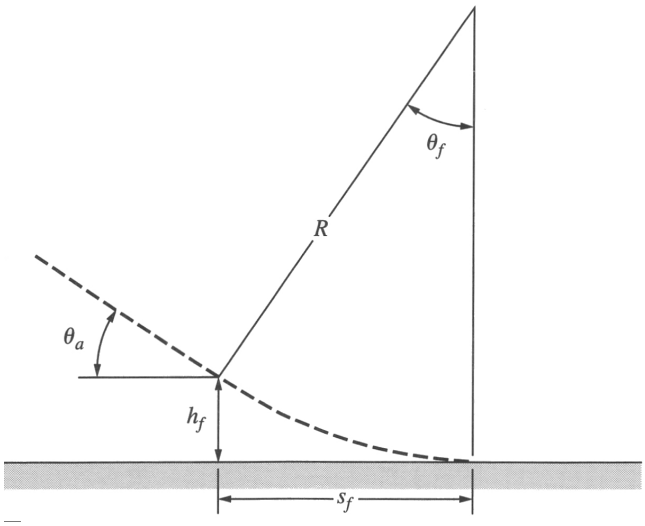

Figure 60: Geometry of Landing Flare [1]

Climb The Jackson Energy Method for climb with acceleration shown in Equation 26 is used to compute the trajectory during the climb segment. This expression assumes the aerodynamic and propulsive forces are constant. The details of this method were presented earlier in Section 2.4.1.3 of the literature review.

The equation is solved by dividing the trajectory segment into a finite set of velocity or altitude intervals and solving for the weight variation incrementally at each of these intervals. These intervals should be set accordingly to more adequately define regions where aerodynamic and propulsive parameters are changing rapidly [71]. Therefore in regions where parameters are rapidly changing as in the case of transonic acceleration, smaller sized intervals should be utilized. The averaged parameters such as dynamic pressure, specific impulse, and aerodynamic coefficients are computed as area averages for each interval. Jackson recommends starting the algorithm with 4 intervals, and halving the interval size until the weight variation is within an accepted limit [41]. In other words, one needs to reduce the interval size until no advantage is gained in accuracy by doing so.

Cruise-Climb The cruise-climb formulation is derived from the equations of motions given in Equations 10-13. These can be linearized and simplified by assuming that the angle of attack, flight path angle, and the engine thrust offset are very small or equal to zero. In

addition, velocity, coefficient of lift, and flight path angle parameters are assumed constant. The simplification of the equations of motion are given in Equations 119-122. These state that the total sum of forces about the point mass is equal to zero.

$$T = D \tag{119}$$

$$L = W \tag{120}$$

$$\dot{y} = V\gamma \tag{121}$$

$$\dot{x} = V \tag{122}$$

The rate of climb dh/dt can be obtained by differentiating the vertical force component in Equation 120 with time as shown in Equations 123-129. Note that the resulting equation for the climb velocity given by Equation 129 has a negative sign because the parameter $d\rho/dh$ is negative, thus the climb velocity is positive. The cruise segment is discretized into finite time intervals and the fuel flowrate of the engine is computed to meet the thrust requirements given in Equation 119. This fuel flowrate can be used to compute the climb velocity with Equation 129. The process is repeated incrementally at each time interval to obtain the flight conditions at the end of the cruise segment, as well as the vehicle weight by subtracting the total fuel burned.

$$\frac{dL}{dt} = \frac{dW}{dt} \tag{123}$$

$$\frac{d\left(\frac{1}{2}\rho V^2 S C_L\right)}{dt} = \frac{dW}{dt} = -\frac{dW_{fuel}}{dt} \tag{124}$$

$$-\frac{1}{2}V^2 S C_L \frac{d\rho}{dt} = \frac{dW_{fuel}}{dt} \tag{125}$$

$$\frac{d\rho}{dt} = -\frac{\frac{dW_{fuel}}{dt}}{\frac{1}{2}V^2SC_L} \tag{126}$$

$$\frac{d\rho}{dt} = \frac{dh}{dt}\frac{d\rho}{dh} = -\frac{\frac{dW_{fuel}}{dt}}{\frac{1}{2}V^2SC_L} \tag{127}$$

$$\frac{d\rho}{dt} = \frac{dh}{dt}\frac{d\rho}{dh} = -\frac{\frac{dW_{fuel}}{dt}}{\frac{1}{2}V^2SC_L} \tag{128}$$

$$\frac{dh}{dt} = -\frac{\frac{dW_{fuel}}{dt}}{\frac{1}{2}V^2SC_L\frac{d\rho}{dh}} \tag{129}$$

Descent A descent trajectory can be predicted by numerical integration of the equations of motion in Equations 10-13. For this case, however, it is assumed that there is no engine thrust and the load factor is varied in order to satisfy the maximum dynamic pressure limit on the vehicle. The engines are assumed to have a fuel flowrate equivalent to that of the given flight conditions using an equivalence ratio of 0.2 [71]. The equivalence ratio is the actual fuel-to-air ratio divided by the stoichiometric fuel-to-air ratio required for complete combustion. The equation for the equivalence ratio is given in Equation 130 [58].

$$\phi = \frac{f}{f_{stoich}} = \frac{(fuel/air)}{(fuel/air)_{stoich}} \tag{130}$$

In the TBCC case utilizing turbojets as the low speed engine and ramjets as the high-speed engine, it is assumed there is no fuel flowrate between the minimum ramjet Mach number and *Mach* 0.8 [71]. In other words, the vehicle becomes a glider once the high-speed engine is turned off until the low speed engine is once again turned back on.

4.2.6.5 Aerothermodynamics

MINIVER is an aerothermal preliminary design tool developed by NASA [28, 29]. This tool was chosen for the computation of the external aerothermal environment because it is a very fast and versatile engineering code which translates well for conceptual design work. It has been used extensively by government and industry and has shown to agree

with more sophisticated codes on various vehicle configurations including the Space Shuttle, HL-20, and X-33 [8]. What makes MINIVER most attractive is its ability to provide time-dependent aerothermal results for the entire mission profile instead of single point flight condition solutions.

The code utilizes a simplified flowfield and geometry to compute the heating profiles along specified streamlines on the vehicle. The simplified flowfield options include: sharp wedge shock angle, sharp cone shock angle, and oblique and normal shock. The shock angles are determined from built-in tables. MINIVER also makes use of approximate heating methods such as Fay and Riddell, Eckert, and Spaldin-Chi with Von Karman Reynolds analogy [28, 29].

The MINIVER input file contains the mission to be flown in a table format of time, altitude, velocity, angle of attack and sideslip angle. Following the mission description is a detailed description of each point which makes up a discretized contour around the vehicle. Each point is described by a block of input parameters which describe inputs such as the x-location, the local slope in degrees from the previous point, flowfield options, heating methods options, and types of outputs desired.

4.2.6.6 Thermal Management System Sizer and Optimizer

The thermal management system will be modeled using TMSS which is a modeling environment developed by the author. TMSS is fully integrated with VSP and MINIVER, and is capable of sizing the TPS for nearly any vehicle and trajectory by solving the 1-D transient heat equation at discrete surface points. The typical runtime for a TMS solution consisting of 14 insulation materials and geometry with 120 discrete computational points is less than 10 minutes. The vehicle geometry is assumed to be symmetrical along the XZ plane. Therefore, only half of the vehicle's surface needs to be sized using TMSS and the solutions can be mirrored on the other half of the vehicle.

The TMSS environment also includes the capability for implementation of heat exchangers to the leading edges. It can predict not only sizing for insulated structures but also the water mass flowrate required for convection cooling (water vaporization) through the heat

exchangers. The aerothermal, sizing, and optimization process for TMSS is provided in Figures 61-62. This figure represents the process within the TMS box in the design structure matrix for the overall modeling and simulation shown in Figure 54.

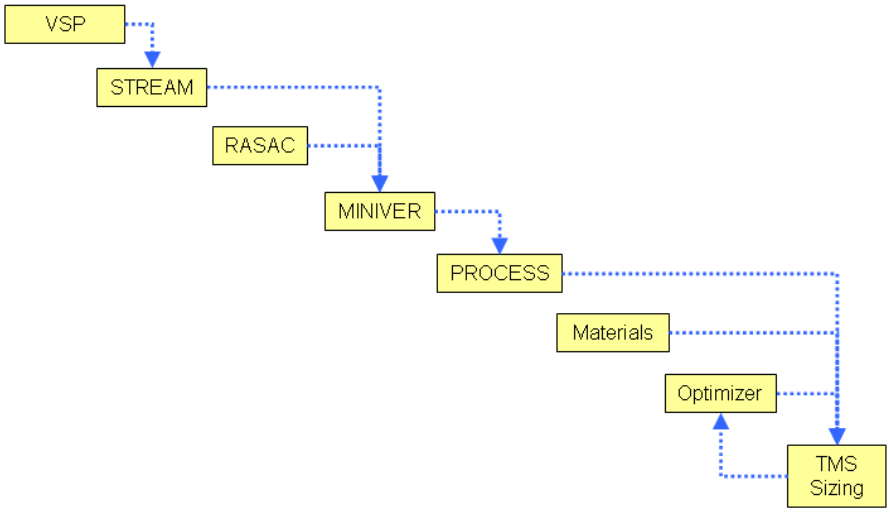

Figure 61: TMSS Design Structure Matrix

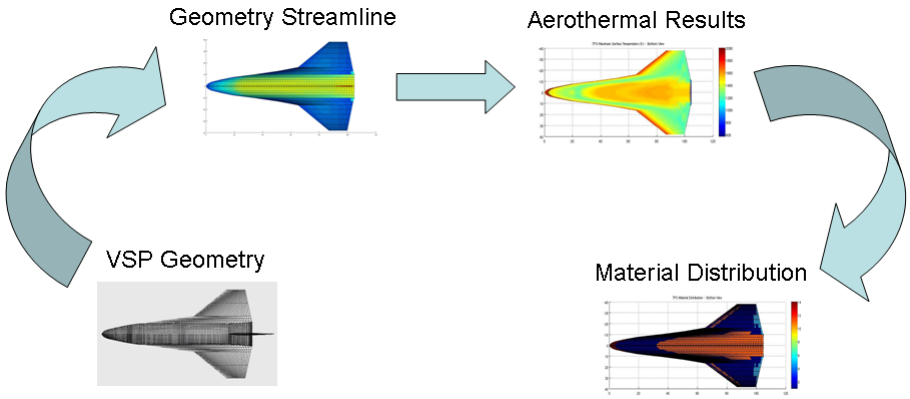

Figure 62: Aerothermodynamic and Material Optimization Process

STREAM The STREAM module is tasked with the following:

1. Read in the mission to be flown
2. Read in 'hermite' geometry out of VSP and generate streamline information
3. Generate MINIVER input files for each streamline

4. Run MINIVER using the input files for each streamline

5. Post-process the output from MINIVER and generate the output files

A sample of this contour at the centerline of sample hypersonic vehicle is shown in Figure 63. The discretized points along these contours are geometrically defined in the MINIVER input file through a run length (x), and local slope (θ) in degrees as shown in Figure 64. These vehicle contours are usually referred to as streamlines.

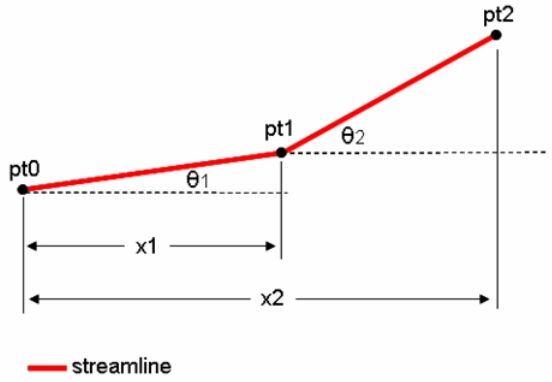

Figure 63: MINIVER's Geometrical Point Inputs

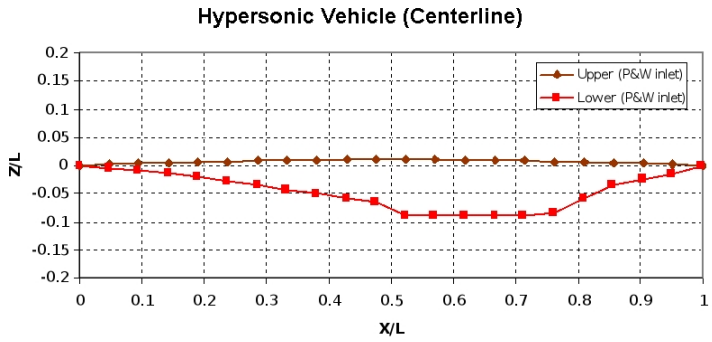

Figure 64: Point Contour in a Streamline

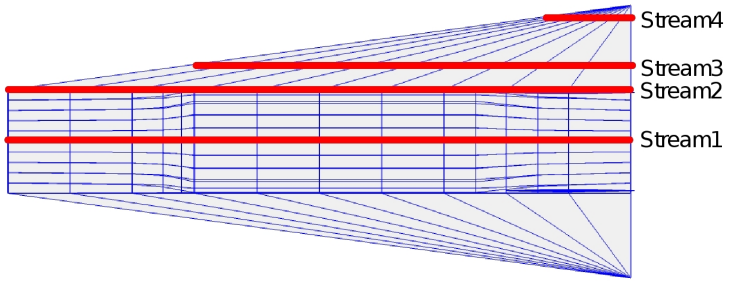

Figure 65: Sample Vehicle Streamline

Each streamline is run through MINIVER using its own input file. TMSS assumes the vehicle is X-Z symmetric, so only half of the vehicle is actually solved by the aerothermal analysis code. The spanwise location of the several example streamlines are shown in Figure 65. However, the streamline locations are specified with a number ranging from (0-1). 'Zero' represents a streamline at the centerline and 'one' represents a stream at the very most outboard section of the vehicle which is typically the wing, but can be any other geometry component.

Once the MINIVER input files are generated, they can be run using a MATLAB script called 'Runminiver'. MINIVER generates an output file for each of the input files or streamlines. Each of the output files will contain detail thermodynamic information for each discrete point on the specific streamline as a function of the mission profile.

PROCESS Once the MINIVER analysis is conducted and the output files are obtained a MATLAB script called 'Process' reads in all the data from the output files for each streamline. The processing script then parses the data and exports it in easier to read tabulated text files containing aerothermodynamics and geometry discretization information. These output and geometry files are used later on by the TMS sizer and optimizer.

TMS Sizing The TMS sizing code solves the 1-D transient heat equation for the sizing of the insulated thermal management systems also known as thermal protection systems. The process by which sizing is performed through the 1-D heat equation was given in more detailed in Section 2.5.2.2 of the literature review. The heatrates are read from the output

of MINIVER, and a material database from NASA's TPSx database is employed [66]. The heat equation algorithm uses Generalized Reduced Gradient to solve the thickness of the insulating material at the surface given the heatrate at each discrete point and the material properties from the database. A numerical algorithm then iterates through every surface point and selects the lightest material solution which still meets the maximum temperature limit of the material. This process determines the entire material distribution over the vehicle's surface.

It is important to note that optimizing the TPS material configuration based solely on weight may not be the best approach because it does not take into consideration the surface smoothness of the vehicle. This thickness discrepancy between neighboring tiles can have a large impact on the aerodynamics of the vehicle and lead to degradation of its performance. Bhungalia et al account for surface smoothness by defining only certain design points over the surface which are optimized for minimum weight while meeting the material temperature limits [7]. The thickness for the rest of the surface points are interpolated from the specified design points using shape functions [7].

The TMS sizing code allows for other technology modules to be added in the future as the need for them arises. The code is capable of defining alternative cooling regions which are typically made of some form of heat exchanger material. Semi-passive and active cooling technologies such as heat pipes and convective vaporization cooling can be applied to these regions once the modeling for the specific technology is developed. The modeling of these technologies is separate from that of the TPS sizing and requires the introduction of new technology modules.

Alternative Cooling System Modeling The sizing methodology for a typical TPS material solution composed of tiles, or blankets presented earlier in Section 2.5.2.2 needs to be slightly modified to be able to properly model those locations on the vehicle where an alternative cooling technology exists such as a heat exchanger. The 1-D transient heat equation shown in Equation 131 is once again applicable. However, the boundary condition at the backplate needs to be modified to account for the removal of heat by the alternative

technology, ie. heat pipe, and vaporization.

$$\frac{\partial T}{\partial t} = \alpha \frac{\partial^2 T}{\partial x^2} \tag{131}$$

A simplified thermal model for a heat exchanger is shown in Figure 66. The external surface boundary condition at (x = 0) and the internal boundary condition at the internal structure (x = L) are given in Equation 132, respectively.

$$q_{conv} - \varepsilon \sigma T_s^4 + \kappa \frac{\partial T}{\partial x} = 0 \quad (x = 0) \tag{132}$$

$$q_{backplate} + \kappa \frac{\partial T}{\partial x} = 0 \quad (x = L)$$

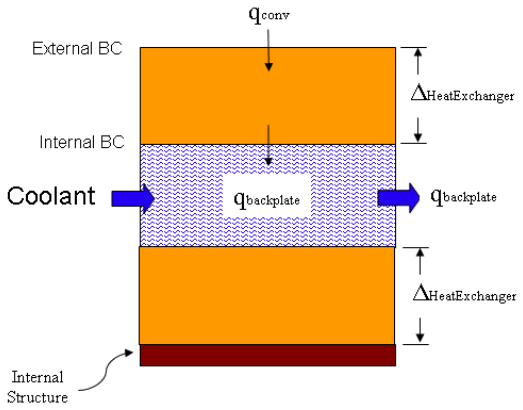

Figure 66: Thermal Model of Alternative Cooling System

The unsteady 1-D heat equation can be discretized as was done earlier using the fully implicit method shown in Equation 133 [22]. The fully implicit discretized formulation in Equation 134 can be obtained by replacing $r = \alpha \frac{\Delta t}{\Delta x^2}$ into Equation 133. The boundary conditions shown in Equations 39-**??** can be also be discretized as shown in Equations 135-136. Note that the heatrates in these equations are all positive by convention since their respective directions have already been accounted for as shown in Figure 66. Recall that the radiative term in the boundary condition at the external surface (Equation 135) introduces a

nonlinear term which means the system of nonlinear equations must be solved by an iterative method such as the Newton-Raphson method.

$$\frac{T_i^{n+1} - T_i^n}{\Delta t} = \alpha \left(\frac{T_{i+1}^{n+1} - 2T_i^{n+1} + T_{i-1}^{n+1}}{\Delta x^2} \right) \tag{133}$$

$$f_i = -rT_{i-1}^{n+1} + (1+2r)T_i^{n+1} - rT_{i+1}^{n+1} - T_i^n = 0 \tag{134}$$

$$f_1 = \left(-\kappa - \varepsilon\sigma\Delta x \left(T_1^{n+1} \right)^3 \right) T_1^{n+1} + \kappa T_2^{n+1} + q_{conv}\Delta x = 0 \;\; (x = 0) \tag{135}$$

$$f_{Nx} = \kappa T_{Nx-1}^{n+1} - \kappa T_{Nx}^{n+1} - q_{backplate}\Delta x = 0 \;\; (x = L) \tag{136}$$

As can be seen, the general method is very similar to that of the TPS sizing. However, in this case the thickness of the heat exchanger which interacts with the outer flow field is specified as a constant. The amount of water boiling required to remove the heatrate entering the internal structure at the backplate of the heat exchanger can be computed using the energy equations 47-48 given earlier in the literature review.

4.2.6.7 Economics

Life cycle cost was chosen as the defining characteristic for the economic dimension of the design space because it is all inclusive. The life cycle cost of the vehicle was computed using the estimating relations given in Appendix **??** which were found in Roskam [79]. The cost relationships for a military vehicle were used as a conservative assumption and they include RDT&E, acquisition and manufacturing, operation, and disposal costs. The author acknowledges that these relations may not be entirely accurate for this application, but in the absence of better cost models they will serve the purpose of providing a better understanding of the interrelationships that exist between economics, performance, and safety. The ultimate goal is not to obtain a high fidelity optimal design point but to demonstrate a methodology that can later be improved with better sources, data, and models.

The life cycle cost for the vehicle needs to account for that of the thermal management system. The life cycle cost for the thermal management system configuration is estimated

using historical data from NASA's TPSx database and the equations given earlier in Section 2.6.2 of the literature review for a 100 flight life.

Heat exchangers for alternative cooling systems in the modeling and simulation are composed of Inconel-617 material. Inconel was chosen because these nickel alloys are good conductors, resistant to oxidation, and thus non-corrosive. The cost of the Inconel heat exchangers was estimated as a nickel heat exchanger rated for a maximum of 150 *psi* and as a function of surface area using the empirical relations found in Matches [56]. For this modeling the heat exchangers are assumed to be able to handle a 100 flight life without replacement or any form of maintenance aside from typical structural airframe tests. This means that the life cycle cost of the heat exchanger will consist simply of the initial price of Inconel heat exchanger. Although this assumption is not entirely accurate, it has been made due to the lack of historical data regarding maintenance, repair, inspection and other related costs of Inconel-617 heat exchangers, or any related high temperature nickel alloy.

When required, the coolant tank cost can also be estimated using the Matches database as a function of tank volume [56]. The tank is modeled as a horizontal fuel storage tank and supports the use of aluminum, copper, and Inconel as the material of choice. However, for this thesis any required coolant tank will be composed of aluminum.

4.2.6.8 Safety

The safety dimension is defined by a safety margin parameter which measures the difference in temperature between the maximum temperature limit of the TPS/TMS material and the mean temperature of the internal structure. A negative safety margin means the mean internal temperature due to a random distribution of thickness failure is greater than the allowable material temperature limit. The greater the safety margin the more likely the material is to survive a failure of the TMS. The flowchart in Figure 67 shows a loss of vehicle event diagram with only the TMS branch expanded to an individual failure cause. Since focus is being placed on the study of TMS, for the purposes of this thesis only the TMS failure branch will be considered in the modeling and simulation of safety. The TMS failure loss event branch shows the two major causes of failure for an insulated type TMS or

TPS to be the result of material debond and debris impact [77]. These two types of failures have been traditionally accounted for through the use of Space Shuttle historical data [77]. Within this thesis, however, an attempt is made to produce a physics-based model that is neither historical-based nor platform dependent.

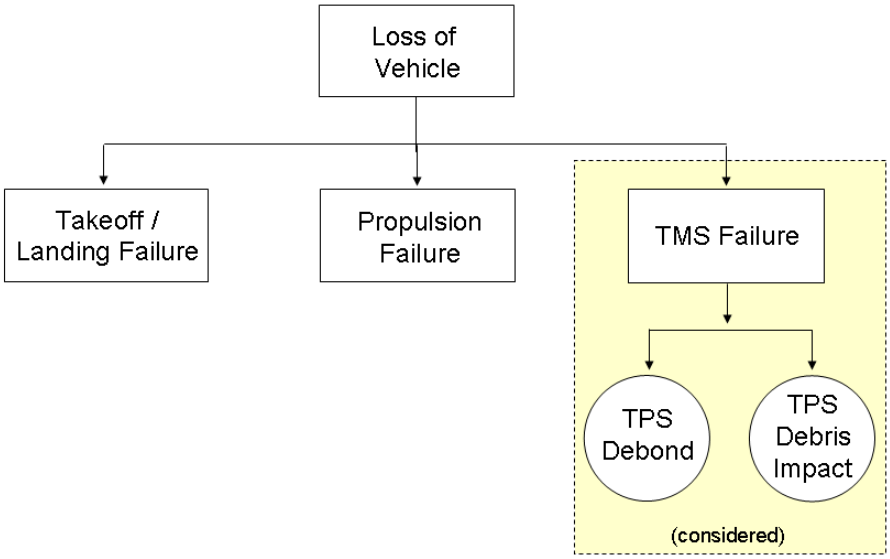

Figure 67: Loss of Vehicle Event Diagram [77]

Debris impact, as the name implies, is a result of a collision in mid-flight or any other event that causes external surface damage and goes unnoticed by maintenance crews. These types of failures usually result in a partial reduction in insulation material thickness or complete destruction of the insulation layer.

In order to better understand this type of failure better one must first analyze the effects of varying thickness on external and internal temperatures for a TPS layer with adiabatic boundary conditions at the internal structure. The study was conducted for a stagnation point on the centerline of the Space Shuttle for the STS1 reentry trajectory. The resulting aerothermal heatrate profile for the stagnation point was computed with MINIVER and is shown in Figure 68. The results of increasing of varying TPS layer thickness of RCC on maximum external and maximum internal temperatures are then shown in Figure 69. This

plot shows that the internal structure below the TPS layer is most susceptible to variations in TPS thickness than the external surface since temperate rate of change with thickness variation is greater for the internal surface. This means that the internal temperature is a key aspect in the evaluation of a safety parameter since it is most likely to be the cause of failure due to damage to the TPS layer.

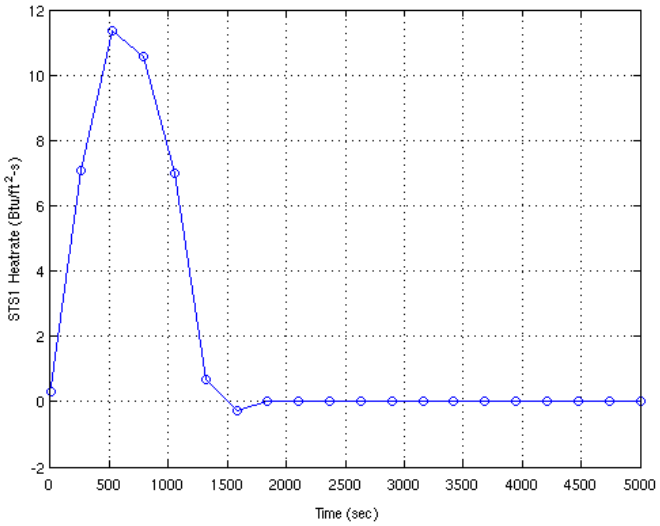

Figure 68: Stagnation Point Heatrate Profile for Thickness Variation Study (STS1 reentry)

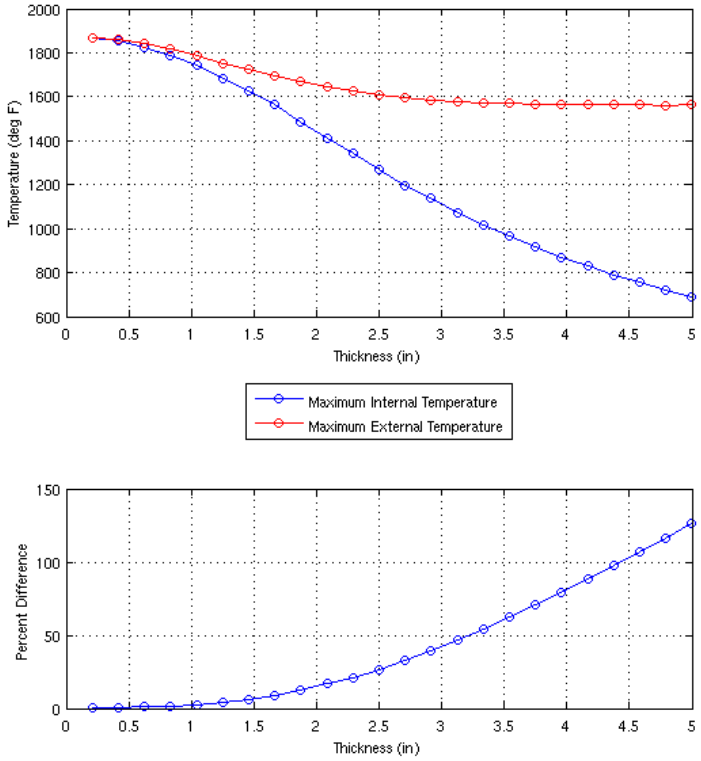

Figure 69: RCC Temperature Change with TPS Thickness Variation (STS1 reentry)

Knowing this, the absolute maximum temperature limit for the internal structure can be defined as its melting temperature. Any cases where the internal temperature is greater than this absolute temperature limit is defined from now on as a catastrophic failure as shown in Figure 71. For the case of a typical aluminum internal structure this absolute temperature limit would be 933.5 Kelvin. The next step is to define a random variable which will be referred to as the thickness failure margin and describes the maximum percent of TPS layer thickness which can be removed before a catastrophic failure occurs as shown in Figure 70. For this problem it is assumed that the probability density function is a uniform distribution as depicted in Figure 38. In order to determine a safety margin, a random variable describing a percent thickness failure of the TPS material is defined with uniform distribution. This percent thickness failure is used to reduce the TPS layer thickness to obtain the thickness failure margin over the entire vehicle and the 1-D transient heat equation is used to compute

the new backplate or internal structure temperature.

A safety margin is computed by subtracting the material temperature limit from the mean internal temperature limit at each point on the vehicle as shown in Equation 137. The greater the value of SM, the more likely the vehicle is to survive a collision or damage to a random point on the external protection. This safety margin will eventually be used as the criteria for the safety dimension of the vehicle's capability-based design space with a maximization objective.

$$SM = T_{limit} - Mean\, T_{internal} \tag{137}$$

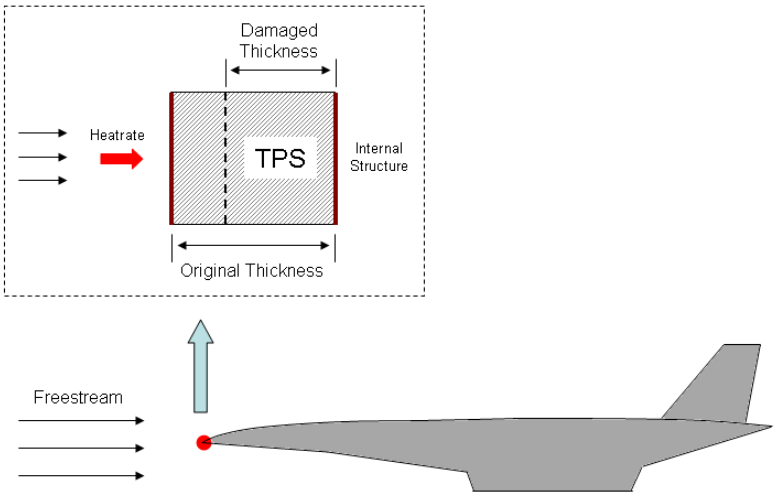

Figure 70: Schematic of Damaged TPS Layer

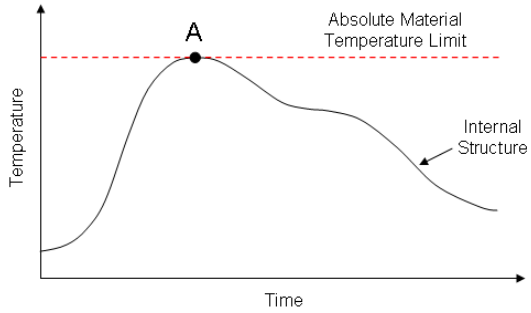

Figure 71: Definition of Catastrophic Failure

The TPS failure due to debonding is not explicitly modeled but accounted for by allowing the uniform thickness distribution to include a zero thickness value which represents a case where the entire TPS layer has fully debonded. The modeling was performed this way because of two main reasons. The first reason is that the implemented model does not rely on any form of historical databases. The disadvantage of this is that no debonding probabilistic characteristics of specific materials are accounted for. The second reason is that the TPS model with an adiabatic wall boundary constraint at the backplate does not allow any heat dissipation into the internal structure. This results in an unrealistically high temperature at the backplate. This means that according to the physics-based heating model, in nearly all TPS debonding cases the internal structure will melt and a catastrophic failure will occur. The Space Shuttle program has proven this is not always the case as TPS debonding has been known to occur in non-critical areas without the loss of the orbiter.

It is also important to note that in some cases an alternative cooling technology which requires the use of some form of heat exchanger instead of the traditional TPS material layer can be used. Since the heat exchangers in the modeling and simulation are composed of a nickel alloy (Inconel-617) which is metallic, the heat exchangers will be assumed non-susceptible to damage from debris as is the case with insulated TPS layers. As a result all discretized points which lie over a heat exchanger on the vehicle are assumed to always have a safety margin based on Equation 138.

$$SM = T_{limit} - T_{h2o_{vaporization}} \tag{138}$$

4.2.6.9 Modeling and Simulation Analysis Limits

The core of the modeling and simulation environment is the trajectory code (RASAC) for air-breathing high-speed vehicles. The main limitations of the modeling and simulation environment hinge on the limits of the aerodynamic and propulsion decks shown in Tables 8-9. In Table 9, the fan pressure ratio, overall pressure ratio, low-speed shock-on-lip Mach number, high-speed shock-on-lip Mach number, throttle ratio, and scramjet capture area are denoted as FPR, OPR, SOL_LS, SOL_HS, TR, Ac, respectively. The proper selection of

disciplinary analysis tools is important in order to ensure their assumptions and limitations meet the requirements of the application and interest of the customer.

Table 8: Aerodynamic Deck Limits

Parameter	Lower Limit	Upper Limit	Units
AoA	-2	8	deg
Mach	0.3	8	

Table 9: Propulsion Deck Limits

	Parameter	Lower Limit	Upper Limit	Units
Turbojet	Altitude	0	90,000	ft
	Mach	0	4	
Scramjet	Altitude	0	100,000	ft
	Mach	2	7	
	FPR	15	30	
	OPR	5	6	
	SOL_LS	2.5	4	
	SOL_HS	4	6	
	TR	300	500	
	Ac	1	1.25	in^2

4.2.7 Surrogate Modeling

The proposed design space exploration environment which will be presented later requires the prediction or identification of the 3-D Pareto frontier for the TMS technologies and configurations being considered. Although the modeling and simulation environment is capable of computing cases in a matter of minutes, it is still not sufficiently fast for the prediction of the Pareto frontiers within the design exploration environment and probabilistic analysis. Benchmarking supporting the need for surrogate models in this design methodology will be provided in more detail in the following section covering the design space exploration.

There are three major components to surrogate model generation including design of experiments, data fitting, and model verification. Numerous candidate techniques and approaches for design of experiments and data fitting were presented in Chapter II. These techniques need to be benchmarked against each other to determine the most suitable candidate for this specific design methodology. The problem that arises when benchmarking the design of experiments and data fitting techniques is that the selection of a design of experiments is directly correlated to the data fitting technique used.

The first thing one needs to remember is that response surface equations are always

preferred over more sophisticated methods such as neural networks and Gaussian processes as long as it can adequately capture the physical behavior. They generally require a lower number of computational runs of the modeling and simulation environment [44]. Response surface equations have been established as a logical starting point for the decision process defined in Figure 72. The diagram shows an initial iteration of RSEs with a model verification and the ability to change the DoE to any of the concepts listed in Table 10 [67]. If RSEs are found to be unsuccessful in modeling the physical behavior, the neural networks and Gaussian processes will be analyzed. Again each of these more sophisticated data fitting techniques will have its own model verification iteration. Various DoE concepts from Table 10 will be considered along with combinations as recommended by Johnson [44]. One of these combinations means using a Latin Hypercube with random points to reduce correlation paired with a two level design for all variables to capture the extreme points of the design. If either neural networks or Gaussian processes are unsuccessful then the clear choice is to use the only technique that was successful. However, if both neural networks and Gaussian processes are found to be successful then a benchmarking process needs to be considered. The principal benchmarking consideration is the total computational time required to not only fit the data but also the time required to run the DoE cases through the modeling and simulation environment since their respective DoE may not be the same.

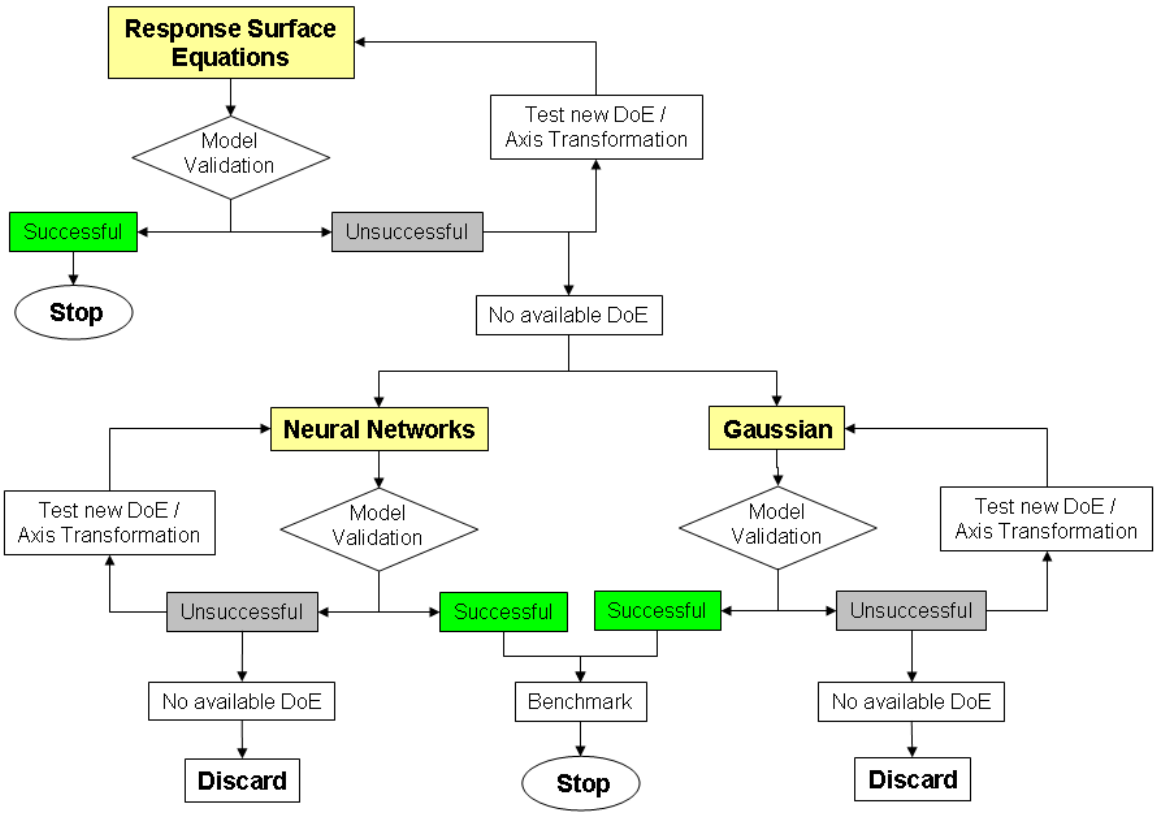

Figure 72: Surrogate Modeling Decision Flowchart

Table 10: Benchmarking of Design of Experiment Designs [67]

Designs / Attributes	Factorial	Central Composite	Box-Behnken	Random	Optimal Designs	Latin Hypercube	Space Filling
Experimenter can specify number of runs	◎	⊘	⊘	●	●	●	●
May be used to fit a wide array of models	◎	◎	◎	●	●	●	●
Design is model independent	⊘	◎	◎	●	⊘	●	⊘
Supports both discrete and continuous variables	◎	◎	◎	●	●	●	●
Orthogonal (effect estimates not correlated)	●	●	●	◎	⊘	⊘	⊘
Computationally cheap to generate	●	●	●	●	◎	●	⊘
Lends well to being sequentially built	●	●	●	◎	●	◎	⊘
Represents all portions of the design space	⊘	◎	⊘	●	◎	●	●
Does not require extrapolation	●	◎	⊘	●	●	◎	●
Can handle constraints on the design space	◎	⊘	⊘	●	●	●	●
Typically avoids most infeasible space	⊘	●	●	◎	⊘	◎	◎
Typically insensitive to failed runs	◎	●	⊘	●	◎	◎	◎
Results used to predict outputs at untried inputs	⊘	◎	◎	●	●	⊘	●

●: Design readily possesses this attribute
◎: Design possesses attribute with limitations or modifications
⊘ Design does not support this capabiltiy or exhibit this attribute

A statistical software developed by SAS, known as JMP, can be used to generate RSEs, neural networks, and Gaussian processes. This will allow a fair benchmarking between neural networks and Gaussian process if they are found to both be adequate and RSEs found to be inadequate. If neural networks are found to be most suitable after benchmarking, a faster and automated tool called BRAINN will be used to develop neural network surrogate models [44].

The surrogate models will define the relationships between the metrics which make up the design space. Due to limitations of the modeling and simulations only certain engineering characteristics such as maximum Mach number, range, and payload can be used as inputs or design variables. The rest of the performance metrics, along with the economic and safety metrics, will be handled as responses. An individual surrogate model will be created for each metric such as LCC, safety margin, TMS weight, and TOGW. These models will become the

core for the design space exploration environment and will facilitate probabilistic studies.

4.2.8 Probability Analysis and Design Space Exploration

This section covers both the probabilistic analysis as well as the definition of the design space exploration environment. The design space exploration will be discussed ahead of the probabilistic analysis despite the probabilistic analysis step being ahead of the design space exploration as stated in the methodology steps. This is done because the selection of the probabilistic analysis will be highly dependent on the approach used for design space exploration.

4.2.8.1 Design Space Exploration

The design space exploration (Pareto-based JPDM) shown in Figure 73 will be performed through the implementation of a 3-D Pareto frontier estimation technique. The process employs surrogate models to capture the behavior of the physics-based analysis tools. With the surrogate models one can now estimate the Pareto frontiers using one of the techniques previously defined in the literature review (NBI or PF). These techniques will be benchmarked and one will be selected later in this section. Once the capability to generate or estimate the Pareto points is achieved, it can employ a probabilistic technique to compute the variability of such Pareto frontiers in the 3-D effectiveness design space (Pareto-Economic-Safety). The 3-D effectiveness design space can then be discretized into cells and the points can then be distributed accordingly into these cells in order to produce a 3-D frequency distribution of the Pareto frontier points. This 3-D frequency distribution space can then be sliced for a specific dimension (performance, economics, or safety) to produce a Pareto-based probability distribution in 2-D for each technology. The right hand side of Figure 73 shows an example of this slicing process for a specific performance effectiveness level and the final result for a Pareto-based JPDM process is demonstrated for three TMS technologies.

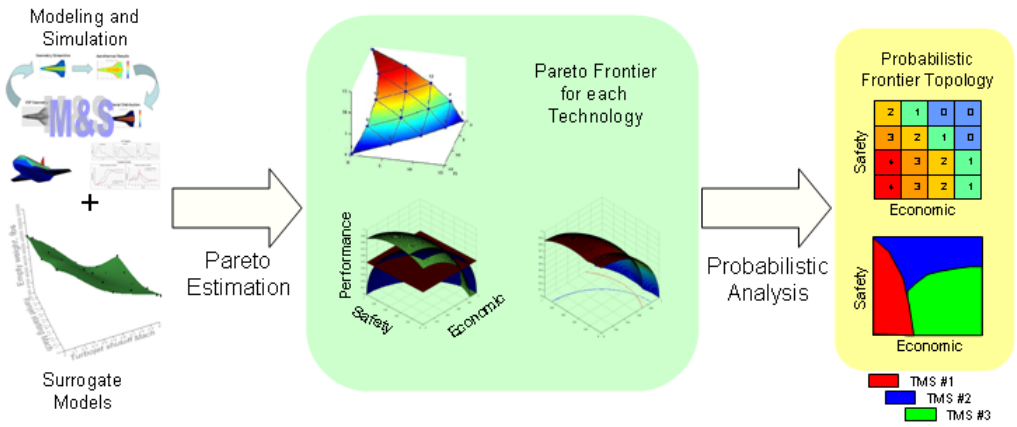

Figure 73: Proposed Design Space Exploration Environment

The proposed Pareto-based JPDM technique is an alternative to traditional JPDM which is capable of producing more information up front to the designer by generating a better 'picture' of the actual probabilistic design space at the cost of greater computational effort. As opposed to JPDM which provides a single point solution with a probabilistic distribution, the proposed Pareto JPDM provides a probabilistic frontier of optimal solutions. The differences in the working process between traditional JPDM and Pareto-based JPDM are given in Figure 74.

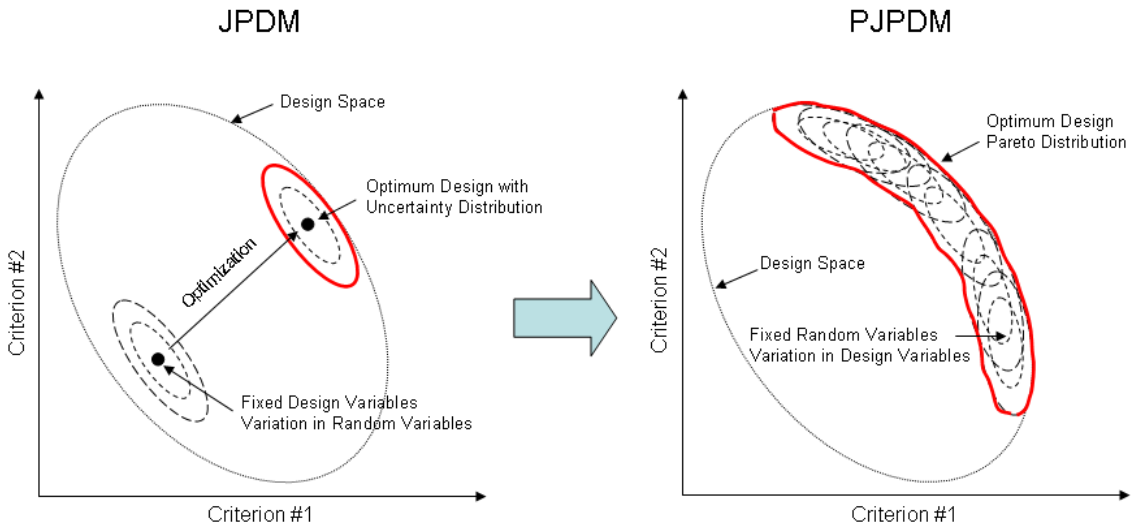

Figure 74: Traditional JPDM and Proposed Pareto JPDM Process Comparison

Benchmarking was performed between the Pareto identification and prediction techniques, NBI and PF respectively, to identify which would be most appropriate. The WS method was not benchmarked because as described in Chapter II, it is highly depended on objective weighting factors and it is difficult to obtain well distributed points on Pareto frontier. The Epsilon-Constraint method was also not benchmarked because as noted in Chapter II, it is similar in nature but less efficient than NBI for 3-D design spaces. The NBI method implements a more intelligent search direction normal to the convex hull which should avoid searching for a Pareto point in the non-feasible region. The 3-D benchmarking problem given in Equation 139 was used to compare NBI and PF on an equal basis. The 3-D problem is essentially that of a sphere with radius equal to 1 and centered at the (0,0,0) origin. The results for total computational time and memory usage for both NBI and PF techniques are given in Figures 75-76 for the sample benchmarking problem. In the case of NBI the discretization parameter (n) represents the number of points assigned along each side of the triangular convex hull and the total number of Pareto points can be computed using Equation 84. However, in the case of PF, the parameter (n) represents the number of points by which each design variable is discretized. However, in the case of Pareto Fitness, this input (n) does not guarantee a specific number of Pareto points and there is unfortunately no way to predict beforehand the total number of points that will be found on the Pareto front as is the case for NBI. Nonetheless, in general the higher (n) is the higher the number of points on the Pareto frontier.

Benchmarking Problem:

$$max: \ \{OEC_1, OEC_2, OEC_3\} \tag{139}$$

$$OEC_1 = r\cos\theta\sin\phi, \ OEC_2 = r\sin\theta\sin\phi, \ OEC_3 = r\cos\phi$$

$$s.t. \ 0 \leq r \leq 1, \ 0 \leq \theta \leq \frac{\pi}{2}, \ 0 \leq \phi \leq \frac{\pi}{2}$$

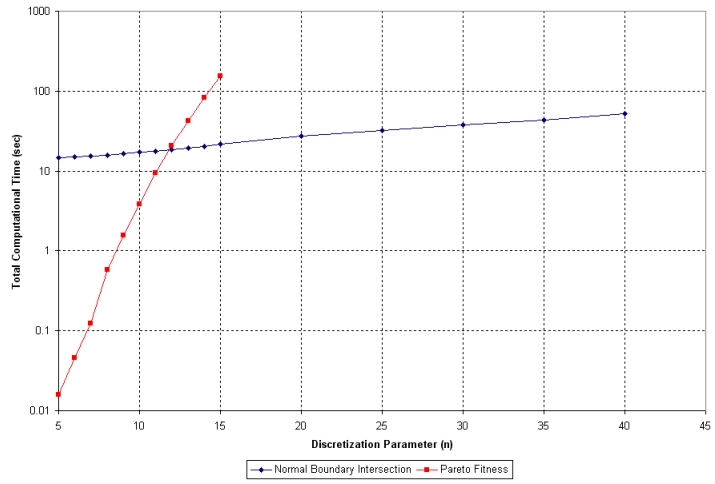

Figure 75: Comparison of Computational Time for Pareto Estimation Techniques

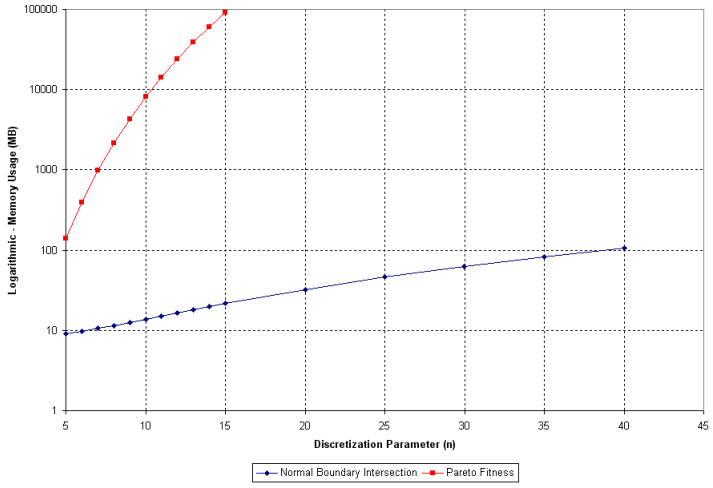

Figure 76: Comparison of Memory Usage for Pareto Estimation Techniques

Pareto Fitness can be very useful for applications where a large technology catalog is represented with two-level discrete variables (on/off settings) and less practical for problems with a large number of continuous variables. The plot in Figure 75 shows that Pareto Fitness in its present state is the better answer for problems with small discretized points ($n < 12$) and small number of continuous variables. Normal Boundary Intersection, on the other hand, is a clearly preferred in terms of scalability, memory usage, and computational time. By utilizing Normal Boundary Intersection, one can significantly increase the discretization parameter, and at the same time greatly improve the accuracy by producing more points on

the Pareto surface. The computed Pareto frontiers obtained through each method for the sample problem are shown in Figures 77-78.

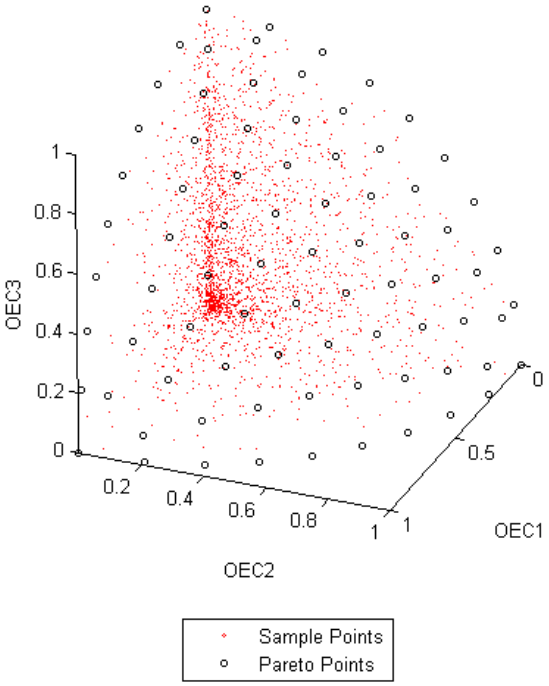

Figure 77: Pareto Frontier from Normal Boundary Intersection

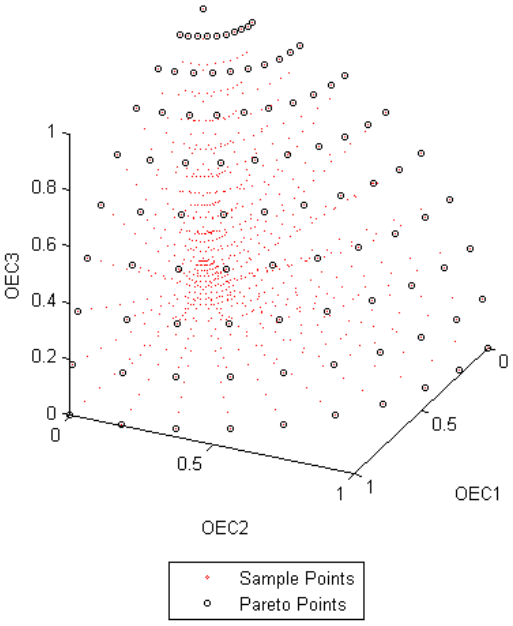

Figure 78: Pareto Frontier from Pareto Fitness

There is unfortunately an inherent disadvantage with NBI which is not visible in these benchmarks and appears when solving more complex design spaces as opposed to the trivial problem of the spherical design space. As mentioned earlier in the literature review, the optimizer on which NBI relies has to work with a very restrictive feasible domain consisting of a single line in a 3-D space. This guarantees that the optimizer is almost always working in the unfeasible domain or approaching the optimum solution from the unfeasible region. This is not only bad practice but it also guarantees that the starting point will almost certainly be unfeasible. In a highly complex problem this can cause the optimizer to never find its way back to the feasible domain, and thus no true Pareto point is found.

Knowing this caveat regarding NBI and realizing the design space complexity of the problem at hand, the author decided to utilize Pareto Fitness as the Pareto identification technique. In comparison to Normal Boundary Intersection, the selected Pareto Fitness provides a more robust algorithm at the expense of computational effort for bigger problems with a higher number of design variables. In addition to this, PF is capable of handling concave or convex frontiers perfectly well. Finally, Pareto Fitness will allow the entire design space exploration process to have no requirement or need for numerical optimization.

The vehicle's capability design space will be formed by three overall evaluation criteria for performance, cost, and safety effectiveness characteristics given in Equations 140-142. These engineering characteristics that make up the OEC were determined by the earlier step which mapped voice of customer to voice of engineer through the house of quality. The top four engineering characteristics found for the performance aspect of the design were 1) maximum Mach number, 2) range, 3) block time, and 4) payload. Maximum Mach number was eliminated from use in the OEC since it does not constitute a true measure of system effectiveness. Maximum Mach number is inherently accounted for within block time and the ultimate interest of the customer is how fast he can transport or get from one point to another. Knowing this, a productivity parameter was identified as the performance OEC which includes the remaining top three engineering characteristics 1) range, 2) block time, and 3) payload as shown in Equation 140.

$$OEC_{performance} = \alpha\left(Productivity\right) = \alpha\left(\frac{Range * Payload}{BlockTime}\right) \tag{140}$$

$$OEC_{cost} = \theta\left(LCC\right) \tag{141}$$

$$OEC_{safety} = \vartheta\left(SafetyMargin\right) \tag{142}$$

A 3-D Pareto frontier will be approximated for each technology based on the three competing objectives denoted by the OEC presented in Equations 140-142. After the Pareto frontiers are generated one can slice the design space for a given value of the performance OEC to obtain a 2-D design space based on the Economic-Safety objectives. The same can be done for a 2-D cross-section of Performance-Economic or Performance-Safety by fixing values of safety and economic OEC, respectively. This 2-D plot will provide a mapping of how the different technologies stack up against each other on the design space. This process can be integrated with a probabilistic process to develop the same 2-D maps but on a probabilistic fashion by assigning variability to the design variables and using the surrogate models to quickly evaluate the responses which make up the design space. The 2-D maps can be discretized as shown on the right hand side of Figure 73 and the frequency of occurrence of Pareto frontier at each cell is recorded. Once the probabilistic study is completed and all occurrences or frequencies are recorded at each appropriate cell in the design space, one can generate a 3-D topology of the occurrences on the 2-D maps for Economics-Safety, Performance-Economics, or Performance-Safety. After superimposing the occurrence topology for each thermal management technology on a given 2-D map one can obtain a probabilistic Pareto frontier which allows for more robust decision making when it comes to the selection of technologies.

4.2.8.2 Probability Analysis

As one can recall from the literature review, there are three main approaches to conducting probabilistic analysis. These probabilistic approaches were defined in Figure 37 and are

repeated below for convenience. A benchmarking exercise is required in order to identify which of these approaches will be the most adequate for the present application.

1. Sophisticated Analysis Code + Monte Carlo
2. Surrogate Models + Monte Carlo
3. Sophisticated Analysis Code + Fast Probability Integration

The third probabilistic method using sophisticated analysis codes and Fast Probability Integration can be immediately eliminated from consideration because it aims at producing the curve for the CDF. However, what is needed for the probabilistic design space exploration environment in Figure 73 is a measure of frequency of occurrences of the Pareto frontier on the 3-D design space. Knowing this, the first two probabilistic methods including 1) sophisticated analysis codes with Monte Carlo simulation, and 2) surrogate modeling with Monte Carlo simulation were benchmarked against each other using once again the spherical design space example given earlier. The results are provided in Tables 11-12 and plotted in Figure 79. The trends in Figure 79 show that the second method consisting of response surface methodology and Monte Carlo simulation is the clear winner due to its total computational time requirements even though the sophisticated analysis codes are assumed to run very quickly at only five minutes (Table 11). In reality a sophisticated analysis code such as CFD can take hours if not days to run a single point solution. This further makes the case for the need to implement surrogate models into the design methodology if a probabilistic analysis of the design space is to be successful.

Table 11: Computational Time Benchmark for Sophisticated Analysis Code and Monte Carlo Simulation

	Normal Boundary Intersection			Pareto Fitness		
Discretization Paremeter (n)	Total Function Calls	Total Computational Time (min) (single case)	Total Computational Time (hr) (10000 cases)	Total Function Calls	Total Computational Time (min) (single case)	Total Computational Time (hr) (10000 cases)
5	2343	5.00	1952500	375	5.00	312500
6	3018	5.00	2515000	648	5.00	540000
7	4023	5.00	3352500	1029	5.00	857500
8	4548	5.00	3790000	1536	5.00	1280000
9	5358	5.00	4465000	2187	5.00	1822500
10	6348	5.00	5290000	3000	5.00	2500000
11	7671	5.00	6392500	3993	5.00	3327500
12	8346	5.00	6955000	5184	5.00	4320000
13	9399	5.00	7832500	6591	5.00	5492500
14	10374	5.00	8645000	8232	5.00	6860000
15	11364	5.00	9470000	10125	5.00	8437500
20	17169	5.00	14307500	24000	5.00	20000000
25	24696	5.00	20580000	46875	5.00	39062500
30	33876	5.00	28230000	81000	5.00	67500000
35	44694	5.00	37245000	128625	5.00	107187500
40	56934	5.00	47445000	192000	5.00	160000000

Table 12: Computational Time Benchmark for Response Surface Methodology and Monte Carlo Simulation

	Normal Boundary Intersection		Pareto Fitness	
Discretization Paremeter (n)	Total Computational Time (sec) (single case)	Total Computational Time (hr) (10000 cases)	Total Computational Time (sec) (single case)	Total Computational Time (hr) (10000 cases)
5	14.58	40.49	0.02	0.04
6	14.94	41.49	0.05	0.13
7	15.33	42.58	0.13	0.35
8	15.75	43.75	0.58	1.61
9	16.30	45.27	1.55	4.30
10	17.13	47.57	3.89	10.81
11	17.64	49.00	9.39	26.09
12	18.58	51.61	20.77	57.68
13	19.38	53.82	42.56	118.23
14	20.20	56.12	82.53	229.25
15	21.88	60.76	153.17	425.47
20	27.52	76.43		
25	32.11	89.19		
30	37.49	104.13		
35	43.41	120.57		
40	52.72	146.44		

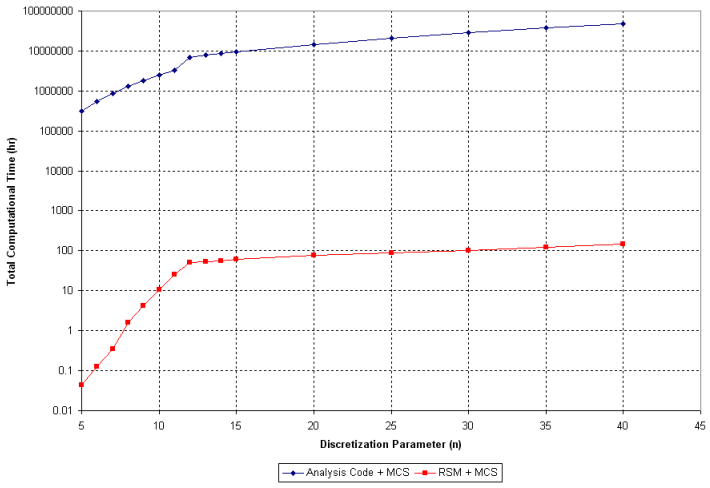

Figure 79: Probabilistic Analysis Benchmark

4.2.9 Inverse Design Space Resolution

The Pareto-based JPDM design space exploration environment described above will provide a design solution for a desired level of effectiveness. This level of effectiveness will be comprised of performance, economics, and safety effectiveness. Once the customer or designer has selected the 'optimal' solution or level of effectiveness for all three dimensions of the design space, a numerical optimizer can be employed to solve for the inverse design space. This inverse design space is based on the original design variables (range, maximum Mach, payload) which describe the actual capability of the vehicle. This will help link vehicle capabilities to TMS technology subsystems in a top-down approach.

The formulation for this problem is loosely based on non-preemptive Goal Programming with equal weighted deviations. The numerical optimization formulation is given in Equation 143. In these equations f is the predicted or current optimizer solution vector, f^* is the optimum solution vector chosen by the designer, N is the total number of dimensions (in this case equal to 3), and ε is a Euclidian distance tolerance.

$$min: \ obj = \sqrt{\sum_{i=1}^{N} (f_i - f_i^*)^2} \tag{143}$$

$$s.t. \sum_{i=1}^{N} (f_i - f_i^*)^2 \leq \varepsilon, \ \ i = \{1, 2, .., N\}$$

$$X_{i,min} \leq X_i \leq X_{i,max}, \ \ i = \{1, 2, .., N\}$$

$$\text{Where: } f = f(X)$$

The optimizer manipulates the controllable design variables denoted by X (range, maximum Mach, payload) in order to minimize the distance or offset from the current solution to the chosen 'effectiveness' solution. Only design variable values that are within the feasible domain are selected and used within the inverse design space. It is important to remember that there is a confounding of effects within the productivity index which makes up the performance effectiveness dimension. This means that there is a large number of non-unique

solutions for range, maximum Mach, and payload that can meet the selected effectiveness levels. A Monte Carlo simulation is implemented in order to populate the design space with a large sample of these non-unique solutions. Multivariate plots can then be created by plotting the resulting values for the design variables with respect to each other.

4.3 Proposed Case Study

A case study based on a recent TBCC joint effort between Pratt & Whitney and ASDL will be used to put into practice the proposed conceptual design methodology [71]. The original effort was intended to help guide investment decisions for Pratt & Whitney by understanding the impact of key design parameters for a TBCC aircraft. The project's main focus was propulsion guided decision making however the end result was a closed TBCC vehicle which was thoroughly scrutinized and validated. This closed TBCC vehicle shown in Figure 80 will serve as the test bed and baseline for the application of thermal management technologies. The mission requirements for the case study are given in Table 13. In addition, the limits for the design and noise variables which make up the three effectiveness objectives (performance, economics, safety) are defined on Table 14. These limits will also be important during the generation of the design of experiment.

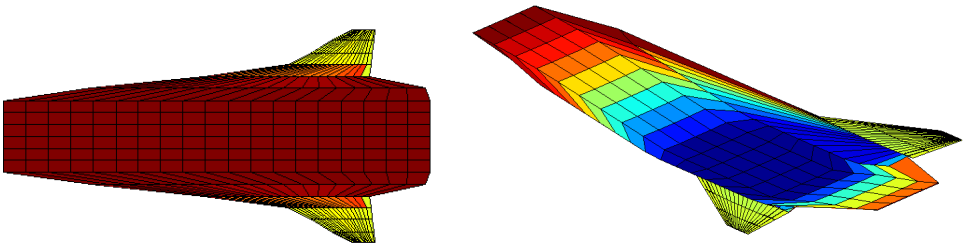

Figure 80: Closed TBCC Vehicle

Table 13: Mission Segment Requirements for Proposed Case Study

Mission Segment Requirements	
1	Takeoff
2	Climb
3	Cruise
4	Turn
5	Descent
6	Landing

Table 14: Design and Noise Variable Limits

	Variable Name	Lower Limit	Upper Limit	Units
Design Variables	Range	1500	3000	nmi
	Mach	4	6.5	
	Payload	0	5000	lbs
Noise Variables	Fuel cost	100	200	$/barrel
	Thickness failure	0	100	%

The propulsion system used for the TBCC vehicle consists of a turbojet engine intended for 'low' speeds and a scramjet engine intended for 'high' supersonic and hypersonic speeds. A specialized inlet geometry configuration allows the transition from turbojet to scramjet power. There are three major propulsive operation states including i) turbojet only, ii) turbojet and scramjet, and iii) scramjet only as depicted in Figure 81-83, respectively. The baseline engine configuration parameters including the fan pressure ratio, overall pressure ratio, low-speed shock-on-lip Mach number, high-speed shock-on-lip Mach number, throttle ratio, and scramjet capture area are provided in Table 15. In addition, the transition Mach numbers are chosen to be $[3.5, 2.5]$ where $Mach$ 3.5 is the Mach number where the turbojet is shut down and $Mach$ 2.5 is the Mach number where the ramjets are turned on. The vehicle consists of one turbojet engine and four ramjet 'rubberized' engines. It is also important to note that a technology k-factor equal to 0.4 was applied to the aerodynamic drag coefficients (k_1, k_2, C_{D_o}) from Equation 144 in order to be able to expand the design space.

$$C_D = C_{D_o} + k_2 C_L + k_1 C_L^2 \tag{144}$$

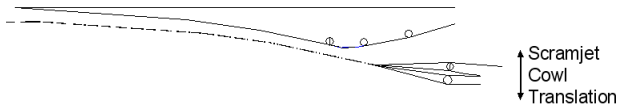

Figure 81: Turbojet Only Configuration

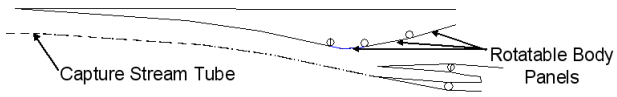

Figure 82: Turbojet-Scramjet Configuration

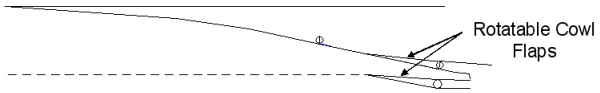

Figure 83: Scramjet Only Configuration

Table 15: Propulsion Parameters for Proposed Case Study

Parameter	Setting
FPR	6.0
OPR	20
SOL_LS	3.0
SOL_HS	5
TR	1.25
Ac	400.0

It is important to note the high degree of interrelationships that exist in high-speed air-breathing vehicles with highly integrated aerodynamics and propulsion systems. One must be able to account for the effects of aerodynamics on propulsion and vice versa. For the TBCC case study the accounting of both aerodynamic and propulsive forces is shown in Figure 84. These trajectory analysis code assumes the vehicle forces are applied to a single point mass. The net propulsive force (NFP) also known as the installed thrust can be computed with Equation 145 [71].

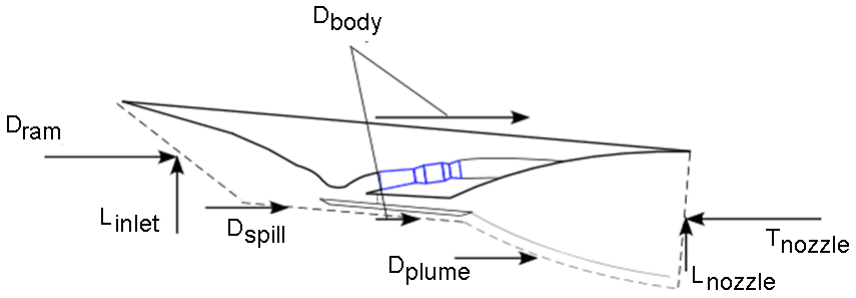

Figure 84: Aerodynamic and Propulsive Accounting of Forces

$$NPF = \left[FG_{sj} - D_{ram_{sj}} - D_{spill_{sj}}\left(\frac{AC_{total}}{AC_{sj}}\right)\right] + \left[FG_{tj} - D_{ram_{tj}} - D_{spill_{tj}}\right] \qquad (145)$$

$$D_{spill_{tj}} = 0, \textit{ during dual turbojet and scramjet operation}$$

$$AC_{total} = AC_{sj} + AC_{tj}$$

$$D_{spill} = D_{spill_{sj}} \left(\frac{AC_{total}}{AC_{sj}} \right)$$

$$D_{ram} = D_{ram_{sj}} - D_{ram_{tj}}$$

Where:

AC_{total} - total capture area

AC_{sj} - scramjet capture area

AC_{tj} - turbojet capture area

D_{body} - body drag

D_{plume} - plume drag

$D_{ram_{sj}}$ - scramjet ram drag

$D_{ram_{tj}}$ - turbojet ram drag

$D_{spill_{sj}}$ - scramjet spillage drag

$D_{spill_{tj}}$ - turbojet spillage drag

FG_{sj} - gross thrust of scramjet

FG_{tj} - gross thrust of turbojet

L_{inlet} - inlet lift

L_{nozzle} - nozzle lift

T_{nozzle} - nozzle thrust

It will be assumed that the customer is ultimately interested in determining the thermal management technology and configuration which provides the best performance, economic, and safety effectiveness on an equal importance weighting. In addition, the customer requires

the decision making to be robust and insensitive to noise and other variables which are out of his/her control, such as cost of fuel and TPS failures.

Chapter V

MODELING VALIDATION

The validation of the modeling and simulation was divided into four tasks: aerodynamics, trajectory and vehicle sizing, aerothermodynamics, and thermal management system sizing. Validation data was provided by literature sources or was generated directly by the author in cases where validation data sources were not available.

5.1 Aerodynamics

NASCART Euler solutions were validated through comparison to experimental data for a simple cone geometry with a 9° half-angle as shown in Figure 85. The experimental aerodynamic data for the cone geometry shown in Figure 86 was found in Bertin [6] and consists of flow conditions of Mach 6.77 and a Reynolds number of $1.35x10^5$ per inch. A total of four Euler computational cases were obtained for the angles of attack of 0°, 10°, 20°, and 30°. Recall that Euler equations can be derived from the Navier-Stokes equations by neglecting viscous effects and thermal effects.

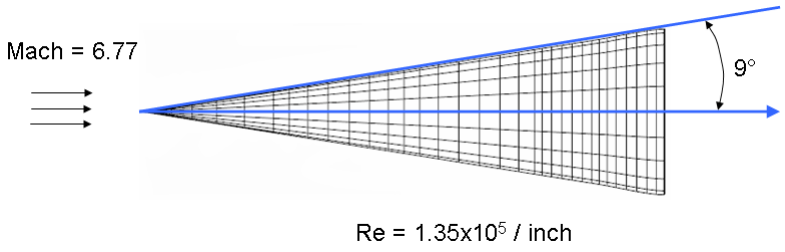

Figure 85: Validation Geometry

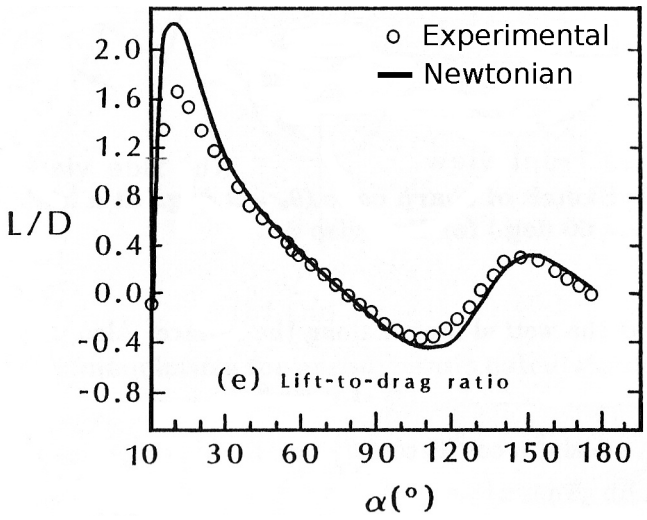

Figure 86: Experimental and Computational Aerodynamic Data for Cone Geometry

The NASCART computational grids for all four validation cases were approximately $4x10^5$ cells. The grids were generated with 256 grid points along the longest body dimension, and a value of $1x10^{-3}$ for the smallest body thickness (normalized by longest body dimension). Two example computational grids are shown in Figures 87-88 for the 0° and 30° angles of attack cases, respectively. Grid adaption was started at iteration number 500 and repeated every 100 iterations after that up to iteration number 1,500.

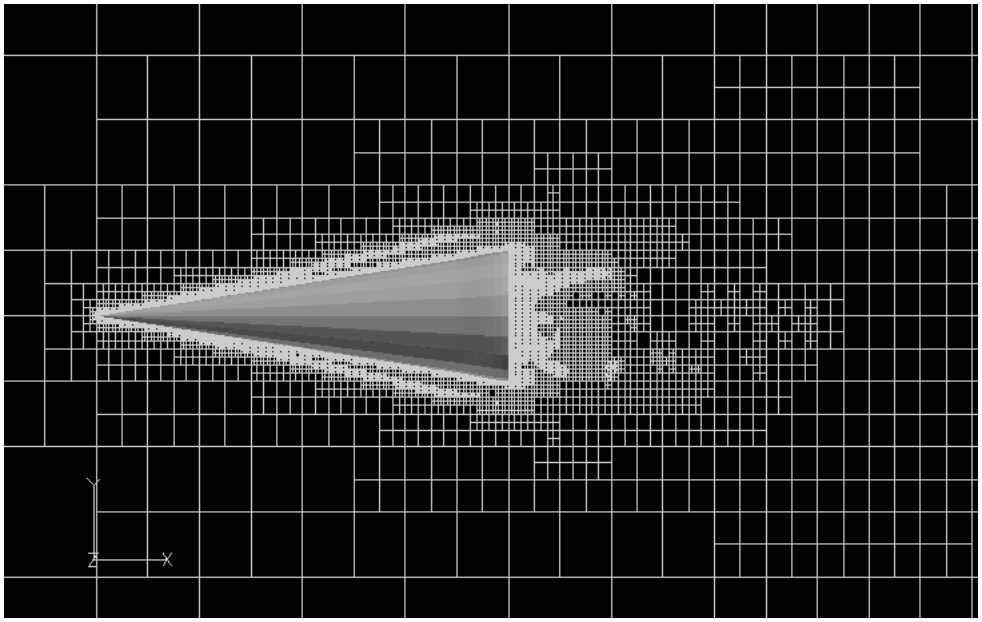

Figure 87: Computational Grid for 9° Half-Angle Cone at 0° AoA

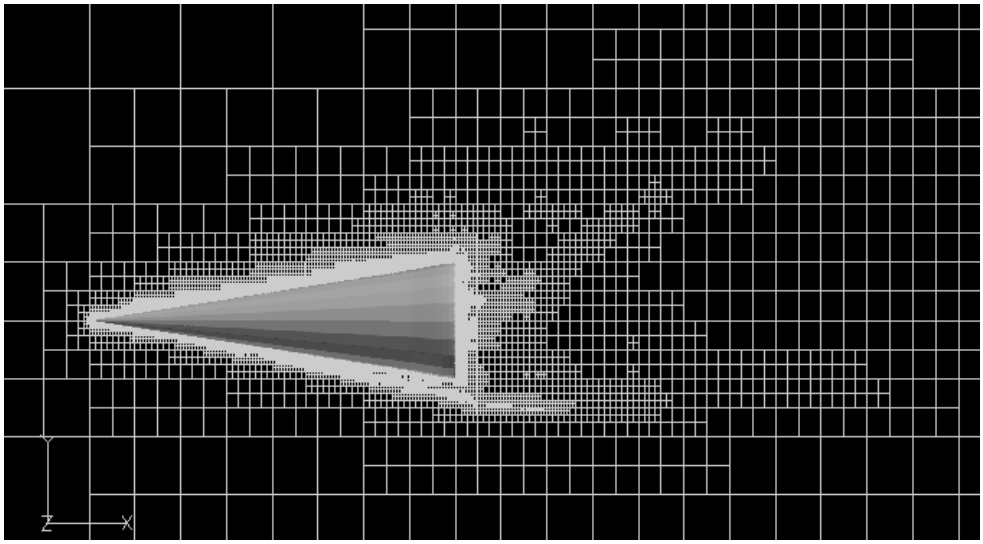

Figure 88: Computational Grid for 9° Half-Angle Cone at 30° AoA

Lift-to-drag (L/D) ratio comparisons were performed for the purpose of validation. Lift-to-drag ratio is useful because it does not require knowledge of the reference area used to normalize the coefficients of lift and drag. The percent error for the lift-to-drag ratio between the Euler and experimental data is given in Table 16 and the results are plotted in Figure 89. The four validation cases are denoted by the blue markers and show adequate agreement with experimental data. The convergence histories of residual RMS and L/D versus iteration for the case with AoA of 10° are shown in Figures 90-91, respectively.

Table 16: Comparison of Aerodynamic Validation Cases

AoA (deg)	Euler L/D	Experimental L/D	Percent Error
0	0.00	-0.08	-
10	2.04	1.62	26.01
20	1.58	1.38	14.90
30	1.14	1.09	5.21

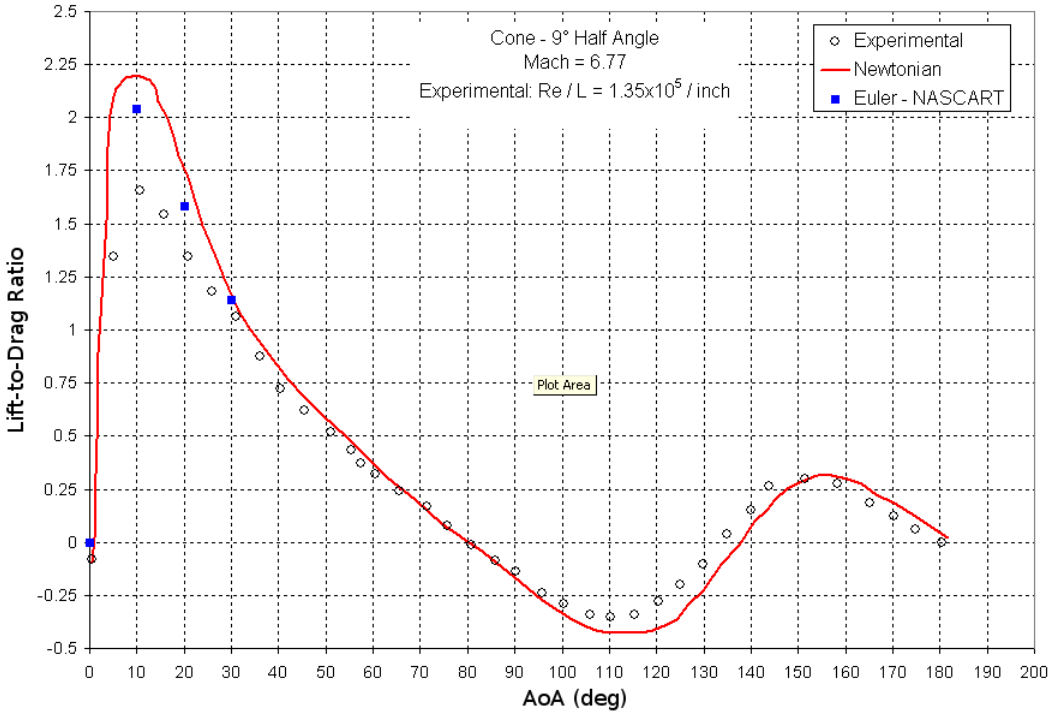

Figure 89: Lift-to-Drag Ratio Validation

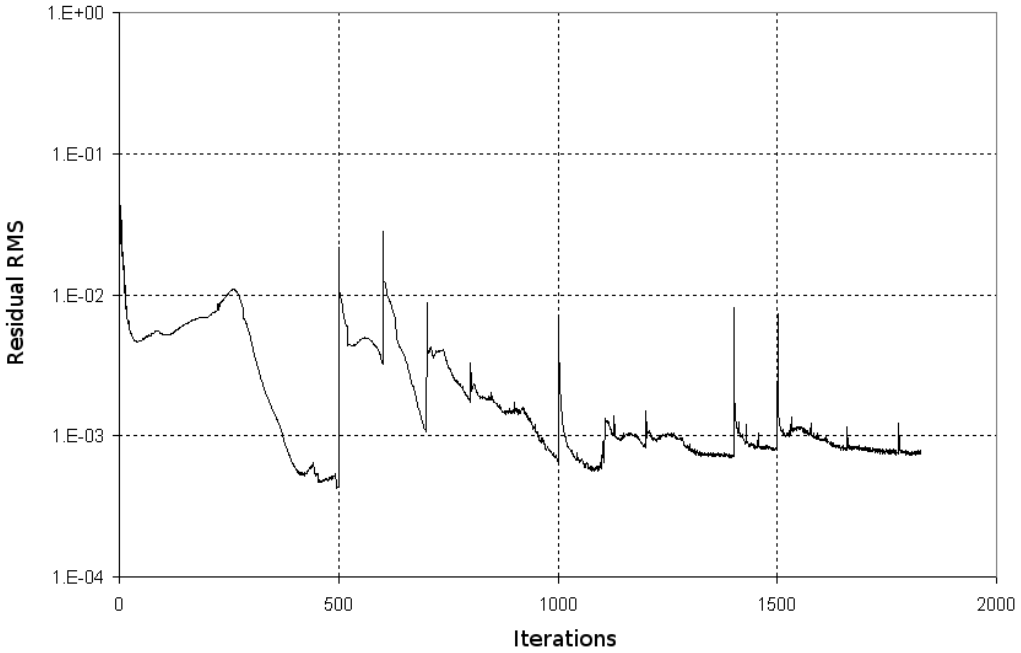

Figure 90: Convergence of Residual RMS for AoA of 10°

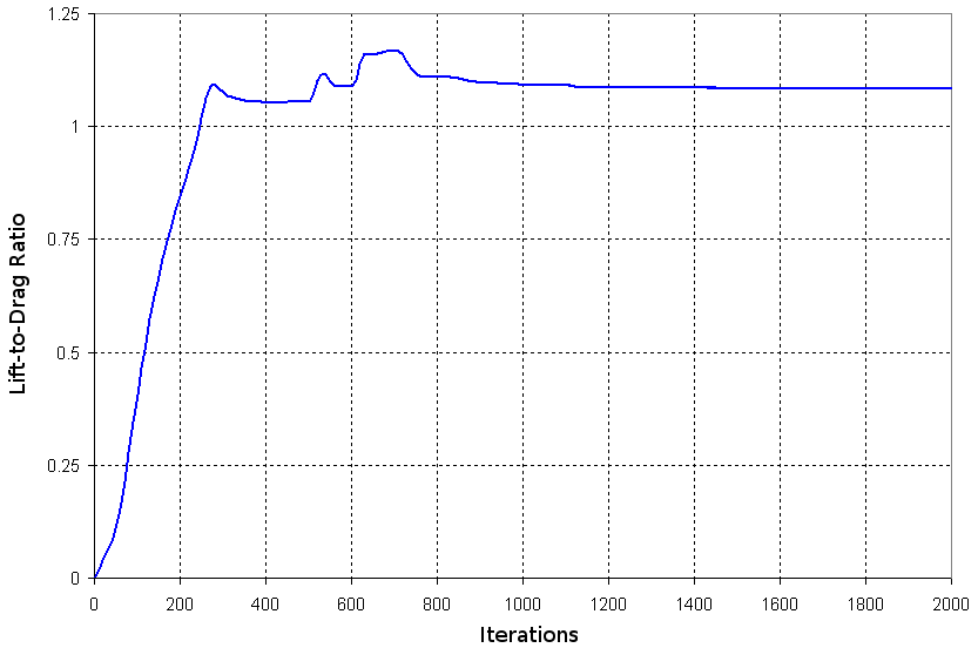

Figure 91: Convergence of Lift-to-Drag Ratio for AoA of 10°

As expected, the Euler solutions provide more accurate aerodynamic solutions than Newtonian theory denoted by the red curve. The error is likely due to the limitations of the Euler equations stated earlier regarding the neglection of viscous and thermal conduction effects. In addition, Euler solutions can also produce poor results if large flow separation regions exist [81]. This is likely the reason for the larger error values along the 10° to 20° angle of attack range. However, at low and beyond 30° angle of attack, the computational and experimental solutions converge as the cone geometry begins to resemble a blunt-shaped object and the separation region decreases in size. Fortunately, the TBCC case study vehicle will not be required to fly at such extreme angles of attack where flow separation becomes more relevant. The angle of attack for the cruise segment of the TBCC vehicle is nearly always less than 4°.

5.2 Trajectory and Vehicle Sizing

First a validation of the trajectory code and vehicle sizing has be performed based on historical data obtained for the XB-70. An existing mission from the XB-70 program was used along with reported aerodynamic characteristics found in Feagin 1978 [32]. In addition,

an engine deck produced by Pratt & Whitney meant to reproduce the performance of the XB-70's GE YJ-93 engines was be utilized. The mission segments for the XB-70 mission are given in Table 17. Aerodynamic drag polars for the XB-70 for a range of Mach numbers are given in Figure 92 [91].

Table 17: XB-70 Mission Segments [91]

Mission Segment Description
1 Takeoff at sea level
2 Climb to cruise Mach number
3 Cruise 3489 nmi at Mach 3 best cruising altitude
4 Loiter 16 min at 20,000 ft
5 Loiter 9 min at sea level
6 Landing at sea level

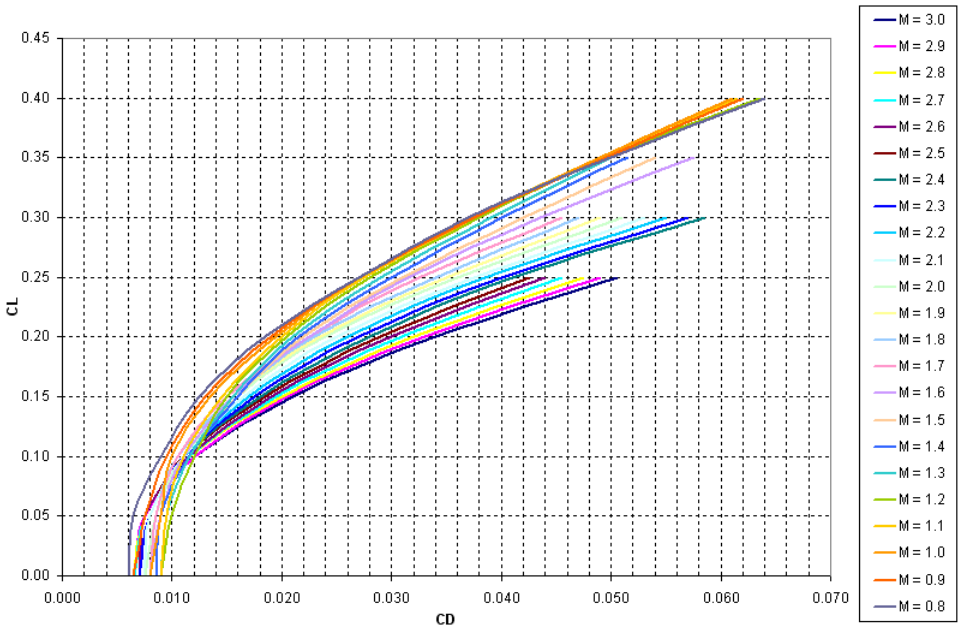

Figure 92: XB-70 Drag Polar [91]

Rapid Access to Space Analysis Code (RASAC) was used to size the vehicle given the previously defined mission, along with the aerodynamic and engine decks. The resulting sizing data for total gross weight, total fuel weight, time to 20,000 feet, time to acceleration altitude, total mission time, total range, initial cruising altitude, and takeoff and landing field lengths are shown in Table 18. The table also shows a direct comparison of existing historical data from the XB-70 program and the RASAC results. The percent difference column shows

very good agreement between the total gross weight, total fuel weight, time to acceleration altitude, total mission time, total range, and initial cruising altitude. The simplified takeoff and landing analysis in RASAC produces a takeoff field length that is underpredicted and a landing field length that is overpredicted. Despite these discrepancies, which are still within reasonable limits, the validation results show that RASAC is adequately accurate and versatile for conceptual design.

Table 18: RASAC Validation Results for XB-70 Vehicle and Mission [91], *[31]

	Predicted	Actual	% Diff
Total Gross Weight	521,056 lbs	534,700 lbs *	2.62
Total Fuel Weight	261,999 lbs	273,063 lbs	4.22
Time to 20,000 ft	4.51 min	3.52 min	21.95
Time to Acceleration Altitude	5.35 min	5.36 min	0.19
Total Mission Time	2.85 hrs	3.0 hrs	5.26
Total Range	3,841 nmi	3,725 nmi	3.02
Initial Cruising Altitude	63,985 ft	65,000 ft	1.59
Takeoff Field Length	10,550 ft	18,074 ft	71.32
Landing Field Length	7,480 ft	4,746 ft	36.55

5.3 Aerothermodynamics

The validation of the aerothermodynamic design tool (MINIVER) was performed through comparison of the heatrate along the centerline of the Space Shuttle for the STS5 reentry. The STS5 validation data was found in Bertin [6] and is shown in Figure 93.

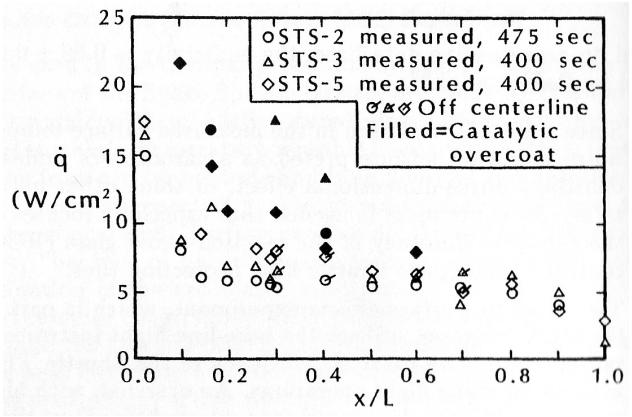

Figure 93: Validation Data for Space Shuttle (STS5) Centerline Heatrate [6]

In Figure 94, the MINIVER solution for the heatrate along the centerline of the Space Shuttle as a function of normalized x-coordinate has been superimposed with the data

plotted earlier in Figure 93. The solution shown is for 400 seconds after the initial reentry, which corresponds to an altitude of 74.7 km, freestream velocity of 7.16 km/s, and an angle of attack of approximately 40°.

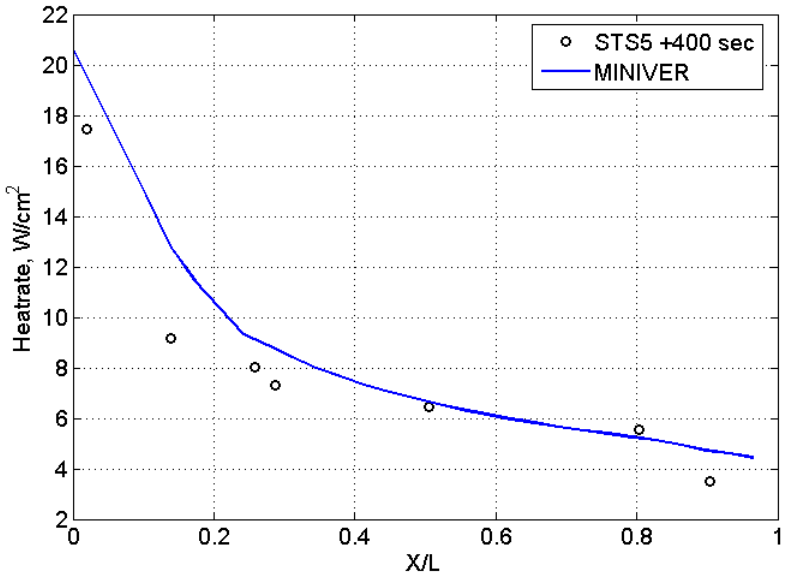

Figure 94: Validation Results for Space Shuttle Centerline Heatrate

The MINIVER results show adequate agreement with Space Shuttle flight data. However, there is a noticeable increase in error towards the forward portion of the vehicle. This is expected since the MINIVER solution is based on a simple sharp cone and does not address bluntness or variable entropy effects [95]. Variable entropy is a result of the bow shock that forms on a blunt nose or leading edge in supersonic and hypersonic flight. In the uniform freestream, the entropy for the streamlines is the constant. As the streamlines cross the shock, they experience an increase in entropy. The magnitude of the entropy increase depends on the location where they cross the shock. A streamline crossing a normal shock will experience greater entropy increase than a streamline crossing a weaker oblique shock. This entropy gradient between streamlines gives way to a rotational flow field.

The MINIVER prediction shows better agreement farther downstream where these effects begin to dissipate. In order to confirm MINIVER's limitations when dealing with blunt geometries, two new validation cases consisting of a sharp and blunt cone geometry were found in Wurster et al [95] and run for comparison. The cone validation data in the reference

has been normalized and does not provide absolute measures of heatrate. Nonetheless, it is still possible to compare the trends in heatrate distribution and prove that the reason for the increase in error is the geometry's bluntness.

The blunt cone geometry is for a 15° half-angle cone with 0.0917 ft nose radius exposed to a $Mach$ 10.6 flow, and Reynolds number of $1.2x10^6/ft$. The results in Figure 95 show a similar trend to that of the Space Shuttle with increased error at the forward portions of the cone and good agreement beyond x/Rn of 0.25. The heatrate at the wall and the reference heatrate is given by $\dot{q}_w$ and $\dot{q}_{ref}$, respectively.

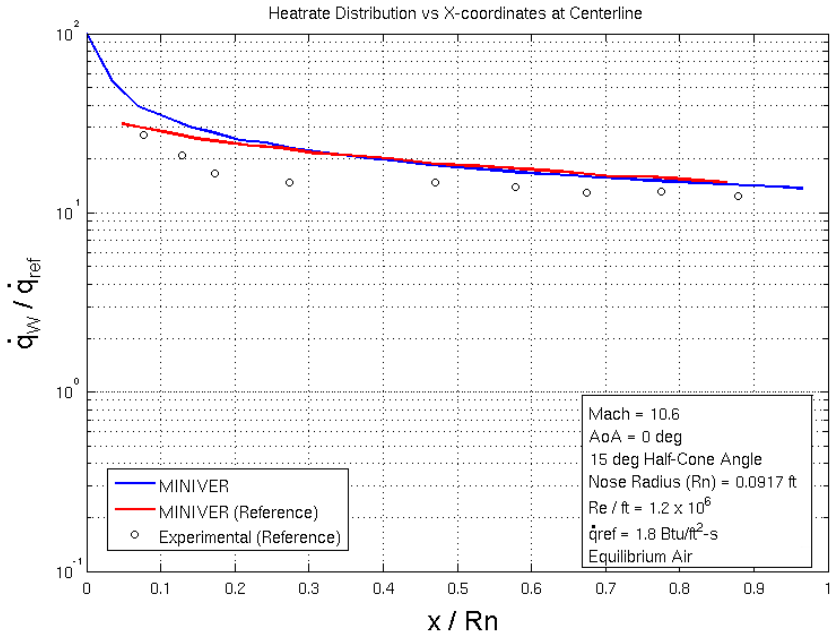

Figure 95: Blunt Cone Aerothermal Trend Validation [95]

The sharp cone validation was performed with a 5° half-angle cone and an actual nose radius of 0.0095 ft. The data was obtained through actual flight data and consists of a $Mach$ 19.3 flow, at an altitude of 120,000 ft, and AoA of 0°. The normalized MINIVER prediction and flight data is given in Figure 96 showing excellent agreement with respect to the overall trend. There is no significant or noticeable error in the forward portion of the sharp cone, confirming that this is a limitation of MINIVER when dealing with blunt geometries.

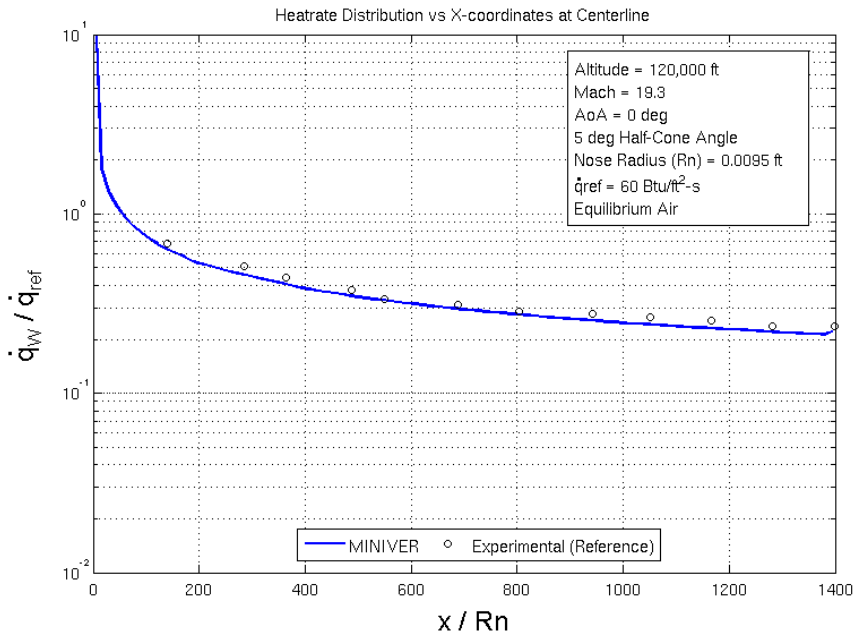

Figure 96: Sharp Cone Aerothermal Trend Validation [95]

Despite the identified limitations of MINIVER, it has been shown that it is still a very powerful tool for conceptual design. MINIVER should perform well when dealing with sharp leading edge geometries as is the case of the TBCC geometry which will be used within the proposed case study.

5.4 Thermal Management System Sizing

The validation of the thermal protection system sizing using the 1-D transient heat equation was performed through 3 validation cases which will be described below. The first two cases are academic in nature while the third is a more practical application based on the Space Shuttle.

5.4.1 Validation Case #1

For the first part of the validation, the temperature at the surface and backplate of a TPS section was computed using the 1-D transient heat equation solver used with the Thermal Management System Sizer (TMSS) and compared to analytical results for steady state for a constant heatrate of $1x10^4\ W/m^2$. The TPS material selected was RCC with a thickness (L) of 2 *inches* (5 *cm*). The physical and thermal properties of RCC are given in Table 26

of Appendix A. The schematic of the validation problem is shown in Figure 97. Note that the diagram shows only conduction heatrates; therefore radiation is not being considered for simplicity.

The validation case with $\dot{q}_A = \dot{q}_B$ and initial material temperature of 300 K was solved using the 1-D transient heat equation. The resulting temperature profile is shown in Figure 99. The numerical solution for temperature A and B was found to be 363.5 K and 236.5 K, respectively.

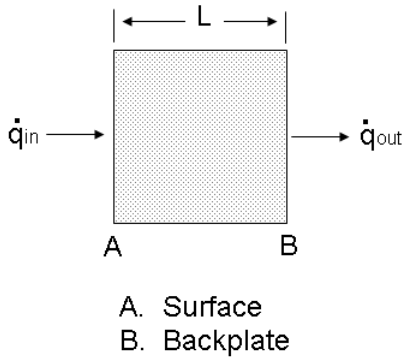

Figure 97: Validation TPS Schematic

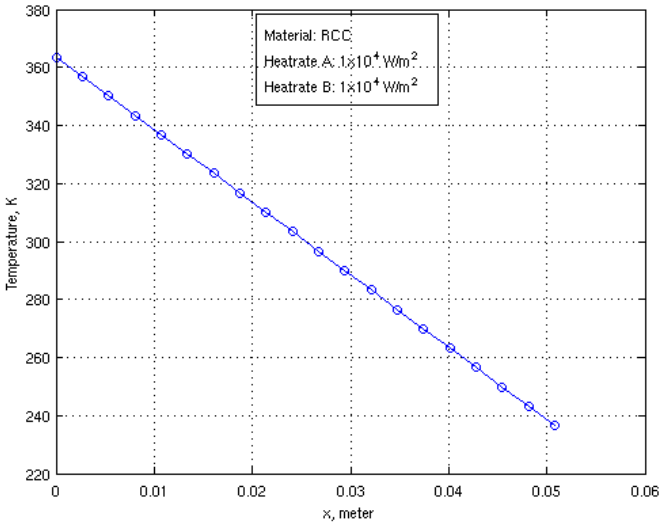

Figure 98: TPS Temperature Profile for Case #1

The analytical heatrate solution to this problem can be obtained with the conduction

relation given in Equation 147. This equation is a simplified form of the general conduction Equation 146 for a homogeneous material with linear temperature profile. The temperatures (T_A and T_B) computed from the numerical heat equation solver can be plugged into the conduction equation to obtain once again the correct original input heatrate $\left(\frac{\dot{q}}{A}\right)$ of $1x10^4\, W/m^2$.

$$\frac{\dot{q}}{A} = \kappa \frac{dT}{dx} = \frac{\kappa}{L} \int_{T_B}^{T_A} dT \tag{146}$$

$$\frac{\dot{q}}{A} = \kappa \frac{(T_A - T_B)}{L} \tag{147}$$

5.4.2 Validation Case #2

The second validation case utilizes the same material and TPS schematic from Figure 97 [21]. However, non-equal heatrates $\dot{q}_A$ and $\dot{q}_B$ were used. In this example $\dot{q}_A$ remains set to $1x10^4\, W/m^2$, but the outgoing heatrate $\dot{q}_B$ was set to zero to model an adiabatic boundary constraint at the backplate. The resulting nonlinear temperature profile is given in Figure 99. The conduction equation can be used once again together with the numerical solution of the temperature profile at each interval of x and the heatrate can be back solved at each interval. Most importantly, the heatrate at each boundary condition A and B was correctly resolved as shown in Table 19.

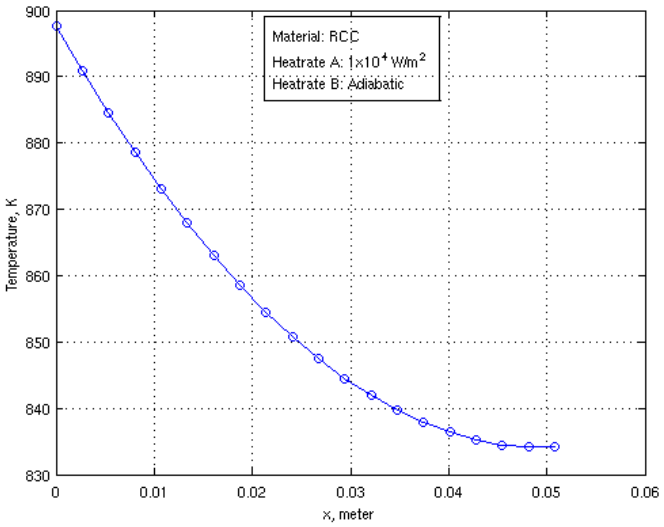

Figure 99: TPS Temperature Profile Adiabatic Case

Table 19: TPS Analytical Solution of Heatrate for Adiabatic Case

x (m)	T (K)	$\dot{q}$ (W/m^2)	Boundary
0	897.6264		
0.002674	890.9422	1.00E+04	A
0.005347	884.6293	9.44E+03	
0.008021	878.6878	8.89E+03	
0.010695	873.1176	8.33E+03	
0.013368	867.9188	7.78E+03	
0.016042	863.0913	7.22E+03	
0.018716	858.6351	6.67E+03	
0.021389	854.5503	6.11E+03	
0.024063	850.8369	5.56E+03	
0.026737	847.4948	5.00E+03	
0.029411	844.524	4.44E+03	
0.032084	841.9246	3.89E+03	
0.034758	839.6965	3.33E+03	
0.037432	837.8398	2.78E+03	
0.040105	836.3544	2.22E+03	
0.042779	835.2404	1.67E+03	
0.045453	834.4977	1.11E+03	
0.048126	834.1264	5.55E+02	
0.0508	834.1264	0.00E+00	B

5.4.3 Validation Case #3

The temperature profile for a point on the Space Shuttle was utilized for the purpose of validating the TMSS environment which sizes and optimizes the TPS based on the 1-D transient heat equation. The validation point is located at X/L = 0.1 on the windward side of the Space Shuttle as shown in Figure 100. The TMSS environment was used to size

an FRCI-12 element at the validation point using the 1-D transient heat equation while assuming an adiabatic backplate boundary condition. The resulting thickness for the FRCI-12 element found by TMSS at X/L = 0.1 was 3.1 *inches* and the temperature profile is plotted and compared to actual STS2 flight data in Figure 101.

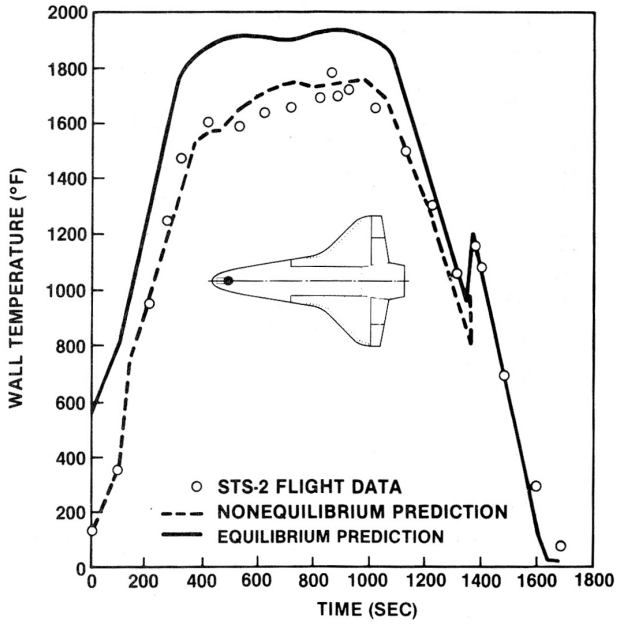

Figure 100: STS2 Temperature History for on Fuselage Lower-Surface Centerline at X/L=0.1 [21]

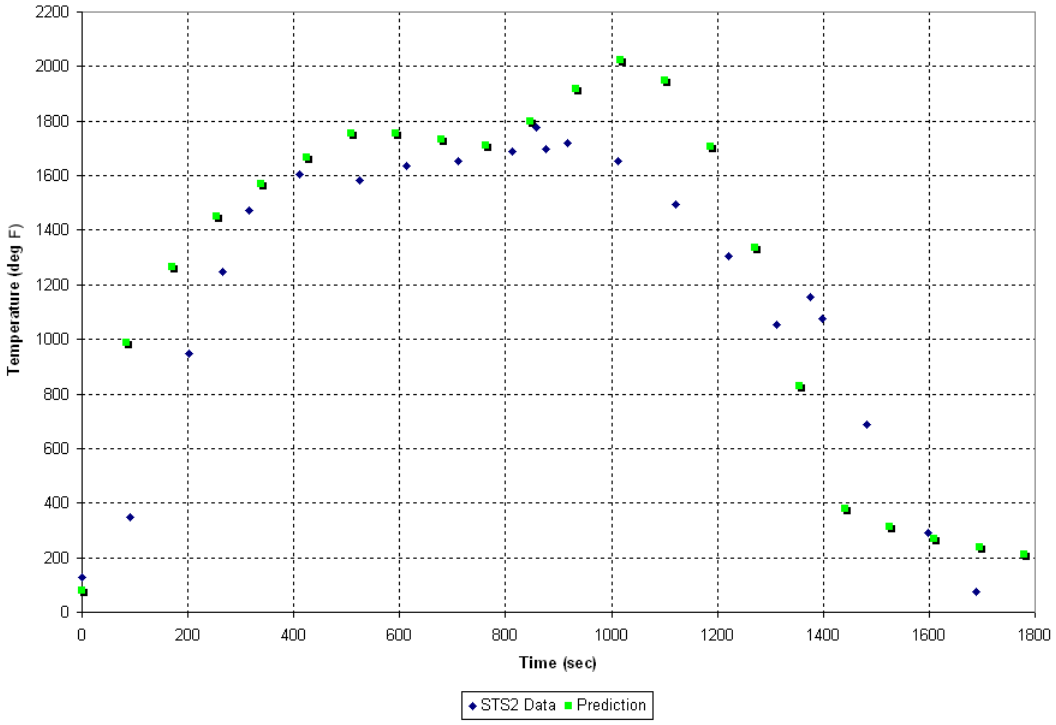

Figure 101: TPS Temperature Profile for FRCI on STS2

Chapter VI

DEMONSTRATION OF METHODOLOGY

In this chapter, the proposed conceptual design methodology will be put in practice by applying it to the previously defined case study of a TBCC vehicle. The results for the air-breathing TBCC application will be analyzed through the design space exploration environment and conclusions will be drawn. In addition to air-breathing vehicles, the proposed methodology presented in Chapter IV can be utilized for other types of applications such as RLVs and missiles. The effectiveness design space, however, needs to be re-produced accordingly to account for the key metrics of interest for those specific applications. In addition, the disciplinary analysis tools need to be re-assessed for new applications to make sure that the physical behavior of the system is properly modeled.

6.1 Concept Down-Selection

For the first milestone, the problem has been identified and a case study has been chosen. By employing a house of quality as shown in Figure 102, the voice of the customer was mapped to the voice of the engineer. This has established a ranking for the most important engineering characteristics which will define the vehicle's capability-based design space. The House of Quality shown in Figure 51 and revisited in Figure 102 was generated by the author to the best of his knowledge. This House of Quality could be improved by surveying a panel of experts in the field of high-speed vehicle design. The morphological matrix in Table 20 shows the large number of candidate concepts which can make the problem unmanageable. As a result of this, a MADM technique has been employed to narrow down the number of concepts and make the scope of work more manageable. TOPSIS was the MADM technique used for the down-selection process because it is repeatable, transparent and can be easily modified to meet changing customer requirements.

The overall process for need identification and results of the TOPSIS concept down-selection in Figure 103 shows a ranking for the eight different families of thermal management concepts. For the demonstration of the proposed design methodology the two families highlighted in green: convective cooling (active), and insulated structures (passive) were selected as shown in Figure 103. The selection of the candidate concepts for this exercise was based on the ability to model performance and economic characteristics. Although TOPSIS shows heat pipes as a very promising concept, it proved very difficult to find sufficient thermodynamic data for the working coolant, as well as life cycle cost data. The modeling of film and transpiration cooling would involve the use of a more sophisticated aerodynamic and aerothermodynamic analysis tool since they have a direct effect on the flowfield at the surface of the vehicle. In the next section, various TMS configurations will be derived from these two concept families (convective cooling and insulated structures) to be carried through the demonstration exercise.

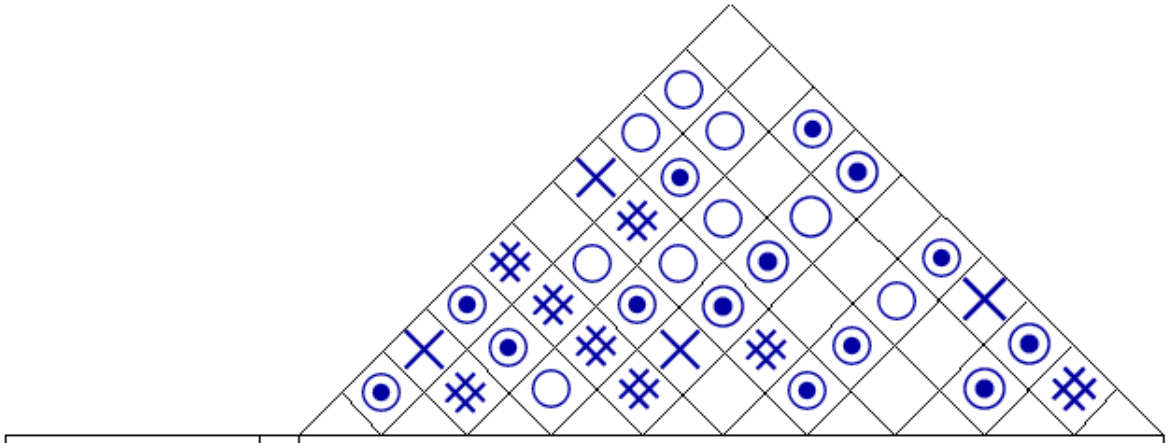

Thermal Management Technology Selection		Customer Importance	HOWs (Voice of the Engineer)									
			Performance								Economic	Safety
			Total Gross Weight	TMS Weight	Range	Maximum Mach	Payload	Block Time	Maximum Altitude	TMS Configuration	Life Cycle Cost	Safety Margin
Direction of Improvement			↓	↓	↑	↑	↑	↓	↑		↓	↑
WHATs (Voice of the Customer)	Rapid Turn Around	5.0	△	◌						✹		
	Vehicle Capability	8.0	◌	◌	✹	✹	✹	✹	✹	✹	✹	◌
	Safety	7.0			△	✹		◌	△	✹	◌	✹
	Durability	4.0			◌	◌		◌		✹	✹	
	Cost	6.0	◌	◌	◌	◌	◌			✹	✹	△
	Integration	1.0		◌			◌			✹	◌	
	Operational Complexity	2.0	△	◌						✹	◌	
	Maintenance	3.0			◌	△		△	◌	✹	✹	◌
Weighted Importance			49	66	118	168	93	108	88	324	219	102
Relative Importance												
Units			lbs	lbs	nmi		lbs	min	ft		US$	K
Target Value			100000	20000	3000	6	5000	80	80000		100	200
Risk Levels			3	3	9	3	9	9	1	3	9	9
Relative Risk												

Correlation:

- ◉ Strong positive
- ○ Positive
- # Negative
- \+ Strong negative

Relationship:

- ◉ Strong
- ○ Neutral
- △ Weak

Figure 102: House of Quality (Demonstration)

Table 20: Morphological Matrix for Thermal Management Systems (Demonstration)

		Categories			
		1	2	3	4
Characteristics	TMS Type	Passive	Semi-passive	Active	
	Passive Type	Heatsink Structure	Hot Structure	Insulated	
	Semi-passive Type	Heatpipe	Ablation		
	Active Cooling Type	Convective	Transpiration	Film	
	Coolant Type	Air	Water	Ethylene Glycol	Lithium
	Thermodynamic System	Closed	Open		
	Convective Process	Sensible	Latent		
	Thermodynamic Cycle	Ideal	Vapor Compression	Reversed Brayton	
	Degenerative Materials	Yes	No		
	Number of Materials	3	4	5	15

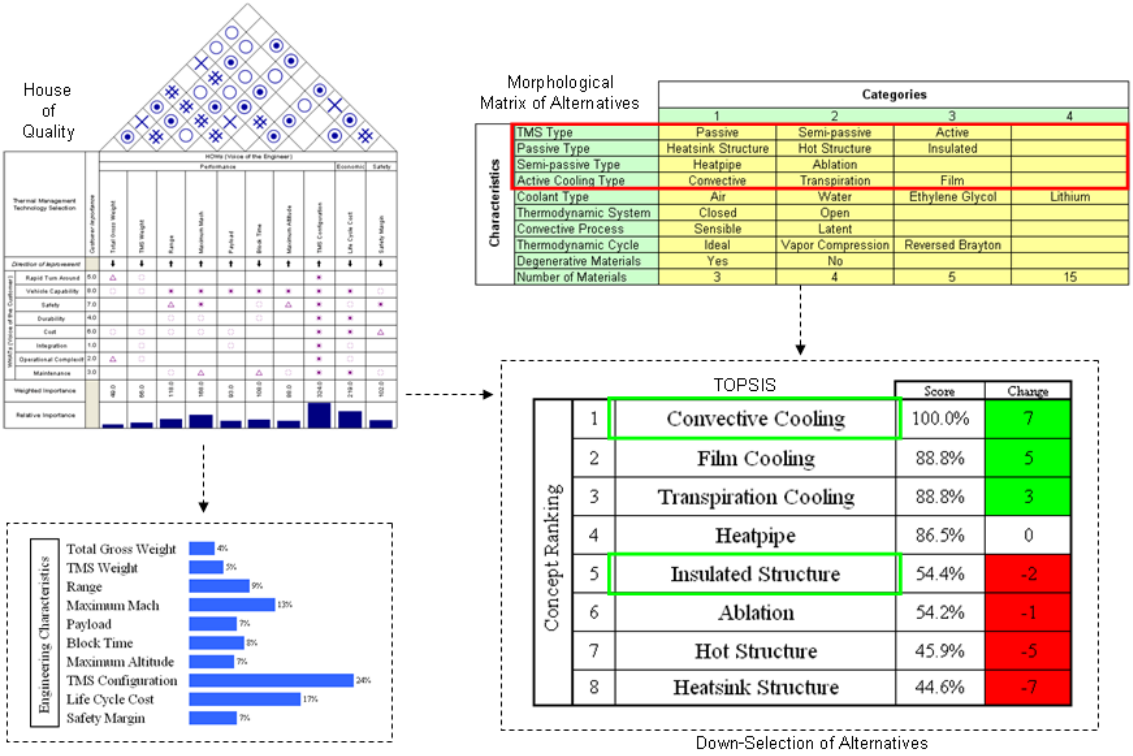

Figure 103: Overall Process for Need Identification and Concept Down-Selection (Demonstration)

6.2 Thermal Management Configurations

Even though the families have been filtered using a MADM technique and the work has been focused on only two families there are still many lower-level combinations that can be formed within each of these concept families. The compatibility matrix shown in Table 21 establishes the compatibility between all eight family concepts. The compatibility matrix

assumes that a maximum of two concept families can be applied to a vehicle since too many onboard concepts can introduce risk and complexity into the program. The compatibility criteria for the matrix is defined by asking the following question: do the two concepts complement each other without disruption? The matrix shown in Table 21 was produced by the author himself, however, this could be further improved by contributing disciplinary experts for the various concepts.

Table 21: Thermal Management Systems Compatibility Matrix

Compatibility Matrix	Heatsink Structure	Hot Structure	Insulated Structure	Ablation	Heatpipe	Transpiration Cooling	Film Cooling	Convective Cooling
Heatsink Structure	1	1	1	0	1	1	1	1
Hot Structure		1	1	1	1	1	1	1
Insulated Structure			1	1	1	1	1	1
Ablation				0	0	0	0	0
Heatpipes					0	0	0	0
Transpiration Cooling						0	0	1
Film Cooling							0	1
Convective Cooling								0

The matrix shows that the two down-selected families, insulated structures and convection cooling, are compatible. Although convective cooling can theoretically work by itself, it would be very complex and impractical to create such an extensive system of piping and heat exchangers for the entire vehicle surface. For this reason, convective cooling is denoted incompatible with itself in Table 21. The four major configurations that will be considered are given in Table 22 and a schematic of each of these configurations are shown in Figures 104-105. Ideally, one would include as many concept families and configurations as possible in order to broaden the technology design space. However, for the purpose of this thesis and given the time constraint only two family concepts and four configurations will be analyzed. Nonetheless the process would be the same and can be repeated no matter how many families and configurations are included.

It is important to note that configurations #1 and #3 are respectively equal to configurations #2 and #4. The first set (configurations #1 and #2) use only insulating materials that are reusable for up to 100 flights according to NASA's TPSx material database in Appendix A. The second set (configurations #3 and #4) considers all available insulating materials whether reusable or not. In configurations #2 and #4, an optimization is performed to determine the amount of water mass flowrate that is required to maintain the external temperature within maximum temperature limit and internal temperature within the limits of the internal structure. The heat exchanger material is fixed as Inconel-617 with a wall thickness of 0.25 *inches*. However, this thickness is modeled as an input variable into the modeling and simulation environment and can be varied if needed.

Table 22: Thermal Management Configurations Considered

	Concept Combination		
Configuration	Leading Edge	Rest of Vehicle	Materials
1	Insulated structures	Insulated structures	Reusable
2	Convective cooling	Insulated structures	Reusable
3	Insulated structures	Insulated structures	All
4	Convective cooling	Insulated structures	All

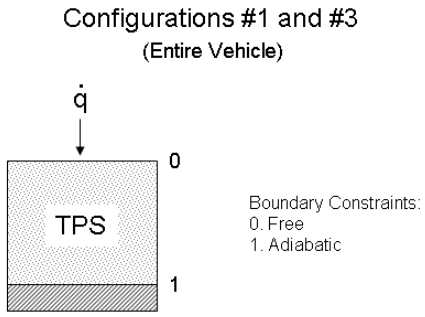

Figure 104: Thermal Management Schematics for Configurations 1 and 3

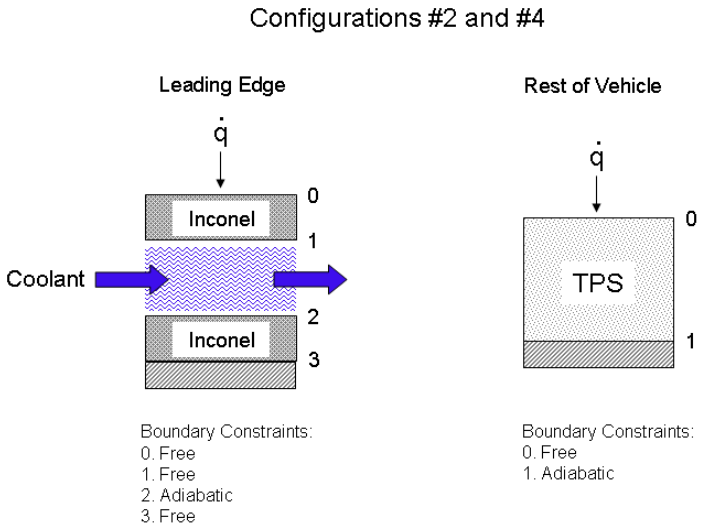

Figure 105: Thermal Management Schematics for Configurations 2 and 4

6.3 Modeling and Simulation Results

The TMSS environment forms the core of the physics-based analysis in the proposed methodology. The TMSS analysis is combined with RSM to generate physics-based surrogate models which can in turn be used to produce probabilistic data with a Monte Carlo simulation. In this section, the TMSS capabilities are demonstrated for the sample mission shown in Figure 106.

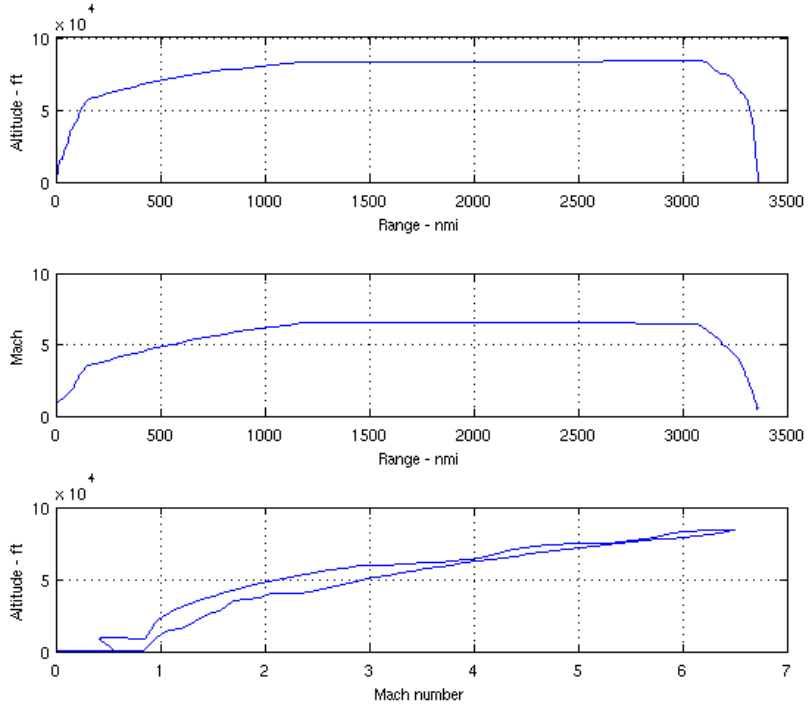

Figure 106: Sample Mission Profile

The TMSS environment automatically discretizes the VSP geometry given a number of x-stations (n_x) and y-stations (n_y) and generates MINIVER input files based on the trajectory provided by RASAC. MINIVER uses these input files to generate the aerothermodynamic heatrate distribution over the discretized surface as shown in Figure 107.

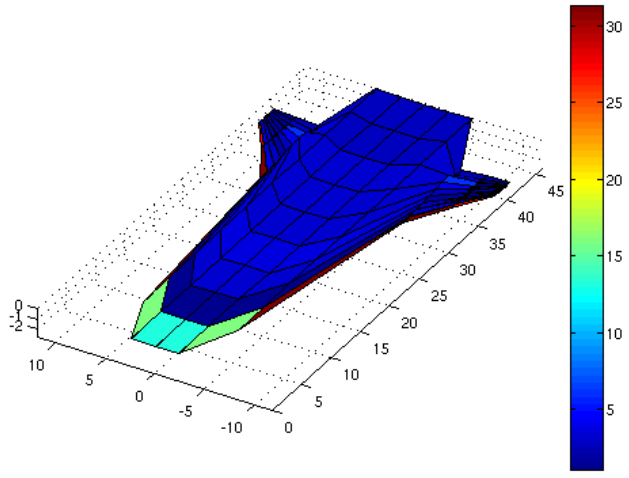

Figure 107: Maximum Aerothermodynamic Heatrate Distribution ($Btu/ft^2 - s$)

Once the aerothermal heatrates are computed, the TMSS environment attempts to size the existing TMS technology at each discretized surface point. For insulated material technologies, TMSS employs the 1-D transient heat equation along with an optimizer to size the thickness of the TPS layer while satisfying an adiabatic wall constraint. This adiabatic constraint ensures a specified maximum temperature for the internal structure is not violated. The TMSS analysis can size and distribute TPS materials from a database at the discretized points where insulated structure technology is desired. In discretized points where convective cooling technology is desired, the methodology for sizing described in Section 4.2.6.6 is employed to determine the amount of coolant required. The resulting maximum temperatures, materials, and material thickness distributions are given in Figure 108.

It is important to note that TMSS tends to oversize the TPS layer since the adiabatic backplate constraint assumes no heat is transferred down to the internal structure. This is an idealistic assumption which is very difficult to achieve in real life applications. In addition, TMSS is not capable at this point in time of multi-layer material stacking and optimization which may further minimize the thickness. Due to these limitations the sized TPS layer can be assumed to be a pessimistic solution or worst case scenario of TPS requirements.

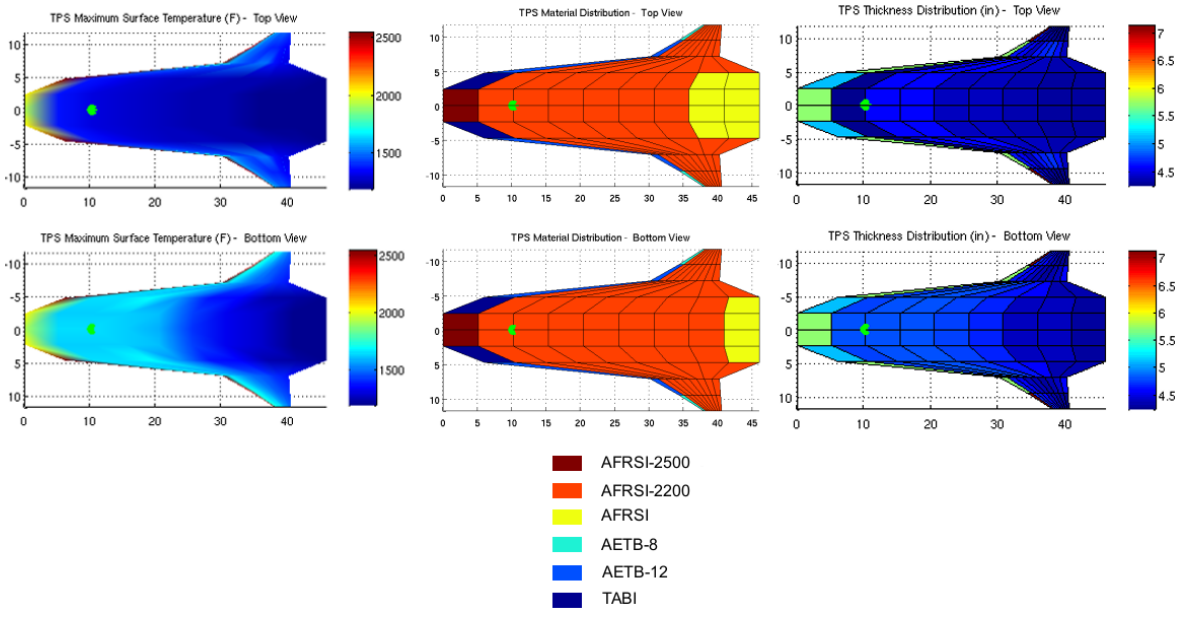

Figure 108: Maximum Surface Temperatures, Materials, and Thickness Distributions

A sample probe point can be placed at any location on the surface of the vehicle to obtain more detailed information regarding heatrate and temperature distributions. The plots on Figure 109 show the leeward and windward heatrate and temperature distributions for the centerline location on the TBCC case study vehicle. The plots on Figure 110 show the leeward and windward heatrate and temperature distributions for the surface probe point at X/L=0.22 as a function of time. This plot shows, as expected, greater aerothermal heatrate on the windward side except in the descent leg of the flight when the vehicle begins to suddenly slow and cool down. Despite this, the windward surface temperature remains greater or close to equal to the leeward side for the entire trajectory.

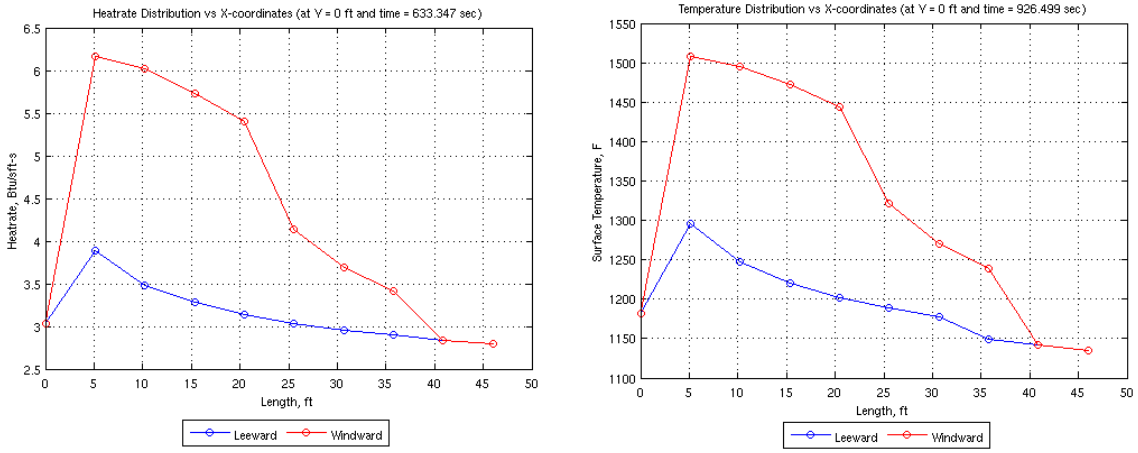

Figure 109: Heatrate and Surface Temperature Distribution at Vehicle Centerline

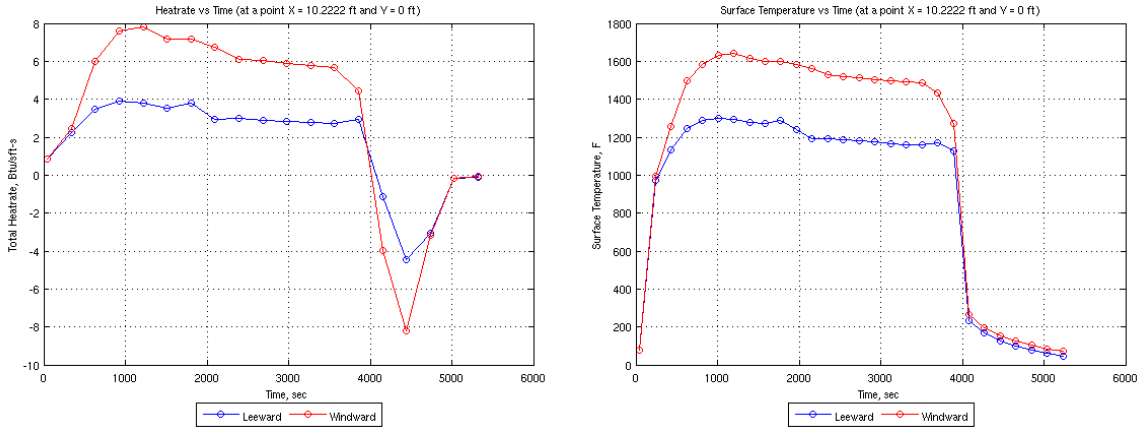

Figure 110: Heatrate and Surface Temperature Profile versus Time at X/L=0.22

6.4 Surrogate Modeling

Surrogate models are a key enabler in the implementation of probabilistics. They allow the rapid evaluation of engineering characteristics or responses making probabilistic studies possible. The process by which surrogate models are generated was defined earlier in Section 2.7.

Due to the low number of input variables (range, maximum Mach, payload, fuel cost) for the particular case study, it was possible to employ a full factorial DoE consisting of 81 total computational cases. The ranges for these DoE input variables are shown in Table 23. As shown earlier in Table 10, the full factorial DoE benefits from being an orthogonal design which contains no effect estimate correlation and requires no extrapolation. The main disadvantages of this design are the high number of cases required for applications with very large number of design variables and failed or erroneous case results due to operation of the analysis tools beyond its assumptions and feasible limits. The TMSS environment was thoroughly tested in advance to ensure that the latter would not become a problem when solving the DoE. The engineering parameters of interest (DoE responses) for the particular TBCC case study include those characteristics identified for the performance, economics, and safety effectiveness OEC in Equations 140-142, which are not explicit input variables to the TMSS analysis. These DoE responses of interest are block time, life cycle cost of total vehicle, and safety margin.

Table 23: Full Factorial DoE Input Variables Ranges

DoE Variable	Minimum	Maximum	Units
Range	1500	3000	nmi
Mach	4	6.5	
Payload	0	5000	lbs
Fuel Cost	100	200	$/barrel

6.4.1 Data Fitting

The objective of the data fitting process is to map the obtained DoE responses to a simplified model that can be rapidly evaluated. The surrogate modeling decision flowchart given earlier in Figure 72 was followed and the implementation of response surface equations was found to be adequate for the proposed case study.

The results of the goodness of fit process are provided in Appendix C for the purposes of validating the surrogate models. The goodness of fit shows adequate modeling by the surrogate models. A total of 100 random DoE cases were computed using TMSS for each of the four technologies in order to generate the MRE plots. It is important to note that several response transformations were required for life cycle cost and safety margin as shown in Appendix D. The safety margin response demonstrated a high level of nonlinearity but the magnitude of the error was determined to be acceptable.

The sensitivity profiles for each of the responses of interest (block time, life cycle cost, and safety margin) as a functions of input variables (design, and random) are provided in Appendix D. These sensitivity profile plots provide a sanity check to make sure the trends in the modeling and simulation are reasonable. Most of these trends are as expected, increase in Mach number, range, and payload lead to an increase in takeoff gross weight, thermal management system weight, and costs. Other trends such as those concerning safety margins are not so straightforward because they are highly dependent on the TPS material distribution over the vehicle generated by the optimizer. The material distribution is a complex process which can vary even across similar mission trajectories due to variations in payload.

6.5 Design Space Exploration Results

A Monte Carlo simulation can be employed once the surrogate models for block time, life cycle cost, and safety margin have been generated and validated. These surrogate models are a function of three controllable input variables: range, maximum Mach, payload, and two noise variables: fuel cost, and TPS thickness failure. The dependency of each response is stated below in Equations 148-150.

$$BlockTime = f(range,\ maximum\ Mach,\ payload) \tag{148}$$

$$LCC = f(range,\ maximum\ Mach,\ payload,\ fuel\ cost) \tag{149}$$

$$SM = f(range,\ maximum\ Mach,\ payload,\ TPS\ thickness\ failure) \qquad (150)$$

An algorithm based on the Pareto Fitness method is used to identify the Pareto frontier points. The Pareto Fitness algorithm determines the Pareto points from a pool of points obtained by the discretization of the design space through the design variables: range, maximum Mach, payload. These are design variables that the trajectory code (RASAC) is capable of utilizing as inputs. Uncertainty is accounted for with the Monte Carlo simulation by varying the two noise variables: fuel cost per barrel, and TPS percent thickness failure. A total of 1,000 Monte Carlo cases were found to be more than adequate for this application. It is important to note that a Monte Carlo simulation must be employed for each thermal management technology. Therefore, for this particular application the total Monte Carlo simulation cases is 4,000, since there are four technology configurations being studied.

The Pareto frontier points for each Monte Carlo case are recorded for each technology. The results of the full probabilistic Pareto frontier design space for all technologies are provided in Figure 111. However, this data is still not very useful as it is difficult to visualize the types of trends taking place.

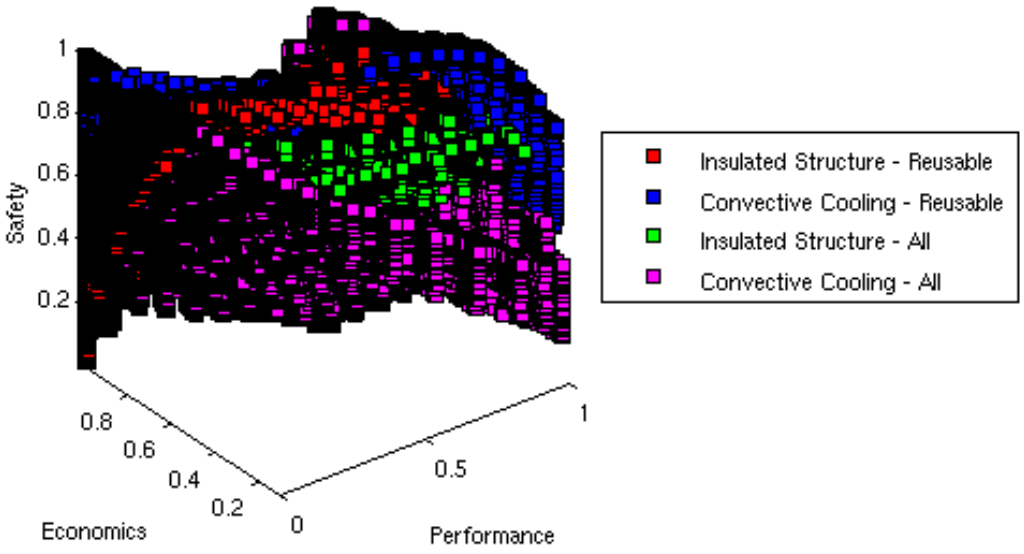

Figure 111: Probabilistic Pareto Frontier Space

This 3-D probabilistic design space can be sliced at a specific dimension to reduce the amount of data being shown and making analysis simpler. In the example shown in Figure 112, the probabilistic design space is sliced at the safety margin effectiveness level of 0.7. Recall that the objective is to maximize each of the three dimensions: performance, economics, and safety. Therefore the positive ideal solution lies at the $[1, 1, 1]$ point on the design space while the negative ideal solution lies at $[0, 0, 0]$. The intersection curves for each 3-D Pareto surface (1,000 for each technology) and the safety plane at 0.7 are shown for each technology. Not all technologies will intersect this specified safety level the same way. It is possible for some technologies to lie mostly above or below this safety plane. An example of this can be observed in Figure 112 for convective cooling technology utilizing all database materials. This case shows low occurrence of Pareto points because a large number of the Pareto surfaces lie below the safety effectiveness of 0.7.

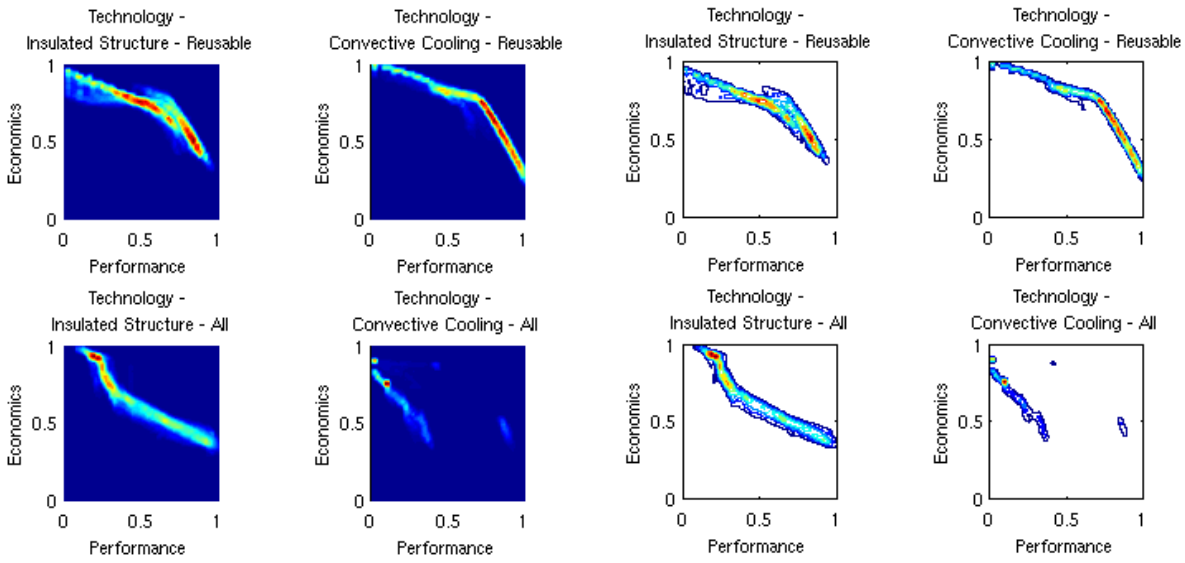

Figure 112: Performance-Economics Pareto Frontiers (Safety Level 0.7)

The technology maps can be superimposed as shown in Figure 113 to more adequately visualize how they stack up against each other. The color bar to the right of each plot in Figure 113 represents a normalized $(0, 1)$ frequency scale of Pareto point occurrences. The map shows where each technology demonstrates strengths and weaknesses as well as the risk that the design of a vehicle with certain effectiveness levels will be successful. The

highest occurrences with lower uncertainty denoted by lighter colors are shown on the plot on the right of Figure 113. These points are not optimized based on closeness to positive ideal solution but instead on the maximum likelihood that an existing design can satisfy the specified safety level.

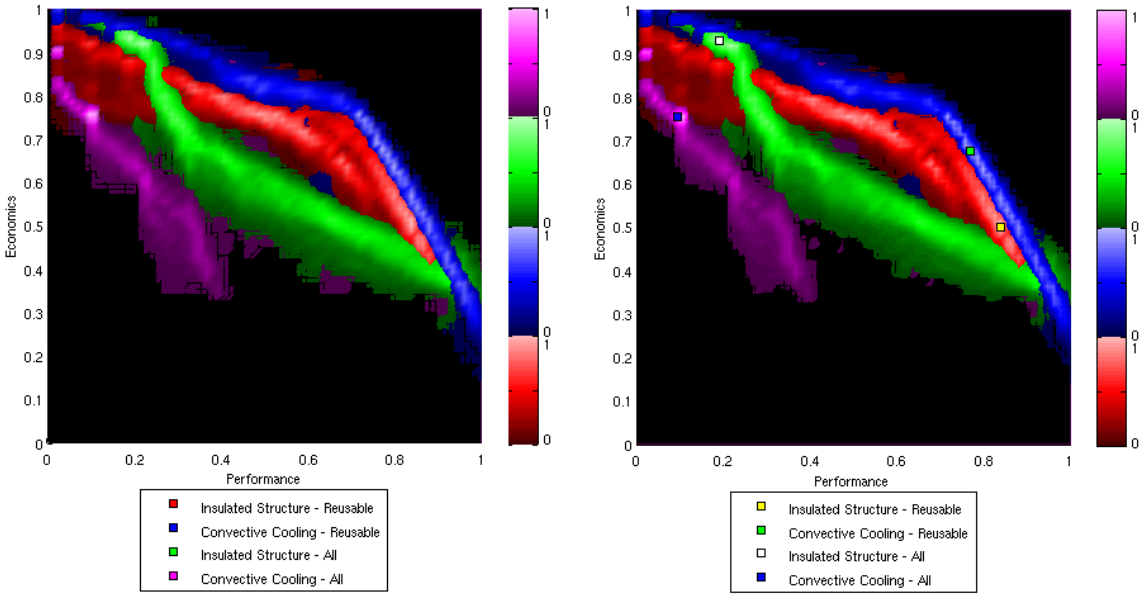

Figure 113: Superimposed Probabilistic Performance-Economics Pareto Frontiers (Safety Level 0.7)

In reality the selection of the "optimum" points is subjective and highly dependent on customer needs. At this point in the design, the designer and the customer can make their decision for the desired effectiveness levels by systematically slicing the 3-D space and observing the tradeoffs taking place for each technology among the three measures of effectiveness. A probability of success approach can also be employed at this point where the likelihood of success is measured for a region of interest in the effectiveness design space. Nonetheless, some conclusions can be drawn out of this example for this particular case study. The technology rankings for 1) equal performance and economic importance, 2) high performance importance, and 3) high economic importance are given in Table 24 based on closeness to positive ideal solution.

Table 24: Technology Ranking Based on Dimensional Importance for Safety Effectiveness of 0.7.

	Technology Ranking		
Technology	Equal Performance-Economic Weighting	Performance Favored	Economics Favored
Insulated Structures - Reusable	2	3	3
Convective Cooling - Reusable	1	2	1
Insulated Structures - All	3	1	2
Convective Cooling - All	4	4	4

For this particular application and example it was found that in general adding convective cooling (heat exchanger) to the windward side of the leading edge improved performance and economic effectiveness when using only reusable insulated structure materials. On the other hand adding convective cooling technology was found to degrade performance and economic effectiveness when using all reusable and non-reusable insulating materials.

It is interesting to note that insulated structures using all materials denoted green in Figure 113 actually exhibit the best performance driven solutions out of all technologies. It also displays good economic effectiveness at the lower performance levels where thermal requirements are lower. This can be a result of many things such as the optimizer switching to non-reusable yet cheaper insulative materials, or perhaps a more significant decrease in insulated layer thickness resulting in lower TMS weight, lower overall vehicle weight, and lower vehicle costs. However, the technology falls behind reusable insulated structures denoted red in the middle performance levels.

Convective cooling using all reusable and non-reusable insulated structures seems to perform the poorest of all four technologies. This seems to be due to the negation of the benefits attained by using convective cooling and high performance non-reusable insulating materials independently. For example, convective cooling appears to have improved operating costs since it does not need to be replaced as often and requires minimal maintenance compared to insulated structures. However, the use of all reusable and non-reusable insulated structures negates this benefit since they carry a large requirement for maintenance and operational costs. At the same time the high performance benefits of non-reusable insulating materials are lost when a heat exchanger is placed instead on the windward side of the leading edge.

This configuration shows that in some cases the combination of several technologies can interfere and actually degrade the final vehicle solution.

It is also important to note that although reusable materials can be used for more than one flight they also require a higher cost up front for purchase than non-reusable materials as shown in the material database in Appendix A. Reusable materials also tend to be more time consuming regarding installation and repairs leading to higher costs than non-reusable materials for each individual installation or repair required.

Another example of the superimposed Pareto distributions for a safety level of 0.5 is shown in Figure 114. Here, it is possible to see that the solution begins to favor insulated structures with all materials denoted by the green distribution as the safety requirements are loosened from 0.7 in Figure 113 to 0.5. Insulated structures with all materials begins to 'drown' the solutions for convective cooling and insulated structures with reusable materials denoted as blue and red, respectively. Nonetheless, the reusable insulated structures distribution is still visible since it has a significantly higher likelihood of occurrence.

This example confirms that with respect to safety effectiveness the benefits of convective cooling coupled with reusable materials start to become less important with lower interest in safety. This gives way to the higher performance capabilities of the non-reusable insulated materials. It is also interesting to note the tightening of the Pareto distributions for all technologies, except that of insulated structures with all materials, as safety requirements are lowered. This implies a lower risk or uncertainty associated with the selection and likelihood of achieving the desired effectiveness solution.

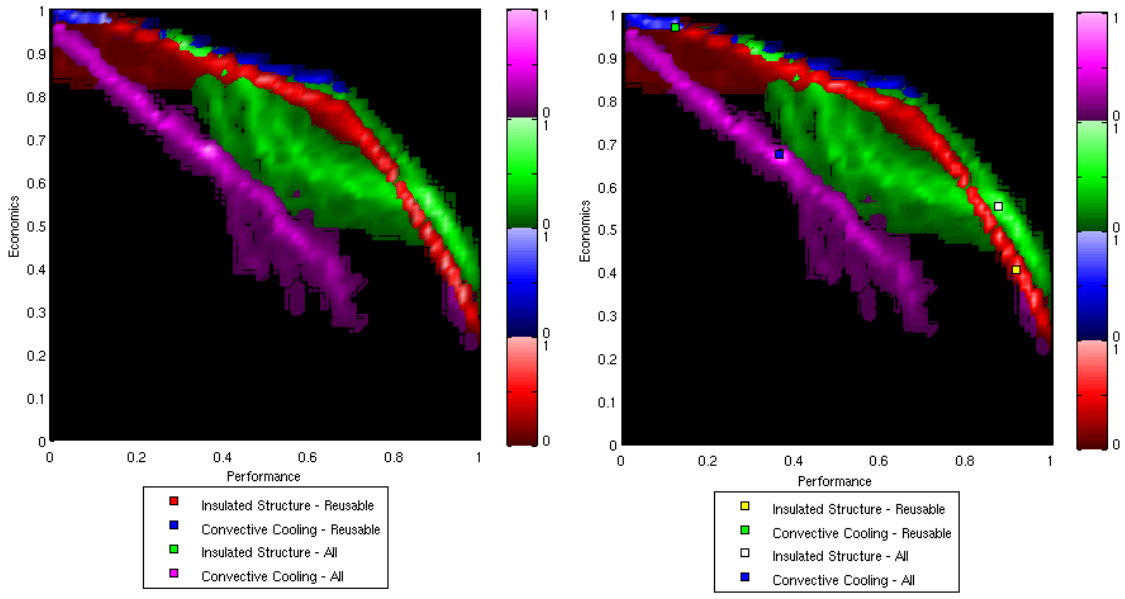

Figure 114: Superimposed Probabilistic Performance-Economics Pareto Frontiers (Safety Level 0.5)

Once the customer has selected the 'optimal' solution or level of effectiveness for all three dimensions of the design space, an optimizer can be employed to solve for the inverse design space. The optimizer manipulates the controllable design variables: range, maximum Mach, and payload, to minimize the deviation from the current solution to the desired effectiveness solution. Only design variable values that are within the feasible domain are selected and used in the inverse design space.

The effectiveness levels plotted in the right hand plot of Figure 113 denoting the points of highest occurrence and lowest associated risk were chosen as the 'optimal' solution. These effectiveness levels shown in Table 25 were then used for each of the technology configurations to resolve their respective inverse design space. The resulting 3-D inverse design space for controllable variables is given in Figure 115 for the earlier example of safety level 0.7.

Table 25: Optimum Effectiveness Designs

		Effectiveness		
Technology	Materials	Performance	Economics	Safety
Insulated Structures	Reusable	0.8378	0.5	0.7
Convective Cooling	Reusable	0.7703	0.6757	0.7
Insulated Structures	All	0.1892	0.9324	0.7
Convective Cooling	All	0.0946	0.7568	0.7

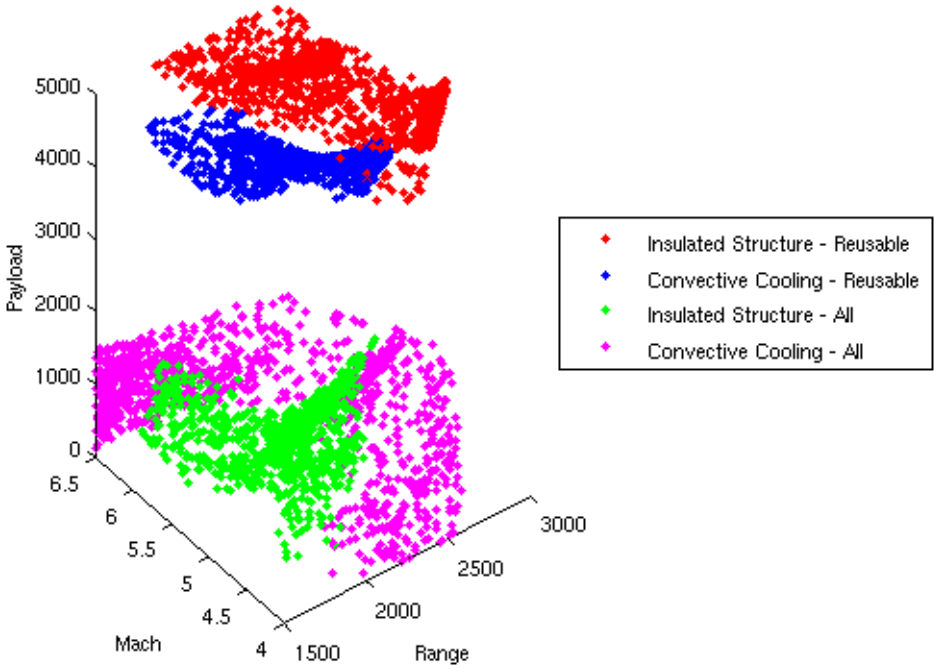

Figure 115: Inverse Design Variable Space (Safety Level 0.7)

In addition, inverse design multivariate plots are given in Figures 116-119 for all four technology configurations and superimposed in Figure 120. These inverse design multivariate plots allow the designer to visualize the true vehicle capabilities of the chosen optimum designs. However, it is important to note that since the inverse multivariate plots for each technology are based on different effectiveness levels they cannot be compared directly against each other. For example, insulated structures and convective cooling with reusable materials appear to have significantly greater performance benefits in terms of range, Mach, and payload compared to the same technologies with all materials. If one refers back to Table 25, it is possible to see this is because the effectiveness solutions for technologies with reusable materials have higher performance effectiveness while technologies with all materials have greater economics effectiveness. The benefits regarding greater economic effectiveness are in this case lost in the inverse multivariate plots. Therefore, both effectiveness distribution and inverse multivariate plots need to be analyzed together. At this point the customer can make a decision regarding which technology would be most appropriate for the application or mission of interest.

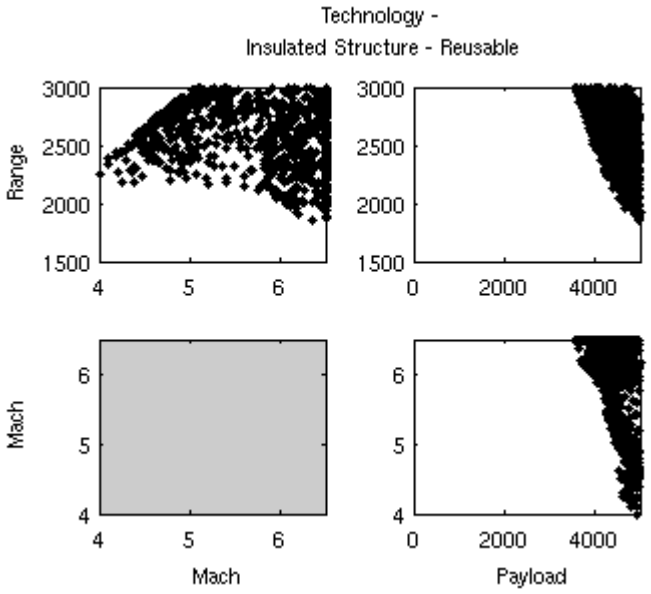

Figure 116: Inverse Design Multivariate Plot for Insulated Structures - Reusable Materials (Safety Level 0.7)

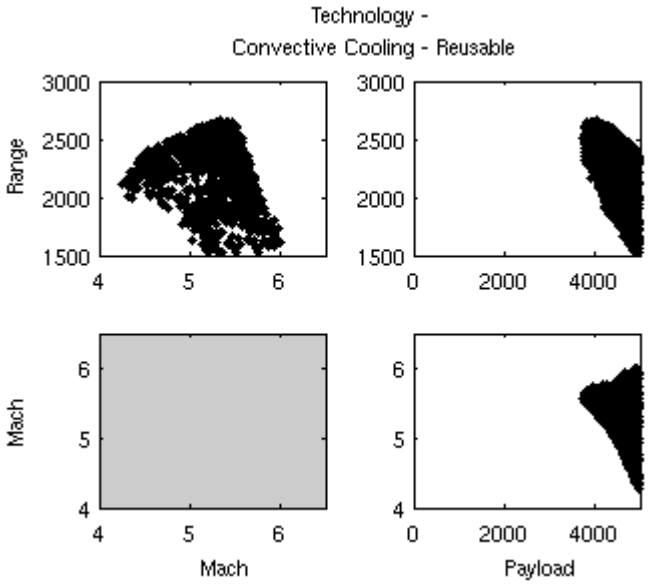

Figure 117: Inverse Design Multivariate Plot for Convective Cooling - Reusable Materials (Safety Level 0.7)

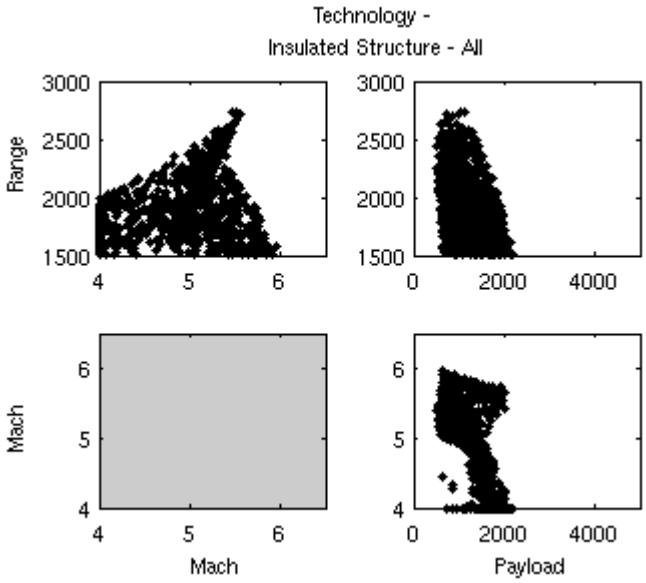

Figure 118: Inverse Design Multivariate Plot for Insulated Structures - All Materials (Safety Level 0.7)

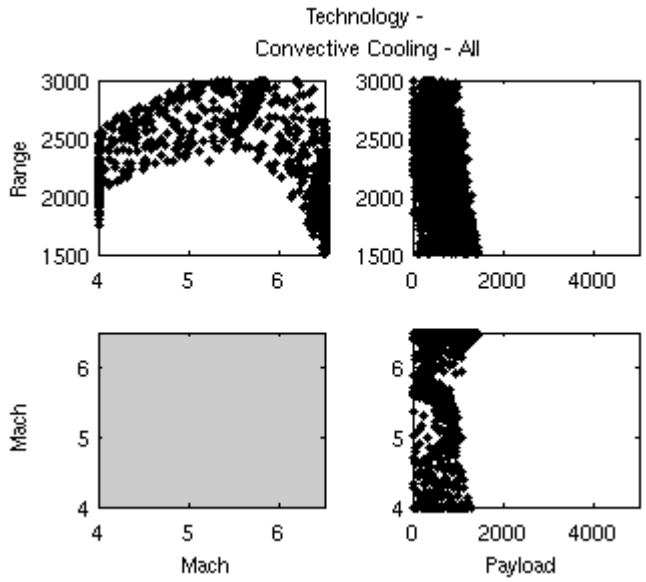

Figure 119: Inverse Design Multivariate Plot for Convective Cooling - All Materials (Safety Level 0.7)

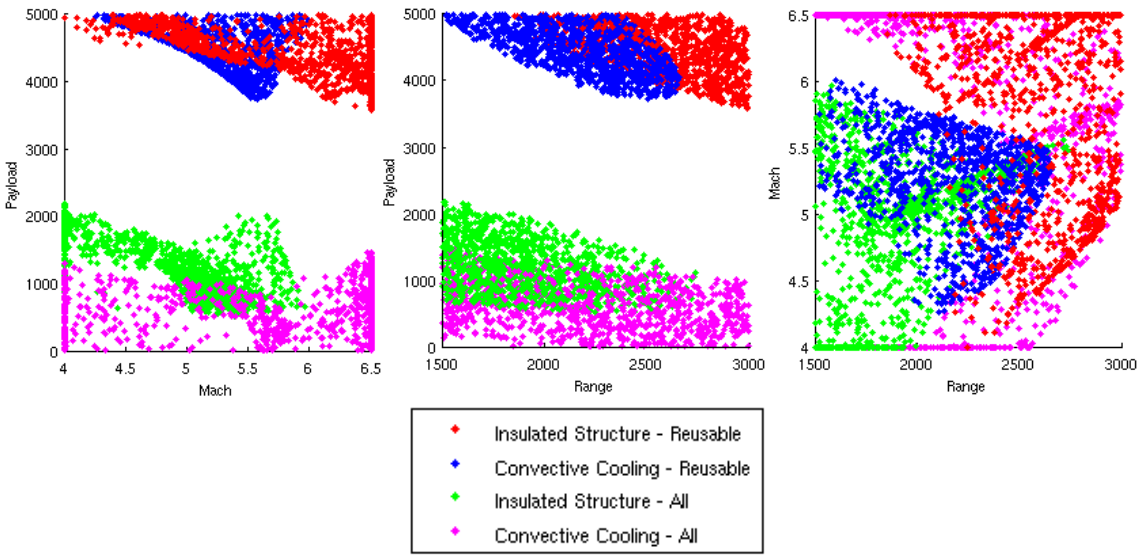

Figure 120: Superimposed Inverse Design Multivariate Plots (Safety Level 0.7)

6.5.1 Risk Mitigation

Risks can be categorized into four major groups including known unknowns, unknown knowns, unknown unknowns, and known knowns [3]. Risk can also be characterized by its likelihood, severity, and addressability. The likelihood characteristic attempts to define how likely it is that a certain outcome will become true. Severity defines the degree of the outcome (ie. the magnitude of a failure scenario). Finally, addressability establishes how can this risk be avoided or prevented. A complete risk assessment methodology is presented by Leonard et al [51] for a military space plane including risk identification, analysis, planning and tracking.

In this section, a risk mitigation example regarding the failure of the TMS is considered by analyzing the likelihood and severity characteristics of each technology. The severity of the risk is based on the *inverse* of the safety margin metric which was formulated for the safety measure of effectiveness. Recall that the safety margin is defined as the temperature difference between the material temperature limit and the maximum temperature experienced by the internal structure after a failure in the TPS thickness.

A Likelihood-Severity plot can be generated once the desired performance and economic effectiveness levels have been selected as shown in Figure 121. The likelihood dimension

pertains only to *Pareto* frontier designs and is normalized by dividing the total number of occurrences of each individual technology by the total number of occurrences for all four technologies. In order to make the example more meaningful, a single performance and economic effectiveness level of 0.84 and 0.5, respectively, was selected for all four technologies. The Likelihood-Severity plot is generated by determining the number of occurrences of Pareto points for a fixed performance and economic level while performing a sweep along the safety effectiveness dimension.

The Likelihood-Severity plot shows that the greatest risk likelihood for all technologies exists between a 0.2 and 0.4 level of severity. The greatest risk likelihood for a severity level of 0.3 (30%) corresponds to convective cooling technology with reusable materials (blue). Convective cooling with all materials (magenta) displays the lowest level of risk severity at the peak of its risk likelihood. On the other hand, insulated structures with both reusable (red) and all materials (green) display the greatest risk severity at the peak of their risk likelihoods. This means that if a failure does occur for insulated structures with both reusable and all materials, the consequences can be catastrophic. The risk likelihood for insulated structures using all materials (green) is distributed over a wider range of risk severity. This means that the severity of a failure can vary greatly with insulated structures using all materials but the likelihood of it happening is lower than for all other technologies. It is important to remember that the risk mitigation approach presented is only valid for the specified performance and economic effectiveness levels of 0.84 and 0.5, respectively. The risk mitigation results and conclusions presented here should not be assumed to hold for other effectiveness levels.

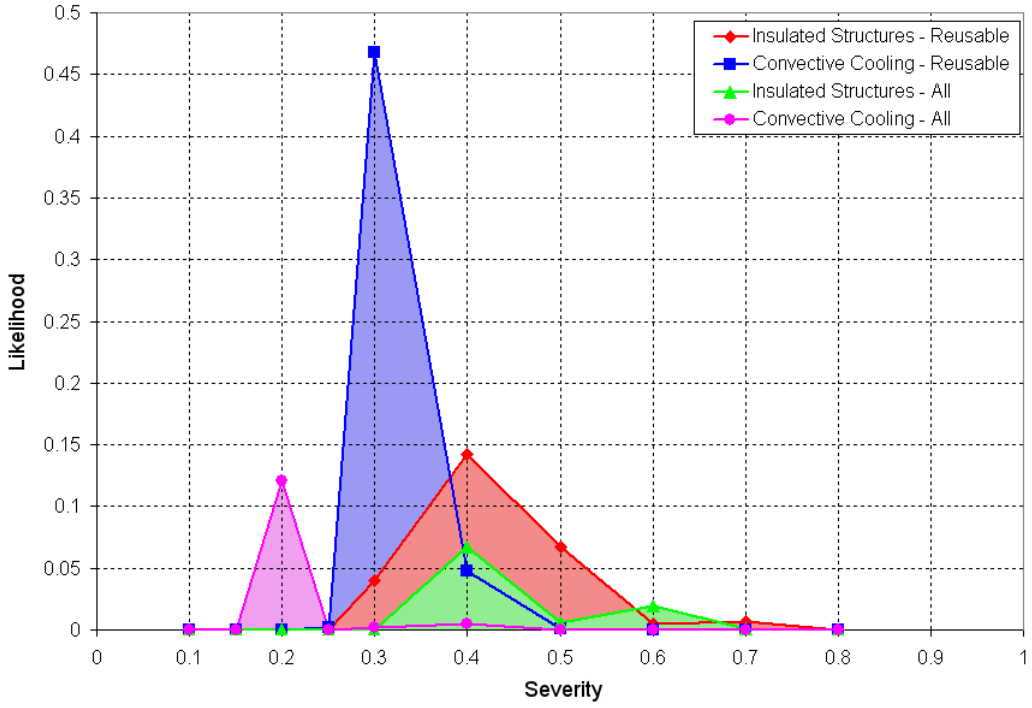

Figure 121: Likelihood-Severity Plot

6.6 Pareto-based JPDM and JPDM Results Compared

As mentioned in previous sections, the proposed Pareto-based JPDM provides an alternative approach to the multi-attribute decision making process. It has the disadvantage of greater computational cost but at the same time produces far more information than JPDM can provide. In this section, example results for the reusable insulated structures technology comparing Pareto-based JPDM and JPDM are provided. The example was generated for a safety effectiveness level of 0.5.

The plot in Figure 122 shows the JPDM solution superimposed on the Pareto-based JPDM results. The objective of the optimizer implemented with JPDM was to attempt to minimize the distance to the positive ideal solution at [1,1,1] effectiveness levels. The white, squared point located at [0.7164, 0.7259] denotes the optimal solution of the JPDM results based on the mean of the entire distribution. The variation distribution for JPDM is denoted by the straight and vertical white points stemming vertically from the optimum mean solution (white square). The JPDM distribution on the Performance-Economics plane

turns out to be linear in nature because of the simplified example used. Recall there are two random variables (fuel cost, and thickness failure) employed in the original example for the TBCC case study. The fuel cost random variable produces a variability on the economic effectiveness dimension alone, while thickness failure produces a variability only on the safety effectiveness dimension.

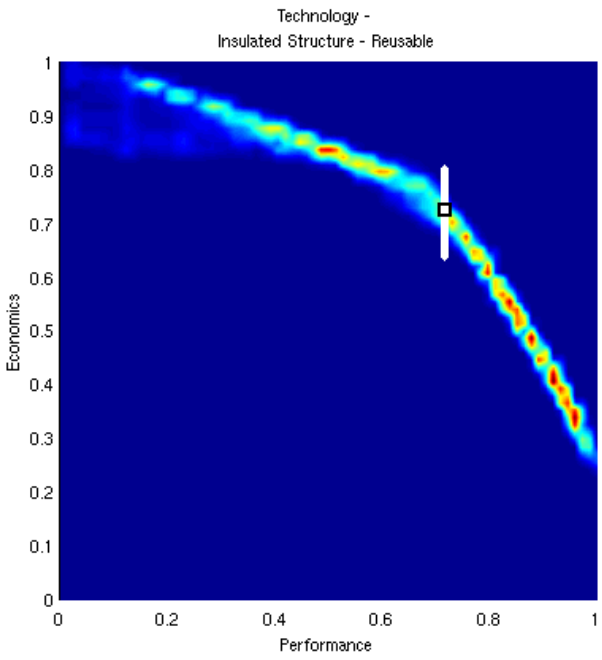

Figure 122: Pareto-based JPDM and JPDM Compared for Reusable Insulated Structures (Safety Effectiveness 0.5)

It is theoretically possible to reproduce the probabilistic Pareto design space obtained with the Pareto-based JPDM by introducing variability into the JPDM weighting factor for each effectiveness dimension (performance, economics, safety). This would result in multiple JPDM solutions which should approximate the Pareto-based JPDM results. The minimum amount of solutions or variations in weighting factors for the effectiveness dimensions required to reproduce the PJPDM results is the total number of cells by which the probabilistic design space is discretized (n_{cell}). There is, however, no guarantee that a total of n_{cell} variations in weighting factors will produce a properly defined space that can capture the detail provided by PJPDM. Nonetheless, if one assumes an ideal scenario where n_{cell} variations in

weighting factors for JPDM provides sufficient detail in the final probabilistic design space then several relations can be derived to establish which approach is more computationally efficient.

The relations in Equations 151-153 define the total number of function calls to the performance, economic, and safety RSEs required to compute the probabilistic design space for JPDM, PJPDM with PF, and PJPDM with NBI, respectively.

$$Total\,Cases\,JPDM = n_{cell} * N_{MCS} * N * fcall_{optimizer_{JPDM}} \tag{151}$$

$$Total\,Cases\,PJPDM\;w/\;PF = N_{MCS} * N * \left(n^{N_{vars}}\right) \tag{152}$$

$$Total\,Cases\,PJPDM\;w/\;NBI = N_{MCS} * N * fcall_{optimizer_{NBI}} \left[\frac{n\,(n+1)}{2}\right] \tag{153}$$

Where:

$fcall_{optimizer_{JPDM}}$ - total function calls of the optimizer for each JPDM solution

$fcall_{optimizer_{NBI}}$ - total function calls of the optimizer required to solve each point on a Pareto frontier with NBI

N - total number of dimensions

N_{MCS} - total number of Monte Carlo simulation cases

N_{vars} - total number of design and random variables

n - discretization parameter for each variable in PF and the total number of points along each edge of the three-sided Pareto front in NBI

n_{cell} - total number of cells which discretizes the design space

The following relations given in Equations 154-155 establish when PJPDM coupled with Pareto Fitness and Normal Boundary Intersection is more computationally efficient than JPDM, respectively. Some things that can be concluded from these relations are that in general the more detailed the final design space the more PJPDM becomes preferable over JPDM. It is also possible to see that for larger problems with numerous design and random

variables (N_{vars}) PJPDM with PF starts to become less preferred and computational intensive. On the other hand, if the previously identified issues currently plaguing NBI when dealing with complex design spaces can be resolved, then PJPDM can potentially become very competitive for large and complex problems compared to JPDM.

$$\frac{n^{N_{vars}}}{n_{cell} * fcall_{optimizer_{JPDM}}} \leq 1 \tag{154}$$

$$\frac{fcall_{optimizer_{NBI}}\left[\frac{n(n+1)}{2}\right]}{fcall_{optimizer_{JPDM}} * n_{cell}} \leq 1 \tag{155}$$

Chapter VII

CONCLUSIONS

7.1 Research Questions and Hypotheses Revisited

In this chapter, the original research questions and hypotheses as well as sub-questions and sub-hypotheses will be revisited in order to establish whether they have been answered or validated, respectively.

> Research Question 1. How can a design methodology be formulated to allow a comparative and systematic evaluation and selection of various classes of thermal management systems in the early phases of conceptual design?
>
> Hypothesis 1. A design methodology can be formulated to evaluate thermal management technologies through the implementation of a capability-based inverse design approach at the vehicle level.

The design methodology based on a vehicle capability inverse design approach was defined in Chapter IV including 10 key steps: 1) Problem definition, 2) Identification of customer need and concept down-selection, 3) Definition of vehicle's capability-based design space, 4) Definition of design space ranges, 5) Definition of design of experiments, 6) Modeling and simulation, 7) Surrogate modeling, 8) Probabilistic analysis, 9) Pareto-based Joint Probability Decision Making, and 10) Inverse design space resolution. The innovations in this methodology come mainly from phases 9 and 10. In phase 9, a new probabilistic design space is defined based on the estimation of the Pareto frontiers (Pareto-based JPDM) which provides an alternative MADM approach to JPDM. In phase 10, a way to solve for the inverse design space is formulated allowing the mapping of vehicle capabilities for all technology configurations. A demonstration of the methodology is provided in Chapter VI for the TBCC case study. Several new research questions arose during the process of defining the design methodology which are listed and discussed below.

Research Question 2.1. What level of aerothermodynamic analysis fidelity is most suitable for the conceptual design methodology?

Hypothesis 2.1. Simplified physics-based tools consisting of 2-D flow analysis and engineering approximations will provide a good compromise between computational speed, fidelity, and flexibility for the aerothermodynamic analysis.

The aerothermodynamic tool based on simplified 2-D flow analysis was proven to be sufficiently adequate for conceptual design through the validation process given in Sections 5.3 and indirectly in case #3 of Section 5.4.3. The aerothermal analysis tool employed is capable of handling any type of design through its simplified geometry inputs consisting of run length and deflection angle. Furthermore with today's computational power, the run time for the 2-D flow aerothermal analysis is essentially insignificant (less than 5 seconds per case). This confirms the hypothesis and makes the case that this type of tool provides the desired level of fidelity along with computational speed and design flexibility.

Research Question 2.2. What would be the most suitable probabilistic analysis approach, which is not only the most computationally effective but also ties well into the design exploration environment?

Hypothesis 2.2. The implementation of surrogate models along with a Monte Carlo simulation will be the most adequate probabilistic approach because it will be able to provide joint probability density functions, and at the same time be the most computationally effective.

The three major approaches for performing probabilistic studies were introduced in the literature chapter. Later in Chapter IV, a benchmarking study was presented to determine the probabilistic approach that is best suited for this methodology. Of the three probabilistic approaches, sophisticated analysis codes coupled with Fast Probability Integration was immediately eliminated because it would not produce the needed measure of Pareto occurrences in the 3-D design space. The benchmarking study clearly showed that with today's computational power the only viable approach would be the one employing surrogate modeling coupled with Monte Carlo simulation.

Research Question 2.3. What surrogate modeling technique would be the most adequate for the implementation of the probabilistic analysis?

Hypothesis 2.3. Response surface equations will provide the appropriate level of accuracy for data fitting of the physics-based analysis.

The selection of the appropriate surrogate modeling technique was based on the decision flowchart shown in Figure 72. Response surface equations were demonstrated to adequately model the underlying physics-based analysis from the modeling and simulation. The validation for this goodness of fit was established in Section 6.4.1. In addition, response prediction profiles were provided in Appendix D as a good sanity check of the sensitivity trends.

Research Question 3. How can the design space exploration be formulated as to allow the designer to make intelligent decisions regarding the options and utilization of the various thermal management technologies?

Hypothesis 3. A probabilistic design space exploration environment can be achieved by implementing surrogate modeling along with numerical techniques for prediction of multi-objective Pareto frontiers.

The design space exploration environment defined as a Pareto-based JPDM was described in Section 4.2.8.1. A 3-D design space was defined based on three measures of merit of great interest to designers. These three measures are performance, economic, and safety effectiveness. This higher level design space of effectiveness was demonstrated in Figure 113 on page 178. It can be used by the designer to evaluate and compare thermal management technologies based on effectiveness level or probability of success for a region of interest. The effectiveness design space is based on surrogate models which are themselves based on the physics-based modeling and simulation analysis. The surrogate models are a key enabler for the implementation of the probabilistic analysis.

Research Question 3.1. What would be the most appropriate approach for the determination of technology Pareto frontiers: identification or prediction?

Hypothesis 3.1. Pareto frontier identification through the implementation of Pareto Fitness will provide the more robust approach for complex 3-D design spaces.

The two emerging techniques for Pareto frontier identification were found to be Normal Boundary Intersection and Pareto Fitness. The advantages and disadvantages of both of these techniques were defined in Sections 2.10.4-2.10.5. In Section 4.2.8.1, several benchmarks were performed comparing computational time and memory requirements for both techniques. These benchmarks showed further strengths and weaknesses between NBI and PF. Normal Boundary Intersection was found to be more scalable for bigger problems consisting of more input variables, and greater Pareto definition (discretization parameter). Pareto Fitness, on the other hand, was found to be far more robust regarding the types of complex design spaces that it is capable of handling. Pareto Fitness was selected as the technique of choice since it was found to work well for smaller problems (low number of input variables and discretization) as in the case for the particular case study demonstrated in this thesis.

Research Question 3.2. How can a capability inverse design space be generated at the vehicle level?

Hypothesis 3.2. The inverse design space describing vehicle capabilities can be produced by implementing a numerical optimizer which manipulates the design variables in order to decrease the Euclidian distance between the current and desired effectiveness solutions.

The inverse design space can be solved once the designer has selected a desired optimum solution from the probabilistic design space exploration environment based on effectiveness levels. Knowing the desired effectiveness levels, one can solve for the corresponding vehicle design variables (range, maximum Mach, payload) which can produce a vehicle solution meeting the desired effectiveness levels. The process by which the inverse design space is attained for vehicle capabilities was presented in detail in Section 4.2.9 and formulated in

Equations 143-??. An example of the inverse design space for the TBCC case study was successfully generate and provided in Section 6.5.

7.2 Problem Statement Revisited

The original problem statement defined in the problem definition section was:

> *How can thermal management technology selection be performed in a way that is structured, robust, accounts for the variability of factors beyond the designer's control, and can provide the most information to the designer early in the phases of conceptual design?*

This problem statement along with the literature review on the subject culminated in the research questions and hypotheses established in Chapter III and later revisited in the previous section. The hypothesis to the first research question addressed the bulk of the problem statement by formulating a well-defined and structured methodology that can deal with emerging and highly varying thermal management technologies while accounting for variability in the design. The end result was a vehicle capability inverse design space which categorizes each thermal management technology with respect to each other. This inverse design space is generated in terms of the parameters that the customer cares about and answers questions such as: how far can it go? how fast can it get there? and how much can it carry?

The hypotheses to research questions 2.1, 2.2, 2.3, 3.1, and 3.2 attempted to address more technical aspects of specific techniques and approaches pertaining to the formulation of the methodology. Some of these technical aspects included the determination of the type of probabilistic and surrogate models to employ, the type of aerothermodynamic analysis sufficiently adequate for the conceptual methodology, benchmarking of Pareto frontier estimation techniques, and establishing a formulation for the resolution of the inverse design space.

The hypothesis to research question 3 addressed the formulation of the design space exploration for the proposed methodology. This formulation accounted for uncertainty, as

well as the complexity and high level of disciplinary dependencies by making the design space transparent and not attempting to perform a global optimization.

The case study results for system effectiveness in Figure 113 demonstrated the high level of design space complexity. This also showed the importance for the designer to be able to thoroughly evaluate and understand the interactions between combinations of different thermal management technologies. It was demonstrated that certain technology combinations may lead to the degradation of overall system effectiveness.

7.3 Summary of Contributions

- The original problem statement has been successfully addressed through the implementation of the proposed conceptual design methodology for thermal management systems. The TBCC case study used to implement and demonstrate the methodology showed the high level of design space complexity inherent to the original problem. This complexity comes as a result of the large number of interrelationships in physical phenomena and compromises that exist in the design of a high-speed vehicle.

- As a by product for the 'proof of concept' or in this case methodology, a fully integrated sizing and synthesis environment has been developed and the most suitable aerothermodynamic and thermal management sizing techniques for conceptual design have been determined. The design environment allows the designer to readily run full design of experiments for various thermal management technologies and configurations in order to analyze their behaviors and characteristics. At this point, the environment can handle two types of technologies which have been used in the TBCC case study, 1) insulated structures, and 2) convective cooling. The thermal management optimizer allows the placement of heat exchangers along the windward or both leeward and windward side of the vehicle. The thermal management optimizer also allows the user to input either specific material configurations which it then sizes accordingly, or it performs a full optimization of not only thickness but also material distribution over the entire vehicle surface.

- A physics-based formulation for the quantification of the TMS' safety effectiveness corresponding to a certain degree of debris impact/damage has been presented in Section 4.2.6.8. It was also shown how this formulation can be applied towards risk mitigation in Section 6.5.1. This formulation carries all advantages of physics-based analysis in that it can deal with novel concepts that have not been studied before with no existing historical data. The disadvantage of this is that no debonding probabilistic characteristics of specific materials are accounted for.

- The formulated probabilistic design space exploration (step 9) of the methodology provides an alternative approach to multi-attribute decision making which does not require the use of a numerical optimizer when coupled with PF. The proposed Pareto-based JPDM provides more information and knowledge up front to the designer regarding the entire probabilistic design space, as opposed to the variability around a single optimum design point (JPDM). This approach also carries certain disadvantages which have been discussed in Section 6.6 and which will lead to lessons learned and tentative future work.

- A formulation has been provided and put into practice for the resolution of the inverse design space once the desired effectiveness level is determined. The formulation is loosely based on non-preemptive Goal Programming with equal weighted deviations. A constraint optimizer (SQP) is implemented which attempts to minimize the deviation between the current solution and the desired effectiveness solution. This key step helps link vehicle capabilities to TMS technology subsystems in a top-down design approach. The inverse design space shows the customer which technology should be invested in depending on the type of mission of interest.

7.4 Lessons Learned and Future Work

- Improvement to the TPS optimization algorithm to reduce not only weight but also to make the vehicle surface smooth and account for aerodynamic efficiency. This requires the implementation of shape functions to the material thickness as discussed

by Bhungalia et al [7].

- Physical limits on material thickness need to be accounted for as constraints to the TMS optimizer. Otherwise, the optimizer may size one material beyond its physical limits simply because it still provides a 'lighter' solution over a different material with feasible thickness but which ultimately ends up being heavier. The main obstacle to accomplishing this is the overall lack of available data regarding the different TMS materials in the database of Appendix A.

- In this thesis, the backplate of the TPS structure was assumed to be adiabatic as is the case for most studies of this nature. This means that there is essentially no heatrate being transferred into the internal structure of the vehicle. This is known to be an idealistic scenario which does not hold true in real world applications. This adiabatic constraint leads the optimizer to unrealistically oversize the TPS structure to ensure the change in temperature at the backplate is zero. A model for the estimation of the heatrate leakage into the internal structure would help the computation of much more realistically sized TPS structures.

- One last improvement to the TMS optimizer implemented in the modeling and simulation is the capability to perform multi-material layer stacking to more adequately optimize the thickness and weight of the TPS layer.

- Pareto Fitness was used within this thesis to identify the Pareto frontier points because it was robust and lent itself well to small problems with low number of variables. Pareto Fitness however becomes highly inefficient for larger problems. Improvements in Normal Boundary Intersection deficiencies when it comes to more complex design spaces will boost the practicality of Pareto-based JPDM for large problems with many design and random variables. The improvements necessary for NBI to become feasible include the capability to predict convex and concave Pareto frontiers, a more robust algorithm for choosing the initial optimizer starting point, and an optimizer which can handle working or starting from the infeasible domain.

- The identification of Pareto points with Pareto Fitness was carried out using a simple design space sampling approach. The advantages of Pareto Fitness could be further improved by implementing a Genetic Algorithm to optimize the Pareto Fitness function of a design population. The addition of an intelligent selection process would add a level of complexity but would also be more efficient and could improve its scalability for applications with a large number of continuous variable.

- Introduction of TPS debonding characteristics and probabilities for each material to complement the physics-based analysis on the effects of debris impact.

Appendix A

MATERIAL PROPERTY DATABASE

The database given in Table 26 provides the material properties (density, specific heat, thermal conductivity, emissivity) which are utilized while solving the 1-D transient heat equation. In addition, the table includes temperature information required during the TPS optimization process to assure that temperature limits are not violated, as well as economic, and operational data that can be used to estimate the life cycle cost of the TPS.

Table 26: Material Property Database

Index	Name	Density kg/m3	Specific Heat J/kg-K	Thermal Conductivity W/m-K	Emissivity	Single Use Temperature Limit K	Multiple Use Temperature Limit K	Purchase Cost $/m2	Installation Time s/m2	(Maintenance) Inspection/Repair Time per Flight s/m2	Replacement Fraction per Flight	Reuse Flight # Limit	Comments
1	TABI	112	741	0.0395	0.87	1480	1480	11100	190000	19000	0.0096	0	Blanket
2	AETB-12	192	628	0.064	0.88	1870	1700	12500	853000	24800	0.0014	100	Tile
3	AETB-8	128	628	0.0684	0.9	1810	1640	12500	853000	24800	0.0014	100	Tile
4	AFRSI	96.1	741.1	0.0329	0.87	1090	922	3550	236000	37200	0.018	0	Blanket
5	AFRSI-2200	96.1	741.1	0.0329	0.56	1480	1310	3550	236000	37200	0.018	0	Blanket
6	AFRSI-2500	96.1	741.1	0.045	0.56	1370	1370	3550	236000	37200	0.018	0	Blanket
7	FRCI-12	192	712	0.05297	0.92	1810	1640	12500	3530000	81400	0.0025	100	Tile
8	FRCI-20	320	712	0.05297	0.92	1810	1640	12500	3530000	81400	0.0025	100	Tile
9	FRSI	86.5	1310	0.0406	0.8	644	506	1720	21300	3490	0.028	0	Blanket
10	LI-2200	352	628	0.07443	0.9	1810	1640	12500	3530000	81400	0.0025	100	Tile
11	LI-900	144.2	628	0.0476	0.88	1760	1590	12500	3530000	81400	0.0025	100	Tile
12	PBI	80.1	1260	0.0547	0.8	756	700	2580	18600	3490	0.024	0	Blanket
13	ACC	1600	712	4	0.78	1870	1870	129000	372000	4260	0.0013	100	Other
14	RCC	1580	712	4	0.78	2030	1920	129000	372000	5430	0.0013	33	Other
15	Inconel-617	8410	456	15.1	0	1680	1680	N/A	N/A	N/A	N/A	100	Metallic

Appendix B

ECONOMIC ESTIMATION RELATIONS

The simple economic relations for the estimation of the life cycle cost of a military vehicle shown below were obtained in Roskam [79]. Cost estimating relations are typically historical-based regressions on past or existing systems, which relate vehicle characteristics such as vehicle geometry, number of engines, maximum velocity, and takeoff gross weight to program costs such as RDTE, acquisition, operational, and disposal costs.

B.1 Life Cycle Cost

$$LCC = C_{rdte} + C_{acq} + C_{ops} + C_{disp}$$

B.2 Research, Development, Testing and Evaluation

$$C_{rdte} = C_{aed_r} + C_{dst_r} + C_{fta_r} + C_{fto_r} + C_{tsf_r} + C_{pro_r} + C_{fin_r}$$

$$C_{aed_r} = (MHR_{aed_r})\, R_{e_r}$$

$$MHR_{aed_r} = 0.0369\, (W_{ampr})^{0.791}\, (V_{max})^{1.526}\, (N_{rdte})^{0.183}\, (F_{diff})\, (F_{cad})$$

$$W_{ampr} = log^{-1}\left[0.1936 + 0.8645\, (log\, (W_{TO}))\right]$$

$$(R_{e_r})_{then\ year} = (R_{e_r})_{1989}\left[(CEF_{then\ year})\,/\,(CEF_{1989})\right]$$

$$C_{dst_r} = 0.008325\, (W_{ampr})^{0.873}\, (V_{max})^{1.890}\, (N_{rdte})^{0.346}\, (CEF)\, (F_{diff})$$

$$C_{fta_r} = C_{(e+a)_r} + C_{man_r} + C_{mat_r} + C_{tool_r} + C_{qc_r}$$

$$C_{(e+a)_r} = (C_{e_r} N_e + C_{p_r} N_p + C_{avionics_r})(N_{rdte} - N_{st})$$

$$C_{man_r} = (MHR_{man_r})\, (R_{m_r})$$

$$MHR_{man_r} = 28.984\, (W_{ampr})^{0.740}\, (V_{max})^{0.543}\, (N_{rdte})^{0.524}\, (F_{diff})$$

$$C_{mat_r} = 37.632\, (F_{mat})\, (W_{ampr})^{0.689}\, (V_{max})^{0.624}\, (N_{rdte})^{0.792}\, (CEF)$$

$$C_{tool_r} = (MHR_{tool_r})\, (R_{t_r})$$

$$MHR_{tool_r} = 4.0127\,(W_{ampr})^{0.764}\,(V_{max})^{0.899}\,(N_{rdte})^{0.178}\,(N_{r_r})^{0.066}\,(F_{diff})$$

$$C_{qc_r} = 0.13\,(C_{man_r})$$

$$C_{fto_r} = 0.001244\,(W_{ampr})^{1.160}\,(V_{max})^{1.371}\,(N_{rdte} - N_{st})^{1.281}\,(CEF)\,(F_{diff})\,(F_{obs})$$

$$C_{tsf_r} = F_{tsf_r} C_{rdte}$$

$$C_{pro_r} = F_{pro_r} C_{rdte}$$

$$C_{fin_r} = F_{fin_r} C_{rdte}$$

B.3 Manufacturing and Acquisition Cost

$$C_{acq} = C_{man} + C_{pro_m}$$

$$C_{man} = C_{aed_m} + C_{apc_m} + C_{fto_m} + C_{fin_m}$$

$$C_{aed_m} = \left(MHR_{aed_{program}}\right)\left(R_{e_m}\right) - C_{aed_r}$$

$$MHR_{aed_{program}} = 0.0396\,(W_{ampr})^{0.791}\,(V_{max})^{1.526}\,(N_{program})^{0.183}\,(F_{diff})\,(F_{cad})$$

$$C_{apc_m} = C_{(e+a)_m} + C_{int_m} + C_{man_m} + C_{mat_m} + C_{tool_m} + C_{qc_m}$$

$$C_{(e+a)_m} = \left(C_{e_m} N_e + C_{p_m} N_p + C_{avionics_m}\right)(N_m)$$

$$C_{int_m} = (F_{int})\,(N_{pax})\,(N_m)\,[(CEF_{then\ year})\,/\,(CEF_{1990})]$$

$$C_{man_m} = \left(MHR_{man_{program}}\right)\left(R_{m_m}\right) - C_{man_r}$$

$$MHR_{man_{program}} = 28.984\,(W_{ampr})^{0.740}\,(V_{max})^{0.543}\,(N_{program})^{0.524}\,(F_{diff})$$

$$C_{mat_m} = C_{mat_{program}} - C_{mat_r}$$

$$C_{mat_{program}} = 37.632\,(F_{mat})\,(W_{ampr})^{0.689}\,(V_{max})^{0.624}\,(N_{program})^{0.792}\,(CEF)$$

$$C_{tool_m} = \left(MHR_{tool_{program}}\right) R_{t_m} - C_{tool_r}$$

$$C_{qc_m} = 0.13\,(C_{man_m})$$

$$C_{fto_m} = N_m\left(C_{ops/hr}\right)(t_{pft})\,(F_{ftoh})$$

$$C_{fin_m} = (F_{fin_m})\,(C_{man})$$

$$C_{pro_m} = (F_{pro_m})\,(C_{man})$$

B.4 Operating Cost

$$C_{ops} = C_{pol} + C_{persdir} + C_{persind} + C_{conmat} + C_{spares} + C_{depot} + C_{misc}$$

$$C_{pol} = (F_{ol})\,(W_{f_{used}})\,((FP)\,/\,(FD))\,(N_{mission})\,(N_{serv})\,(N_{yr})$$

$$N_{mission} = \left(U_{ann_{flt}}\right)\,/\,(t_{mis})$$

$$C_{persdir} = C_{crewpr} + C_{mpersdir}$$

$$C_{crewpr} = (N_{serv})\,(N_{crew})\,(R_{cr})\,(Pay_{crew})\,(OHR_{crew})\,(N_{yr})$$

$$C_{mpersdir} = (N_{serv})\,(N_{yr})\,\left(U_{ann_{flt}}\right)\,(MHR_{flthr})\,(R_{m_{ml}})$$

$$C_{persind} = (f_{persind})\,(C_{ops})$$

$$C_{conmat} = (N_{serv})\,(N_{yr})\,\left(U_{ann_{flt}}\right)\,(MHR_{flthr})\,(R_{conmat})$$

$$C_{spares} = (f_{spares})\,(C_{ops})$$

$$C_{depot} = (f_{depot})\,(C_{ops})$$

$$C_{misc} = (f_{misc})\,(C_{ops}) \approx 4\,(C_{conmat})$$

B.5 Disposal Cost

$$C_{disp} = 0.01\,(LCC)$$

Appendix C

SURROGATE MODEL VALIDATION RESULTS

It is important to validate the surrogate models to assure they properly represent the behavior of the system. This appendix contains a series of analyses which can be performed in order to ensure the 'goodness of fit' of these surrogate models. The results shown here correspond to the response surface equation surrogate models which were implemented for the TBCC demonstration case study.

Ideally, the coefficient of determination will be as close to one as possible, while the actual versus predicted should show a tight fit along the one-to-one trend line extending from the bottom left to the upper right corner of the plot. The residual versus predicted plot should show random distribution of the points with no noticeable trends or non-linearities. This could mean there are higher order terms which exist but are not accounted for in the surrogate model. It is still acceptable for a residual versus predicted plot to show non-linearity or clumping as long as the total error for the residual is relatively small. A residual percent error of less than 10% is typically deemed acceptable. The model fit error is used to ensure that the error from higher order effects is normally distributed. The normal distribution is expected to have mean and standard deviation values as close as possible to zero and one, respectively. The final step is the model representation error which requires running a set of random cases in order to check how the surrogate models behave with off-design settings. In other words, one must test experimental settings which were not used within the design of experiments. The error distributions are checked again in the same way as was done for the model fit error.

C.1 Coefficient of Determination (R^2) and Actual versus Predicted

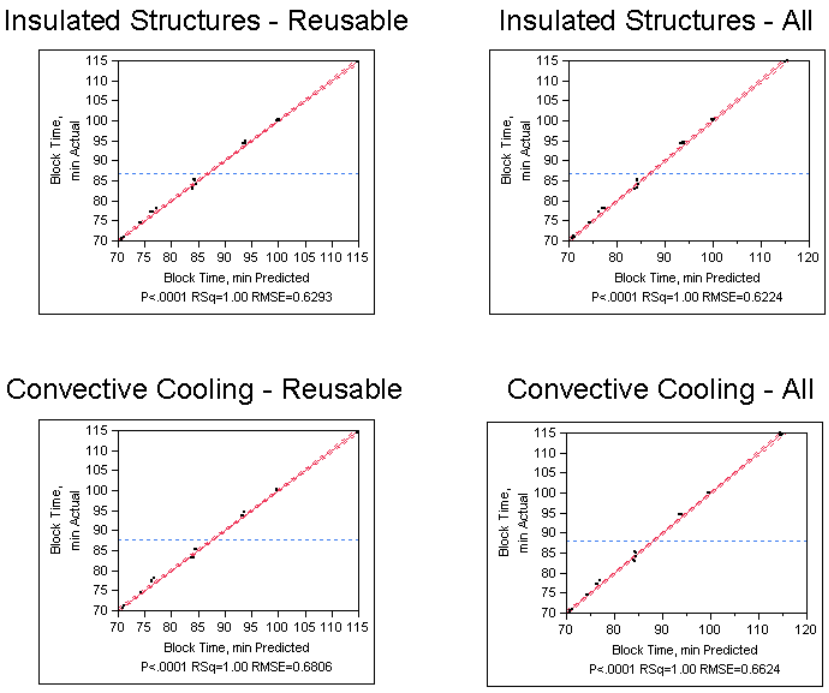

Figure 123: Actual versus Predicted - Block Time

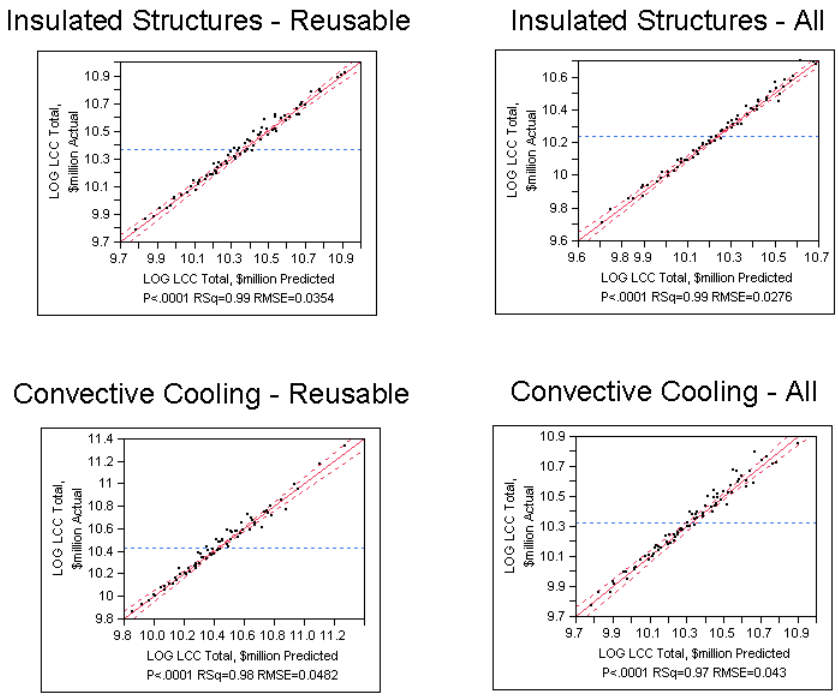

Figure 124: Actual versus Predicted - Life Cycle Cost (LCC)

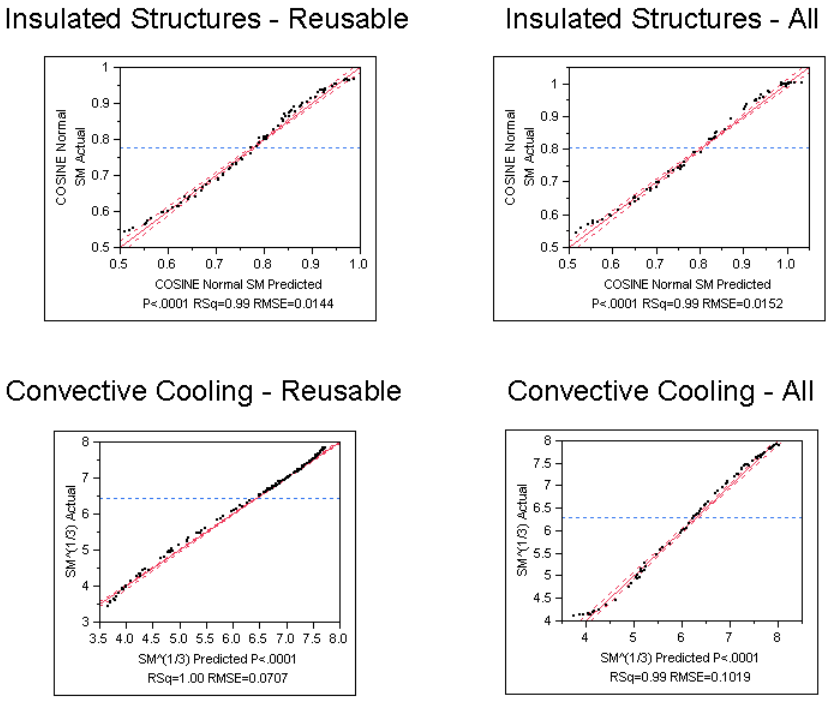

Figure 125: Actual versus Predicted - Safety Margin (SM)

C.2 Residual versus Predicted

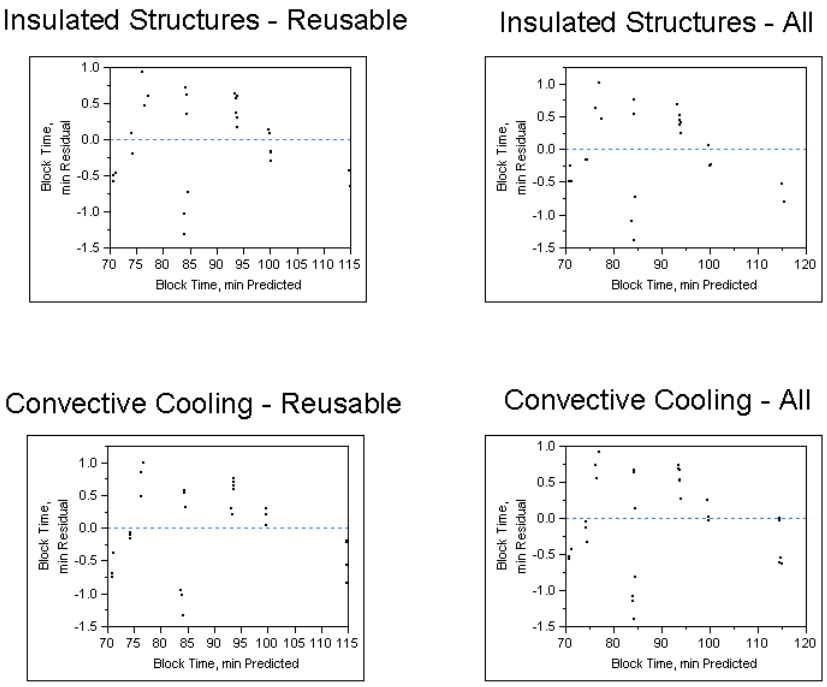

Figure 126: Residual versus Predicted - Block Time

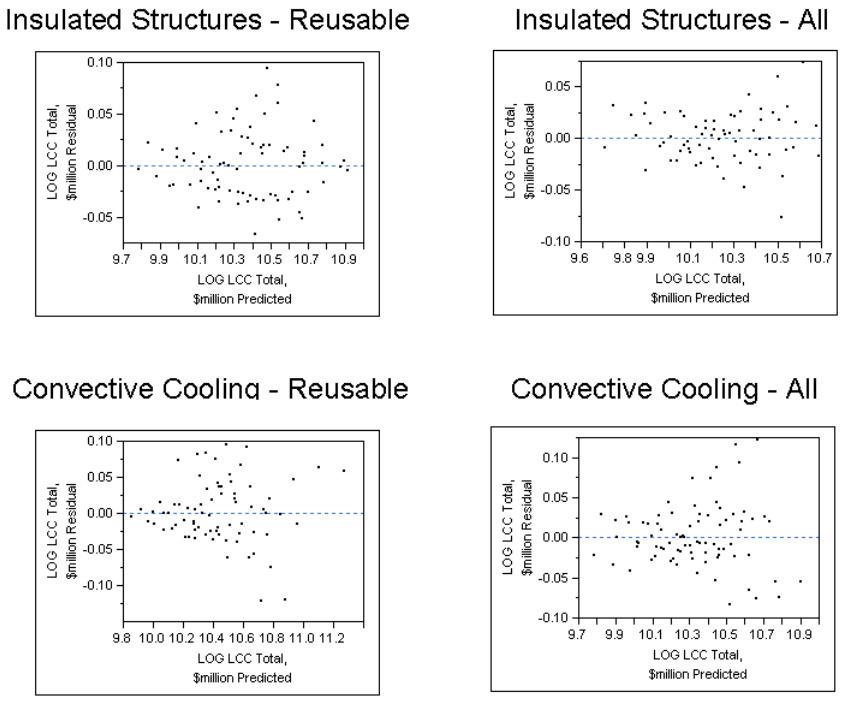

Figure 127: Residual versus Predicted - Life Cycle Cost (LCC)

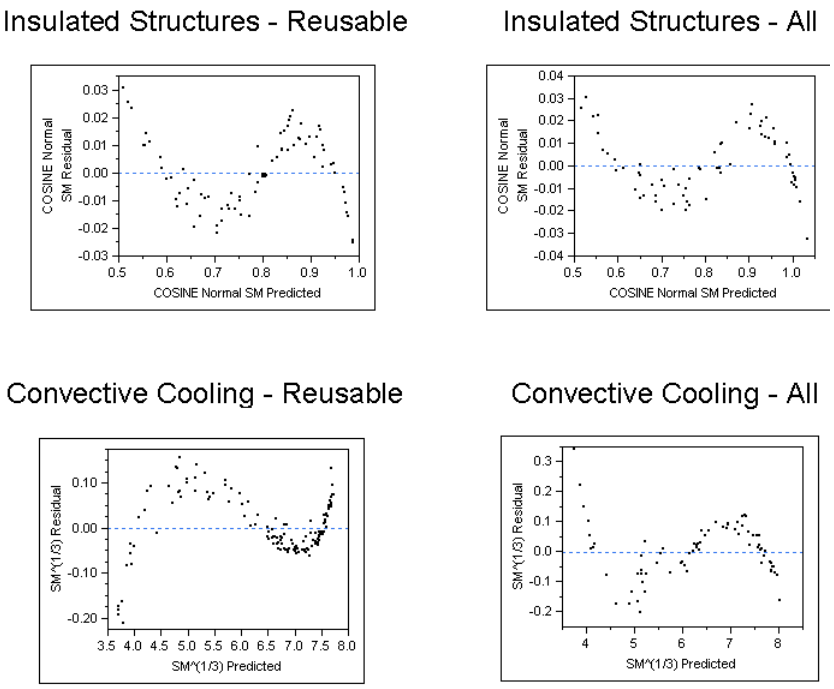

Figure 128: Residual versus Predicted - Safety Margin (SM)

C.3 Model Fit Error and Model Representation Error

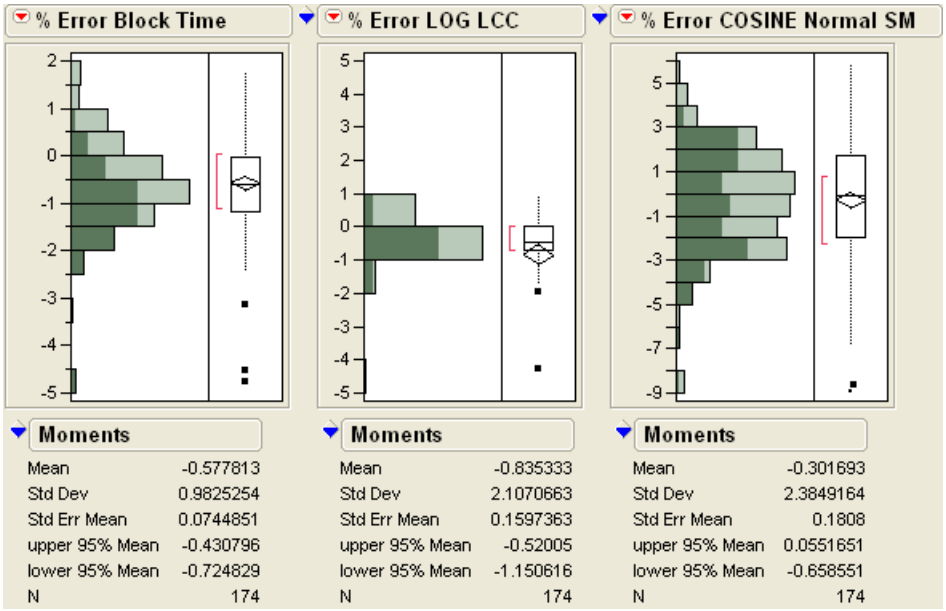

Figure 129: MFE and MRE - Insulated Structures (Reusable)

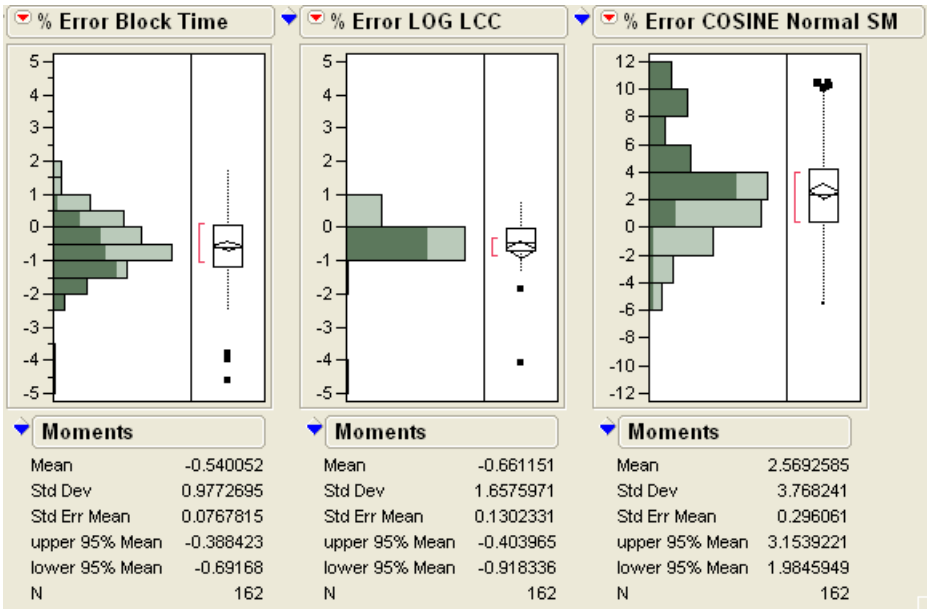

Figure 130: MFE and MRE - Insulated Structures (All)

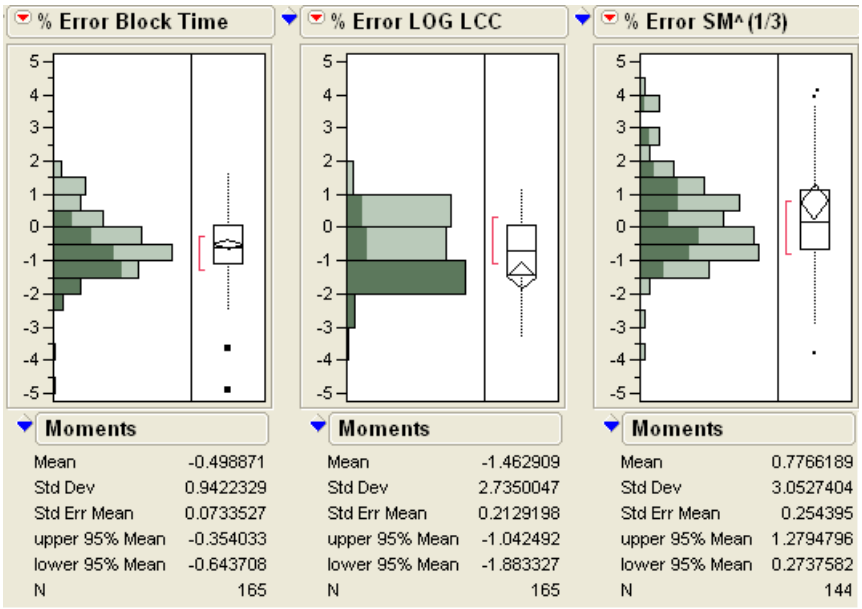

Figure 131: MFE and MRE - Convective Cooling (Reusable)

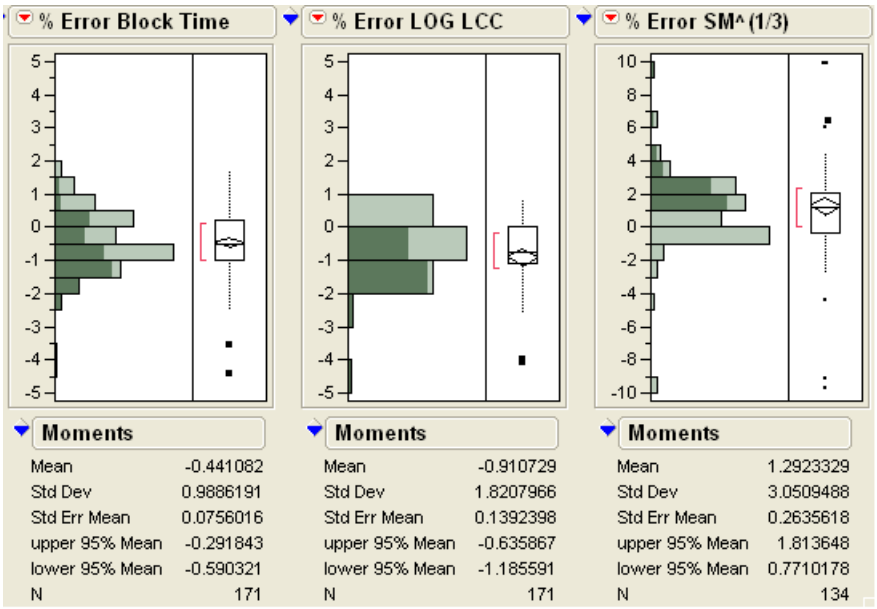

Figure 132: MFE and MRE - Convective Cooling (All)

Appendix D

SENSITIVITY PROFILES

The sensitivity profiles given in this appendix are based on the response surface equations obtained for the TBCC case study. These sensitivities can be used as a sanity check and for the sake of transparency to ensure that the trends being modeled are reasonable. The blue trend lines surrounding the sensitivity curves denote the confidence levels.

The sensitivities given below show an expected increase in block time as range increases, and a decrease in block time as Mach number increases. It is important to note the small increase in block time at the higher Mach numbers which is likely due to the longer time required to slow down the vehicle. Payload does not seem to affect the block time much as the trend line appears relatively flat compared to that of range and Mach number.

Life cycle cost typically increases with range, payload, and fuel cost per barrel. On the other hand, LCC appears to first decrease and the increase as the Mach number increases. The reason for this could be an improvement in propulsive efficiency for the TBCC vehicle which yields a smaller vehicle. This in turn translates into lower vehicle cost, as well lower thermal requirements, thermal management system acreage and cost.

Safety margin shows very little sensitivity to range, Mach number, and payload but shows significant negative correlation with TPS thickness failure. The sensitivity trend line for SM appears to have a positive correlation with TPS thickness failure because a Cosine transformation has been applied in order to improve the accuracy of the surrogate model. In reality, as is expected, SM decreases as the thickness of the TPS decreases.

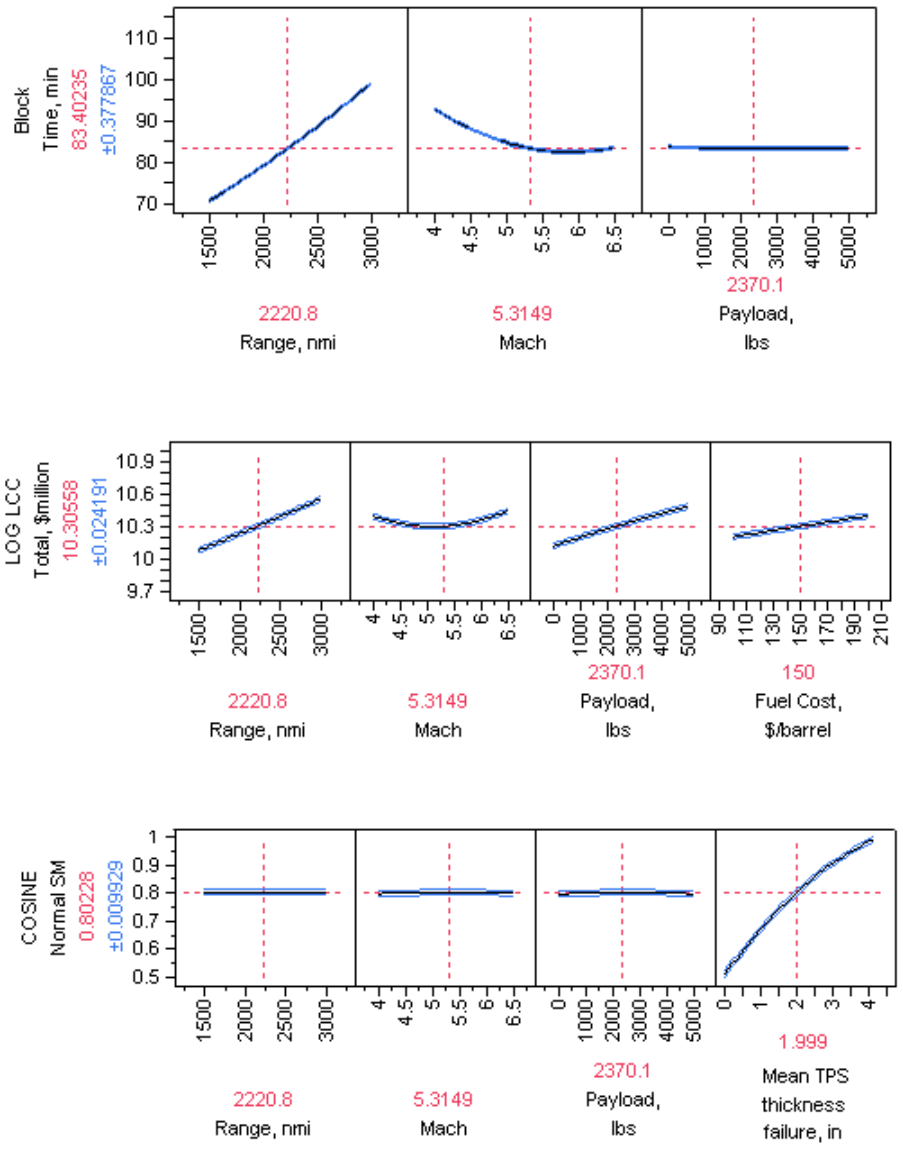

Figure 133: Sensitivity Profiles for Insulated Structures - Reusable Materials

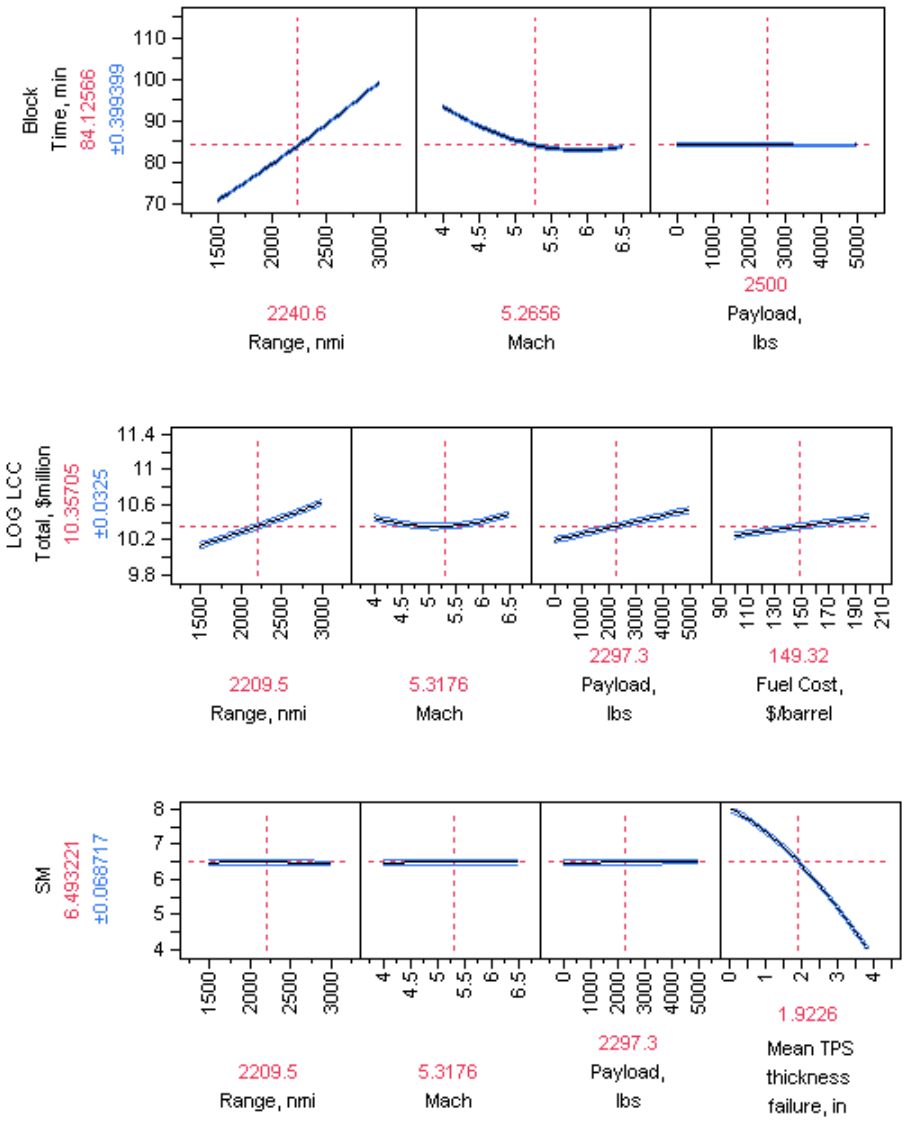

Figure 134: Sensitivity Profiles for Convective Cooling - Reusable Materials

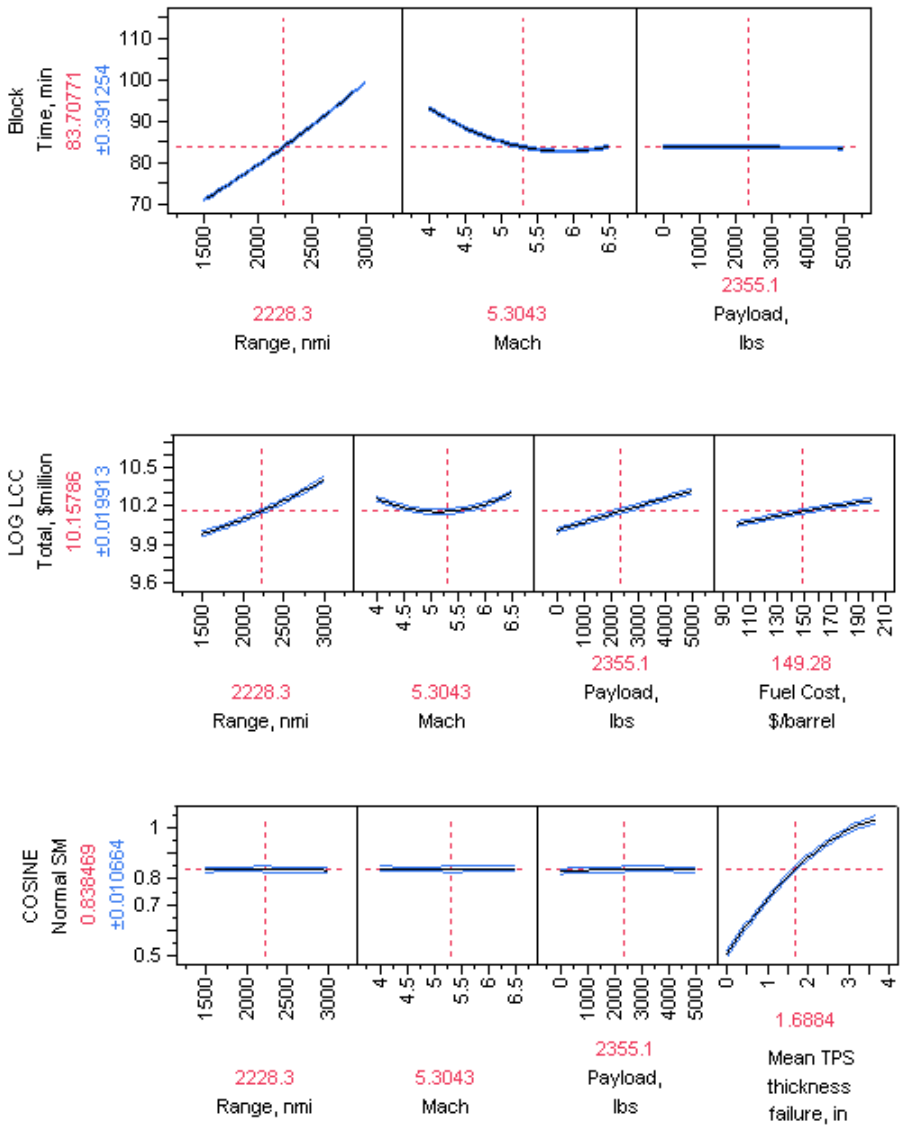

Figure 135: Sensitivity Profiles for Insulated Structures - All Materials

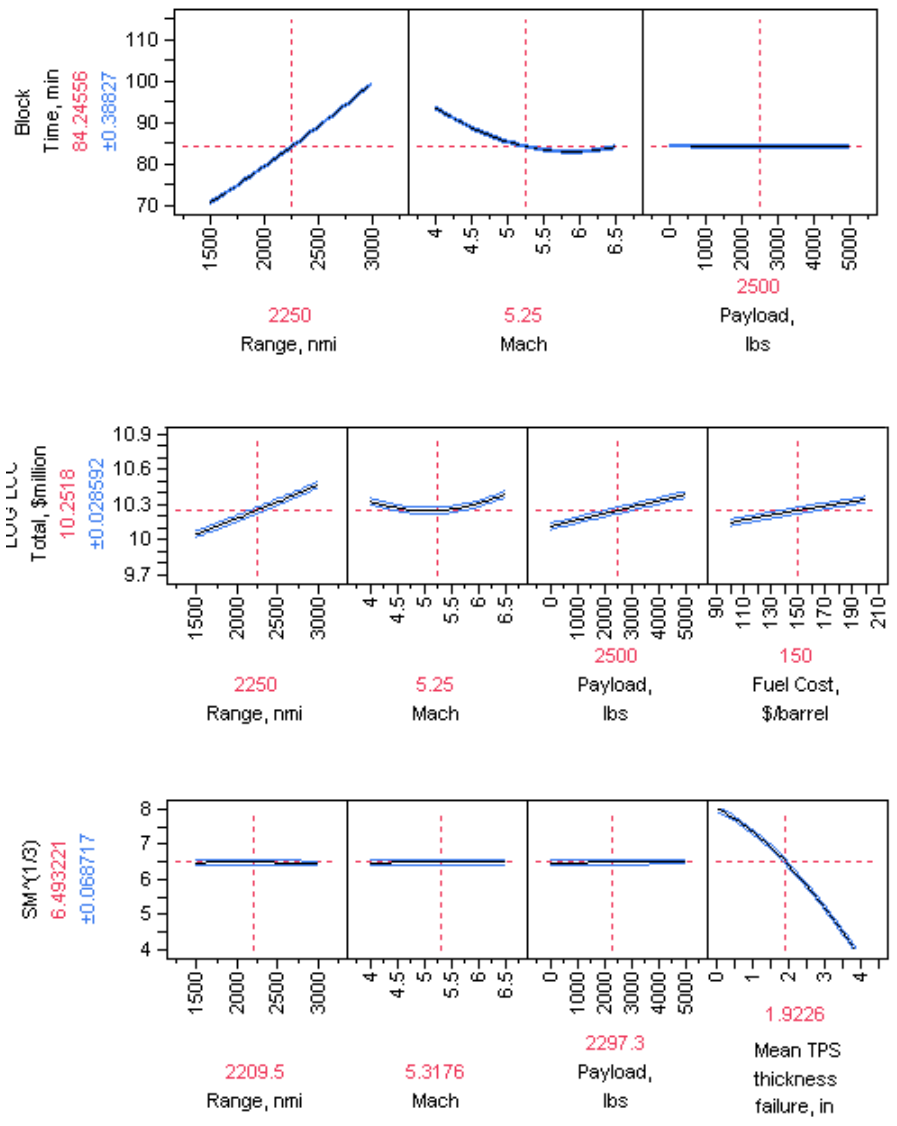

Figure 136: Sensitivity Profiles for Convective Cooling - All Materials

Appendix E

SOURCE CODE

The MATLAB source code for several key elements within the modeling and simulation are given below. These include the algorithm for the 1-D transient heat equation solver which is coupled with an SQP optimizer in order to size and optimize the TPS layer, as well as two Pareto determination techniques.

E.1 1-D Transient Heat Equation Solver

```
function [Tmax1,Tmax2] = Heat1D_implicit(xf)
global Tmax1 Tmax2 T1_h T2_h t timef qu_in qu qcond Nx Nt rho cp
global k e sig negativeheatrates
% Nx number of total points on TPS
% Nt number of total time points

if xf <= 1e-6
xf = 1e-4;
end

% Computational constants
error = 1e-3;
niter = 1e4; % maximum number of iterations for convergence
sig = 5.6704e-8; % Stefan-Boltzman constant W/m2-K4
xo = 0;

% Time
to = timef(1,1);
tf = timef(1,end);
% Discretization
dx = (xf-xo)/(Nx-1);
x = xo:dx:xf;
```

```
dt = (tf-to)/(Nt-1);
t = to:dt:tf;

% Convection heatrate interpolation
qu = interp1(timef,qu_in,t,'linear'); % W/m2
qu2 = qu;

% Generate coefficients and populate matrix
alpha = k/(rho*cp);
r = alpha*dt/(dx^2);
V1 = -r*ones(Nx-1,1);
V2 = (1+2*r)*ones(Nx,1);
J = diag(V1,-1) + diag(V2,0) + diag(V1,1);

% Specify initial temperatures
To = 300*ones(Nx,1);
T(:,1) = To;

% Solve 1D unsteady heat equation
for i = 2:Nt
if negativeheatrates == 1
if qu(i) < 0
qu(i) = 1e-9;
end
end
Told = T(:,i-1);

for z = 1:niter
% Set up BC1 (free flow)
J1 = zeros(1,Nx); J1(1,1) = -k - 4*e*sig*dx*(Told(1)^3); J1(1,2) = k;
J(1,:) = J1;

% Set up BC2 adiabatic internal structure
J2 = zeros(1,Nx); J2(1,end-1) = -1; J2(1,end) = 1;
J(end,:) = J2;
```

```
f = J*Told - T(:,i-1); % Told here is really Tnew

% Set up f(1) at BC1 and f(end) at BC2
f(1) = (-k - e*sig*dx*(Told(1)^3))*Told(1) + k*Told(2) + qu(i)*dx;
f(end) = 0; %Told(Nx-1) - Told(Nx); %f(end) = 0;
dT = -inv(J)*f;
Tnew = Told + dT;
conv = sqrt(dT'*dT);

if conv < error
T(:,i) = Tnew;
break
end

Told = Tnew;
end
end

Tmax1 = max(T(1,:));
Tmax2 = max(T(end,:));
T1_h = T(1,:);
T2_h = T(end,:);
qrad = e*sig*(T(1,:).^4);
qcond = qu - qrad;
qu = qu2; % Restore original heatrates

end
```

E.2 Pareto Fitness Algorithm

```
function [f_vector,f1_vector,f2_vector,f3_vector,npareto] = PF3_SMP(DIR,INPUT)
global fcount flagstart f_limits_current

ncores = INPUT.ncores; % only use (1, 4, 16)
% flag for drawing design space contour (0 = no, 1 = yes)
flag_draw = 0;
```

```
% flag for drawing the negative ideal frontier (0 = no, 1 = yes), only if flag_draw = 1
negative_draw = 0;
% objective (minimize = lower is better, maximize = greater is better)
objective = INPUT.objective;
ND = INPUT.N; % number of dimensions in design space
Ntech = INPUT.Ntech; % number of Pareto frontiers
n = INPUT.n; % discretization parameter (even numbers only)
dimension_flag = INPUT.dimension_flag;
flag_normal_dimension = INPUT.flag_normal_dimension;

% main working directory
DIRmain = DIR.DIRmain;
DIRPF3 = DIR.DIRPF3;
f_vector_out = NaN*ones(n^ND,3,Ntech);
DIRcurrent = pwd;
for z = 1:Ntech
clear pareto_set_pos pareto_set_neg pareto_set_pos_normal

% Box constraints
DIRobj = [DIRcurrent,'/objfunction/tech',num2str(z),'/'];
cd(DIRobj);
rehash
[x_limit] = const;
size_x_limit = size(x_limit);
Nvars = size_x_limit(1);
cd(DIRcurrent);

% Compute time intervals
for i = 1:Nvars
dx(i) = (x_limit(i,2) - x_limit(i,1))/(n - 1);
if dx(i) == 0
dx(i) = 0.0001;
end
end

% Parametization
```

```
for i = 1:Nvars
x(i,1:n) = x_limit(i,1):dx(i):x_limit(i,2);
end

% Define input structure
param = [ncores, ND, Nvars, Ntech, n];
flagstart = 1;
cd(DIRPF3)
clear f1 f2 f3
[f1,f2,f3] = evaluatefun(DIRobj,DIRPF3,x,param);
cd(DIRcurrent);

% Make objective functions into single vectors
f1vector = zeros(1,n^ND);
f2vector = zeros(1,n^ND);
f3vector = zeros(1,n^ND);
c = 1;
for i = 1:n
for j = 1:n
for k = 1:n
f1vector(1,c) = f1(i,j,k);
f2vector(1,c) = f2(i,j,k);
f3vector(1,c) = f3(i,j,k);
c = c + 1;
end
end
end

% Normalize function values
if strcmp(objective,'minimize') ~= 1 || strcmp(objective,'min') ~= 1
direct = -1;
else
direct = 1;
end
rawf1min = min(f1vector);
rawf1max = max(f1vector);
```

```
rawf2min = min(f2vector);
rawf2max = max(f2vector);
rawf3min = min(f3vector);
rawf3max = max(f3vector);
f1norm = (f1vector - rawf1min)./(rawf1max - rawf1min);
f2norm = (f2vector - rawf2min)./(rawf2max - rawf2min);
f3norm = (f3vector - rawf3min)./(rawf3max - rawf3min);

% Set appropriate direction for the previously design space dimensions f1, and f2
if dimension_flag(1) == -1
f1temp = (1-f1norm);
f1norm = f1temp;
end
if dimension_flag(2) == -1
f2temp = (1-f2norm);
f2norm = f2temp;
end
if dimension_flag(3) == -1
f3temp = (1-f3norm);
f3norm = f3temp;
end
f1norm = direct*f1norm;
f2norm = direct*f2norm;
f3norm = direct*f3norm;

% Determine Pareto fitness function
c = 1;
f1temp = zeros(n^ND,n^ND);
f2temp = zeros(n^ND,n^ND);
f3temp = zeros(n^ND,n^ND);
for i = 1:(n^ND)
for j = 1:(n^ND)
f1temp(i,c) = f1norm(1,i) - f1norm(1,j);
f2temp(i,c) = f2norm(1,i) - f2norm(1,j);
f3temp(i,c) = f3norm(1,i) - f3norm(1,j);
c = c + 1;
```

```
end
c = 1;
end

% Place inf at i=j so we do not use them
for i = 1:(n^ND)
for j = 1:(n^ND)
if i == j
f1temp(i,j) = -inf;
f2temp(i,j) = -inf;
f3temp(i,j) = -inf;
end
end
end

% Find minimums
for i = 1:(n^ND)
fmin(i,1:(n^ND)) = min([f1temp(i,1:(n^ND));f2temp(i,1:(n^ND));f3temp(i,1:(n^ND))]);
fmax(i) = max(transpose(fmin(i,1:(n^ND))));
F(i) = 1-fmax(i);
end

% Write back in design space matrix form
i = 1; j = 1; k = 1;
for nn = 1:(n^ND)
Ftemp(i,j,k) = F(nn);
k = k + 1;
if mod(nn,n) == 0
j = j + 1;
k = 1;
end
if mod(nn,n^2) == 0
i = i + 1;
j = 1;
k = 1;
end
```

```
end

% Free up memory
clear f1temp f2temp fmin fmax F
F = Ftemp;
clear Ftemp

% Determine where the positive Pareto set lies
flag_pareto_pos = zeros(n,n,n);
for i = 1:n
for j = 1:n
for k = 1:n
if F(i,j,k) > 1
flag_pareto_pos(i,j,k) = 1;
end
end
end
end

% Create positive Pareto vector from flag_pareto_pos
numtotal = sum(sum(sum(flag_pareto_pos)));
pareto_set_pos = zeros(ND,numtotal);
nn = 1;
for j = 1:n
for i = 1:n
for k = 1:n
if flag_pareto_pos(i,j,k) == 1
pareto_set_pos(1,nn) = f1(i,j,k);
pareto_set_pos(2,nn) = f2(i,j,k);
pareto_set_pos(3,nn) = f3(i,j,k);
nn = nn + 1;
end
end
end
end
```

```
% Sort Pareto set by increasing first dimension
pareto_set_pos = transpose(pareto_set_pos);
pareto_set_pos = sortrows(pareto_set_pos);
pareto_set_pos = transpose(pareto_set_pos);
if negative_draw == 1 % Draw the contour of the entire design space

% Normalize function values
direct = -direct;
f1norm = direct*(f1vector - rawf1min)./(rawf1max - rawf1min);
f2norm = direct*(f2vector - rawf2min)./(rawf2max - rawf2min);
f3norm = direct*(f3vector - rawf3min)./(rawf3max - rawf3min);

% Determine Pareto fitness function
c = 1;
f1temp = zeros(n^ND,n^ND);
f2temp = zeros(n^ND,n^ND);
f3temp = zeros(n^ND,n^ND);
for i = 1:(n^ND)
for j = 1:(n^ND)
f1temp(i,c) = f1norm(1,i) - f1norm(1,j);
f2temp(i,c) = f2norm(1,i) - f2norm(1,j);
f3temp(i,c) = f3norm(1,i) - f3norm(1,j);
c = c + 1;
end
c = 1;
end

% Place inf at i=j so we do not use them
for i = 1:(n^ND)
for j = 1:(n^ND)
if i == j
f1temp(i,j) = -inf;
f2temp(i,j) = -inf;
f3temp(i,j) = -inf;
end
end
```

```
end

% Find minimums
for i = 1:(n^ND)
fmin(i,1:(n^ND)) = min([f1temp(i,1:(n^ND));f2temp(i,1:(n^ND));f3temp(i,1:(n^ND))]);
fmax(i) = max(transpose(fmin(i,1:(n^ND))));
F(i) = 1-fmax(i);
end

% Write back in design space matrix form
i = 1; j = 1; k = 1;
for nn = 1:(n^ND)
Ftemp(i,j,k) = F(nn);
k = k + 1;
if mod(nn,n) == 0
j = j + 1;
k = 1;
end
if mod(nn,n^2) == 0
i = i + 1;
j = 1;
k = 1;
end
end

% Free up memory
clear f1temp f2temp fmin fmax F
F = Ftemp;
clear Ftemp

% Determine where the negative Pareto set lies
flag_pareto_neg = zeros(n,n,n);
for i = 1:n
for j = 1:n
for k = 1:n
if F(i,j,k) >= 1
```

```
flag_pareto_neg(i,j,k) = 1;
end
end
end
end

% Create positive Pareto vector from flag_pareto_neg
numtotal = sum(sum(sum(flag_pareto_neg)));
pareto_set_neg = zeros(ND,numtotal);
nn = 1;
for j = 1:n
for i = 1:n
for k = 1:n
if flag_pareto_neg(i,j,k) == 1
pareto_set_neg(1,nn) = f1(i,j,k);
pareto_set_neg(2,nn) = f2(i,j,k);
pareto_set_neg(3,nn) = f3(i,j,k);
nn = nn + 1;
end
end
end
end

% Sort Pareto set by increasing first dimension
pareto_set_neg = transpose(pareto_set_neg);
pareto_set_neg = sortrows(pareto_set_neg);
pareto_set_neg = transpose(pareto_set_neg);
end

% Plot results
if flag_draw == 1
figure(1)
plot3(f1vector,f2vector,f3vector,'o','MarkerSize',2)
xlabel('OEC1');
ylabel('OEC2');
zlabel('OEC3');
```

```
hold on
view([-1 -1 1]);
plot3(pareto_set_pos(1,:),pareto_set_pos(2,:),pareto_set_pos(3,:),'k.','MarkerSize',25)
if negative_draw == 1
plot3(pareto_set_neg(1,:),pareto_set_neg(2,:),pareto_set_neg(3,:),'r.')
end
end

% Assign and normalize output if needed
sizeit = size(pareto_set_pos);
lengthit = sizeit(2);
npareto(z) = lengthit;
if flag_normal_dimension == 1
pareto_set_pos_normal(1,:) = (pareto_set_pos(1,:) - rawf1min)./(rawf1max - rawf1min);
pareto_set_pos_normal(2,:) = (pareto_set_pos(2,:) - rawf2min)./(rawf2max - rawf2min);
pareto_set_pos_normal(3,:) = (pareto_set_pos(3,:) - rawf3min)./(rawf3max - rawf3min);
f_vector_out(1:lengthit,1:ND,z) = pareto_set_pos_normal';
else
f_vector_out(1:lengthit,1:ND,z) = pareto_set_pos';
end

% Set appropriate direction for the previously design space dimensions f1, and f2
clear f1temp f2temp f3temp
if dimension_flag(1) == -1
f1temp = (1-f_vector_out(:,1,z));
f_vector_out(:,1,z) = f1temp;
end
if dimension_flag(2) == -1
f2temp = (1-f_vector_out(:,2,z));
f_vector_out(:,2,z) = f2temp;
end
if dimension_flag(3) == -1
f3temp = (1-f_vector_out(:,3,z));
f_vector_out(:,3,z) = f3temp;
end
```

```
% Assign design space samples
f1_vector_out(1:(n^ND),z) = direct*f1norm;
f2_vector_out(1:(n^ND),z) = direct*f2norm;
f3_vector_out(1:(n^ND),z) = direct*f3norm;
end
clear f_vector f1_vector f2_vector f3_vector
f_vector = f_vector_out;
f1_vector = f1_vector_out;
f2_vector = f2_vector_out;
f3_vector = f3_vector_out;
end
```

E.3 Normal Boundary Intersection Algorithm

```
function [] = NBI3_SMP()
global direction fcount flag_2d objective e f1min f2min f3min fmin fmax
global H nnormal x_limit Nvars flagnormal objflag DIRmain DIRobj DIRcurrent
global f_limits flagstart flag_normal_dimension objflagvector fvalue fvalue2d
global flagstart f_limits_overall f_limits_current t_constraint
flag_2d = 0; % 2D optimization flag
fcount = 0; % total number of function calls

% Read in numeric variables
load('input_vars');
x0ini = x0;
Nrandom = nrand;
corenumber = icore;
t_incremental0_original = t_incremental;
stol = 1e-3; % distance between backsolved point and original point

% Read in w list
w = w_list;
sizew = size(w);
nsamples = sizew(1);

% Set appropriate direction for the previously design space dimensions f1, and f2
```

```
if dimension_flag(1) == -1
f1temp = (1-f1);
clear f1
f1 = f1temp;
end
if dimension_flag(2) == -1
f2temp = (1-f2);
clear f2
f2 = f2temp;
end
if dimension_flag(3) == -1
f3temp = (1-f3);
clear f3
f3 = f3temp;
end

% % Optimizer settings
options = optimset('Display','iter','LargeScale','off','TolCon',1e-9); % show progress after each iteration
if x0ini == -1
if flag_initial == 1 % start with min and max closest to objective
Ncombinations = 2^Nvars;
d = fullfact([2*ones(1,Nvars)]);
for i = 1:Ncombinations % number of possible combinationations for variables (2 settings min and max)
for j = 1:Nvars
x(i,j) = x_limit(j,d(i,j));
end
flagnormal = 0; objflag = 1;
[f1(i)] = objfun(x(i,1:Nvars));
flagnormal = 0; objflag = 2;
[f2(i)] = objfun(x(i,1:Nvars));
flagnormal = 0; objflag = 3;
[f3(i)] = objfun(x(i,1:Nvars));
end
[fmin,imin] = min([f1+f2+f3]);
```

```
[fmax,imax] = max([f1+f2+f3]);
for i = 1:Nvars
if objective == 1
x0(1,i) = x(imin,i);
else
x0(1,i) = x(imax,i);
end
end
elseif flag_initial == 2 % random initial point within the design space
for i = 1:Nvars
% starting point for individual minima and maxima (step 1), circle = [3 pi] (must have length of Nvars)
x0(1,i) = [x_limit(i,1) + rand*(x_limit(i,2)-x_limit(i,1))];
end
% start with max values of constraints (works well for spheres)
elseif flag_initial == 3
for i = 1:Nvars
x0(i) = x_limit(i,2);
end
% start with min or max values determined through a random exploration of design space (depends on Nrandom)
elseif flag_initial == 4
% if objective == 1 % minimization (use min)
[minf1,indxf1] = min(f1);
[minf2,indxf2] = min(f2);
[minf3,indxf3] = min(f3);
x0min1(1,1:Nvars) = xrecord(indxf1,1:Nvars);
x0min2(1,1:Nvars) = xrecord(indxf2,1:Nvars);
x0min3(1,1:Nvars) = xrecord(indxf3,1:Nvars);
% else % maximization (use max)
[maxf1,indxf1] = max(f1);
[maxf2,indxf2] = max(f2);
[maxf3,indxf3] = max(f3);
x0max1(1,1:Nvars) = xrecord(indxf1,1:Nvars);
x0max2(1,1:Nvars) = xrecord(indxf2,1:Nvars);
x0max3(1,1:Nvars) = xrecord(indxf3,1:Nvars);
```

```
% end
end
else
x0 = x0ini;
end

% Step 1: Individual minima and maxima
% Objective #1
x0 = x0min1;
flagnormal = 0; objflag = 1;
[x1min,f1min] = fmincon('objfun',x0,[],[],[],[],[],[],'nonlcon',options);
% Objective #2
x0 = x0min2;
flagnormal = 0; objflag = 2;
[x2min,f2min] = fmincon('objfun',x0,[],[],[],[],[],[],'nonlcon',options);
% Objective #3
x0 = x0min3;
flagnormal = 0; objflag = 3;
[x3min,f3min] = fmincon('objfun',x0,[],[],[],[],[],[],'nonlcon',options);
% Objective #1 maximum
x0 = x0max1;
flagnormal = 0; objflag = 4;
[x1max,f1max] = fmincon('objfun',x0,[],[],[],[],[],[],'nonlcon',options);
% Objective #2 maximum
x0 = x0max2;
flagnormal = 0; objflag = 5;
[x2max,f2max] = fmincon('objfun',x0,[],[],[],[],[],[],'nonlcon',options);
% Objective #3 maximum
x0 = x0max3;
flagnormal = 0; objflag = 6;
[x3max,f3max] = fmincon('objfun',x0,[],[],[],[],[],[],'nonlcon',options);
% Evaluate the other dimension
if objective == 1
f = [f1min 0 0; 0 f2min 0; 0 0 f3min];
flagnormal = 0; objflag = 2;
[f(objflag,1)] = objfun(x1min);
```

```
flagnormal = 0; objflag = 3;
[f(objflag,1)] = objfun(x1min);
flagnormal = 0; objflag = 1;
[f(objflag,2)] = objfun(x2min);
flagnormal = 0; objflag = 3;
[f(objflag,2)] = objfun(x2min);
flagnormal = 0; objflag = 1;
[f(objflag,3)] = objfun(x3min);
flagnormal = 0; objflag = 2;
[f(objflag,3)] = objfun(x3min);
else
f = -[f1max 0 0; 0 f2max 0; 0 0 f3max];
flagnormal = 0; objflag = 2;
[f(objflag,1)] = objfun(x1max);
flagnormal = 0; objflag = 3;
[f(objflag,1)] = objfun(x1max);
flagnormal = 0; objflag = 1;
[f(objflag,2)] = objfun(x2max);
flagnormal = 0; objflag = 3;
[f(objflag,2)] = objfun(x2max);
flagnormal = 0; objflag = 1;
[f(objflag,3)] = objfun(x3max);
flagnormal = 0; objflag = 2;
[f(objflag,3)] = objfun(x3max);
end

% Check if two points lie along the same value on one dimension
% This happens with boxy type design spaces
if individual_optima == 1
if objective == 1
% Check 1-2
for i = 1:N
[ftemp,xtemp,flagpoint_dimension] = getlimits(objective,f,N,x1min,x2min,x3min,[1 2],m);
if flagpoint_dimension > 0
f = ftemp;
x2min = xtemp;
```

```
end
end
% Check 2-3
for m = 1:N
[ftemp,xtemp,flagpoint_dimension] = getlimits(objective,f,N,x1min,x2min,x3min,[2 3],m);
if flagpoint_dimension > 0
f = ftemp;
x3min = xtemp;
end
end
% Check 1-3
for m = 1:N
[ftemp,xtemp,flagpoint_dimension] = getlimits(objective,f,N,x1min,x2min,x3min,[1 3],m);
if flagpoint_dimension > 0
f = ftemp;
x3min = xtemp;
end
end
% Check 2-1
for m = 1:N
[ftemp,xtemp,flagpoint_dimension] = getlimits(objective,f,N,x1min,x2min,x3min,[2 1],m);
if flagpoint_dimension > 0
f = ftemp;
x1min = xtemp;
end
end
% Check 3-2
for m = 1:N
[ftemp,xtemp,flagpoint_dimension] = getlimits(objective,f,N,x1min,x2min,x3min,[3 2],m);
if flagpoint_dimension > 0
f = ftemp;
x2min = xtemp;
end
end
% Check 3-1
for m = 1:N
```

```
[ftemp,xtemp,flagpoint_dimension] = getlimits(objective,f,N,x1min,x2min,x3min,[3 1],m);
if flagpoint_dimension > 0
f = ftemp;
x1min = xtemp;
end
end
else
% Check 1-2
for m = 1:N
[ftemp,xtemp,flagpoint_dimension] = getlimits(objective,f,N,x1max,x2max,x3max,[1 2],m);
if flagpoint_dimension > 0
f = ftemp;
x2max = xtemp;
end
end
% Check 2-3
for m = 1:N
[ftemp,xtemp,flagpoint_dimension] = getlimits(objective,f,N,x1max,x2max,x3max,[2 3],m);
if flagpoint_dimension > 0
f = ftemp;
x3max = xtemp;
end
end
% Check 1-3
for m = 1:N
[ftemp,xtemp,flagpoint_dimension] = getlimits(objective,f,N,x1max,x2max,x3max,[1 3],m);
if flagpoint_dimension > 0
f = ftemp;
x3max = xtemp;
end
end
% Check 2-1
for m = 1:N
[ftemp,xtemp,flagpoint_dimension] = getlimits(objective,f,N,x1max,x2max,x3max,[2 1],m);
if flagpoint_dimension > 0
f = ftemp;
```

```
x1max = xtemp;
end
end
% Check 3-2
for m = 1:N
[ftemp,xtemp,flagpoint_dimension] = getlimits(objective,f,N,x1max,x2max,x3max,[3 2],m);
if flagpoint_dimension > 0
f = ftemp;
x2max = xtemp;
end
end
% Check 3-1
for m = 1:N
[ftemp,xtemp,flagpoint_dimension] = getlimits(objective,f,N,x1max,x2max,x3max,[3 1],m);
if flagpoint_dimension > 0
f = ftemp;
x1max = xtemp;
end
end
end
end

% Normalization
fmin = [f1min f2min f3min];
fmax_original = -[f1max f2max f3max];
fmax = max(fmax_original);
f_hat = zeros(N,N);
for i = 1:N
for j = 1:N
[temp] = normalizefun(f(i,j),fmin(i),fmax);
f_hat(i,j) = temp;
end
end

% Iterative Steps
% ————————
```

```
count = 1;
F = f_hat; % non-iterative
for i = 1:nsamples
wi = w(i,1:N)';
H = dotprod(F,wi);

% Step 3: Approximate normal vector
if objective == 1
L = -ones(N,1);
nnormal = dotprod(F,L); % non-iterative
nnormal = nnormal./(max(nnormal));
else
L = ones(N,1);
nnormal = dotprod(F,L); % non-iterative
nnormal = nnormal./(max(nnormal));
end

% Step 4: Compute Pareto point
% Determine x values for starting point on convex hull H
if NBI3mode == 0
if i == 1
if objective == 1
x0 = [x1min t0]; % x1min for sphere ellipse
else
x0 = [x2max t0]; % x2max for sphere ellipse
end
end
else
f1norm = nonnormalizefun(f1,f_limits_overall(1,1),f_limits_overall(1,2));
f2norm = nonnormalizefun(f2,f_limits_overall(2,1),f_limits_overall(2,2));
f3norm = nonnormalizefun(f3,f_limits_overall(3,1),f_limits_overall(3,2));
f1norm = normalizefun(f1norm,f_limits_current(1,1),f_limits_current(1,2));
f2norm = normalizefun(f2norm,f_limits_current(2,1),f_limits_current(2,2));
f3norm = normalizefun(f3norm,f_limits_current(3,1),f_limits_current(3,2));
S_hull = sqrt(((H(1)-f1norm).^2) + ((H(2)-f2norm).^2) + ((H(3)-f3norm).^2));
[S_hull_sorted,indx] = sort(S_hull,'ascend');
```

```
end
if NBI3mode == 0
direction = 1;
[x,t,exitflag,output,lambda,grad,hessian] = fmincon('objfun4',x0,[],[],[],[],[],[],'nonlcon4',options);
if exitflag ~= 1
DIRcurrent = pwd;

% Compute the x values of H for x0
f1norm = nonnormalizefun(f1,f_limits_overall(1,1),f_limits_overall(1,2));
f2norm = nonnormalizefun(f2,f_limits_overall(2,1),f_limits_overall(2,2));
f3norm = nonnormalizefun(f3,f_limits_overall(3,1),f_limits_overall(3,2));
f1norm = normalizefun(f1norm,f_limits_current(1,1),f_limits_current(1,2));
f2norm = normalizefun(f2norm,f_limits_current(2,1),f_limits_current(2,2));
f3norm = normalizefun(f3norm,f_limits_current(3,1),f_limits_current(3,2));
S_hull = sqrt(((H(1)-f1norm).^2) + ((H(2)-f2norm).^2) + ((H(3)-f3norm).^2));
[S_hull_sorted,indx] = sort(S_hull,'ascend');
x0 = [xrecord(indx(1),1:Nvars) 0];
[x,S,exitflag] = run_backsolve(H(1),H(2),H(3),x0); % uses x0 = xrecord closest to H(1),H(2),H(3)

% Recompute H with backsolved x to check if correct
flagnormal = 0; objflag = 1;
H_computed(1) = objfun(x(1:end-1));
flagnormal = 0; objflag = 2;
H_computed(2) = objfun(x(1:end-1));
flagnormal = 0; objflag = 3;
H_computed(3) = objfun(x(1:end-1));

if flag_goldensearch == 1 % Golden Search
t_line = 0:0.001:sqrt(3);
clear f_line
for ii = 1:N
f_line(ii,:) = H(ii) + t_line*nnormal(ii);
end
for ii = 1:length(t_line)
if f_line(1,ii) > 1 || f_line(2,ii) > 1 || f_line(3,ii) > 1
index_1 = ii-1;
```

```
    break
    end
    end
    f_line_temp = f_line(1:N,1:index_1);
    clear f_line
    f_line = f_line_temp;
    if isempty(f_line) == 1
    S_max = 0;
    else
    S_max = sqrt( ((H(1)-f_line(1,end))^2) + ((H(2)-f_line(2,end))^2) + ((H(3)-f_line(3,end))^2)
);
    end
    if S_max > 0
    tol = golden_tol;
    at = 0;
    bt = 0.5*S_max;
    ct = S_max;
    C = (3-sqrt(5))/2;
    R = 1-C;
    t1 = at;
    t4 = ct;
    if (abs(ct-bt) > abs(bt-at)),
    t2 = bt;
    t3 = bt + C*(ct-bt);
    else
    t3 = bt;
    t2 = bt - C*(bt-at);
    end

    % Compute the new f1,f2,f3 for point 1 on Golden Search
    f_step_1 = H + t2*nnormal;
    clear global f1_sample f2_sample f3_sample
    [x1new,S1,exitflag] = run_backsolve(f_step_1(1),f_step_1(2),f_step_1(3),[x0 0]); % uses
x0 = xrecord closest to f_step (this does not prove feasibility)
    f_step_2 = H + t3*nnormal;
    clear global f1_sample f2_sample f3_sample
```

```
[x2new,S2,exitflag] = run_backsolve(f_step_2(1),f_step_2(2),f_step_2(3),[x0 0]); % uses
x0 = xrecord closest to f_step (this does not prove feasibility)
flagstop = 0;
if (S1 < stol) && (S2 < stol)
f1 = 2;
f2 = 1;
elseif (S1 < stol) && (S2 > stol)
f1 = 2;
f2 = 1;
elseif (S1 > stol) && (S2 < stol)
f1 = 1;
f2 = 2;
else
flagstop = 1;
end
if flagstop == 0
k = 1;
while (abs(t4-t1) > tol) && (flagstop ~= 1)
if f2 < f1
t1 = t2;
t2 = t3;
t3 = R*t2 + C*t4;
S1 = S2;
f_step_2 = H + t3*nnormal;
clear global f1_sample f2_sample f3_sample
[x2new,S2,exitflag] = run_backsolve(f_step_2(1),f_step_2(2),f_step_2(3),[x2new 0]); %
uses x0 = xrecord closest to f_step (this does not prove feasibility)
else
t4 = t3;
t3 = t2;
t2 = R*t3 + C*t1;
S2 = S1;
f_step_1 = H + t2*nnormal;
clear global f1_sample f2_sample f3_sample
[x1new,S1,exitflag] = run_backsolve(f_step_1(1),f_step_1(2),f_step_1(3),[x1new 0]); %
uses x0 = xrecord closest to f_step (this does not prove feasibility)
```

```
end
if (S1 < stol) && (S2 < stol)
f1 = 2;
f2 = 1;
elseif (S1 < stol) && (S2 > stol)
f1 = 2;
f2 = 1;
elseif (S1 > stol) && (S2 < stol)
f1 = 1;
f2 = 2;
else
flagstop = 1;
end
k = k+1;
end
end
if (S1 < stol) && (S2 < stol)
t = -t3;
elseif (S1 < stol) && (S2 > stol)
t = -t2;
elseif (S1 > stol) && (S2 < stol) % shouldnt happen
t = -t1;
else
t = -t1;
end
else
t = 0;
end

else % incremental instead of Golden Search

t_incremental0 = t_incremental0_original;
t_incremental = 0;
i_iter = 0;
feasible = 1;
```

```
while i_iter <= n_iter && t_incremental >= 0
% Compute the new f1,f2,f3
f_step = H + t_incremental*nnormal;
clear global f1_sample f2_sample f3_sample
[x,S,exitflag] = run_backsolve(f_step(1),f_step(2),f_step(3),x0); % uses x0 = xrecord closest to f_step (this does not prove feasibility)
x_prev = x0;

% Recompute f with backsolved x to check if correct
flagnormal = 0; objflag = 1;
f_computed(1) = objfun(x(1:end-1));
flagnormal = 0; objflag = 2;
f_computed(2) = objfun(x(1:end-1));
flagnormal = 0; objflag = 3;
f_computed(3) = objfun(x(1:end-1));

% Check if it is feasible or not
% if the run_backsolve optimizer found exitflag = 1 then it
% means it hit a contraint before minimizing the distance
% from f_step to f_computed, so the point is infeasible. An
% exitflag = 0 means the points is feasible
if S <= stol
feasible = 1;
t_incremental = t_incremental + t_incremental0;
i_iter = 1;
else
t_incremental = t_incremental - t_incremental0;
t_incremental0 = 0.5*t_incremental0;
t_incremental = t_incremental + t_incremental0;
i_iter = i_iter + 1;
feasible = 1;
end
end
t = -(abs(t_incremental) - t_incremental0);
end
else
```

```
x0 = [x(1:end-1) t0];
end
else % use closest existing sample point as a starting point
nloop = 1;
exitflag = -1;
while (nloop <= 5) && (exitflag < 0)
x0 = [xrecord(indx(nloop),1:Nvars) t0];
[x,t,exitflag,output,lambda,grad,hessian] = fmincon('objfun4',x0,[],[],[],[],[],[],'nonlcon4',options);
nloop = nloop + 1;
end
end
exitflag_record(i) = exitflag;
t_vector(i) = -t;
f_vector_normal(i,1:N) = H + t_vector(i)*nnormal;
if flag_normal_dimension == 1
f_vector(count,1) = nonnormalizefun(f_vector_normal(i,1),f_limits_current(1,1),f_limits_current(1,2));
f_vector(count,2) = nonnormalizefun(f_vector_normal(i,2),f_limits_current(2,1),f_limits_current(2,2));
f_vector(count,3) = nonnormalizefun(f_vector_normal(i,3),f_limits_current(3,1),f_limits_current(3,2));
f_vector(count,1) = normalizefun(f_vector(count,1),f_limits_overall(1,1),f_limits_overall(1,2));
f_vector(count,2) = normalizefun(f_vector(count,2),f_limits_overall(2,1),f_limits_overall(2,2));
f_vector(count,3) = normalizefun(f_vector(count,3),f_limits_overall(3,1),f_limits_overall(3,2));
H_vector(count,1) = nonnormalizefun(H(1),f_limits_current(1,1),f_limits_current(1,2));
H_vector(count,2) = nonnormalizefun(H(2),f_limits_current(2,1),f_limits_current(2,2));
H_vector(count,3) = nonnormalizefun(H(3),f_limits_current(3,1),f_limits_current(3,2));
H_vector(count,1) = normalizefun(H_vector(count,1),f_limits_overall(1,1),f_limits_overall(1,2));
H_vector(count,2) = normalizefun(H_vector(count,2),f_limits_overall(2,1),f_limits_overall(2,2));
H_vector(count,3) = normalizefun(H_vector(count,3),f_limits_overall(3,1),f_limits_overall(3,2));
else
f_vector(count,1) = nonnormalizefun(f_vector_normal(i,1),f_limits_current(1,1),f_limits_current(1,2));
f_vector(count,2) = nonnormalizefun(f_vector_normal(i,2),f_limits_current(2,1),f_limits_current(2,2));
f_vector(count,3) = nonnormalizefun(f_vector_normal(i,3),f_limits_current(3,1),f_limits_current(3,2));

% Record convex hull H_vector
H_vector(count,1) = nonnormalizefun(H(1),f_limits_current(1,1),f_limits_current(1,2));
H_vector(count,2) = nonnormalizefun(H(2),f_limits_current(2,1),f_limits_current(2,2));
H_vector(count,3) = nonnormalizefun(H(3),f_limits_current(3,1),f_limits_current(3,2));
```

```
end
if strcmp(iteration_display,'iter') == 1
fprintf('Completed convex hull points: %5.2f%%\n',(100*count/nsamples));
end
count = count + 1;
end

% Compute exterior (edges) points on the 2D sections f1-f3, f1-f2, f2-f3
if flag_edge == 1
flag_2d = corenumber;
if corenumber <= N

% Compute 2D weighted vector which determines location of points on convex hull
n_exterior = n - 2; % Substract 2 to account for extreme points which will be added later
dw = 1/(n-1);
wvector = ones(1,n_exterior)*dw;
for i = 2:n_exterior
wvector(i) = wvector(i)+wvector(i-1);
end
clear F wi L nnormal x0 x t t_vector f_vector_normal
clear global nnormal H
global H nnormal
count = 1;
for i = 1:n_exterior % n_exterior is the total number of points along each edge not including the corner points
F = f_hat; % non-iterative
F(:,corenumber) = zeros(3,1);
if corenumber == 1
wi = [0; wvector(i); 1-wvector(i)];
elseif corenumber == 2
wi = [wvector(i); 0; 1-wvector(i)];
else
wi = [wvector(i); 1-wvector(i); 0];
end
H = dotprod(F,wi);
```

```
% Step 3: Approximate normal vector
if objective == 1
L = -ones(N,1);
nnormal = dotprod(F,L); % non-iterative
else
L = ones(N,1);
nnormal = dotprod(F,L); % non-iterative
end

% Step 4: Compute Pareto point
% Determin x values for starting point on convex hull H
if i == 1
if objective == 1 % objective direction minimization
% set the starting point to one on the feasible plane (ie.
% for plane f1-f2 start with either x1min or x2min, for
% f2-f3 use x2min or x3min, for plane f1-f3 use x1min or x3min
if flag_2d == 1
x0 = [x2min t0];
elseif flag_2d == 2
x0 = [x1min t0];
elseif flag_2d == 3
x0 = [x1min t0];
end

else % objective direction maximization

% set the starting point to one on the feasible plane (ie.
% for plane f1-f2 start with either x1max or x2max, for
% f2-f3 use x2max or x3max, for plane f1-f3 use x1max or x3max
if flag_2d == 1
x0 = [x2max t0];
elseif flag_2d == 2
x0 = [x1max t0];
elseif flag_2d == 3
x0 = [x1max t0];
end
```

```
end
end

[x,t] = fmincon('objfun4',x0,[],[],[],[],[],[],'nonlcon4',options);
x0 = x;
t_vector(i) = -t;
f_vector_normal(i,1:N) = H + t_vector(i)*nnormal;

% Transform to original dimension (non-normalized)
fmin_current(1) = f_limits_current(1,1);
fmin_current(2) = f_limits_current(2,1);
fmin_current(3) = f_limits_current(3,1);
fmax_current(1) = f_limits_current(1,2);
fmax_current(2) = f_limits_current(2,2);
fmax_current(3) = f_limits_current(3,2);
f_vector_edge(count,1) = nonnormalizefun(f_vector_normal(i,1),fmin_current(1),fmax_current(1));
f_vector_edge(count,2) = nonnormalizefun(f_vector_normal(i,2),fmin_current(2),fmax_current(2));
f_vector_edge(count,3) = nonnormalizefun(f_vector_normal(i,3),fmin_current(3),fmax_current(3));

% Record convex hull H_vector
H_vector_edge(count,1) = nonnormalizefun(H(1),fmin_current(1),fmax_current(1));
H_vector_edge(count,2) = nonnormalizefun(H(2),fmin_current(2),fmax_current(2));
H_vector_edge(count,3) = nonnormalizefun(H(3),fmin_current(3),fmax_current(3));
if strcmp(iteration_display,'iter') == 1
fprintf('Completed edge points: %5.2f%%\n',(100*count/n_exterior));
end
count = count + 1;
end
end
end

% Save results workspace
f_limit = [fmin(1) fmin(2) fmin(3) fmax_original(1) fmax_original(2) fmax_original(3)];
if corenumber <= N
if flag_edge == 1
save(['Core',num2str(corenumber),'_Results'],'f_limit','H_vector','f_vector','H_vector_edge','f_vector_edge','f1
```

```
else
save(['Core',num2str(corenumber),'_Results'],'f_limit','H_vector','f_vector','f1','f2','f3','fcount');
end
else
save(['Core',num2str(corenumber),'_Results'],'f_limit','H_vector','f_vector','f1','f2','f3','fcount');
end
end

%% Check real limits in boxy design spaces
function [f,x,flagpoint_dimension] = getlimits(objective,f,N,x1,x2,x3,dimensions,j)
global flagnormal objflag objflagvector fvalue2d fvalue
if objective == 1
x1min = x1;
x2min = x2;
x3min = x3;
else
x1max = x1;
x2max = x2;
x3max = x3;
end
% Check points 1 and 2
ftemp = f(:,dimensions(2)) - f(:,dimensions(1));
if abs(ftemp(j,1)) < 0.05
global flagpoint_dimension
flagpoint_dimension = j;
flag_first_point = dimensions(1);
fvalue = f(j,flag_first_point);
end
if exist('flagpoint_dimension') == 1
if objective == 1
if dimensions(2) == 1
x0 = x1min;
elseif dimensions(2) == 2
x0 = x2min;
else
x0 = x3min;
```

```
end
else
if dimensions(2) == 1
x0 = x1max;
elseif dimensions(2) == 2
x0 = x2max;
else
x0 = x3max;
end
end
objflagvector = 1:3;
objflagvector(flagpoint_dimension) = [];
fvalue2d(1) = f(objflagvector(1),flag_first_point);
fvalue2d(2) = f(objflagvector(2),flag_first_point);
options = optimset('Display','iter','LargeScale','off','TolCon',1e-9); % show progress after
each iteration
[x,S] = fmincon('myfun_2d',x0,[],[],[],[],[],[],'nonlcon_2d',options);

% Compute new f values of point for convex hull
flagnormal = 0; objflag = objflagvector(1);
[f(objflag,dimensions(2))] = objfun(x);
flagnormal = 0; objflag = objflagvector(2);
[f(objflag,dimensions(2))] = objfun(x);
else
f = 0;
x = 0;
flagpoint_dimension = 0;
end
end
```

REFERENCES

[1] Anderson, J., *Aircraft Performance and Design*. McGraw-Hill, 1999.

[2] Anderson, J. D., *Fundamentals of Aerodynamics*. McGraw-Hill, 2001.

[3] Bain, S., "Design, analysis, and risk mitigation." http://www.netobjectives.com/blogs/design-patterns-analysis-risk-mitigation-tdd-test-driven-design, November 16th 2007.

[4] Bandte, O. and Mavris, D. N., "Comparison of two probabilistic techniques for the assessment of economic uncertainty." Georgia Institute of Technology.

[5] Bandte, O. and Mavris, D. N., "Multi-objective optimization using a joint probabilistic technique," in *8th AIAA/NASA/USAF/ISSMO Symposium on Multidisciplinary Analysis and Optimization, Long Beach, CA, AIAA-2000-4758*, September 6-8, 2000.

[6] Bertin, J. J., *Hypersonic Aerothermodynamics*. AIAA Educational Series, 1994.

[7] Bhungalia, A. A., Beran, P. S., Chen, P. C., Lee, D. H., and Liu, D. D., "Hypersonic aerothermodynamics TPS design, analysis and optimization: Affordable responsive spacelift (ARES) booster case study." 11th AIAA/ISSMO Multidisciplinary Analysis and Optimization Conference, Portsmouth, Virginia, AIAA-2006-7124, September 6-8, 2006.

[8] Bhungalia, A. A., Clewett, L. C., Croop, H., and Brown, D. A., "Thermal protection system (TPS) optimization," in *Soace 2004 Conference and Exhibit, San Diego, California, AIAA-2004-5826*, September 28-30, 2004.

[9] Biltgen, P. T. and Mavris, D. N., "A technique for interactive probabilistic multiple attribute decision making," in *45th AIAA Aerospace Sciences Meeting and Exhibit, Reno, Nevada, AIAA-2007-1332*, January 8-11, 2007.

[10] Blanchard, B. S., *System Engineering Management*. John Wiley & Sons, Inc., 2003.

[11] Blosser, M., "Thermal protection systems for reusable launch vehicles; short course: Thermal control hardware," August 2003.

[12] Borer, N. K. and Mavris, D. N., "Multiple criteria decision making for large scale systems design." AIAA 5th Aviation, Technology, Integration, and Operations Conference (ATIO), Arlington, Virginia, AIAA-2005-7437, September 26-28, 2005.

[13] Bowcutt, K. G., "Technical fellowship advisory board study: Hypersonic technology status and development roadmap." Presentation to AIAA HyTASP Program Committee, December 18, 2003.

[14] Bryson, A. E., Desai, M. N., and Hohhman, W., "Energy-state approximation in performance optimization of supersonic aircraft," *Journal of Aircraft*, vol. 6, pp. 481–488, 1969.

[15] Cengel, Y. A. and Boles, M. A., *Thermodynamics: An Engineering Approach, 4th Ed.* McGraw-Hill Science/Engineering/Math, 2001.

[16] Center, O. T., "Sequential quadratic programming." http://www-fp.mcs.anl.gov/otc/Guide/OptWeb/, March 28, 1996.

[17] Chen, A. Y. and Dang, L., "Characterization of supercritical JP-7's heat transfer and coking properties," *AIAA-2002-0005*, 2002.

[18] Chen, P., Liu, D., Chang, K., Tang, L., and Gao, X., "Aerothermodynamic optimization of hypersonic vehicle TPS design by POD/RSM-based approach," in *44th AIAA Aerospace Sciences Meeting and Exhibit, Reno, Nevada, AIAA-2006-777*, Jan. 9-12, 2006.

[19] Chou, H., Ardema, M. D., and Bowles, J. V., "Near-optimal entry trajectories for reusable launch vehicles," *Journal of Guidance, Control, and Dynamics*, vol. 21 no.6, pp. 983–990, 1998.

[20] Co, H. C., "Goal programming example." California Polytechnic & State University.

[21] Compiled by Arrington, J. P. and Jones, J. J., *Shuttle Performance: Lessons Learned.* NASA Conference Publication 2283, March 8-10, 1983.

[22] Cowart, K. K. and Olds, J. R., "TCAT - a tool for automated thermal protection system design," in *AIAA Space 2000 Conference and Exposition, A00-42949*, 2000.

[23] Daberkow, D. D. and Mavris, D. N., "An investigation of metamodeling techniques for complex systems design," in *9th AIAA/ISSMO Symposium on Multidisciplinary Analysis and Optimization, Atlanta, Georgia, AIAA-2002-5457*, 2002.

[24] Dieter, G. E., *Engineering Design: A Material and Processes Approach, 3rd Ed.* McGraw-Hill, 2000.

[25] Du, X. and Chen, W., "A most probable point based method for uncertainty analysis." ASME 2000 Design Engineering Technical Conferences and Computers and Information in Engineering Conference, 2000.

[26] Ehrgott, M. and Gandibleu, X., "A survey and annotated bibliography of multiobjective combinatorial optimization." OR Spektrum (2000) 22: 425-460, 2000.

[27] Ehrlich, C. e. a., "Advanced manned launch system study (AMLS); Final technical review - task 5; TPS/insulation concepts for reusable cryo tanks," *SSD93D0310, Contract NAS1-18975 DRD-9, Rockwell International, Space Systems Division, Downey, CA*, p. 359., July 1993.

[28] Engel, C. D. and Praharaj, S. C., *MINIVER Upgrade for the AVID System, Vol 1: LANMIN User's Manual.* REMTECH, Inc., Huntsville, AL, contract nas1-16983 ed., August 1983.

[29] Engel, C. D. and Schmitz, C. P., *MINIVER Upgrade for the AVID System, Vol 2: LANMIN Input Guide*. REMTECH, Inc., Huntsville, AL, contract nas1-16983 ed., August 1983.

[30] Faghri, A., *Heat Pipe Science And Technology*. US: Taylor & Francis, 1995.

[31] FAS, "B-70 Valkyrie." http://www.fas.org/nuke/guide/usa/bomber/b-70.htm.

[32] Feagin, R., "Transonic aircraft drag techniques applied to military aircraft, volume 2." NASA Contract No. NAS2-8612, 1978.

[33] Garcia, F. J. and Fowler, W. T., "Thermal protection system weight minimization for the space shuttle through trajectory optimization," *Journal of Spacecraft and Rockets*, vol. 0022-4650 vol.11 no.4, pp. 241–245, 1974.

[34] Giunta, A., Wojtkiewicz, S. J., and M.S., E., "Overview of modern design of experiments methods for computational simulations," in *Proceedings of the 41st AIAA Aerospace Sciences Meeting and Exhibiy, Reno, Nevada, AIAA-2003-0649*, January 6-9, 2003.

[35] Gloudemans, J. R., Davis, P. C., and Gelhausen, P. A., "A rapid geometry modeler for conceptual aircraft." American Institute of Aeronautics and Astronautics, Inc., AIAA-96-0052, 1996.

[36] Gockenbach, M. S., "Introduction to sequential quadratic programming." http://www.math.mtu.edu/ msgocken/ma5630spring2003/, 2003.

[37] Gupta, S., "On nonlinear determination of Pareto fronts." Internal Report - University of Munich.

[38] Hallion, R. P., "The history of hypersonics: or, "Back to the future-again and again"," in *43rd AIAA Aerospace Sciences Meeting and Exhibit, AIAA-2005-0329*, January 10-13, 2005.

[39] Hollingsworth, P. M. and Mavris, D. N., "Gaussian process meta-modeling: Comparison of Gaussian process trainning methods," in *AIAA's 3rd Annual Aviation Technology, Integration, and Operations (ATIO) Tech, Denver, Colorado, AIAA-2003-6761*, 2003.

[40] J., F. M., *Engineering Design: The Conceptual Stage*. Heinemann Educational Books, 1971.

[41] Jackson, Jr., C. M., "Estimation of flight performance with closed-form approximations to the equations of motion," tech. rep., NASA Langley Research Center, Hampton, VA, 1966.

[42] Jacques, S., "The basic Monte Carlo technique." Oregon Medical Laser Center, http://omlc.ogi.edu/news/sep98/montecarlosampling/montecarlo1.html, September 1998.

[43] Johns Manville, F. D., *Q-Fiber*. http://www.jm.com/.

[44] Johnson, C. and Schutte, J., *Basic Regression Analysis for Integrated Neural Networks (BRAINN) Documentation, ver 2.1.* Aerospace Systems Design Lab, June 21, 2007.

[45] Johnson, V. S., "Minimizing life cycle cost for subsonic commercial aircraft," *Journal of Aircraft*, vol. 27, No. 2, pp. 139–145, February 1990.

[46] Kim, I. Y. and de Weck, O., "Adaptive weighted sum method for multi-objective optimization: A new method for Pareto front generation." Struct Multidisc Optim (2006) 31: 105-116, 2006.

[47] Kokan, T., Olds, J. R., Hutchinson, V., and Reeves, J. D., "Aztec: A TSTO hypersonic vehicle concept utilizing TBCC and HEDM propulsion technologies," in *40th AIAA/ASME/SAE/ASEE Joint Propulsion Conference and Exhibit, AIAA-2004-3728*, 2004.

[48] Kolodziej, P., Bowles, J. V., and Roberts, C., "Optimizing hypersonic sharp body concepts from a thermal protection system perspective," *American Institute of Aeronautics and Astronautics, Inc., AIAA-98-1610*, pp. 556–571, 1998.

[49] Laumanns, M., Thiele, L., and Zitzler, E., "An adaptive scheme to generate the pareto front based on the epsilon-constraint method." Internationales Begegnungs- und Forschungszentrum fuer Informatik (IBFI), Schloss Dagstuhl, Germany, 2005.

[50] Lenne, D. L., Meyer, M. L., Edwards, T., and Eitman, D. A., "Evaluation of heat transfer and thermal stability of supercritical JP-7 fuel," in *AIAA/ASME/SAE/ASEE 33rd Joint Propulsion Conference and Exhibit*, July 1997.

[51] Leonard, B. G., Charette, R. O., Ferguson, Preston W., S., and J., W., "Technology advanced requirements for effective military spaceplanes." American Institute of Aeronautics and Astronautics, Inc., AIAA-1997-3927-843, 1997.

[52] Leonard, C. P., Amundsen, R. M., and Bruce III, W. E., "Hyper-X hot structures design and comparison with flight data," in *AIAA/CIRA 13th International Space Planes and Hypersonics Systems and Technologies, AIAA-2005-3438*, 2005.

[53] Liu, D., Chen, P., Tang, L., and Chang, K., "Hypersonic aerothermodynamics/aerothermoelastics methodology for reusable launch vehicles/TPS design and analysis." 41st Aerospace Sciences Meeting and Exhibit, Reno, Nevada, AIAA-2003-897, January 6-9, 2003.

[54] Loerch, A. G., "Linear goal programming." Military Operations Research Department of Systems Engineering and Operations Research, George Mason University.

[55] Lotov, A. V., *Interactive Decision Maps.* Kluwer Academic Publishers, 2004.

[56] Matches., "Exchanger cost." http://www.matche.com/EquipCost/Exchanger.htm.

[57] MathWorks, T., "MATLAB - The language of technical computing." http://www.mathworks.com/products/matlab/.

[58] Mattingly, J. D., *Elements of Gas Turbine Propulsion.* McGraw-Hill, 1996.

[59] Mavris, D. M., "A stochastic IPPD approach to system affordability." ASDL Georgia Tech.

[60] Mavris, D. M., "Overview of Georgia Tech systems engineering analysis techniques," May 2003.

[61] McGuire, M. K., Gage, P., Galloway, E. T., Huynh, L., Nguyen, J., and Bowles, Jeffrey., W. R., "Trajectory and thermal protection system design for reusable launch vehicles," in *10th AIAA/ISSMO Multidisciplinary Analysis and Optimization Conference, Albany, NY, AIAA-2004-4490*, 2004.

[62] Mor, M. and Livne, E., "Multidisciplinary design optimization of reentry vehicles: Trajectory optimization and sensitivities," in *47th AIAA/ASME/ASCE/AHS/ASC Structures, Structural Dynamics, and Materials Conference*, 2006.

[63] Moser, T., "Review of the design and development orbiter structure and thermal protection system (TPS)." MIT Lecture, September 22 2005.

[64] Myers, D. E., Martin, C. J., and Blosser, M. L., "Parametric weight comparison of current and proposed thermal protection system (TPS) concepts," in *33rd Thermophysics Conference, AIAA-1999-3459*, 1999.

[65] Nam, T., "Advanced design methodology - PhD qualification exam study guide (ver 2.0)," September 19, 2004.

[66] NASA, "TPSX material properties database, web edition ver. 4." http://tpsx.arc.nasa.gov/.

[67] Nixon, J., *A Systematic Process for Adaptive Concept Exploration*. PhD thesis, Georgia Institute of Technology, School of Aerospace Engineering, December 2006.

[68] Ogasawara, K. and Nishioka, T., "Proposal of the reentry vehicle design index to minimize integrated heat load," in *39th AIAA Aerospace Sciences Meeting and Exhibit, A01-16890*, 2001.

[69] Olds, J. R., "Results of a rocket-based combined-cycle SST0 design using parametric MD0 methods." SAE 94-1165, Aerospace Atlantic Conference, Dayton, OH, April 1994.

[70] Olds, J. R., Bradford, J., Charania, A., Ledsinger, L., McCormick, D., and Sorensen, K., "An SST0, vision vehicle concept utilizing hyperion: Rocket-based combined cycle propulsion." American Institute of Aeronautics and Astronautics, Inc., AIAA-1999-4944-265.

[71] Osburg, J. and Mavris, D. N., "Support of Pratt & Whitney TBCC propulsion system design space exploration," June 2007.

[72] Powell, R. W., "Six-degree-of-freedom guidance and control-entry analysis of the HL-20," *Journals of Spacecraft and Rockets*, vol. 30 no.5, pp. 537–542, 1993.

[73] Prabhu, D. K., Loomis, M. P., Venkatapathy, E., Polsky, S., Papadopoulos, P., and Davies, C. B., "X-33 aerothermal environment simulations and aerothermodynamic design," in *Aerospace Sciences Meeting and Exhibit, 36th, Reno, NV, AIAA-1998-868*, January 12-15, 1998.

[74] Ran, H. and Mavris, D. N., "A framework for determination of the weak Pareto frontier design solutions under probabilistic constraints," in *11th AIAA/ISSMO Multidisciplinary Analysis and Optimization Conference, Portsmouth, Virginia, AIAA-2006-6960*, 2006.

[75] Raymer, D. P., *Aircraft Design: A Conceptual Design Approach.* AIAA Educational Series, 2006.

[76] Richman, M. S., Kenyon, J. A., and Sega, R. M., "High speed and hypersonic science and technology," in *41 AIAA/ASME/SAE/ASEE Joint Propulsion Conference and Exhibit, Tucson, Arizona, AIAA-2005-4099*, July 10-13, 2005.

[77] Robinson, J. S., "Life cycle analysis of a single stage to orbit (SSTO) reusable launch vehicle," in *39th AIAA/ASME/SAE/ASEE Joint Propulsion Conference and Exhibit, Huntsville, Alabama, AIAA-2003-5264*, July 20-23, 2003.

[78] Rode, D., "Introduction to linear programming." Decision Analysis and Decision Support Systems - The "Unofficial" Website, Dept. of Social and Decision Sciences, Carnegie Mellon University.

[79] Roskam, J., *Airplane Design. Part VIII: Airplane Cost Estimation: Design, Development, Manufacturing and Operating.* Roskam Aviation and Engineering Corporation, 1990.

[80] Ruffin, S. M., "Numerical aerodynamic simulation via Cartesian grid techniques." http://www.ae.gatech.edu/people/sruffin/nascart/.

[81] Ruffin, S. M., "Hypersonic flow introduction, course: AE6020 - high speed flow," 2003.

[82] Sachs, G. and Dinkelmann, M., "Heat input reduction in hypersonic flight by optimal trajectory control," in *Guidance, Navigation and Control Conference, San Diego, CA, AIAA-1996-3905*, July 29-31, 1996.

[83] Schaumann, E. J., Balling, R. J., and Day, K., "Genetic algorithms with multiple objectives." American Institute of Aeronautics and Astronautics, Inc., AIAA-98-4974, 1998.

[84] Schrage, D. and DeLaurentis, D., "IPPD concept development process for future combat system," in *9th AIAA/ISSMO Symposium on Multidisciplinary Analysis and Optimization, Atlanta, Georgia*, September 4-6, 2002.

[85] Soban, D. S. and Mavris, D. N., "The need for a military system effectiveness framework: The system of systems approach," *American Institute of Aeronautics and Astronautics, Inc., AIAA-2001-5226*, 2001.

[86] Stehr, G., Graeb, H., and Antreich, K., "Performance tradeoff analysis of analog circuits by normal boundary intersection," in *DAC 2003, Anaheim, California*, June 2-6, 2003.

[87] Strager, M., "Goal programming - guest lecture," Oct 19.

[88] Sudmeijer, K. and Mooij, E., "Shape optimization for a small experimental reentry module," in *AIAA/AAAF 11th International Space Planes and Hypersonic Systems and Technologies Conference*, 2002.

[89] Tava, M. and Suzuki, S., "Multidisciplinary design optimization of reentry vehicle shape and trajectory," in *AIAA/NAL-NASDA-ISAS 10th International Space Planes and Hypersonic Systems and Technologies Conference*, 2001.

[90] Vanderplaats, G. N., *Numerical Optimization Techniques for Engineering Design (3rd Edition)*. Vanderplaats Research & Development, Inc., 2001.

[91] Villeneuve, F., "Pratt & Whitney / Georgia Tech hypersonic vehicle design effort - XB-70 validation." ASDL - Georgia Institute of Technology, 2007.

[92] Wilson, B., Cappelleri, D., Simpson, T. W., and Frecker, M., "Efficient Pareto frontier exploration using surrogate approximations." Optimization and Engineering, Kluwer Academic Publishers, May 2001.

[93] Windhorst, R., Galloway, E., Lau, E., Saunders, D., and Gage, P., "Aerospace vehicle trajectory design and optimization within a multi-disciplinary environment," *Journal of Aerospace Computing, Information, and Communication*, vol. 3 no.9, pp. 471–485, 2006.

[94] Wurster, K. E. and Stone, H. W., "Aerodynamic heating environment definition/thermal protection system selection for the HL-20," *Journal of Spacecraft and Rockets*, vol. 30 no.5, pp. 549–557, 1993.

[95] Wurster, K. E., Zoby, E. V., and Thompson, R. A., "Flowfield and vehicle parameter influence on results of engineering aerothermal methods." Journal of Spacecraft and Rockets, Vol. 28, No. 1, 0022-4650, 1991.

[96] Zink, P. S., Mavris, D. N., Love, M. H., and Karpel, M., "Robust design for aeroelastically tailored / active aeroelastic wing," *American Institute of Aeronautics and Astronautics, Inc., AIAA-98-4781*, pp. pp. 559–569, 1998.

[97] Zweber, J. V. and Pendleton, E., "Multiple attribute decision making techniques applied to reusable responsive spacelift," in *48th AIAA/ASME/ASCE/AHS/ASC Structures, Structural Dynamics, and Materials Conference, Honolulu, Hawaii, AIAA-2007-1861*, April 23-26, 2007.

VITA

Irian Ordaz was born in Habana, Cuba, on January 13, 1980, son to Miriam and Rolando A. Ordaz. At the age of 13, he and his family moved to Miami, Florida, where he continued his studies at Miami Coral Park High School.

After graduating high school with honors in 1998, he enrolled in the Aerospace Engineering program at University of Miami. After completing his first two years, he transferred to Georgia Institute of Technology where he earned his Bachelor's in Aerospace engineering with high honors in the summer of 2002, and Masters in the summer of 2004. He successfully passed the PhD qualifier exams in the area of Advanced Design Methods, Fixed Wing Design, and Rotorcraft Aeromechanics in the Fall of 2006, and is expected to be awarded his PhD in Fall 2008. During his undergraduate and graduate studies he was involved in a variety of projects including aerodynamic prediction for channel wings and wing blowing, aerodynamic analysis and tool integration for a morphing UCAV supported by Boeing Phantom Works.

During his years of graduate studies he worked on the development of improved techniques to bring engineering knowledge to the early phases of aircraft design, as well as integration and automation methods for various disciplinary tools in conceptual design. His work has also included the analysis of mission requirements and impact of current technologies to help guide future technology development.